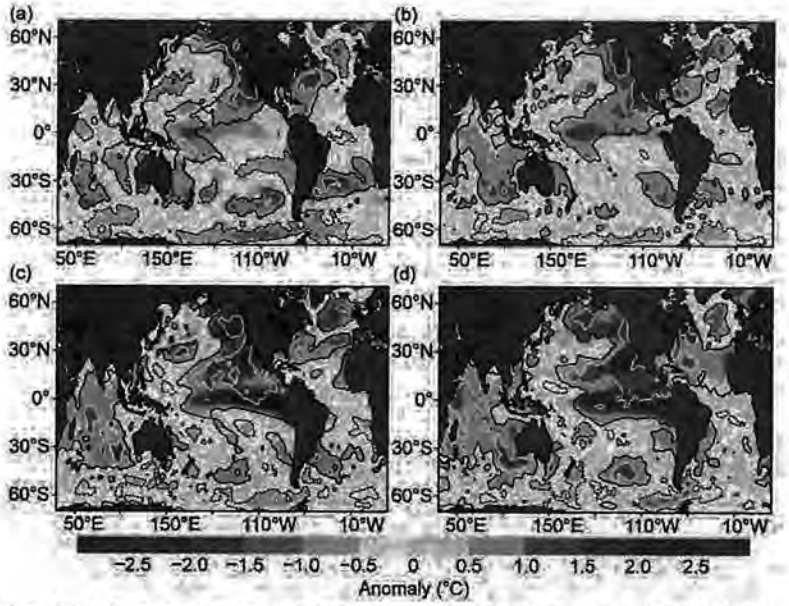

Fig. 3.2. Seasonal mean SSTA from OISST (shading, °C, relative to the 1981–2010 average) for (a) Dec 2014 to Feb 2015, (b) Mar to May 2015, (c) Jun to Aug 2015, and (d) Sep to Nov 2015. Black solid contours are +1, black dashed −1, white solid +2.5, and white dashed −2.5 normalized seasonal mean SSTA, based on 1981–2010 seasonal mean standard deviations.

sis (OISST) from 1982 to 2015 (Fig. 3.3). The SSTA time series of OISST is largely consistent with those of ERSST.v3b in the common period, 1982–2015. HadISST also agrees well with OISST and ERSST.v3b except it is generally cooler in the tropical Indian Ocean and the differences can reach 0.2°C. However, ERSST.v4 is noticeably warmer than other SST products (Karl et al. 2015), as discussed below.

The global mean SSTA is dominated by a warming trend superimposed with interannual variations largely associated with El Niño and La Niña events (Fig. 3.3a), where the peaks and valleys in the global ocean SSTA often correspond with those in the tropical Pacific SSTA (Fig. 3.3b). The mean SSTA in the tropical Pacific increased by 0.23°–0.29°C from 2014 to 2015, and 2015 surpassed 1997 as the warmest year since 1950. Partially owing to the strong warming in the tropical Pacific, the mean SSTA in the global ocean increased by 0.08°–0.11°C from 2014 to 2015, depending on the dataset examined, and 2015 surpassed 2014 as the warmest year since 1950.

For the global ocean, the surface warming trend for 2000–15 increased by 0.03°–0.04°C decade^{-1} compared to the 2000–14 trend. Because of this increase, the warming trend in 2000–15 (rising 0.13°C, 0.07°C, 0.08°C, and 0.08°C decade^{-1} in ERSST.v4, ERSST.v3b, HadISST, and OISST, respectively) became comparable to the warming trend in 1950–99 (rising 0.09°C, 0.07°C, and 0.06°C decade^{-1} in ERSST.v4, ERSST.v3b, and HadISST, respectively). Compared to ERSST.v3b and HadISST, the warming trend in ERSST.v4 was 0.05°–0.06°C decade^{-1} higher in 2000–15. Three factors contribute to the stronger warming trend in ERSST.v4 relative to other products in the more recent period (Karl et al. 2015; Huang et al. 2015): 1) the correction of buoy data to ship data and an increase in buoy data (which were not included in ERSST.v3b and OISST); 2) more weight given to more accurate buoy data in the reconstruction of SST; and 3) a continuous correction of ship data based on night marine air temperature. Huang et al. (2015) and Kennedy (2014) discuss bias correction uncertainties of ship and buoy data and reconstruction of historical SST analyses.

The tropical Indian Ocean SSTA is dominated by an upward trend superimposed with interannual

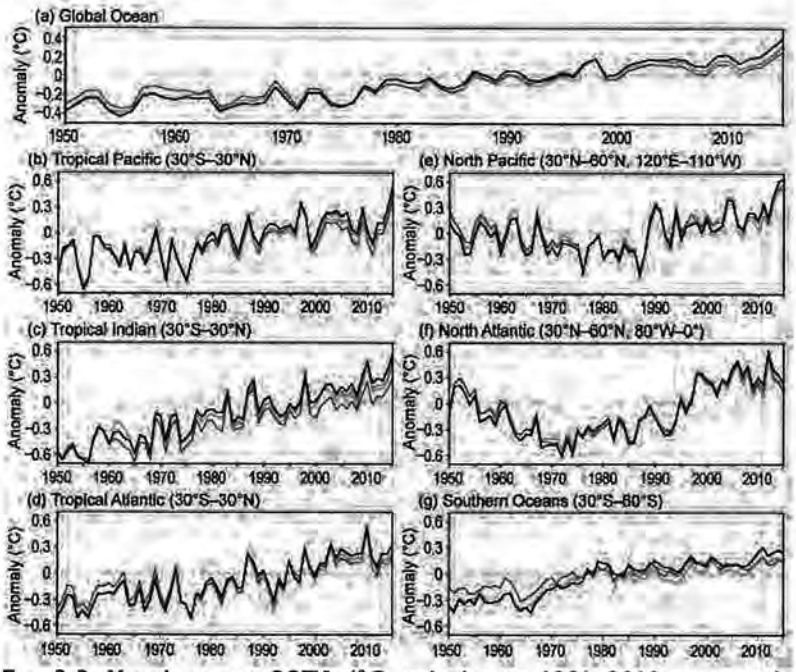

Fig. 3.3. Yearly mean SSTA (°C, relative to 1981–2010 averages) for ERSST.v4 (black), ERSST.v3b (blue), and HadISST (purple) for 1950–2015 and OISST (yellow) for 1982–2015, averaged over the (a) global, (b) tropical Pacific, (c) tropical Indian, (d) tropical Atlantic, (e) North Pacific, (f) North Atlantic, and (g) Southern Ocean.

variations (Fig. 3.3c). The interannual variations in the tropical Indian Ocean SSTA correspond well with those in the tropical Pacific SSTA due to the remote influences of ENSO (Kumar et al. 2014). The tropical Indian Ocean SSTA increased by 0.13°–0.20°C from 2014 to 2015, making 2015 the warmest year since 1950.

Tropical Atlantic SST reached a historical high in 2010, cooled down substantially in 2011/12, and rebounded gradually in 2013–15 (Fig. 3.3d). North Pacific SSTA increased by 0.10°–0.17°C from 2013 to 2014, and changed little from 2014 to 2015 (Fig. 3.3e). North Atlantic SSTA reached a historical high in 2012, and cooled since that time (Fig. 3.3f). In the Southern Ocean, ERSST.v4 was warmer by about 0.08°C than ERSST.v3b, HadISST, and OISST, which show consistent values after 2009 (Fig. 3.3g).

c. Ocean heat content—G. C. Johnson, J. M. Lyman, T. Boyer, C. M. Domingues, M. Ishii, R. Killick, D. Monselesan, and S. E. Wijffels

Storage and transport of heat in the ocean are central to aspects of climate such as ENSO (Roemmich and Gilson 2011), tropical cyclones (Goni et al. 2009), sea level rise (e.g., Domingues et al. 2008), variations

SIDEBAR 3.1: A WIDESPREAD HARMFUL ALGAL BLOOM IN THE NORTHEAST PACIFIC—V. L. TRAINER, Q. DORTCH, N. G. ADAMS, B. D. BILL, G. DOUCETTE, AND R. KUDELA

In the late spring and summer 2015, a widespread harmful algal bloom (HAB) of the marine diatom *Pseudo-nitzschia*, stretching off the west coast of North America from central California to British Columbia, Canada, resulted in significant impacts to marine life, coastal resources, and the human communities that depend on these resources. Blooms of *Pseudo-nitzschia* produce a potent neurotoxin, domoic acid, which can accumulate in shellfish, other invertebrates, and sometimes fish, leading to illness and death in a variety of seabirds and marine mammals. Human consumption of toxin-contaminated shellfish can result in Amnesic Shellfish Poisoning (ASP), which can be life threatening. Detectable concentrations of toxin, although well below levels of concern for human consumption, have been measured in finfish like salmon, tuna, and pollock. The greatest human health risk is from recreationally harvested shellfish; commercial supplies are closely monitored and have not resulted in human illnesses. States maintain websites indicating where shellfish can be safely harvested.

Although these blooms can occur annually at "hot spots" along the U.S. West Coast, the largest impacts and most widespread closures typically occur in autumn. Samples collected on two research cruises in June and July 2015 demonstrated that domoic acid was measurable at most sites in Washington and Oregon (Fig. SB3.1).

The 2015 bloom was detected in early May, and in response, Washington State closed its scheduled razor clam digs on coastal beaches. The abundance of *Pseudo-nitzschia* and concentrations of domoic acid in razor clams on Washington State beaches in 2015 greatly exceeded values observed during springtime blooms that have only rarely occurred on the Washington coast since 1991, when domoic acid events were first recognized on the U.S. West Coast. Comparison with a typical springtime bloom experienced in 2005 illustrates the magnitude of the 2015 domoic acid event (Fig. SB3.2).

Scientists quickly recognized that the bloom extended from California's Channel Islands to as far north as Vancouver Island. The bloom is the largest and its effects have been the

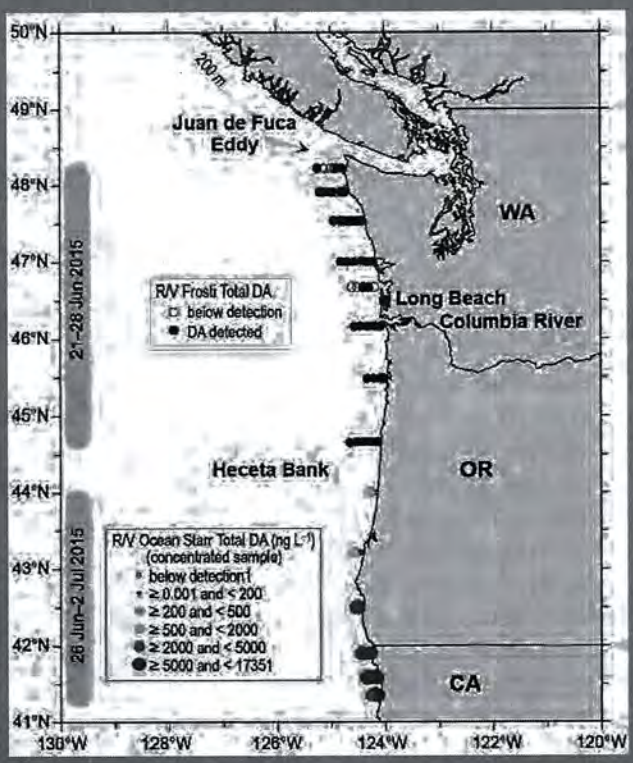

FIG. SB3.1. Cellular domoic acid (DA) in phytoplankton net tows (several liters seawater filtered; Research Vessel (R/V) *Frosti*, sampled north to south) or quantified on 0.45 mm filters (1 liter seawater filtered; R/V *Ocean Starr*, sampled south to north).

in the global average surface warming rate (Meehl et al. 2013), and melting of ice sheet outlet glaciers around Greenland (Straneo and Heimbach 2013) and Antarctica (Rignot et al. 2013). Ocean warming accounts for about 93% of the total increase in energy storage in the climate system from 1971 to 2010 (Rhein et al. 2013).

Maps of annual (Fig. 3.4) upper (0–700 m) ocean heat content anomaly (OHCA) relative to a 1993–2015 baseline mean are generated from a combination of in situ ocean temperature data and satellite altimetry data following Johnson et al. (2015a), but using Argo (Riser et al. 2016) data downloaded in January 2016. Near-global average seasonal temperature anomalies (Fig. 3.5) vs. pressure from Argo data (Roemmich and Gilson 2009, updated) since 2004 and in situ global estimates of OHCA (Fig. 3.6) for various pressure layers from multiple research groups are also discussed. Here, increases in OHCA are sometimes referred to as warming and OHCA decreases as cooling.

For the second consecutive year (see Johnson et al. 2015a) dramatic upper OHCA cooling east of the Philippines fed warming in the equatorial Pacific between 2014 and 2015 (Fig. 3.4b) via

longest-lasting of all U.S. West Coast *Pseudo-nitzschia* events in at least the past 15 years; concentrations of domoic acid in seawater, some forage fish, and crab samples were among the highest ever reported for this region. By mid-May, domoic acid concentrations in Monterey Bay, California, were 10 to 30 times the level that would be considered high for a normal *Pseudo-nitzschia* bloom. Other HAB toxins also have been detected on the West Coast in 2015. For example, an increase in saxitoxin-producing algae has been reported in areas of Alaska.

Impacts include shellfish and Dungeness crab harvesting closures in multiple states, targeted finfish closures, public health advisories for certain fish species in some areas of California, and sea lion strandings in California and Washington. Other marine mammal and bird mortalities have been reported in multiple states; domoic acid has not been confirmed as the primary cause of death, although the toxin has been detected in recovered birds. On 20 August 2015, NOAA declared an Unusual Mortality Event for large whales in the western Gulf of Alaska. Scientists have recorded the mortality of 30 large whales between May 2015 and February 2016. HABs are suspected of playing a role in the deaths of these whales given the noted warmer-than-average ocean temperatures in the Gulf of Alaska and the algal bloom documented in neighboring areas. However, there is as of this writing no conclusive evidence linking the whale deaths to HAB toxins.

While exact causes of the severity and early onset of the bloom are not yet known, unusually warm surface water in the Pacific is considered a factor (R. M. McCabe et al. 2016, manuscript submitted to *Nat. Commun.*). First reported along the West Coast in the 1990s, *Pseudo-nitzschia* blooms have also been observed off the U.S. East Coast and in the Gulf of Mexico.

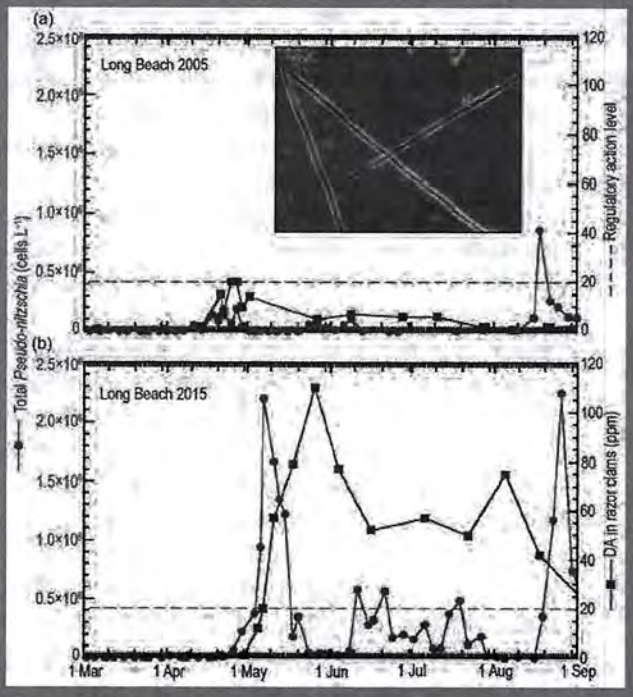

FIG. SB3.2. Concentrations of *Pseudo-nitzschia* (cells liter^{-1} from 1 Mar–1 Sep) and domoic acid in razor clams (ppm) in (a) 2005 and (b) 2015 on Long Beach, Wash. (location shown in Fig. SB3.1). Inset: Chains of overlapping *Pseudo-nitzschia* cells, the diatom that produces the toxin domoic acid. [*Pseudo-nitzschia* image courtesy of Zachary Forster, Washington Department of Fish and Wildlife.]

stronger-than-normal eastward flow in the North Equatorial Countercurrent and along the equator (see Fig. 3.19). Hence, most of the equatorial Pacific was anomalously warm in 2015 (Fig. 3.4a), consistent with El Niño conditions (see section 4b). The cooling east of the Philippines brought upper OHCA (Fig. 3.4a) and sea level (see Fig. 3.15) in 2015 well below mean values there.

Conversely, eastern North Pacific upper OHCA warmed from 2014 to 2015 all along the west coast of North America (Fig. 3.4b), whereas the central North Pacific cooled. This pattern of change, together with the equatorial warming, reflects a transition of the Pacific decadal oscillation (PDO; Mantua et al. 1997) from negative in 2013 to positive in 2014 (http://research.jisao.washington.edu/pdo/). In 2015, North Pacific SST anomalies (see Fig. 3.1), upper OHCA anomalies (Fig. 3.4a), and sea level anomalies (see Fig. 3.15) reflect this positive PDO. This shift may result in an increased rate of global average surface warming (e.g., Meehl et al. 2013) and also affects regional rates of sea level rise (e.g., Zhang and Church 2012).

In the South Pacific, there was a large patch of cooling in the subtropics between 2014 and 2015 (Fig. 3.4b), but much of the South Pacific remained warm relative to 1993–2015 (Fig. 3.4a). In the Indian Ocean there was generally warming, with weak cooling in the far east and a zonal band of stronger cooling extending east of Madagascar, consistent with a reduction in the strength of the South Equatorial Current in 2015 relative to 2014 (an increase in eastward flow, see Fig. 3.19). The Brazil Current in the South Atlantic and Agulhas Current in the South Indian Ocean remained warm in 2015, despite some cooling of the latter from 2014 to 2015. Upper OHCA in the Indian Ocean remained mostly warm in 2015 (Fig. 3.4a), with cool patches in the far east and also east of Madagascar. In both locations there was cooling from 2014 to 2015 (Fig. 3.4b).

Much of the subpolar North Atlantic cooled from 2014 to 2015 while much of the Nordic Seas warmed. With these changes, in 2015 the subpolar region was anomalously cool (Fig. 3.4a), although warm upper OHCA persisted offshore of much of the east coast of North America, north of the Gulf Stream Extension. These changes may be related to a reduction in the strength of the Atlantic meridional overturning circulation (AMOC; see section 3h) in recent years (e.g., Saba et al. 2016).

Distinct and statistically significant (Fig. 3.4c) regional patterns stand out in the 1993–2015 local linear trends of upper OHCA. In the Indian Ocean, the warming trend is widespread and statistically

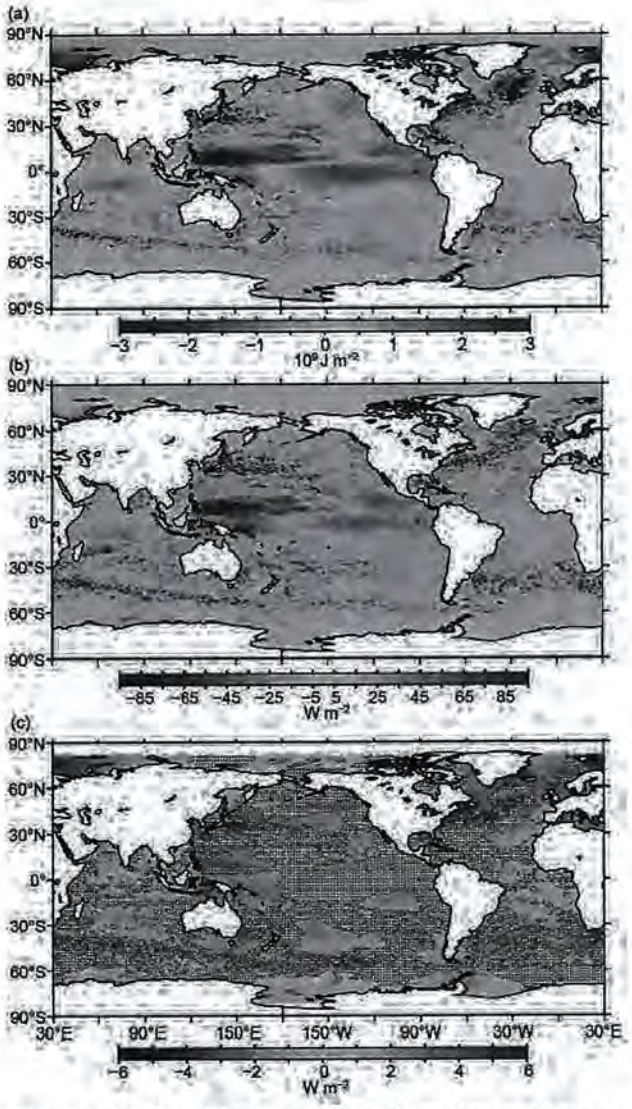

Fig. 3.4. (a) Combined satellite altimeter and in situ ocean temperature data estimate of upper (0–700 m) OHCA ($\times 10^9$ J m^{-2}) for 2015 analyzed following Willis et al. (2004), but using an Argo monthly climatology and displayed relative to the 1993–2015 baseline. (b) 2015 minus 2014 combined estimates of OHCA expressed as a local surface heat flux equivalent (W m^{-2}). For panel (a) and (b) comparisons, note that 95 W m^{-2} applied over one year results in a 3×10^9 J m^{-2} change of OHCA. (c) Linear trend from 1993–2015 of the combined estimates of upper (0–700 m) annual OHCA (W m^{-2}). Areas with statistically insignificant trends are stippled.

significant over much of the area north of 35°S, with almost no statistically significant cooling trends in that region.

In the Atlantic Ocean, the eastern seaboard of the North Atlantic, the Labrador Sea, and the Nordic Seas all trend warmer over 1993–2015 (Fig. 3.4c), all statistically robust over that interval. Eastern portions of the subtropical Atlantic and most of the tropics also

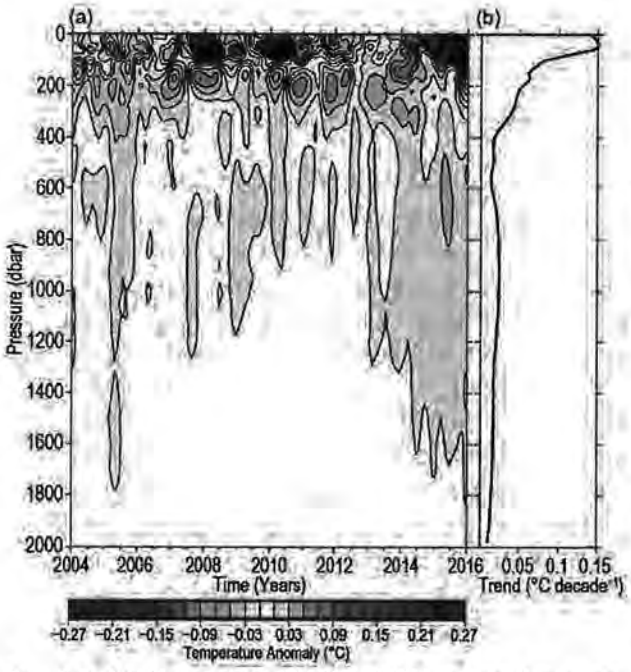

FIG. 3.5. (a) Near-global (60°S–60°N, excluding marginal seas and continental shelves) integrals of monthly temperature anomalies [°C; updated from Roemmich and Gilson (2009)] relative to record-length average monthly values, smoothed with a 5-month Hanning filter and contoured at odd 0.02°C intervals (see colorbar) vs. pressure and time. (b) Linear trend of temperature anomalies over time for the length of the record in (a) plotted vs. pressure in °C decade^{-1}.

trend warmer across both hemispheres. There is also a warming trend in the western South Atlantic around the Brazil Current. Statistically significant cooling trends in the Atlantic are found east of Argentina and in the region of the Gulf Stream Extension and North Atlantic Current.

Statistically significant 1993–2015 regional trends (Fig. 3.4a) in the Pacific Ocean include warming in the western tropical Pacific and extra-equatorial cooling in the east, consistent with strengthening of the interior subtropical–tropical circulation attributed to trade-wind intensification (Merrifield et al. 2012). This pattern, linked to the surface warming hiatus (England et al. 2014), weakened in 2014 (Johnson et al. 2015a) and reversed in 2015 (Fig. 3.4a), reducing the strength of the long-term trend through 2015 compared with that through 2013 (Johnson et al. 2014).

In the Southern Ocean, a distinct trend of upper OHCA over 1993–2015 (Fig. 3.4c) emerges: a primarily zonal narrow band of warming immediately north of a band of cooling is visible from the western South Atlantic where the Brazil and Falkland/Malvinas Currents meet, extending eastward across much of the South Atlantic and Indian Oceans all the way to south of New Zealand. The geostrophic relation implies a strengthening of eastward currents across this dipole, in the region of the Antarctic Circumpolar Current. Elsewhere in the region there is a cooling around South America. The apparent warming trends adjacent to Antarctica are located in both in situ and altimeter data-sparse regions and are not as robust as suggested by the statistics.

Near-global average seasonal temperature anomalies (Fig. 3.5a) largely reflect ENSO redistributing heat (e.g., Roemmich and Gilson 2011) in the upper 400 dbar (1 dbar ~ 1 m). During La Niña (most notably around 2008 in the Argo era), temperatures in the upper 100 dbar tend to be colder than average and those from around 100–300 dbar warmer because cold water is brought to the surface in the eastern equatorial Pacific as the thermocline shoals, and warm water is sequestered below the surface in the western equatorial Pacific as the thermocline deepens there. During El Niño years (most notably around the end of 2015), the sign of this pattern flips, resulting in very warm SSTs (section 3b) that, along with global warming, contributed to record high global average surface temperatures in 2015. In addition to the ENSO signature, there is an overall warming trend (Fig. 3.5b) from 2004 to 2015 that approaches 0.15°C decade^{-1} near the surface, declines to around 0.02°C decade^{-1} by 400 dbar, and remains near that rate down to 2000 dbar. This warming trend is found mostly south of the equator since 2006 (Roemmich et al. 2015; Wijffels et al. 2016).

A decade is short for defining long-term trends with statistical confidence, especially in the upper ocean where ENSO causes large interannual perturbations, so the analysis is extended further back in time and deeper using historical data collected mostly from ships. Five different estimates of globally integrated in situ upper (0–700 m) OHCA (Fig. 3.6a) all reveal a large increase since 1993 and indicate a record high OHCA value in 2015. Causes of the differences among estimates are discussed in previous reports (e.g., Johnson et al. 2015a). OHCA variability and net increases are also found from 700 to 2000 m (Fig. 3.6b) and even deeper in the ocean from 2000 to 6000 m (Fig. 3.6b), though for the latter, trends can only be estimated from differences between decadal surveys (Purkey and Johnson 2013).

The rate of heat gain from linear trends fit to each of the global integral estimates of 0–700 m OHCA from 1993 through 2015 (Fig. 3.6a) are 0.26 (±0.05), 0.31 (±0.12), 0.43 (±0.11), 0.35 (±0.07), and 0.41 (±0.22) W m^{-2} applied over the surface area of the Earth (5.1×10^{14} m^2) for the MRI/JMA, CSIRO/ACE CRC/IMAS-UTAS, PMEL/JPL/JIMAR, NCEI, and Met Office Hadley Centre estimates, respectively. Linear trends

for 1993–2015 are 0.19 (±0.09) W m^{-2} from 700 to 2000 m, 0.24 (±0.04) W m^{-2} from 700 to 1800 m, and 0.19 (±0.08) W m^{-2} from 700 to 2000 m for the MRI/JMA, PMEL/JPL/JIMAR, and NCEI estimates, respectively. Here, 5%–95% uncertainty estimates for the trends are based on the residuals, taking their temporal correlation into account when estimating degrees of freedom (Von Storch and Zwiers 1999). For 2000–6000 m, the linear trends are about 0.07 (±0.04) W m^{-2} (again at 5%–95% uncertainty) from 1992 to 2009 (update of Purkey and Johnson 2010; D. Desbruyères and S. G. Purkey, 2016, personal communication).

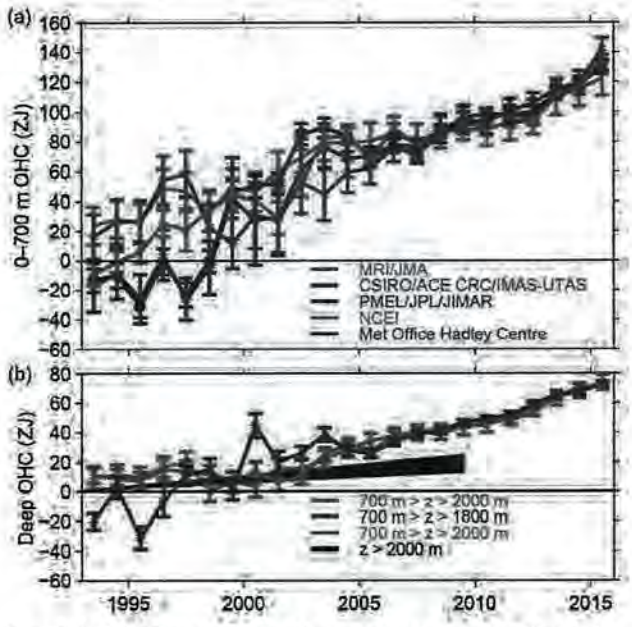

FIG. 3.6. (a) Time series of annual average global integrals of in situ estimates of upper (0–700 m) OHCA (1 ZJ = 10^{21} J) for 1993–2015 with standard errors of the mean. The MRI/JMA estimate is an update of Ishii and Kimoto (2009). The CSIRO/ACE CRC/IMAS-UTAS estimate is an update of Domingues et al. (2008). The PMEL/JPL/JIMAR estimate is an update of Lyman and Johnson (2014). The NCEI estimate follows Levitus et al. (2012). The Met Office Hadley Centre estimate is computed from gridded monthly temperature anomalies (relative to 1950–2015) following Palmer et al. (2007). See Johnson et al. (2014) for more details on uncertainties, methods, and datasets. For comparison, all estimates have been individually offset (vertically on the plot), first to their individual 2005–15 means (the best sampled time period), and then to their collective 1993 mean. (b) Time series of annual average global integrals of in situ estimates of intermediate (700–2000 m for MRI/JMA and NCEI, 700–1800 m for PMEL/JPL/JIMAR) OHCA for 1993–2015 with standard errors of the mean, and a long-term trend with one standard error uncertainty shown from 1992–2009 for deep and abyssal (z > 2000 m) OHCA updated (D. Desbruyères and S. G. Purkey, 2016, personal communication) following Purkey and Johnson (2010).

Summing the three layers, the full-depth ocean heat gain rate ranges from 0.52 to 0.74 W m^{-2}.

d. Salinity—G. C. Johnson, J. Reagan, J. M. Lyman, T. Boyer, C. Schmid, and R. Locarnini

1) INTRODUCTION—G. C. Johnson and J. Reagan

Salinity patterns, both long-term means and their variations, reflect ocean storage and transport of freshwater, a key aspect of global climate (e.g., Rhein et al. 2013). Ocean salinity distributions are largely determined by patterns of evaporation, precipitation, and river runoff (e.g., Schanze et al. 2010), and in some high-latitude regions, sea ice formation, advection, and melt (e.g., Petty et al. 2014). The result is relatively salty sea surface salinity (SSS) values in the subtropics, where evaporation dominates, and fresher SSS values under the intertropical convergence zones (ITCZs) and in the subpolar regions, where precipitation dominates. These fields are further modified by ocean advection (e.g., Yu 2011). In the subsurface, fresher subpolar waters slide along isopycnals to intermediate depths, underneath saltier subtropical waters, which are in turn capped at low latitudes by fresher tropical waters (e.g., Skliris et al. 2014). Salinity changes in these layers quantify the increase of the hydrological cycle with global warming over the recent decades, likely more accurately and directly than evaporation and precipitation estimates (Skliris et al. 2014). Below that, the salty North Atlantic Deep Waters formed mostly by open ocean convection are found, with salinities that vary over decades (e.g., van Aken et al. 2011). Fresher and colder Antarctic Bottom Waters, formed mostly in proximity to ice shelves, fill the abyss of much of the ocean (Johnson 2008), freshening in recent decades (e.g., Purkey and Johnson 2013). Salinity changes also have an effect on sea level (e.g., Durack et al. 2014) and the thermohaline circulation (e.g., Kuhlbrodt et al. 2007).

To investigate interannual changes of subsurface salinity, all available subsurface salinity profile data are quality controlled following Boyer et al. (2013) and then used to derive 1° monthly mean gridded salinity anomalies relative to a long-term monthly mean for years 1955–2006 (World Ocean Atlas 2009; Antonov et al. 2010) at standard depths from the surface to 2000 m (Boyer et al. 2012). In recent years, the single largest source of salinity profiles for the world's ocean is the Argo program with its fleet of profiling floats (Riser et al. 2016). These data are a mix of real-time (preliminary) and delayed-mode (scientific quality controlled). Hence, the estimates presented here could change after all data have been subjected to scientific quality control. The SSS analysis relies on Argo in situ

data downloaded in January 2016, with annual maps generated following Johnson and Lyman (2012) as well as monthly maps from BASS (Xie et al. 2014), a bulk (as opposed to skin) SSS data product that blends in situ SSS data with data from the Aquarius (Le Vine et al. 2014) and SMOS (Soil Moisture and Ocean Salinity; Font et al. 2013) satellite missions. The Aquarius mission ended in June 2015, leaving SMOS as the sole source for satellite SSS for the rest of 2015. BASS maps can be biased fresh around land (including islands) and should be compared carefully with in situ data-based maps at high latitudes before trusting features there. Salinity is measured as a dimensionless quantity and reported on the 1978 Practical Salinity Scale, or PSS-78 (Fofonoff and Lewis 1979). Surface salinity values in the open ocean range from about 32 to 37.5, with seasonal variations exceeding 1 in a few locations (Johnson et al. 2012).

2) Sea surface salinity (SSS)—G. C. Johnson and J. M. Lyman

The 2015 SSS anomalies (Fig. 3.7a, colors) reveal some large-scale patterns that largely held from 2004 to 2014 (e.g., Johnson et al. 2015b, and previous *State of the Climate* reports.). Regions around the subtropical salinity maxima are generally salty with respect to *World Ocean Atlas* (*WOA*) *2009* (Antonov et al. 2010). Most of the high latitude, low-salinity regions appear fresher overall than *WOA 2009*, both in the vicinity of much of the Antarctic Circumpolar Current near 50°S and in portions of the subpolar gyres of the North Pacific and North Atlantic. These multiyear patterns are consistent with an increase in the hydrological cycle (that is, more evaporation in drier locations and more precipitation in rainy areas) over the ocean expected in a warming climate (Rhein et al. 2013). The large, relatively fresh patch in 2015 west of Australia and the Indonesian Throughflow was more prominent in previous years back to 2011 (Johnson and Lyman 2012). Its origin is associated with the strong 2010–12 La Niña and other climate indices (Fasullo et al. 2013; Johnson et al. 2015b).

Sea surface salinity changes from 2014 to 2015 (Fig. 3.7b, colors) strongly reflect 2014 anomalies in evaporation minus precipitation (see Fig. 3.12). Advection by anomalous ocean currents (see Fig. 3.19) also plays a role in SSS changes. The most prominent large-scale SSS changes from 2014 to 2015 were freshening under the Pacific ITCZ and salinification in the tropical warm pool around the Maritime Continent (Fig. 3.7b). The freshening is associated with stronger-than-usual freshwater fluxes into the ocean under the ITCZ (see Fig. 3.12) and anomalous eastward flow

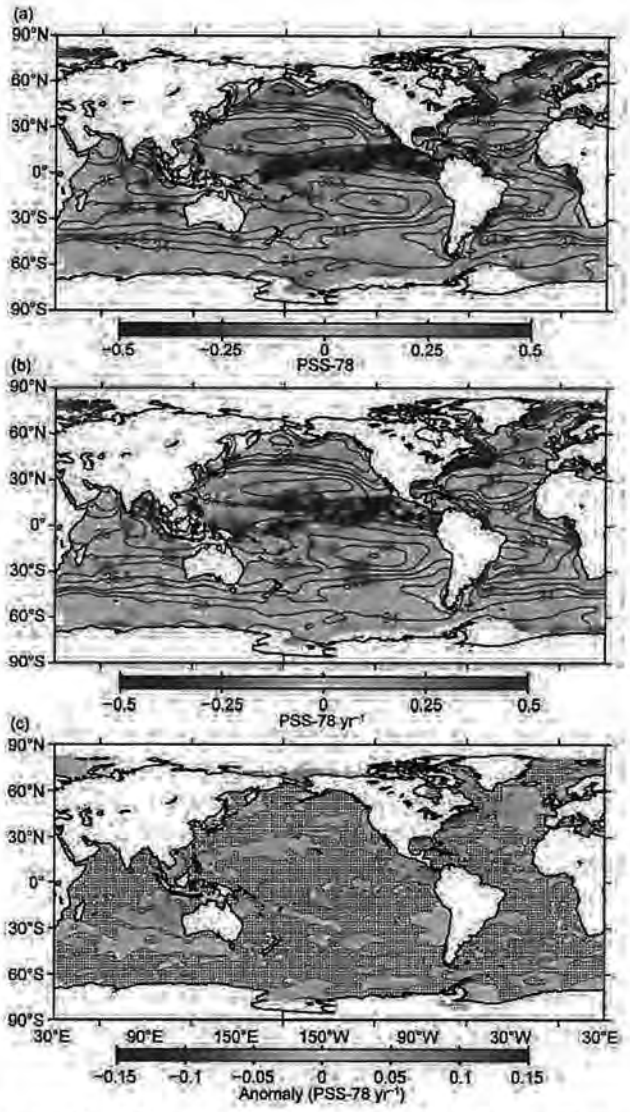

Fig 3.7. (a) Map of the 2015 annual surface salinity anomaly (colors in PSS-78) with respect to monthly climatological salinity fields from WOA 2009 (yearly average—gray contours at 0.5 PSS-78 intervals). (b) Difference of 2015 and 2014 surface salinity maps [colors in PSS-78 yr^{-1} to allow direct comparison with (a)]. White ocean areas are too data-poor (retaining < 80% of a large-scale signal) to map. (c) Map of local linear trends estimated from annual surface salinity anomalies for 2005–15 (colors in PSS-78 yr^{-1}). Areas with statistically insignificant trends are stippled. All maps are made using Argo data.

(see Fig. 3.19) of relatively fresh water in the tropical Pacific. The salinification over the tropical warm pool is associated with reduction in freshwater flux anomalies there. These changes are related to the strong El Niño event of 2015 (section 4b). In the subpolar North Atlantic, there was widespread freshening, strongest south of Iceland, but north of Iceland SSS becomes saltier. In the Indian Ocean, SSS decreased south of India from 2014 to 2015, consistent with the

westward spreading and weakening of the prominent fresh anomaly generated west of Australia circa 2011.

Seasonal variations of SSS anomalies in 2015 (Fig. 3.8) from BASS (Xie et al. 2014) show the buildup of anomalously fresh water associated with the tropical Pacific and western tropical Atlantic ITCZs (including just offshore of the Orinoco and Amazon Rivers), the increase in SSS in the tropical warm pool, and the decrease in fresh anomalies under the South Pacific convergence zone (SPCZ). Despite the lower accuracies of the satellite data relative to that of the Argo data, their higher spatial and temporal sampling allows higher spatial and temporal resolution maps than are possible using in situ data alone.

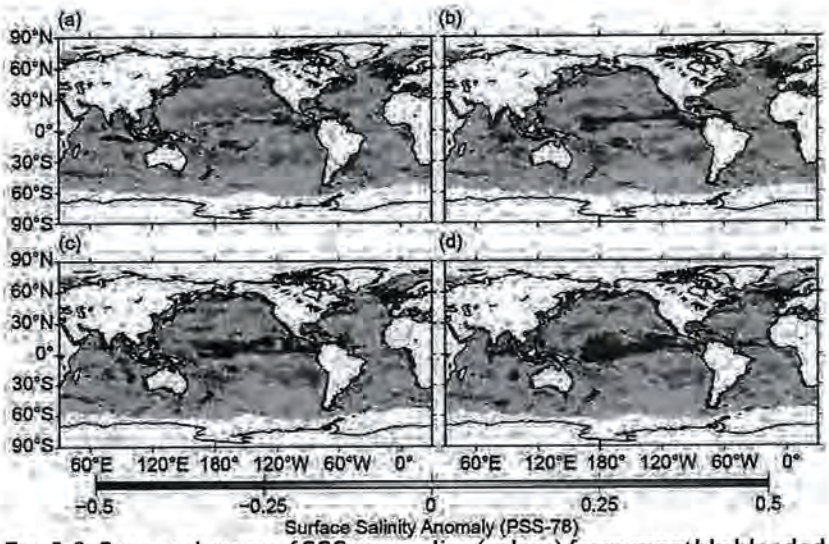

Fig. 3.8. Seasonal maps of SSS anomalies (colors) from monthly blended maps of satellite and in situ salinity data (BASS; Xie et al. 2014) relative to monthly climatological salinity fields from WOA 2009 for (a) Dec–Feb 2014/15, (b) Mar–May 2015, (c) Jun–Aug 2015, and (d) Sep–Nov 2015. Areas with maximum monthly errors exceeding 10 PSS-78 are left white.

Sea surface salinity trends for 2005–15 exhibit striking patterns in all three oceans (Fig. 3.7c). These trends are estimated by local linear fits to annual average SSS maps from Argo data with a starting year of 2005, because that is when Argo coverage became near-global. Near the salinity maxima in each basin (mostly in the subtropics but closer to 30°S in the Indian Ocean), there are regions of increasing salinity, especially in the North Pacific to the west of Hawaii. In contrast, there are regions in the Southern Ocean where the trend is toward freshening. Again, these patterns are reminiscent of the multidecadal changes discussed above and suggest an intensification of the hydrological cycle over the ocean, even over the last 11 years. There is a strong freshening trend in much of the subpolar North Atlantic, roughly coincident with anomalously low upper ocean heat content there (see Fig. 3.4) suggesting an eastward expansion of the subpolar gyre that may be linked to reductions in the AMOC over the past decade (section 3h). In addition to these patterns there is a freshening trend in the eastern Indian Ocean, probably owing to a lingering signature of the strong 2010–12 La Niña, as discussed above. Freshening trends are also apparent in the eastern tropical Pacific and the South China Sea. The region to the northwest of the Gulf Stream is trending saltier, as well as warmer (section 3c).

3) Subsurface salinity—J. Reagan, T. Boyer, C. Schmid, and R. Locarnini

Atlantic Ocean basin-average monthly salinity anomalies for 0–1500 m depth displayed a pattern during 2015 similar to the previous 10 years, with salty anomalies above 700 m and fresh anomalies below (Fig. 3.9a). From 2014 to 2015 salinity increased in the upper 300 m of the Atlantic, reaching a maximum increase of ~0.01 near the surface (Fig. 3.9b). The Pacific Ocean has exhibited fresh anomalies of about −0.02 from 200 to 500 m over the last five years (Fig. 3.9c). However, the upper 75 m was about −0.04 fresher in 2015, in contrast to salty conditions there from mid-2008 to mid-2014. This change reflects the enhanced precipitation along the ITCZ (see Fig. 3.12d) and anomalous eastward equatorial currents (see Fig. 3.19) during the 2015 El Niño (see section 4b). Salty anomalies from 100 to 200 m have been present since 2011. From 2014 to 2015 the Pacific (Fig. 3.9d) freshened in the upper 75 m, approaching about −0.03 at 30 m, and became saltier from 100 to 200 m, approaching ~0.01 at 125 m. The Indian Ocean continued to show similar salinity anomaly structure to that of the previous two years, with a fresh surface anomaly from 0 to 75 m, salty subsurface anomaly from 100 to 300 m, a slightly fresh anomaly (maximum of about −0.01) from 400 to 600 m, and a slightly salty anomaly (maximum of ~0.01) from 600 to 800 m (Fig. 3.9e). From 2014 to 2015 there was weak freshening (maximum of about −0.01 at 50 m) near the surface and salinification from 100 to 200 m, with a maximum of ~0.014 at 150 m (Fig. 3.9f).

North Atlantic 2015 volume-weighted salinity anomalies from 0 to 1500 m (Fig. 3.10a) were mostly positive, with values >0.10 along the Gulf Stream. The eastern portion of the subpolar gyre in the North

Atlantic exhibited a large (about −0.10) fresh anomaly. This fresh feature coincided with anomalously cool upper ocean heat content (see Fig. 3.4). The South Atlantic was dominated by positive salinity anomalies in 2015, with fresh anomalies south of 40°S, perhaps reflecting an anomalously northward position of the low salinity subantarctic front. From 2014 to 2015, positive salinity anomalies in the subtropics persisted with little change in strength, while the freshening north of the Azores Islands continued to strengthen (Fig. 3.10b).

The Indian Ocean displayed a dipole of salinity anomalies north of the equator during 2015, with salty anomalies in the Arabian Sea and fresh anomalies in the Bay of Bengal (Fig. 3.10a). Salty anomalies along the equator transitioned to fresh anomalies across the entire basin south of 15°S to 30°S. These fresh anomalies strengthened east of Madagascar from 2014 to 2015 but weakened west of Australia (Fig. 3.10b) as discussed in section 3d2. From 35°S to 50°S there was a transition from salty to fresh salinity anomalies, likely due to the position of the subantarctic front in 2015 (Fig. 3.10a).

The North Pacific, north of 20°N, was dominated by fresh anomalies in 2015; however, in the northeast Pacific there was a salty anomaly (Fig. 3.10a) in close proximity to a region of anomalously warm SSTs (see Fig. 3.1). The warm SSTs were at least partly due to a persistent atmospheric ridge in the region (Bond et al. 2015). With ridging, less precipitation and more evaporation are expected. This expectation was partially met (see Fig. 3.12) and likely to have been partially responsible for the observed salty anomaly strengthening from 2014 to 2015 (Fig. 3.10b). The subtropical North Pacific was anomalously salty in 2015, contrasting with fresh anomalies along the ITCZ, consistent with the 2015 $P-E$ anomalies (see Fig. 3.12). Salty anomalies were present in the subtropical South Pacific in 2015, with fresh anomalies along the SPCZ. These tropical and subtropical salinity anomaly features were mostly enhanced when compared to 2014, with the exception of a weakening

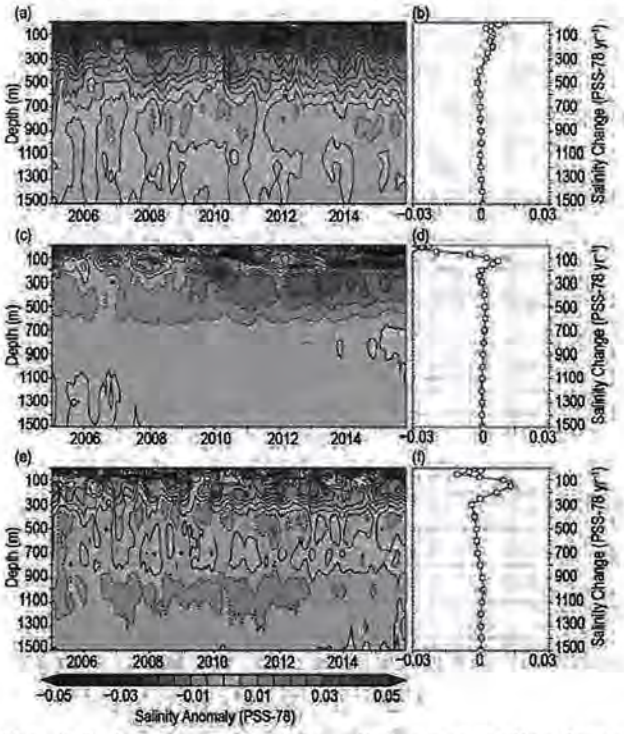

Fig. 3.9. Average monthly salinity anomalies from 0–1500 m for the (a) Atlantic from 2005–15 and (b) the change from 2014 to 2015; (c) Pacific from 2005–15 and (d) the change from 2014 to 2015; and (e) Indian from 2005–15 and (f) the change from 2014 to 2015. Data were smoothed using a 3-month running mean. Anomalies are relative to the long-term WOA 2009 monthly salinity climatology (Antonov et al. 2010).

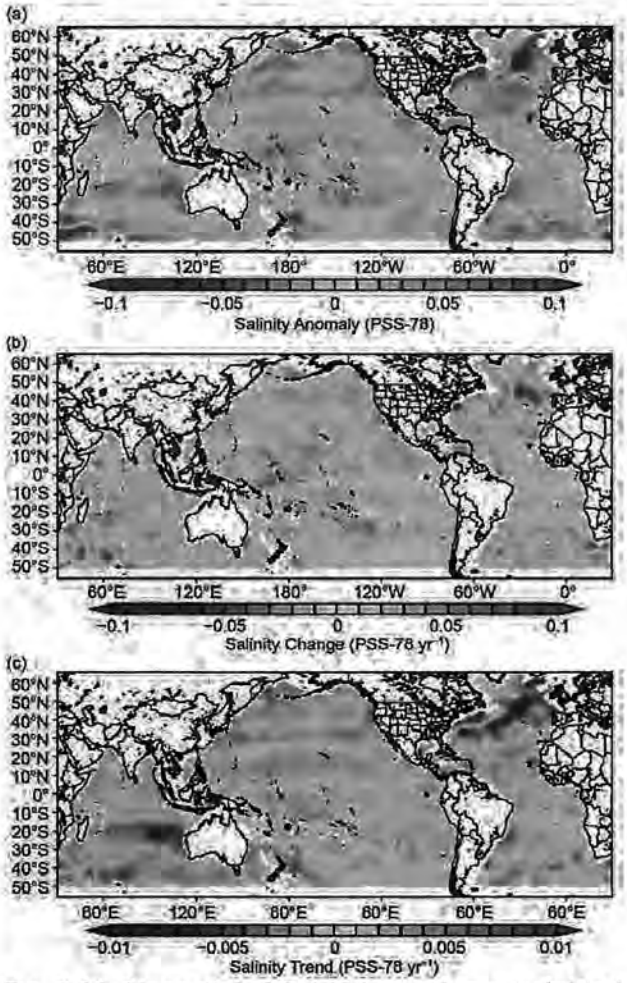

Fig. 3.10. Near-global 0–1500 m volume-weighted salinity anomalies (a) for 2015, (b) change from 2014 to 2015, and (c) linear trend from 2005 to 2015 (yr^{-1}). Anomalies are relative to the long-term WOA 2009 monthly salinity climatology (Antonov et al. 2010). Annual figures were computed by averaging the 12 monthly salinity anomalies over calendar years.

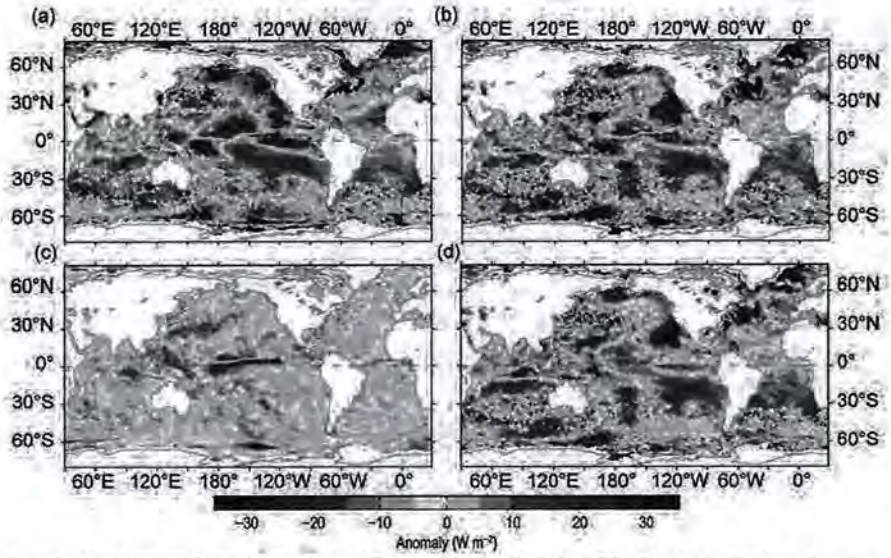

Fig. 3.11. (a) Surface heat flux (Q_{net}) anomalies for 2015 relative to a 5-year (2010–14) mean. Positive values denote ocean heat gain. Panels (b), (c), and (d) are the 2015–2014 anomaly tendencies for Q_{net}, surface radiation (SW+LW), and turbulent heat fluxes (LH+SH), respectively. Positive anomalies denote that the ocean gained more heat in 2015 than in 2014. LH+SH are produced by the OAFlux high-resolution satellite-based analysis, and SW+LW by the NASA FLASHFlux project.

positive salinity anomaly over the central subtropical North Pacific in 2015 (Fig. 3.10b). The South Pacific enhancement from 2014 to 2015 is inconsistent with 2015 $P-E$ anomalies (see Fig. 3.12).

The 2005–15 linear trends of the 0–1500 m salinity anomalies (Fig. 3.10c) reveal strong similarities to SSS trends over the same time period (see Fig. 3.7c and discussion above). This match is not surprising as most of the salinity variability from 0 to 1500 m over the global ocean occurs in the upper 300 m (Fig. 3.9). The large (> -0.01 yr^{-1}) freshening trend in the North Atlantic subpolar gyre could be partially responsible for the observed decline in the strength of the AMOC (Smeed et al. 2014).

e. *Ocean surface heat, freshwater, and momentum fluxes*—L. Yu, R. F. Adler, G. J. Huffman, X. Jin, S. Kato, N. G. Loeb, P. W. Stackhouse, R. A. Weller, and A. C. Wilber

The ocean and atmosphere communicate via interfacial exchanges of heat, freshwater, and momentum. These air–sea fluxes are the primary mechanisms for keeping the global climate system in balance with the incoming insolation at Earth's surface. Most of the shortwave radiation (SW) absorbed by the ocean's surface is vented into the atmosphere by three processes: longwave radiation (LW), turbulent heat loss by evaporation (latent heat flux, or LH), and turbulent heat loss by conduction (sensible heat flux, or SH). The residual heat is stored in the ocean and transported away by the ocean's surface circulation, forced primarily by the momentum transferred to the ocean by wind stress. Evaporation connects heat and moisture transfers, and the latter, together with precipitation, determines the local surface freshwater flux. Identifying changes in the air–sea fluxes is essential in deciphering observed changes in ocean circulation and its transport of heat and salt from the tropics to the poles. In particular, 2015 witnessed the interplay of three different warmings: the warm "Blob" in the

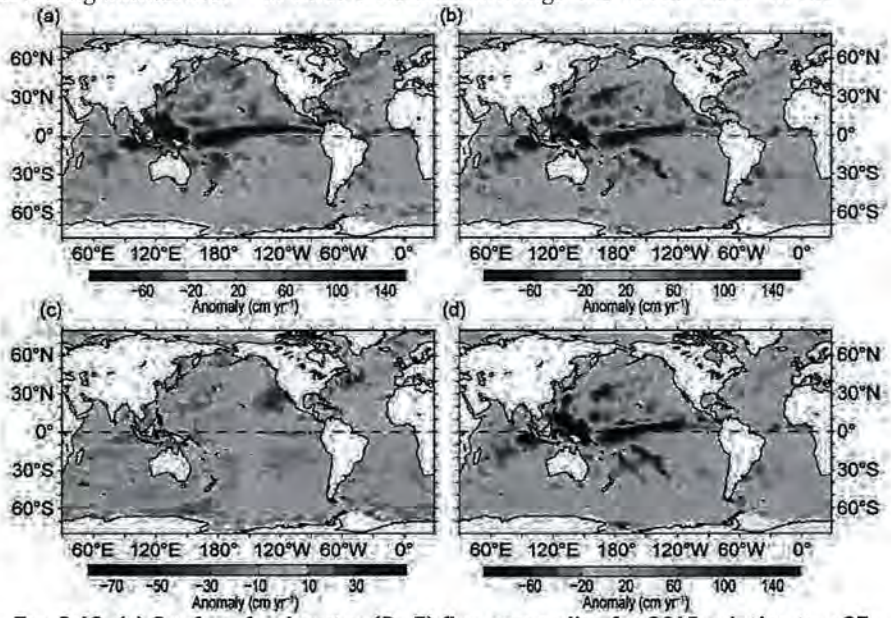

Fig. 3.12. (a) Surface freshwater ($P-E$) flux anomalies for 2015 relative to a 27-year (1988–2014) climatology. 2015–2014 anomaly tendencies for (b) $P-E$, (c) evaporation (E), and (d) precipitation (P), respectively. Green colors denote anomalous ocean moisture gain, and browns denote loss, consistent with the reversal of the color scheme in (c). P is computed from the GPCP version 2.2 product, and E from OAFlux high-resolution satellite-based analysis.

North Pacific (Bond et al. 2015), a strong El Niño in the tropical Pacific, and a warm PDO phase. Large-scale anomalies appear in observations of SST (see Fig. 3.1), heat content (see Fig. 3.4), sea surface salinity (see Fig. 3.7), sea level (see Fig. 3.15), ocean surface currents (see Fig. 3.19), and chlorophyll-*a* (see Fig. 3.26a). All of these anomalies are related to changes in ocean surface forcing functions in 2015 and how the ocean and atmosphere generated anomalous conditions with unusual magnitudes and spatial dimensions.

Air–sea heat flux, freshwater flux, and wind stress in 2015 and their relationships with the ocean are assessed. The net surface heat flux, Q_{net}, is the sum of four terms: SW + LW + LH + SH. The net surface freshwater flux into the ocean (neglecting riverine and glacial fluxes from land) is simply Precipitation (P) minus Evaporation (E), or the $P-E$ flux. Wind stress is computed from satellite wind retrievals using the bulk parameterization of Edson et al. (2013). The production of the global maps of Q_{net}, $P-E$, and wind stress in 2015 (Figs. 3.11–3.13) and the long-term perspective of the change of the forcing functions (Fig. 3.14) are made possible by integrating the efforts of four world-class flux analysis groups. The Objectively Analyzed air–sea Fluxes (OAFlux; http://oaflux.whoi.edu/) project at the Woods Hole Oceanographic Institution (Yu and Weller 2007) provides the satellite-based high-resolution version of the turbulent ocean flux components, including LH, SH, E, and wind stress (Yu and Jin 2012; 2014a,b; Jin and Yu 2013; Jin et al. 2015). The Clouds and the Earth's Radiant Energy Systems (CERES) Fast Longwave and Shortwave Radiative Fluxes (FLASHFlux; https://eosweb.larc.nasa.gov/project/ceres/ceres_table) project at the NASA Langley Research Center (Stackhouse et al. 2006) provides the surface SW and LW products. The Global Precipitation Climatology Project (GPCP; http://precip.gsfc.nasa.gov) at the NASA Goddard Space Flight Center (Adler et al. 2003) provides the precipitation products. The CERES Energy Balanced and Filled (EBAF) surface SW and LW products (http://ceres.larc.nasa.gov; Kato et al. 2013) are used in the time series analysis.

1) Surface heat fluxes

The global Q_{net} anomaly pattern in 2015 overall showed a remarkable hemispheric asymmetry (Fig. 3.11a), with net ocean heat loss (negative) anomalies dominating the Northern Hemisphere and net heat gain (positive) anomalies commanding the Southern Hemisphere. The 2015 minus 2014 Q_{net} tendency map (Fig. 3.11b) had a similar pattern, except for the northeast Pacific, where the net heat loss associated with the warm "Blob" was more intense and widespread compared to the long-term mean background. The Q_{net} anomaly pattern was determined primarily by the LH+SH anomaly pattern (Fig. 3.11d), with the SW+LW anomalies contributing mostly in the tropical ocean.

The 2015 Q_{net} anomalies in the tropical Pacific are associated with El Niño, with mean 2015 SST in the eastern equatorial Pacific more than 2°C above normal (see Fig. 3.1). The eastward displacement of convection typically found over the west tropical Pacific is identified in the SW+LW anomaly field, featuring a striking band of negative SW+LW anomalies of magnitude exceeding 20 W m^{-2} in the central and eastern equatorial Pacific (Fig. 3.11c). The band's core was centered near the international date line and zonally elongated, extending eastward along 2°–3°N. The precipitation anomaly field (Fig. 3.12d) reveals an almost identical band structure of enhanced tropical rainfall. During an El Niño, the eastward movement of the ITCZ leads to the suppression of deep convective clouds over the Indo-Pacific warm pool and the Maritime Continent, and consequently, an increase in the net downward radiation. These typical ENSO composite features (Rasmusson and Wallace 1983), that is, negative SW+LW anomalies in the central and eastern equatorial basin and positive SW+LW anomalies in the equatorial Indo-Pacific, were clear in 2015.

The ENSO LH+SH anomalies (Fig. 3.11d) were dominated by the LH anomalies and produced largely by SST and wind anomalies. As the warmer sea surface tends to evaporate more quickly, latent heat loss increased along the equatorial warm tongue in the eastern Pacific. In the central and western equatorial basin, however, the LH anomalies were not a response to the SST condition; instead they were the source of heating contributing to the ocean warming there: trade winds weakened considerably within the deep convection center near the date line (Fig. 3.13a). This weakening, in turn, subdued the latent heat loss by more than 20 W m^{-2}, creating a warming effect at the ocean surface. The warming effect of the LH+SH anomalies exceeded the cooling effect of the SW+LW anomalies, leading to a marginally positive net heat input to the ocean area that hosted the center of deep convection.

The changing SST–Q_{net} relationship from the eastern to the central equatorial Pacific demonstrates that Q_{net} has a dual role in the dynamics of large-scale SST anomalies. On one hand, Q_{net} contributes to the generation of SST anomalies. On the other hand, Q_{net} acts as a damping mechanism to suppress the SST anomalies once they are generated, thereby providing a feedback to control the persistence

and the amplitude of the SST anomalies (Frankignoul and Hasselmann 1977). Outside the equatorial ocean, the heat flux feedback offers an explanation for the large heat loss over the exceptionally warm waters off the North American coast. The warm "Blob" has persisted since 2013, and the enormous latent heat loss that it produced in 2015 exceeds the climatological background by a large amount (Fig. 3.11a).

The Q_{net} forcing is evident in basinwide warming in the subtropical Indian and Atlantic sectors, as well as in the southeast Pacific. The southeast trade winds are usually weaker during an El Niño (Rasmusson and Carpenter 1982). Similar to the wind–evaporation–SST mechanism that operated in the central equatorial Pacific, the subdued LH+SH loss due to the weakened winds appears to be a source of surface heating for the region.

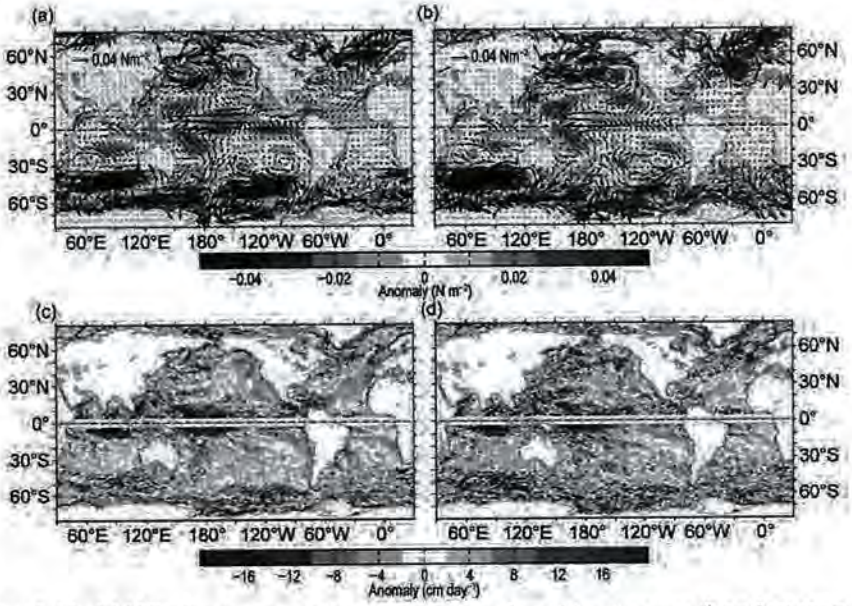

FIG. 3.13. (a) Wind stress magnitude (N m^{-2}; colored background) and vector anomalies for 2015 relative to a 27-yr (1988–2014) climatology, (b) 2015–2014 anomaly tendencies in wind stress, (c) Ekman vertical velocity (W_{EK}) anomalies (cm day^{-1}) for 2015 relative to a 27-year (1988–2014) climatology, and (d) 2015–2014 anomaly tendencies in W_{EK}. In (c) and (d), positive values denote upwelling anomalies and negative downwelling. Winds are computed from the OAFlux high-resolution satellite-based vector wind analysis.

The 2015 Q_{net} anomalies in the North Atlantic exhibited a tripole-like pattern, with strong net heat loss (negative) anomalies (< –20 W m^{-2}) centered in the Labrador Sea and extending across the subpolar gyre north of 50°N, net heat gain (positive) anomalies (10–15 W m^{-2}) in the eastern region between 30° and 50°N, and strong net heat loss anomalies (< –20 W m^{-2}) in the northwest Atlantic, including the Gulf Stream region. The Q_{net} anomalies in this tripole-like pattern were generally negative in regions of positive SST anomalies and positive in regions of negative SST anomalies (Fig. 3.1), indicating that the atmospheric thermal forcing in the North Atlantic was a response to the SST variability.

2) Surface freshwater fluxes

The 2014 to 2015 $P-E$ anomaly tendency (Fig. 3.12a,b) is dominated by precipitation (Fig. 3.12d) over the globe except for the extratropical North Pacific, where evaporation (Fig. 3.12c) is stronger in 2015 than 2014. The hemispheric asymmetry, which is featured in the 2015 Q_{net} anomaly map, is not as obvious in the 2015 $P-E$ anomalies (Fig. 3.12a) but is visible in the E tendencies (Fig. 3.12c). In the latter, the asymmetry is more about the contrast in the signs of the E tendencies in the subtropical sectors, with the northern basin evaporating more and the southern basin less.

In the North Pacific, one interesting anomaly feature in 2015 is the concurrence of increased evaporation with reduced precipitation along a band that extended northeastward across the central Pacific, from the western tropical Pacific toward the Gulf of Alaska. Both effects resulted in an enhanced net moisture release to the atmosphere. This band of $P-E$ anomalies is not a standalone feature. Along the location of the $P-E$ anomaly band, downward SW + LW increased (Fig. 3.11a), and wind-induced Ekman upwelling anomalies were observed (Fig. 3.13c). More importantly, ocean surface warming occurred. The net downward heating, net moisture loss from the ocean, and the surface warming imply a close coupling between the atmosphere and the ocean in the extratropical central Pacific.

Above-normal freshwater input was observed in the tropical Pacific, associated with the development of the strong El Niño. Consistent with the eastward displacement of the ITCZ, the core of the precipitation band was centered near the date line and elongated eastward along the El Niño region. Along the band, the maximum increase of rainfall exceeded 1.5 m during 2015, and its impact on the tropical sea surface salinity (see Fig. 3.7) is evident. The entire

equatorial Pacific experienced a surface freshening by as much as 0.1 PSS-78. As a consequence of the ITCZ migration, the rainfall deficit over the Indo-Pacific warm pool and the Maritime Continent was as large as 80 cm.

Interestingly, the changing $P-E$ forcing in the Indian and Atlantic basins is only loosely linked to observed SSS anomalies (see Fig. 3.7). For instance, the tropical Indian Ocean was mostly in a wetter condition, whereas the regional sea surface became saltier over a wide area. The southern Atlantic was mostly in a drier condition, whereas the regional sea surface was fresher. The low correlation between salinity and $P-E$, in sharp contrast to the close correlation between SST and Q_{net} discussed above, reflects that $P-E$ variations can create or modify existing salinity anomalies but are not a damping mechanism for existing anomalies. The lack of a negative feedback of SSS to the $P-E$ flux suggests that SSS anomalies have a longer persistence than SST, and are more strongly influenced by horizontal processes anomalies such as wind-driven Ekman advection (Yu 2015).

3) Wind stress

The 2015 wind stress anomalies were largely aligned zonally, reflecting the fluctuations of the major wind belts (Fig. 3.13a,b). The vector wind anomaly directions indicate that there was a coherent weakening of the midlatitude westerlies in the Northern and Southern Hemispheres (30°–60°N and 30°–60°S). In response to the strong El Niño in the Pacific, the tropical trade winds were also weaker (Rasmusson and Carpenter 1982). The reduction in the magnitude of the trades is most evident in the center of the southeast trades (e.g., ~15°S in the Indian and Pacific basins). In the equatorial region, the shift of the deep convection to the date-line moved the Walker Circulation eastward, resulting in the equatorial westerly anomalies in the west and equatorial easterly anomalies in the east.

The spatial variations of wind stress (τ) cause divergence and convergence of the Ekman transport, leading to a vertical velocity, denoted by Ekman pumping (downward) or suction (upward) velocity, W_{EK}, at the base of the Ekman layer. Computation of W_{EK} follows the equation: $W_{EK} = 1/\rho\nabla \times (\tau/f)$, where ρ is density, and f the Coriolis force. The 2015 W_{EK} pattern (Fig. 3.13c,d) shows strong upwelling (positive) anomalies in the western and central equatorial Pacific. The pattern corresponds well with the cooling of the upper ocean in the observed region in OHC (see Fig. 3.4) and SSH (see Fig. 3.15). In the North Atlantic, a W_{EK} tripole anomaly pattern is present: positive upwelling anomalies poleward of 60°N, negative downwelling anomalies between 40° and 60°N, and positive downwelling anomalies in the northwest subtropical Atlantic. The region of the warm "Blob" in the northeast Pacific experienced an enhanced downwelling motion.

4) Long-term perspective

The time series of yearly variations of Q_{net}, $P-E$, and wind stress averaged over the global oceans (Fig. 3.14) provide decadal perspective on the ocean-surface forcing functions in 2015. The Q_{net} time series (Fig. 3.14a) indicates that, despite interannual variability, net heat gain by the ocean shifted from nearly steady to higher variability around 2007, after which Q_{net} shows a slight upward tendency. Whether the change is associated with the phase transition of the PDO is yet to be determined. The global average does not represent the change on the regional scale: for instance, decadal decrease of net downward heat flux is observed at a buoy off northern Chile (Weller 2015).

The $P-E$ time series (Fig. 3.14b) is up slightly in 2015, perhaps reflecting the 2015 El Niño's influence on tropical oceanic precipitation. The GPCP precipitation dataset shows that changes over land and ocean during El Niño or La Niña years balance to first

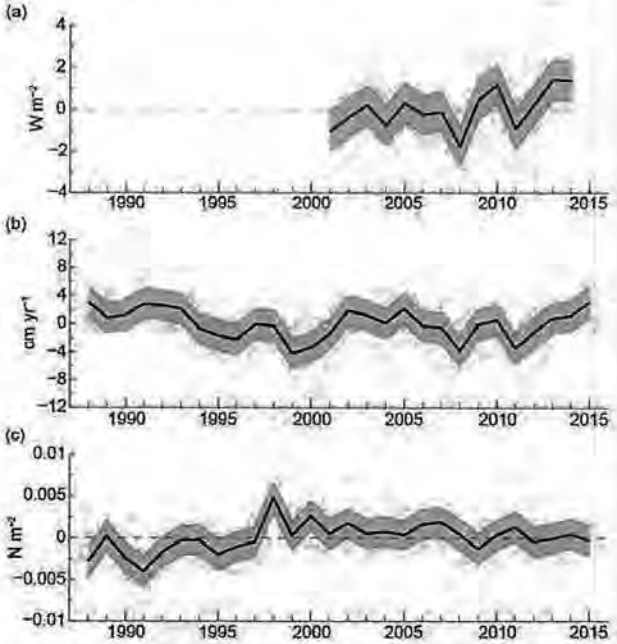

Fig. 3.14. Annual-mean time series of global averages of (a) net surface heat flux (Q_{net}) from the combination of CERES EBAF SW+LW and OAFlux LH+SH, (b) net freshwater flux ($P-E$) from the combination of GPCP P and OAFlux E, and (c) wind stress magnitude from OAFlux high-resolution vector wind analysis. Shaded areas indicate one standard deviation of annual-mean variability.

SIDEBAR 3.2: EXTRAORDINARILY WEAK EIGHTEEN DEGREE WATER PRODUCTION CONCURS WITH STRONGLY POSITIVE NORTH ATLANTIC OSCILLATION IN LATE WINTER 2014/15—S. BILLHEIMER AND L. D. TALLEY

The Gulf Stream and Kuroshio Extension are the largest oceanic heat loss regions in the Northern Hemisphere. Associated with that enormous winter cooling are deep winter mixed layers, which become what is referred to as subtropical mode water.

Mode waters constitute a large portion of the upper ocean volume and are composed of nearly uniform temperature and salinity. These water masses outcrop at the surface during winter, at which point they are stamped with the current atmospheric conditions. Vigorous convection drives the creation of deep mixed layers that entrain heat, freshwater, and anthropogenic CO_2 into the upper ocean. When air–sea heat flux changes sign, generally in the spring, the upper ocean begins to restratify, and the thick subtropical mode water layer (Fig. SB3.3a) is isolated from the atmosphere by the development of a seasonal pycnocline (a strong vertical density gradient). In subsequent winters, when the seasonal pycnocline breaks down, it exposes a thick layer of nearly uniform temperature set by previous winters' heat loss to the atmosphere, which renews the mode water. During normal seasonal cycles, mode water acts both to integrate several years of likely variable atmospheric conditions and to modify wintertime air–sea exchange. With several years of abnormally limited mode water renewal, the anomalous heat, freshwater, and anthropogenic CO_2 associated with the mode water reservoir would diffuse into the permanent thermocline below.

Eighteen Degree Water (EDW) is the subtropical mode water associated with the Gulf Stream extension in the western North Atlantic (Worthington 1959). EDW volume and properties are affected both regionally by the Gulf Stream and by large-scale atmospheric conditions.

The strength of EDW formation during winter is strongly associated with the North Atlantic Oscillation (NAO; Talley 1996; Joyce et al. 2000; Fig. SB3.4). During strongly negative NAO index winters, including 2014/15, the ocean-to-atmosphere heat flux that produces deep mixed layers occurs primarily in the subtropical regions (Dickson et al. 1996), resulting in vigorous EDW formation. During strongly positive NAO winters, vigorous buoyancy forcing occurs in the subpolar regions and the subtropical EDW region is deprived of strong winter atmospheric forcing, resulting in weak to near cessation of EDW formation, as demonstrated for winter 2011/12

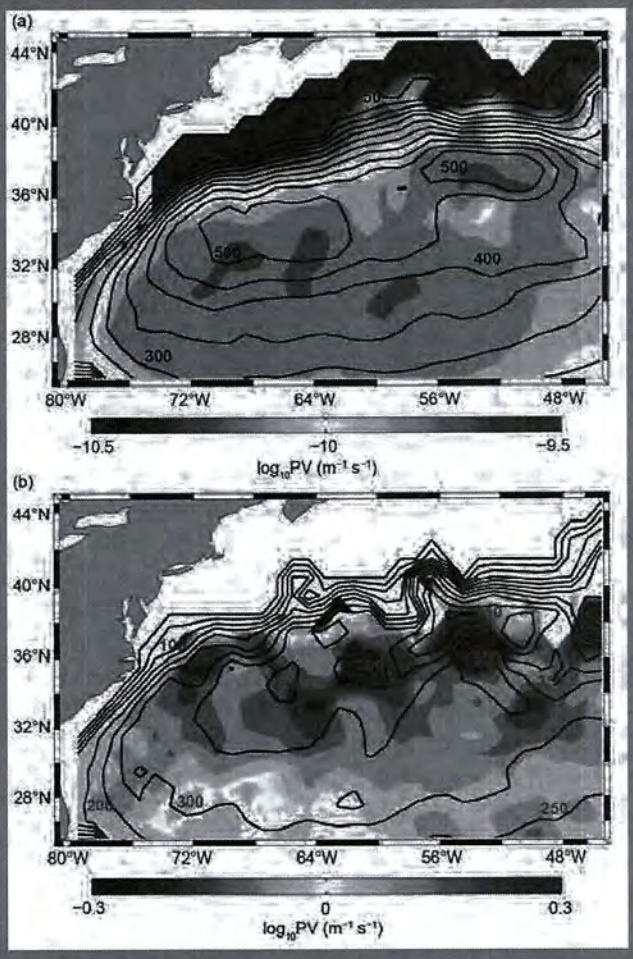

FIG. SB3.3. Eighteen Degree Water (EDW) potential vorticity (log scale color) and EDW thickness (black contours). "EDW PV" is taken as potential vorticity on the σ_Θ = 26.5 kg m^{-3} potential density surface. "EDW thickness" is the thickness of the σ_Θ = 26.2–26.7 kg m^{-3} potential density layer. Contours are at 50 m intervals. High PV (orange/brown) corresponds with very weak (thin) EDW. (a) Climatology of Mar/Apr EDW PV and thickness during the Argo era. (b) 2015 Mar/Apr EDW PV anomaly and Mar/Apr 2015 EDW thickness.

by Billheimer and Talley (2013). In late winter 2013/14, extraordinary ocean cooling in the subpolar North Atlantic that created an extreme type of Labrador Sea Water (Josey et al. 2015) coincided with a strongly positive NAO index and weak EDW formation, illustrating the spatially bimodal nature of NAO-related surface buoyancy forcing.

The Gulf Stream also plays a role in EDW formation. Strong lateral and vertical shears within the Gulf Stream

jet modify convective processes, driving cross-frontal mixing (Joyce et al. 2009, 2013; Thomas et al. 2013). The entrainment of fresh slope water originating north of the Gulf Stream, which occurs approximately between 65°W and 55°W, produces a colder, fresher variety of EDW. This mechanism of EDW formation is apparently much less affected by the intensity of winter subtropical surface heat flux (Billheimer and Talley 2013).

One measure of EDW formation strength is its winter Potential Vorticity (PV), defined by the planetary component only, neglecting relative vorticity:

$$PV = \frac{f}{\rho}\frac{\partial \rho}{\partial z},$$

where f is the Coriolis parameter and ρ is density. High PV is associated with strong stratification. Hence, high EDW PV during the EDW formation season indicates strong stratification and abnormally weak EDW formation.

Here, EDW PV is calculated using the Roemmich–Gilson climatology of Argo profiling floats (Roemmich and Gilson 2009). EDW PV is taken as the PV along the potential density contour $\sigma_\Theta = 26.5$ kg m^{-3}, considered the "EDW core" of low PV EDW (Talley and Raymer 1982; Talley 1996).

The map of climatological EDW PV for March/April, when EDW PV is lowest, shows the thickest, low PV EDW concentrated in two pools (Fig. SB3.3a). We hypothesize that the pool centered at 52°W near the Gulf Stream extension in the northeastern Sargasso Sea is largely produced within the Gulf Stream via cross-frontal mixing (Joyce et al. 2009, 2013; Joyce 2012), whereas the pool centered at roughly 66°W within the tight recirculation gyre of the Sargasso Sea is largely formed and renewed by simple one-dimensional convection—driven by surface buoyancy flux (Worthington 1959).

In March/April 2015, EDW PV was substantially higher, hence EDW was abnormally weak throughout the entire EDW region, particularly in the northern Sargasso Sea (Fig. SB3.3b). A thick (~450–500 m) EDW density layer persisted in the northeastern Sargasso Sea near the Gulf Stream, where one would expect to find EDW formed via cross-frontal mixing, though in 2015 its PV was anomalously high.

Atmospheric conditions of late winter 2014/15 appeared to be a continuation of conditions of the previous winter (Josey et al. 2015; section 3e). A strong correlation exists between EDW PV and the NAO, where high NAO winters, particularly the late winter of 2014/15, are associated with abnormally weak EDW formation (Fig. SB3.4a). EDW volume in 2014/15 was consistent with the lack of EDW formation indicated by high winter EDW PV (Fig. SB3.4b). Peak EDW volume in late winter 2014/15 was at a minimum over the past 10 years, indicating an extraordinary lack of EDW production for a second consecutive year.

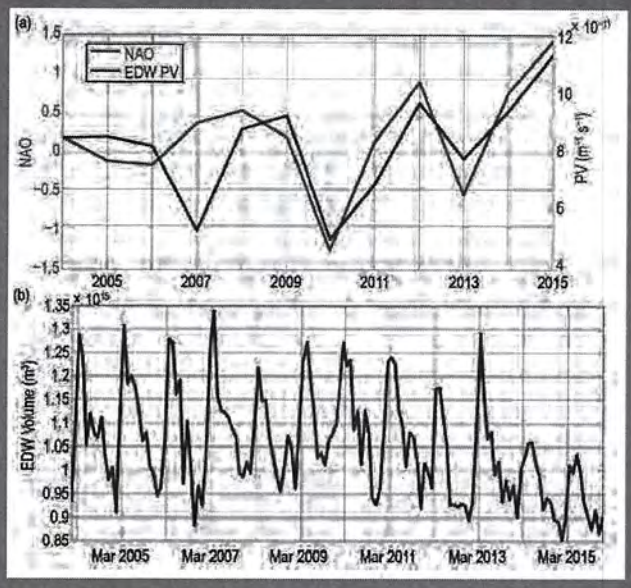

FIG. SB3.4. (a) Jan–Mar 2015 NAO index (red) and annual minimum EDW PV (blue), which tends to be in Mar or Apr. EDW PV is the regional average of the domain mapped in Fig. SB3.3. (b) EDW volume, taken as the volume of the σ_Θ = 26.2–26.7 kg m^{-3} potential density layer integrated over the domain mapped in Fig. SB3.3. The Gulf Stream north wall is the EDW northern boundary.

Lack of EDW renewal prior to 2011/12 was very unusual. Since 1954, when the time series at Bermuda station "S" was established, only one instance of near EDW depletion occurred, coinciding with the strongly positive NAO during the mid-1970s (Talley and Raymer 1982; Talley 1996; Joyce et al. 2000).

In summary, winter 2014/15 was the weakest EDW formation year on record during the Argo era and was associated with an extreme, strongly positive winter NAO. Three of the past four winters have had below average EDW renewal, with the most recent being the most extreme.

order, giving a global time series that is much more nearly constant than the land-only or ocean-only time series. Over the 27-year period, the $P-E$ time series shows a slight decrease during the 1990s, then no obvious subsequent trend. A strengthening of the global winds in the 1990s, also indicated in the global wind time series (Fig. 3.14c), leveled off since the late 1990s. Global average winds were slightly reduced after the dip in 2009.

f. Sea level variability and change—M. A. Merrifield, E. Leuliette, P. Thompson, D. Chambers, B. D. Hamlington, S. Jevrejeva, J. J. Marra, M. Menéndez, G. T. Mitchum, R. S. Nerem, and W. Sweet

Sea level variations and trends during 2015 feature the largest El Niño event since 1997/98, the highest annual average global mean sea level (GMSL) recorded since the altimeter era began in 1993, and reversals in short-term regional trends reflecting the changing state of the PDO and other climate modes. Regional and global sea level patterns are described here using satellite altimeter data, and extreme coastal sea levels are described using tide gauge data.

The signature of El Niño is clear in the 2015 annual mean sea level anomaly (Fig. 3.15a), the change in sea level from 2014 to 2015 (Fig. 3.15b), and the 2015 deviation of sea level (minus GMSL) (Fig. 3.15c). All show the characteristic El Niño sea level pattern resulting from weakened trades and westerly wind anomalies in the tropical Pacific (see Fig. 3.13a), i.e., low sea levels in the western equatorial Pacific and high sea levels in the cold tongue region of the eastern equatorial Pacific. During the growth phase of El Niño in 2015, low sea levels in the western equatorial Pacific were more prominent north of the equator than south, with weak negative anomalies in the southern convergence zone region (Fig. 3.15c). Peak low sea levels south of the equator are expected during the decline phase of El Niño in 2016 (Widlansky et al. 2014). The poleward extension of high sea levels to mid- and high latitudes along the Pacific coasts of North and South America signifies coastal-trapped wave propagation of the high anomaly from the tropics, as well as local wind forcing at midlatitudes that drives positive anomalies along the eastern boundaries, particularly off North America (Enfield and Allen 1980; Chelton and Davis 1982). The El Niño–related negative sea level anomaly in the western equatorial Pacific is associated with reduced transport and a shallower thermocline in the Indonesian Throughflow (Sprintall et al. 2014). The thermocline depth anomalies propagate into the Indian Ocean along the coastal waveguide, reducing sea level along the west coast of Australia (Fig. 3.15c). High sea levels in the western equatorial Indian

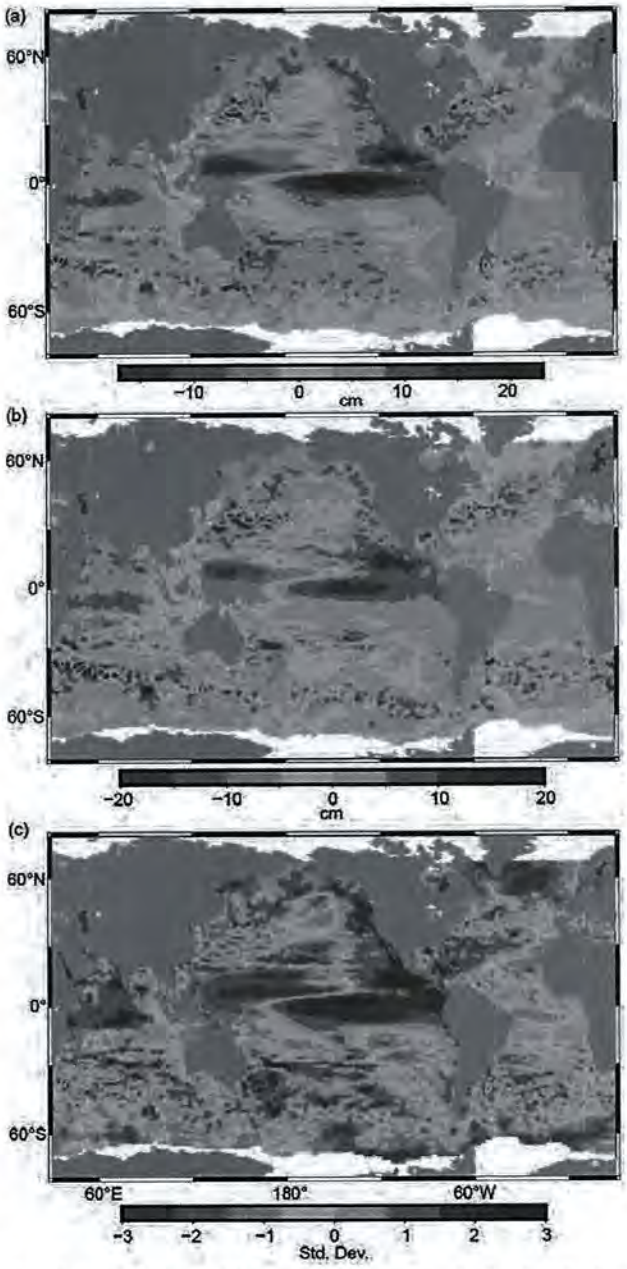

Fig. 3.15. (a) Mean 2015 sea level anomaly (cm) relative to a 1993–2014 baseline; (b) 2015 minus 2014 annual means; and (c) 2015 annual mean sea level anomaly with the GMSL trend removed and normalized by the standard deviation of annual mean anomalies from 1993–2014. Data from the multimission gridded sea surface height altimeter product produced by Ssalto/Duacs, distributed by AVISO, with support from CNES (www.aviso.altimetry.fr).

Ocean are likely associated with anomalous easterlies linked to El Niño.

Other prominent patterns in the annual mean anomalies, particularly in the standard deviations (Fig. 3.15c), include: 1) anomalously low sea levels around Antarctica and an associated meridional sea level gradient, indicative of an intensified Antarctic

Circumpolar Current (ACC); 2) generally high sea levels between 30° and 60°S related to the subtropical gyre circulations (see Fig. 3.4a; Roemmich et al. 2007); 3) high sea levels in the North Atlantic subtropical gyre region suggesting an intensified anticyclonic gyre circulation; and 4) low sea levels in the North Atlantic subpolar region corresponding to a strengthened cyclonic gyre circulation.

The seasonal progression of the 2015 El Niño (Fig. 3.16) was marked by a steady autumn of western Pacific sea levels throughout the year and the eastward propagating equatorial Kelvin waves that strengthened in boreal spring (March–May) and fully impacted the South American coast by autumn (September–November). High sea levels along North and South America preceded the arrival of the propagating high anomaly from the equatorial Pacific, indicating that these high anomalies were partly remnants from the previous year, which featured a weak Modoki-like (Ashok et al. 2007) near-El Niño, as well as locally generated wind-forced anomalies.

Other features in the annual mean sea level (Fig. 3.15) that exhibited a marked variation over the year (Fig. 3.16) include the Indian Ocean high sea levels that developed over the second half of 2015. In addition, the low sea levels along Antarctica and the heightened ACC sea level gradient were more prominent in the first half of 2015 than the second half. Sea level changes over the course of the year were also evident in the marginal seas of the North Atlantic, with high sea levels in the North Sea peaking in summer and dropping in autumn, low sea levels in the Mediterranean over most of the year switching to high levels during autumn, and high sea levels in Hudson Bay peaking in spring that fell below climatology levels over the remainder of the year.

GMSL has risen over the satellite altimeter record (1993–present) at an average rate of 3.3 ± 0.4 mm yr^{-1} (Fig. 3.17a). GMSL in 2015 was the highest yearly average over the record and ~70 mm greater than the 1993 average, due in part to the linear trend but also to the 2015 El Niño, which caused sea level to rise an additional ~10 mm above the long-term trend (Fig. 3.17b). The high GMSL anomaly during 2015 exceeded the anomaly during the previous large El Niño in 1997/98 (Fig. 3.17b).

The rise in sea level over the altimeter period has not been uniform, with regions of high rates located in the western Pacific and Indian Oceans (Fig. 3.17c). Sea level rates have been near zero or falling over areas of the eastern Pacific, Southern, and North Atlantic Oceans. These regional patterns are largely linked to trending wind patterns over the past 20 years associated with climate modes, such as the PDO (e.g., Merrifield et al. 2012). These are not long-term trends and have reversed in many regions over the past five years (Fig. 3.17c compared to 3.17d). In particular, sea level has been falling in the western tropical Pacific and rising in the eastern Pacific due to a change from negative to positive PDO phase, and with that a shift in basin-scale wind patterns, as well as the 2014 weak Modoki-like near-El Niño and the strong 2015 El Niño.

Extreme sea level events, measured as the average of the 2% highest daily values above the annual mean from tide gauges, showed a characteristic dependence on latitude, reflecting stronger atmospheric forcings outside the tropics (Fig. 3.18a). The 2015 extreme levels were above climatology at the eastern equatorial Pacific and along the Pacific coast of North America (Fig. 3.18b), reflecting the contribution of positive El Niño anomalies and possibly some shifts in storm forcing. The high pattern did not extend to mid-latitudes along the South American coast. Extremes were below climatology along the east coast of North America, due in part to slightly below average Atlantic hurricane activity (section 4e2).

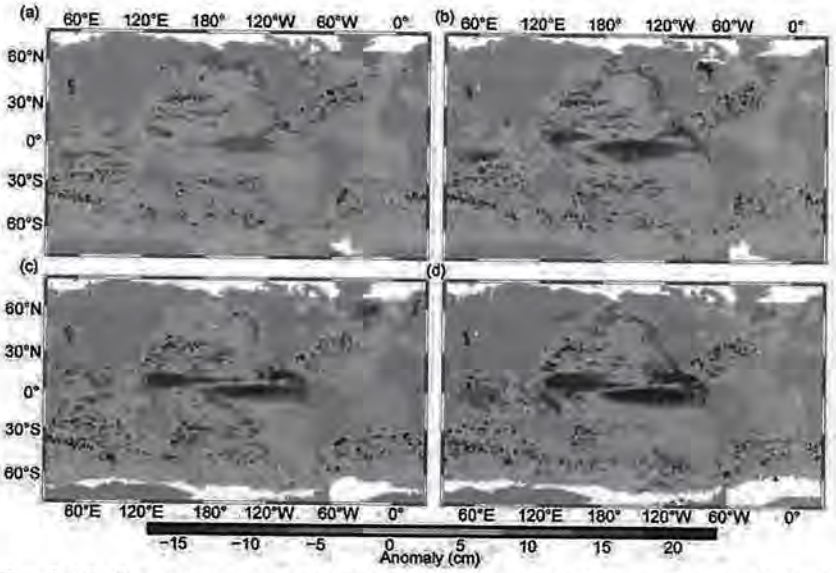

Fig. 3.16. Seasonal sea level anomalies (cm, relative to the 1993-2014 average) for (a) Dec–Feb 2014/15, (b) Mar–May 2015, (c) Jun–Aug 2015, and (d) Sep–Nov 2015.

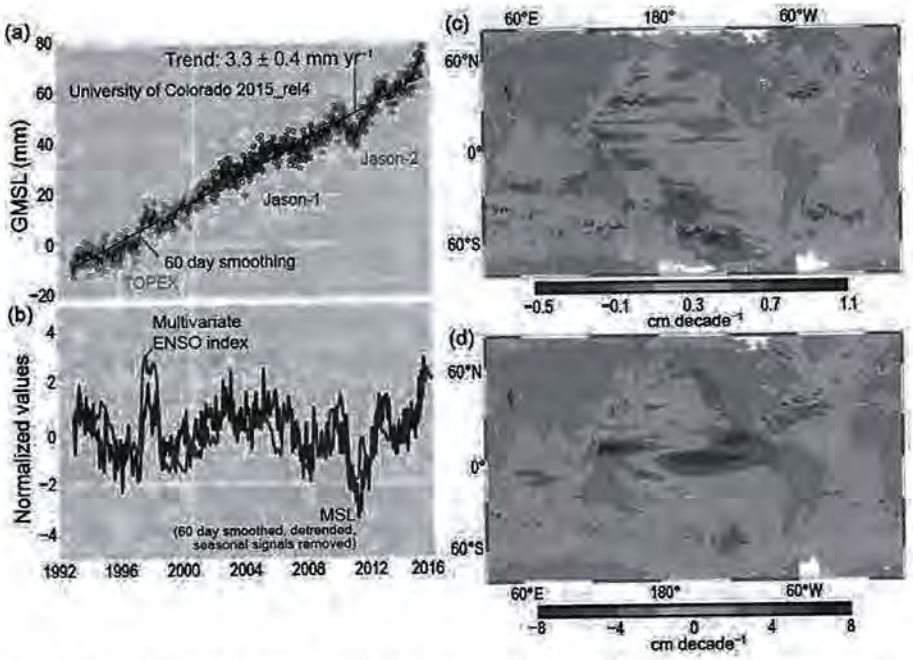

Fig. 3.17. (a) Global mean sea level (mm) obtained from consecutive satellite altimeter missions, with 60-day smoothing and seasonal signals removed (black line indicates a rise rate of 3.3 mm yr^{-1}); (b) Detrended GMSL compared with the multivariate ENSO index (MEI; obtained from http://sealevel.colorado.edu); (c) Sea level trends (cm decade^{-1}) 1993–2015; and (d) Sea level trends (cm decade^{-1}) 2011–15. Scales differ in (c) and (d).

g. Surface currents—R. Lumpkin, G. Goni, and K. Dohan

Ocean surface current changes, transports derived from ocean surface currents, and features such as rings inferred from surface currents, all play a role in ocean climate variations. Surface currents described here are obtained from in situ (global array of drogued drifters and moorings) and satellite (altimetry, wind stress, and SST) observations. Transports are derived from a combination of sea level anomalies (from altimetry) and climatological hydrography. For details of these calculations, see Lumpkin et al. (2011). Anomalies are calculated with respect to 1992–2007. Annually averaged zonal current anomalies for 2015, changes in anomalies from 2014 to 2015 (Fig. 3.19), and seasonal average 2015 anomalies (Fig. 3.20) are discussed below by individual ocean basin.

The dramatic El Niño of 2015/16 dominated annual mean current anomalies in the Pacific basin (Fig. 3.19a), with annually averaged eastward anomalies >20 cm s^{-1} between 1.5° and 6°N and weaker eastward anomalies in the rest of the latitude band between 10°S and 10°N. Because 2014 was characterized by westward anomalies on the equator and eastward anomalies in a strengthened North Equatorial Countercurrent (NECC) at 5°–6°N, the 2015 minus 2014 map (Fig. 3.19b) has larger eastward anomaly tendencies on the equator and weaker tendencies along the NECC than the 2015 anomaly map (Fig. 3.20).

In contrast to the annual mean picture, 2015 began with westward anomalies between 5°S and 5°N across the eastern half of the basin (Fig. 3.20a), with peak westward anomalies of ~25 cm s^{-1} at 1°N. These anomalies were an enhancement of the northern branch of the westward South Equatorial Current (SEC) as seen in December 2014 (Dohan et al. 2015). Immediately north of 5°N, the eastward NECC was only marginally faster than its climatological January strength. In February, intense El Niño–related eastward anomalies first appeared in the western tropical Pacific as anomalies of 20–40 cm s^{-1} at 145°–175°E, 2.5°S–4°N.

Throughout boreal spring, the El Niño–related anomaly pattern propagated eastward (Fig. 3.20b), reaching 160°W by March and 90°W by April. During these months, warm water advected by these current anomalies caused the NINO3 and NINO3.4 SST indices to increase rapidly (see section 4b). In April, eastward anomalies of 40–50 cm s^{-1} were present at 95°–130°W, 2.5°S–2.5°N. Throughout March and April, equatorial zonal currents in the band 120°W–180° were close to their climatological average, straddled by the eastward anomalies centered at 5°–6°N (the latitude of the NECC) and 1°–2°S (Fig. 3.20b). In May, the anomalies south of the equator diminished to <20 cm s^{-1}, while anomalies of 35–40 cm s^{-1} persisted in the NECC band. The eastward advection of relatively fresh water, combined with an El Niño–driven shift in the ITCZ (section 3e), likely accounts for the development of fresh SSS anomalies (section 3d).

Throughout boreal summer (June–August; Fig. 3.20c), eastward anomalies persisted across the basin, with equatorial eastward anomalies returning across the western half of the basin in July and across the entire basin in August. Averaged over these three months (Fig. 3.20c), eastward anomalies exceeded 5 cm s^{-1} from 6°S to 9°N, with peak anomalies of 30–35 cm s^{-1} at 4°–6°N. This pattern persisted in boreal

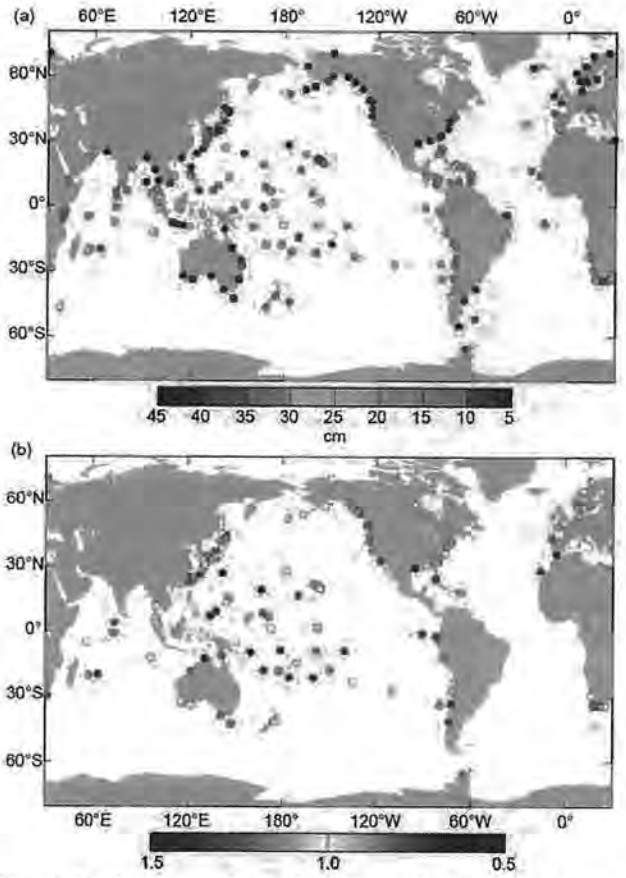

FIG. 3.18. (a) Annual maximum sea level (cm) during 2015 computed from the mean of the 2% highest daily values relative to the 2015 annual mean, measured at tide gauges (http://uhslc.soest.hawaii.edu); (b) The 2015 annual maximum from (a) divided by the time-averaged annual maximum measured at each station with at least 20 years of data.

autumn (Fig. 3.20d), with another pulse of extremely strong (>50 cm s^{-1}) eastward anomalies appearing at 170°E–150°W, 3°–5°N in August and peaking at >60 cm s^{-1} in October; these were the strongest monthly averaged broad-scale current anomalies seen in 2015. This pattern propagated eastward in November and weakened significantly through December. The year concluded with eastward anomalies of ~20 cm s^{-1} across the basin from 3°N to 6°N, consistent with a stronger and wider NECC than in the December climatology. The northern edge of this NECC was close to its climatological northern extent but extended south to 2°N, compared to 3.5°N in climatology.

The Kuroshio was shifted anomalously northward in 2010–14, although this shift diminished during 2014 (Dohan et al. 2015). During 2015, the Kuroshio was close to its climatological latitude, with a maximum annually averaged speed of 35 cm s^{-1} at 35°N between 140° and 170°E (Fig. 3.19).

Surface current anomalies in the equatorial Pacific typically lead SST anomalies by several months, with a magnitude that scales with the SST anomaly magnitude. A return to normal current conditions is also typically seen before SST returns to normal. Thus, current anomalies in this region are a valuable predictor of the evolution of SST anomalies and their related climate impacts. This leading nature can be seen in the first principal empirical orthogonal function (EOF) of surface current (SC) anomaly and separately of SST anomaly in the tropical Pacific basin (Fig. 3.21). For 1993–2015, the maximum correlation between SC and SST is 0.70 with SC leading SST by 71 days. Both SC and SST EOF amplitudes were positive throughout 2015, with the cumulative effect of positive SC EOF amplitude resulting in a steadily increasing SST EOF amplitude to almost 3 standard deviations in November 2015, nearing the November 1997 value of 3.2.

Throughout most of 2015, Indian Ocean monsoon-driven currents were much closer to climatology than the dramatic anomalies seen in the Pacific (Fig. 3.19a). This normality is in contrast to the strong eastward anomalies seen across the basin in 2013–14 (Lumpkin et al. 2014; Dohan et al. 2015). Those eastward anomalies dominate the 2015 minus 2014

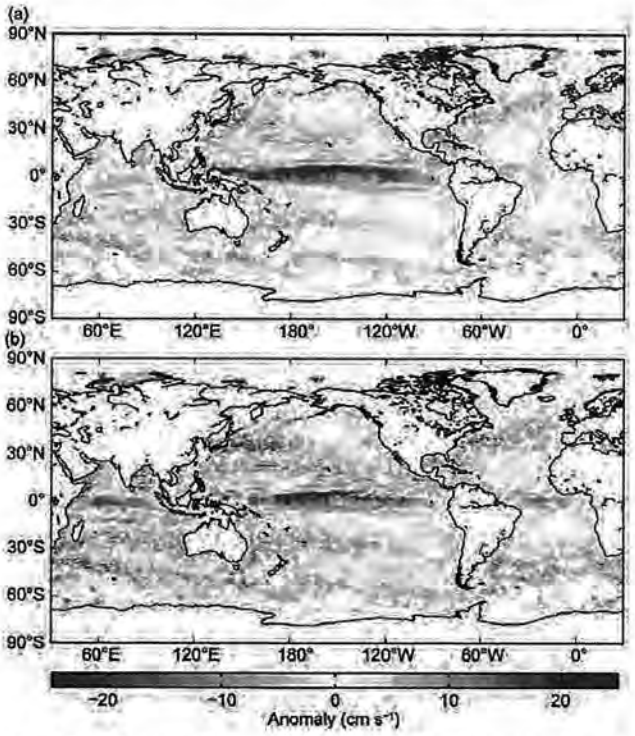

FIG. 3.19. Annually averaged geostrophic zonal current anomalies (cm s^{-1}) for (a) 2015 and (b) 2015 minus 2014 derived from a synthesis of drifters, altimetry, and winds. Positive (red) values denote anomalously eastward velocity.

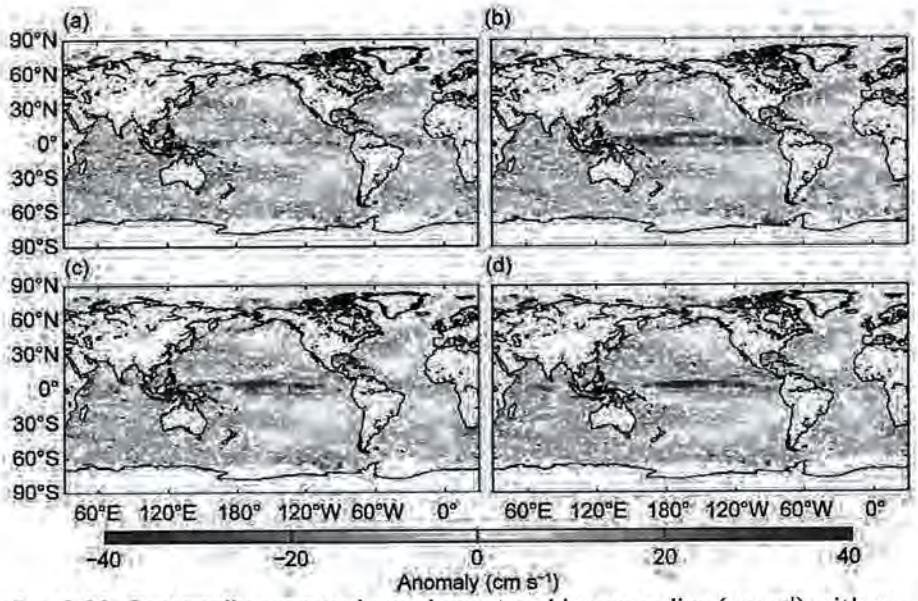

FIG. 3.20. Seasonally averaged zonal geostrophic anomalies (cm s^{-1}) with respect to seasonal climatology, for (a) Dec 2014–Feb 2015, (b) Mar–May 2015, (c) Jun–Aug 2015, and (d) Sep–Nov 2015.

zonal current tendencies in the Indian Ocean basin (Fig. 3.19b). In 2015, the strongest anomalies with respect to monthly climatology were seen in October and November, with an unusually early development of the North Monsoon Current (e.g., Beal et al. 2013) associated with westward anomalies of ~30 cm s^{-1} at 3°S–2°N, 60°–80°E during these months (Fig. 3.20d). Large-scale current anomalies returned to near-climatological December values by the end of 2015.

The Agulhas Current transport is a key indicator of Indian–Atlantic Ocean interbasin water exchanges. The annual mean transport of the Agulhas Current has been decreasing from a high set in 2013, with values of 56 Sv in 2013 (1 Sv $\equiv 10^6$ m^3 s^{-1}), 53 Sv in 2014, and 50 Sv in 2015. The 2015 transport of 50 Sv is equal to the Agulhas' long-term (1993–2015) mean.

Annual mean anomalies in the Atlantic Ocean (Fig. 3.19a) indicate a 5–7 cm s^{-1} strengthening of the eastward NECC at 4.5°–6.5°N, 30°–50°W, and conditions close to climatology along the equator. However, the annual average hides a pattern of reversing equatorial anomalies between boreal winter and spring (Fig. 3.20). The year began with eastward anomalies of 20 cm s^{-1} from 3°S to 2°N across much of the basin, which weakened through February and were present only at 25°–35°W in March/April. In May, westward anomalies of 10–15 cm s^{-1} developed across the basin from 2°S to 2°N. These anomalies weakened considerably through June and were no longer present in July. No significant basinwide equatorial anomalies were seen in the remainder of 2015.

The Gulf Stream in 2015 remained close to its climatological position with little change from 2014 (Fig. 3.19).

The North Brazil Current, which sheds rings that carry waters from the Southern Hemisphere into the North Atlantic and has important ecosystem impacts downstream (Kelly et al. 2000), exhibited an annual transport smaller than its long-term (1993–2015) value. As in 2014, it shed eight rings in 2015, a larger-than-average value. Sea level anomalies in the region, which have generally increased since 2001 (apart from lows in 2003 and 2008), remained higher than average in 2015.

In the southwest Atlantic Ocean, the Brazil Current carries waters from subtropical to subpolar regions, mainly in the form of large anticyclonic rings (Lentini et al. 2006). The separation of the Brazil Current front from the continental shelf break continued to exhibit a seasonal cycle, which is mainly driven by wind stress curl variations and the transport of this current. During 1993–98, the annual mean separation of the front shifted southward in response to a long-term warming in South Atlantic temperatures (cf. Lumpkin and Garzoli 2010; Goni et al. 2011). In 2015, the Brazil Current front and its separation from the continental shelf break persisted south of its mean position, unchanged from 2014.

h. Meridional overturning circulation observations in the North Atlantic Ocean—M. O. Baringer, M. Lankhorst, D. Volkov, S. Garzoli, S. Dong, U. Send, and C. S. Meinen

This section describes the Atlantic meridional overturning circulation (AMOC) and the Atlantic meridional heat transport (AMHT), determined by the large-scale ocean circulation wherein northward moving upper layer waters are transformed into deep waters that return southward, redistributing heat, freshwater, carbon, and nutrients. Previous *State of the Climate* reports (e.g., Baringer et al. 2013) and reviews (e.g., Srokosz and Bryden 2015; Perez et al. 2015; Carton et al. 2014; Srokosz et al. 2012) discuss the AMOC's impact on climate variability and ecosystems. The AMOC is computed as the maximum of the

vertical accumulation of the horizontally integrated velocity across a section (i.e., the maximum transport that occurs in either the upper or lower layer before the circulation starts to change direction again). The AMHT involves the co-variability of temperature and velocity and is only meaningful as a flux (and hence, independent of the absolute temperature scale used) when the total mass transport can be accounted for (i.e., sums to zero). Observing systems can measure both temperature and velocity, usually with tradeoffs in system design that favor the computation of one quantity over the other. Here we describe the AMOC from observing systems at 41°N, 26°N, and 16°N, and AMHT at 41°N, 26°N, and 35°S. In the future, AMOC observing systems in the South Atlantic and subpolar North Atlantic should provide additional time series (e.g., Srokosz et al. 2012).

The longest time series of ocean transport to serve as an index of the AMOC's strength in the North Atlantic (e.g., Frajka-Williams 2015; Duchez et al. 2014) is from the Florida Current (FC, as the Gulf Stream is called at 26°N), measured since 1982 (Fig. 3.22). FC and AMOC transport variations at all time scales also are inversely linked to sea level variations along the east coast (Goddard et al. 2015; McCarthy et al. 2015). The median 1982–2015 transport of the FC is 31.9 ± 0.25 Sv (one standard error of the mean assuming a 20-day integral time scale) with a small downward trend of −0.31 ± 0.26 Sv decade^{-1} (errors estimating 95% significance as above). The 2015 median FC transport was 31.7 ± 1.7 Sv, only slightly below the long-term average. Daily FC transports compared to those of all previous years (Fig. 3.22) indicate that

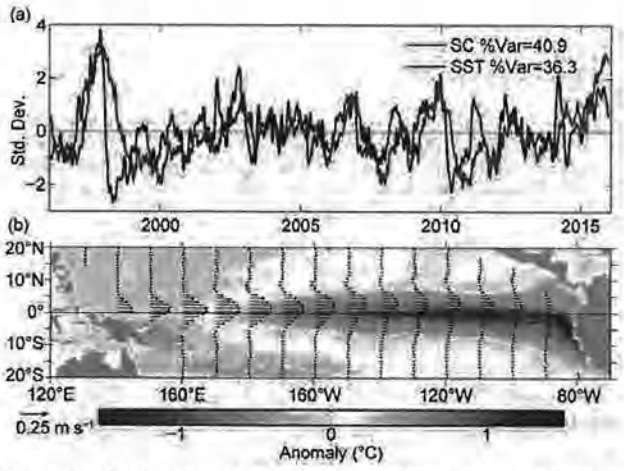

Fig. 3.21. EOF of surface current (SC) and SST anomaly variations in the tropical Pacific from the OSCAR model (Bonjean and Lagerloef 2002; www.esr.org /enso_index.html). (a) EOF Amplitude time series normalized by their respective standard deviations. (b) EOF Spatial structures.

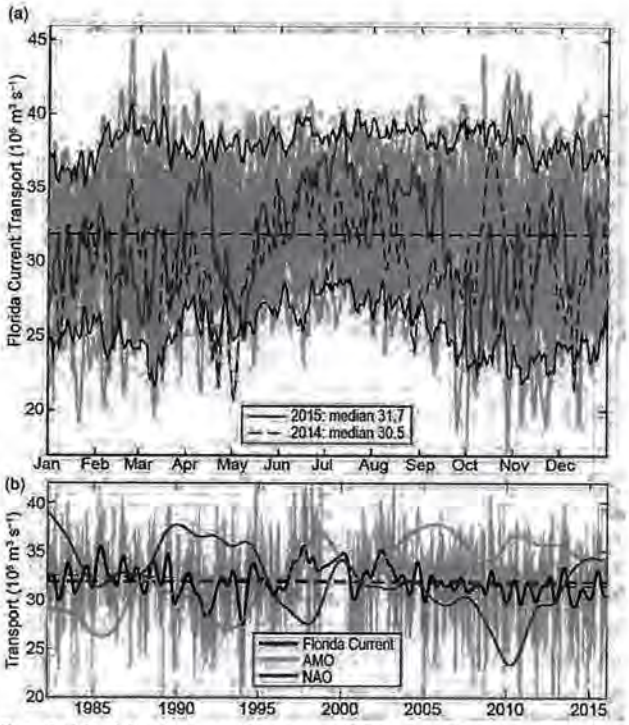

Fig. 3.22. (a) Daily estimates of Florida Current transport (10^6 m^3 s^{-1}) during 2015 (orange solid line), 2014 (dashed purple line), and 1982–2012 (light gray lines) with 95% confidence interval of daily transport values computed from all years (black solid line) and the long-term mean (dashed black). (b) Daily estimates of Florida Current transport (10^6 m^3 s^{-1}) for the full time series record (light gray), smoothed using a 12-month second-order Butterworth filter (heavy black line), mean transport for the full record (dashed black line), and linear trend from 1982 through 2015 (dashed blue line). Two-year low-passed Atlantic Multidecadal (AMO, yellow line) and North Atlantic Oscillation (NAO, red line) indices are also shown.

2015, like 2014, had several unusually low transport anomalies (extremes defined as outside the 95% confidence limits for daily values). These occurred during 8–9 May, 24–29 September, and 5–9 October 2015. The lowest daily 2015 FC transport was 22.2 Sv on 8 October, with transports < 23 Sv for five days around this date. During 2015 there was only one high transport event, with an average transport of > 39 Sv from 8 to 13 July.

At 41°N, a combination of profiling Argo floats (that measure ocean temperature and salinity for the upper 2000 m on broad spatial scales, as well as velocity at 1000 m) and altimetry-derived surface velocity (Willis and Fu 2008) are used to estimate the AMOC (Fig. 3.23) and AMHT (Fig. 3.24). This time series has not been updated since last year's report (Baringer et al. 2015a,b), extending from January 2002 to December 2014. At 26°N, the AMOC/AMHT (Figs. 3.23 and 3.24) is measured with full-water column moorings

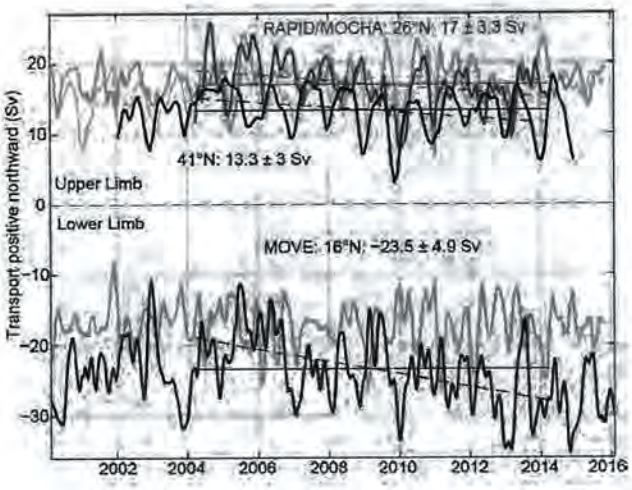

Fig. 3.23. Estimates of Atlantic meridional overturning circulation (1 Sv ≡ 10^6 m^3 s^{-1}; AMOC) from the Argo/Altimetry estimate at 41°N (black; Willis 2010), the RAPID-MOC/MOCHA/WBTS 26°N array (red; McCarthy et al. 2015), and the German/NOAA MOVE array at 16°N (blue; Send et al. 2011) shown versus year. All time series have a three-month second-order Butterworth low-pass filter applied. Horizontal lines are mean transports during similar time periods as listed in the corresponding text. Dashed lines are trends for each series over the same time period. For MOVE data, the net zonal and vertical integral of the deep circulation represents the lower limb of the AMOC (with a negative sign indicating southward flow), and hence a stronger negative (southward) flow represents an increase in the AMOC amplitude. Light gray lines show ECCO2-derived transports: (top) thin gray is the 41°N transport, thick gray is the 26°N transport, (bottom) shows the negative meridional overturning circulation in the model for ease of comparison with the 16°N data.

that span the full basin and include direct transport measurements in the boundary currents as part of the large RAPID-MOC/MOCHA/WBTS 26°N mooring array (Smeed et al. 2015). The data from these moorings are collected every 18 months, most recently in December 2015; too late to be calibrated and finalized for this report. The 26°N data shown here extend from April 2004 to March 2014 (see last year's report for full details). At 16°N, a mooring array of inverted echo sounders, current meters, and dynamic height moorings (Send et al. 2011) measures the flow below 1000 m (the southward flowing part of the AMOC "conveyor belt") that sends North Atlantic Deep Water toward the equator; hence, the AMOC estimate at this latitude (Fig. 3.23) is a negative number (southward deep flow) to distinguish these observations from the full water column systems. Since this array only measures the deep circulation, an estimate of the AMHT is impossible at 16°N because of the missed large signals and high correlations in the surface waters. These data have been updated since last year's report and now extend from February 2000 to February 2016. At 35°S in the South Atlantic, the AMHT (Fig. 3.24) is estimated using a combination of high-density (closely spaced) expendable bathythermograph (XBT) and broader-scale Argo profiling float data (Garzoli et al. 2012). While the AMOC has also been estimated at 35°S (e.g., Dong et al. 2009), those estimates (not shown) are rough because the XBTs only extend to 750 m. These data are collected and analyzed in near–real time, with values spanning July 2002 to October 2015.

Some guidance on 2015 AMOC and AMHT variability can be gained from state estimation model output, constrained by observations. February 1992–November 2015 monthly estimates of AMOC and AMHT from the global MITgcm in ECCO2 (cube-sphere) configuration (e.g., Menemenlis et al. 2008), forced with the new JRA-55 atmospheric fields (Kobayashi et al. 2016) and GPCP precipitation

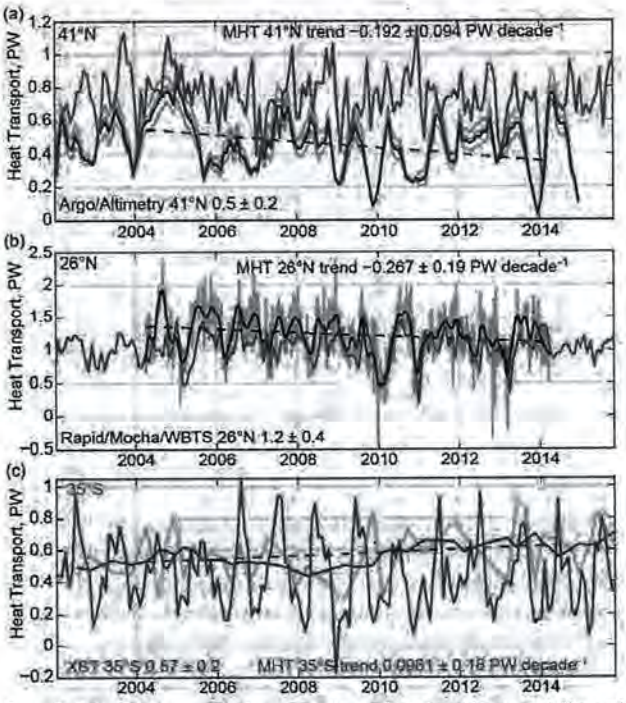

Fig. 3.24. Observed time series of Atlantic meridional heat transport (PW; AMHT) at (a) 41°N (from profiling floats following Hobbs and Willis 2012; blue lines), with uncertainties (light blue lines) and the trend (dashed blue line), at (b) 26°N (from mooring/hydrography data) 12-hourly values (gray line), filtered with a 3-month low-pass filter (black line), and the trend (black dashed line), and at (c) 30°–35°S (from XBTs) quarterly values (light green), filtered with yearly boxcar (dark green line), and the trend (dashed green line). Heat transports simulated by ECCO2 (orange lines) are shown at all latitudes.

(Huffman et al. 2012), are analyzed here. The ECCO2 model output is well correlated with the instrument-based measurement of the AMOC (Fig. 3.23) and AMHT (Fig. 3.24) at 26°N and 41°N, with correlations of 0.58/0.59 and 0.57/0.38, respectively, all significantly above the 95% confidence level. ECCO2 model output is not statistically significantly correlated with the 16°N AMOC or 35°S AMHT transports (correlation values of 0.12 and 0.13, respectively). At 26°N and 41°N the AMOC and AMHT in the ECCO2 output show a slight increase from 17.6 Sv and 1.02 PW (1 PW = 10^{15} W) in 2014 to 18.3 Sv and 1.09 PW in 2015. Preliminary analysis of the new data from 26°N (not shown) indicates that the transport has continued fairly unchanged since 2011 (through December 2015), with values lower than the earlier part of the record (D. A. Smeed, 2016, personal communication). Additionally, there is no unusual "event" in the assimilation time series, as has been clearly seen in other time periods (e.g., Fig. 3.24). This finding is supported by the FC time series and the ECCO2 state estimation (Fig. 3.22).

At 16°N, the time series of the AMOC estimate decreased from 29.0 Sv in 2013, to 28.4 Sv in 2014, and to 27.2 Sv in 2015 (as stated earlier the decrease in southward flow implies an increase in the AMOC at this latitude; Fig. 3.23). This reduction has led to a reduced estimate of the long-term trend of the AMOC from February 2000 to February 2016 at 16°N to be +3.6 Sv ± 2.5 Sv decade^{-1}. This trend is of the opposite sign from the trends at 26°N and 41°N (−4.1 ± 3.2 Sv decade^{-1} and −1.3 ± 4.9 Sv decade^{-1}). A similar situation exists with the 35°S AMHT transport estimate. In the south, the AMHT has remained essentially constant for the last three years (mean value 0.6 PW northward). This implies a virtually steady AMOC as well (the AMOC and AMHT being highly correlated). This recently constant AMHT has reduced the long-term trend of an increasing AMHT to +0.11 ± 0.10 PW decade^{-1}. From these data it is clear that the variability at all latitudes in the Atlantic is not well correlated and, therefore, data from more than one latitude are needed to describe the state of the ocean.

i. Global ocean phytoplankton—B. A. Franz, M. J. Behrenfeld, D. A. Siegel, and S. R. Signorini

Marine phytoplankton represent roughly half the net primary production (NPP) on Earth, fixing atmospheric CO_2 into food that fuels global ocean ecosystems and drives biogeochemical cycles (e.g., Field et al. 1998; Falkowski et al. 1998). Satellite ocean color sensors, such as SeaWiFS (McClain 2009), MODIS (Esaias et al. 1998), and VIIRS (Oudrari et al. 2014), provide observations of sufficient frequency and geographic coverage to globally monitor changes in the near-surface concentrations of the phytoplankton pigment chlorophyll-*a* (Chl*a*; mg m^{-3}). Chl*a* provides a first-order index of phytoplankton abundance and is proportional to the maximum sunlight energy absorbed for photosynthesis (Behrenfeld et al. 2006). Here, global Chl*a* distributions for 2015 are evaluated within the context of the 18-year continuous record provided through the combined observations of SeaWiFS (1997–2010), MODIS on *Aqua* (MODISA, 2002–present), and VIIRS on *Suomi-NPP* (2011–present). All Chl*a* data used in this analysis correspond to version R2014.0 (http://oceancolor.gsfc.nasa.gov/cms/reprocessing/), which uses common algorithms and calibration methods to maximize consistency in the multimission satellite record.

The spatial distribution of VIIRS annual mean Chl*a* for 2015 (Fig. 3.25) is generally consistent with the well-established, physically driven distribution of nutrients (e.g., Siegel et al. 2013). To assess changes in Chl*a* for 2015, mean values for VIIRS Chl*a* in each month of 2015 were subtracted from monthly climatological means for MODISA (2003–2011) within globally distributed geographic bins, and then those monthly anomaly fields were averaged (Fig. 3.26a). Identical calculations were performed on MODISA SST (°C) data to produce a companion SST annual mean anomaly (Fig. 3.26b).

In 2015, the phytoplankton Chl*a* concentrations across much of the equatorial Pacific were strongly depressed, with concentrations 20%–50% below the climatological norm. This response is generally corre-

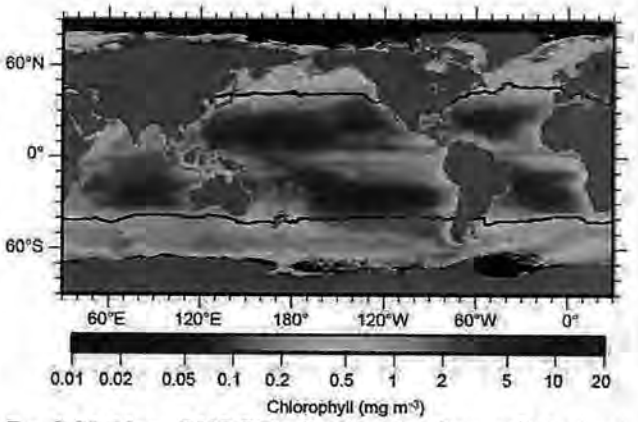

FIG. 3.25. Mean 2015 Chl*a* distribution (mg m^{-3}) derived from VIIRS with the location of the mean 15°C SST isotherm (black lines) delineating boundaries of the permanently stratified ocean (PSO). Chl*a* data are from NASA Reprocessing version 2014.0. Data are averaged into geo-referenced equal area bins of approximately 4.6 km × 4.6 km and mapped to an equi-rectangular projection centered at 150°W.

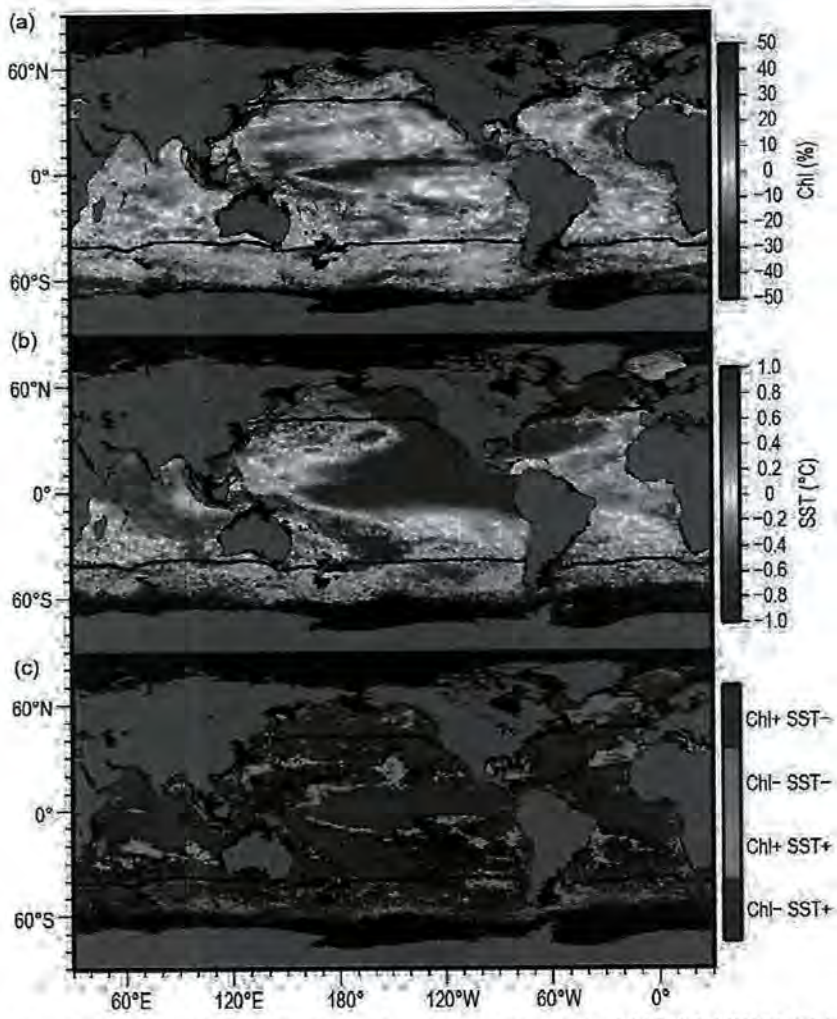

Fig. 3.26. Spatial distribution of summed monthly 2015 (a) VIIRS Chl*a* anomalies expressed as % difference from climatology and (b) MODISA SST anomalies shown as absolute differences. (c) Relationships between the signs of SST and Chl*a* anomalies from (a) and (b), with colors differentiating sign pairs and absolute changes of less than 3% in Chl*a* or 0.1°C in SST masked in black. Monthly differences are derived relative to a MODISA 9-year climatological record (2003–11). Location of the mean 15°C SST isotherm (black lines) delineates the PSO.

lated with elevated surface temperatures (Fig. 3.26c), consistent with a well-developed El Niño. Depressed Chl*a* was also observed in climatologically warmer waters of the northern Indian Ocean, northeastern Pacific, and Sargasso Sea, while elevated Chl*a* was observed in the cooler waters of the western North Pacific, much of the South Pacific, and throughout the tropical Atlantic. These regions fall within the permanently stratified ocean (PSO; Figs. 3.25 and 3.26, black lines at approximately 40°N and 40°S), defined here as the region where annual average surface temperatures are >15°C (Behrenfeld et al. 2006). The PSO is characterized by nutrient-depleted surface mixed layers shallower than the nutricline.

Typically, chlorophyll anomalies in the PSO exhibit an inverse relationship with SST anomalies (Behrenfeld et al. 2006), as annual mean SST anomalies largely coincide with surface mixed layer depth (MLD) changes in the PSO. A shallower MLD means that phytoplankton spend more time near the ocean's surface and thus have higher daily sunlight exposures than deeper mixing populations. Phytoplankton respond to this increased light by decreasing their cellular chlorophyll levels in a response called photoacclimation (thus, increased SST leads to decreased MLD, which leads to decreased Chl*a*). A potential second consequence of a decrease in MLD is a decrease in the vertical transport of nutrients to the surface layer, but coupling between the MLD and nutricline depths throughout much of the PSO is known to be weak (Lozier et al. 2011). In the equatorial Pacific, however, the anomalously low Chl*a* and high SST in 2015 were primarily driven by nutrient availability changes due to the El Niño event, wherein the westerly winds weaken along the equator allowing warm water, normally confined to the western Pacific, to migrate eastward. Wind-driven upwelling, a process that brings cold, nutrient-rich water to the surface along the equator, was also greatly reduced, causing SST to rise and significantly lowering biological productivity. At higher latitudes, outside the PSO, the relationship between SST changes and light and nutrient conditions is more complex, resulting in a wide diversity of responses between anomalies in SST and Chl*a*, (Fig. 3.26c).

Spatially integrated monthly mean Chl*a* concentrations in the PSO (Fig. 3.27a) vary by ~20% (±0.03 mg m^{-3}) around a long-term mean of approximately 0.15 mg m^{-3} over the 18-year time series. This variability includes seasonal cycles and larger departures from the climatological mean associated with climatic events. The long-term mean is approximately 0.01 mg m^{-3} higher than previous reports (Franz et al.

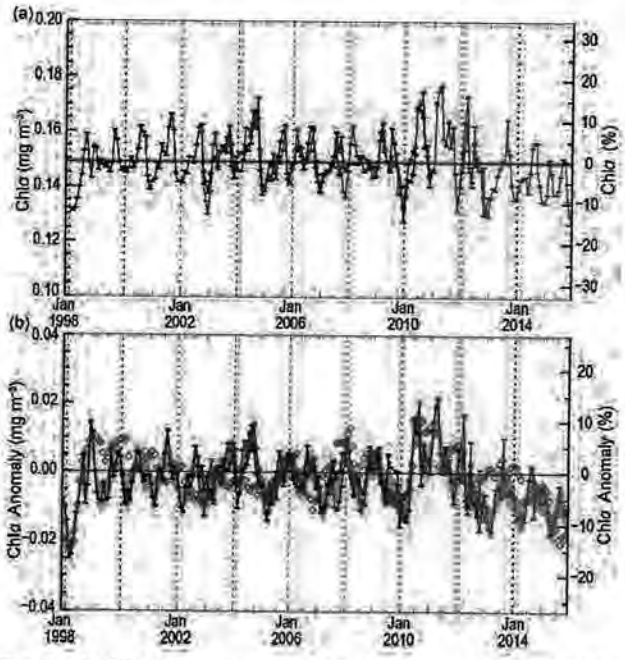

Fig. 3.27. Eighteen-year, multimission record of Chl*a* averaged over the PSO (see Fig. 3.25) for (black) SeaWiFS, (blue) MODISA, and (red) VIIRS. (a) Independent records from each mission, with the multimission mean Chl*a* concentration for the region (horizontal black line). (b) Monthly anomalies for SeaWiFS, MODISA, and VIIRS after subtraction of the 9-year MODISA monthly climatological mean (2003–11), with the averaged difference between SeaWiFS and MODISA over the common mission lifetime (gray region). The MEI (green diamonds, see text) inverted and scaled to match the range of the Chl*a* anomalies.

2015). This difference is not due to a change in global phytoplankton abundances but rather is a consequence of the R2014.0 reprocessing that includes calibration updates and a revised chlorophyll algorithm (Hu et al. 2012). The time series demonstrates the high level of consistency between the overlapping periods of the SeaWiFS and MODISA missions. Beyond 2012, the MODISA time series becomes increasingly erratic (not shown), reflecting a growing uncertainty in the calibration of that instrument (Franz et al. 2015). Consistency between MODISA and VIIRS in 2012, however, provides confidence for extension of the multimission trends into 2015.

Chl*a* monthly anomalies within the PSO (Fig. 3.27b) exhibit variations of ~15% over the multimission time series, with climatic events such as El Niño and La Niña clearly delineated. In 2015, consistent with a strong El Niño, Chl*a* trends in the PSO approached the lowest levels measured since the 1997/98 El Niño. Furthermore, mean Chl*a* concentrations in the PSO declined by approximately 20% from the peak observed during the 2010/11 La Niña, consistent with expectations based on multivariate ENSO index variations (MEI; Wolter and Timlin 1998).

Distinguishing the different drivers of Chl*a* variability is important for interpreting the satellite record. Light-driven decreases in chlorophyll are associated with constant or even increased rates of photosynthesis, while nutrient-driven decreases are associated with decreased photosynthesis. An analysis of photoacclimation and nutrient-driven changes in growth rate and biomass from the MODIS record shows that the inverse relationship between SST and Chl*a* anomalies is overwhelmingly due to light- and division rate-driven changes in cellular pigmentation, rather than changes in biomass (Behrenfeld et al. 2016). This study also shows that photoacclimation contributed 10%–80% of the variability in cellular pigmentation, suggesting the 2015 anomaly patterns in Chl*a* for the PSO (Fig. 3.26c) were largely driven by photoacclimation. An additional contributor to the anomaly patterns in Chl*a* is the misrepresentation of Chl*a* changes due to colored dissolved organic matter (cDOM) signals (Siegel et al. 2005). Sunlight degrades cDOM, and this degradation is more extensive for shallow MLDs, yielding in the PSO an inverse relationship between cDOM and SST (Nelson and Siegel 2013) that may be mistakenly attributed to Chl*a* changes (Siegel et al. 2013).

j. Global ocean carbon cycle—R. A. Feely, R. Wanninkhof, B. R. Carter, J. N. Cross, J. T. Mathis, C. L. Sabine, C. E. Cosca, and J. A. Tirnanes

The global ocean is a major sink for anthropogenic carbon dioxide (CO_2) that is released into the atmosphere from fossil fuel combustion, cement production, and land-use changes. Over the last decade, the global ocean has continued to take up a substantial fraction of anthropogenic carbon (C_{anth}) emissions and is therefore a major mediator of global climate change. Air–sea flux studies, general ocean circulation models including biogeochemistry, and data-constrained inverse models suggest the ocean absorbed approximately 46 Pg C (1 Pg C ≡ 10^{15} grams of carbon) of C_{anth} between 1994 and 2014 (Le Quéré et al. 2015; DeVries 2014), with an increase in the rate of C_{anth} uptake from 2.2 ± 0.5 Pg C yr^{-1} during the 1990s to approximately 2.6 ± 0.5 Pg C yr^{-1} during the most recent decade from 2005 to 2014 (Table 3.1). A summary of the air–sea exchange and ocean inventory of C_{anth} based on both observations and model results through 2014 is presented. Data for 2015 are not available owing to the need for careful scientific quality control of ocean carbon data prior to analysis.

l) Air–sea carbon dioxide fluxes

Ocean CO_2 uptake can be estimated from air–sea differences in CO_2 partial pressure (pCO_2) and gas transfer velocity, which is mainly a function of wind speed. Significant improvement in global and regional CO_2 flux estimates have been made in the past year as part of Surface Ocean pCO_2 Mapping Intercomparison (SOCOM), comparing 13 independent data-based methods of global interpolation of pCO_2 (Rödenbeck et al. 2015). Recent research has also decreased uncertainty on the equations used to estimate CO_2 exchange from air–sea pCO_2 differences (Wanninkhof 2014; Ho and Wanninkhof 2016). Large increases in autonomous pCO_2 measurements over time have been achieved with ships of opportunity (SOOP-CO_2) and moorings. The third update of the Surface Ocean CO_2 Atlas (SOCAT) with over 14 million data points was released to the public in 2015 (Bakker et al. 2016). Subsequent data releases will occur annually such that the data can inform the annual assessment of global CO_2 sources and sinks provided by the Global Carbon Project (www.globalcarbonproject.org). The increased data coverage and new mapping techniques make it possible to obtain air–sea CO_2 fluxes at monthly time scales, allowing investigation of variability on subannual to decadal time scales and the causes thereof. An important recent result illuminated by these improved approaches is the reinvigoration of the Southern Ocean carbon sink since 2002 (Landschützer et al. 2015), which had previously been found to be decreasing (Le Quéré et al. 2007).

The newly released datasets have been used to verify the magnitude of the anthropogenic air–sea CO_2 fluxes over the last decade and in 2014. The ocean sink in 2014 was 10% above the 2005–14 average of 2.6 ± 0.5 Pg C yr^{-1} (Table 3.1). In 2014, the ocean and land carbon sinks removed 27% and 37% of total CO_2 emissions, respectively, leaving 36% of emissions in the atmosphere, compared to 44% as a decadal average (Le Quéré et al. 2015).

Ocean uptake anomalies (Fig. 3.28b) in 2014 relative to the 2005–14 average (Fig. 3.28a) are attributed to several climate reorganizations. The lower CO_2 effluxes in the equatorial Pacific are attributed to anomalously high regional SST and reduced upwelling of CO_2-rich subsurface waters due to a weak Modoki-like near-El Niño in 2014. Stronger effluxes are evident in the northeast Pacific due to the warm "Blob" (Bond et al. 2015) as well as warm conditions offshore of the California coast (Fig. 3.29). A cold anomaly in the southern Labrador Sea and adjacent regions (Josey et al. 2015) associated with deep mix-

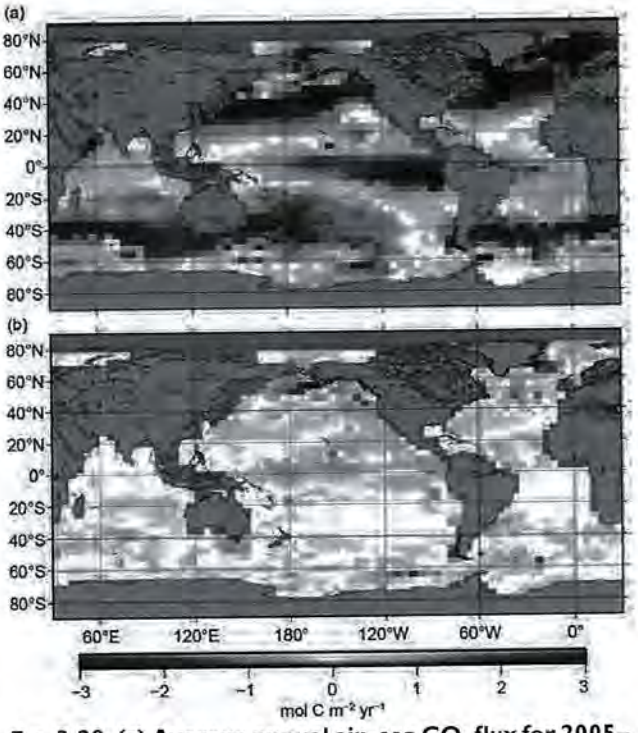

Fig. 3.28. (a) Average annual air–sea CO_2 flux for 2005–14 based on the AOML–EMP approach (Park et al. 2010). Positive values are effluxes and negative values are influxes. The SST anomaly interpolation method used for this analysis is less robust than more recent and sophisticated approaches (Rödenbeck et al. 2015), but faithfully reproduces the major anomaly features, especially in the highly data-constrained equatorial Pacific. (b) Air–sea CO_2 flux anomaly in 2014 compared to ten-year average (2005–14). Positive values are increased effluxes (or decreased influxes) and negative values are increased influxes (or decreased effluxes).

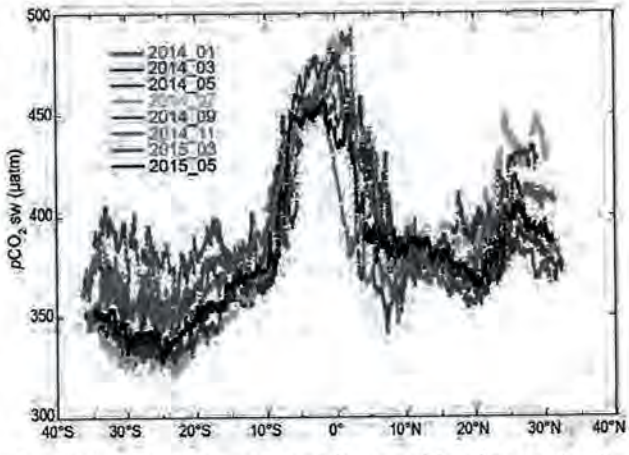

Fig. 3.29. CO_2 measurement from a ship of opportunity (SOOP) from New Zealand to Long Beach, CA, showing anomalously high surface water partial pressure of CO_2 (pCO_2) values in 2014 and 2015 in the anomalously warm surface water offshore of the California coast. Equatorial pCO_2 values are depressed in the boreal spring of 2014 and 2015 compared to climatological values.

Table 3.1. Global ocean C_{anth} uptake rates. All uncertainties are reported as ±1σ.		
Years	**Mean C_{anth} Uptake (Pg C yr^{-1})**	**Reference**
1960–69	1.1 ± 0.5	Le Quéré et al. 2015
1970–79	1.5 ± 0.5	Le Quéré et al. 2015
1980–89	2.0 ± 0.5	Le Quéré et al. 2015
1990–99	2.2 ± 0.5	Le Quéré et al. 2015
1994–2006	2.6 ± 0.5	Sabine and Tanhua 2010
2000–09	2.3 ± 0.5	Le Quéré et al. 2015
1994–2010	2.3 ± 0.5	Khatiwala et al. 2013
2000–10	2.9 ± 0.4	Kouketsu and Murata 2014
2005–14	2.6 ± 0.5	Le Quéré et al. 2015
2014	2.9 ± 0.5	Le Quéré et al. 2015

ing led to larger effluxes in the northwest Atlantic. A large negative anomaly in the northwest Pacific, perhaps related to a shift in the PDO, contributed to the higher-than-average 2014 ocean CO_2 uptake.

A recent synthesis of pCO_2 data in the western Arctic showed that the Arctic biogeochemical seascape is in rapid transition. An analysis of nearly 600 000 surface seawater pCO_2 measurements from 2003 to 2014 found 0.0109 ± 0.0057 Pg C yr^{-1} entered the ocean in the western Arctic coastal ocean (north of the Bering Strait) during this period, and that this uptake would be expected to increase by 30% under decreased sea ice cover conditions expected with Arctic warming (Evans et al. 2015). Reductions in ice cover may have a more moderate impact on other areas of the western Arctic, such as south of Bering Strait (Cross et al. 2014).

2) Carbon inventories from the GO-SHIP surveys

The CLIVAR/CO_2 Repeat Hydrography Global Ocean Ship-Based Hydrographic Investigations Program (GO-SHIP; www.go-ship.org/) collects high-quality surface-to-bottom water property measurements along transoceanic sections at decadal intervals. These data are essential for estimating decadal C_{anth} storage changes within the ocean interior. The extended multiple linear regression method (eMLR) distinguishes these changes from large natural decadal changes in dissolved inorganic carbon (DIC) concentrations between cruises (e.g., Friis et al. 2005; Sabine et al. 2008). The method has recently been modified to permit basinwide estimates of C_{anth} trends by utilizing data from repeat hydrography cruises and climatological data from World Ocean Atlas 2013 (Sabine and Tanhua 2010; Locarnini et al. 2013; Zweng et al. 2013; Williams et al. 2015). Global-scale results from this modified eMLR approach indicate a C_{anth} uptake rate of ~2.6 Pg C yr^{-1} (1994–2006). This estimate is consistent (within uncertainties) with model-based (Khatiwala et al. 2013; Talley et al. 2016) and data-based estimates (Table 3.1) for this period.

C_{anth} storage rates vary widely regionally (Fig. 3.30), ranging from 0.1 ± 0.02 to 2.2 ± 0.7 mol C m^{-2} yr^{-1} (Williams et al. 2015). For comparison, the 2.3–2.9 Pg C yr^{-1} global mean uptake rate estimates above correspond to a global mean C_{anth} storage rate between 0.53 and 0.67 mol C m^{-2} yr^{-1}. Updating regional storage estimates with measurements from the most recent GO-SHIP hydrographic surveys is an ongoing effort. Recent estimates (Fig. 3.30b) suggest greater storage in the Atlantic in the recent decade than in the preceding decade (Woosley et al. 2016), but consistent storage between the two decades in the Pacific.

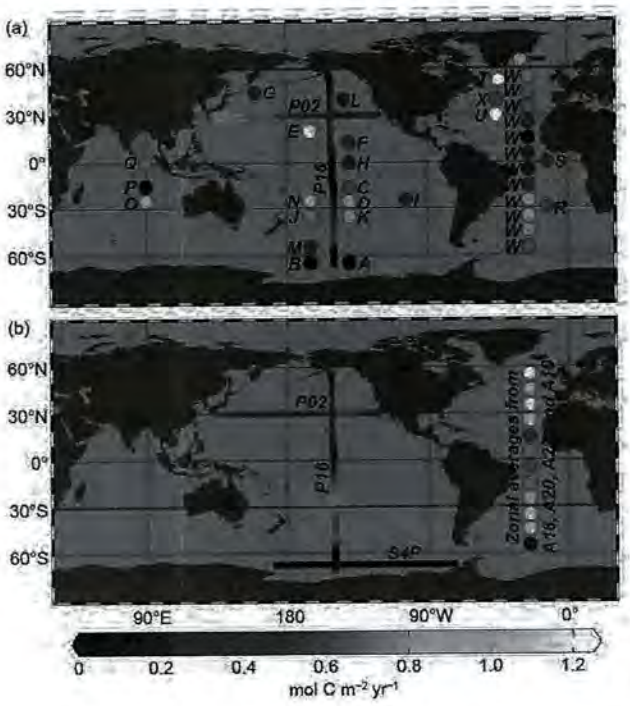

FIG. 3.30. Regional C_{anth} (anthropogenic carbon) storage rate estimates in literature as colored dots with positions corresponding to the approximate centers of the broad regions considered. Estimates are from: A. Williams et al. (2015), B. Sabine et al. (2008), C. Sabine et al. (2008), D. Peng et al. (2003), E. Peng et al. (2003), F. Murata et al. (2009), G. Wakita et al. (2010), H. Sabine et al. (2008), I. Waters et al. (2011), J. Waters et al. (2011), K. Waters et al. (2011), L. Sabine et al. (2008), M. Matear and McNeil (2003), N. Murata et al. (2007), O. Murata et al. (2010), P. Peng et al. (1998), Q. Peng et al. (1998), R. Murata et al. (2008), S. Peng and Wanninkhof (2010), T. Friis et al. (2005), U. Tanhua et al. (2007), V. Olsen et al. (2006), W. Wanninkhof et al. (2010), and X. Quay et al. (2007). Storage rate estimates that use data from cruises in the year 2011 or afterward are mapped in (b), and all other estimates are mapped in (a). Atlantic estimates in (b) are from Woosley et al. (2016). Colored lines are provided representing preliminary storage rate estimates along the labeled P16 and P02 sections in the decades spanning the (a) 1990s to 2000s and (b) 2000s to 2010s occupations. The similar line in (b) for S4P is from Williams et al. (2015).

4. THE TROPICS—H. J. Diamond and C. J. Schreck, Eds.

a. *Overview*—H. J. Diamond and C. J. Schreck

From the standpoint of the El Niño–Southern Oscillation (ENSO), 2015 featured one of the three strongest El Niño episodes (1982/83, 1997/98, and 2015) since 1950. The end of 2014 was characterized by borderline El Niño conditions, and 2015 began with above-average SSTs across the central and east-central equatorial Pacific, with the largest anomalies (>1°C) confined to the region around the international date line. However, this warmth was accompanied by little-to-no atmospheric response, indicating that El Niño had not fully developed. SST anomalies then increased across the central and eastern equatorial Pacific during March–May. This evolution, combined with a coupling of the SST anomalies to the atmospheric wind and convection patterns, resulted in the development of El Niño conditions during March 2015. El Niño's strengthening accelerated during June–August, and again during September–November, when SST anomalies increased sharply across the eastern half of the equatorial Pacific.

Globally, 101 named tropical storms were observed during 2015. This overall tropical cyclone (TC) activity is well above the 1981–2010 global average of 82 storms and 10% higher than the 91 TCs recorded in 2014 (Diamond 2015). The eastern/central Pacific experienced significantly above-normal activity in 2015, and the western north Pacific and north and south Indian Ocean basins were also above normal; all other basins featured either near or below-normal TC activity. These levels of activity are consistent with the El Niño conditions in place. The 26 named storms in the eastern/central Pacific basin was the highest count in that basin since 1992 and was four more than the previous record of 22 named storms recorded in 2014, as documented in the International Best Tracks Archive for Climate Stewardship (IBTrACS; Knapp et al. 2010). Globally, eight TCs reached the Saffir–Simpson hurricane wind scale Category 5 intensity level—five in the western North Pacific basin, one in the southern Indian Ocean, one in the eastern North Pacific, and one in the southwest Pacific. This was three more than were recorded in 2013 and one more than recorded in 2014 (Diamond 2014, 2015). In terms of accumulated cyclone energy (ACE), the North Atlantic basin season was below normal, also consistent with the El Niño conditions in place. The actual number of storms, on the other hand, was close to normal due to a large number of weak and short-lived storms. Following a near-normal hurricane season in 2014 and a below-normal season in 2013, this marked the first time since 1992–94 in which three consecutive seasons in the North Atlantic were not above normal in terms of ACE (Bell et al. 2015).

The editors of this chapter would like to insert a personal note recognizing Dr. William M. (Bill) Gray, emeritus professor of atmospheric science at Colorado State University. Dr. Gray, who pioneered the development of seasonal tropical cyclone outlooks and was one of the most influential meteorologists of the past 50 years, passed away on 16 April 2016 in Fort Collins, Colorado, at the age of 86. Speaking on behalf of the entire community, we will always be indebted to, and benefit from, the accomplishments made during his incredibly long and outstanding career.

b. *ENSO and the tropical Pacific*—G. D. Bell, M. Halpert, and M. L'Heureux

The El Niño–Southern Oscillation is a coupled ocean–atmosphere phenomenon over the tropical Pacific Ocean. Two indices used to monitor and as-

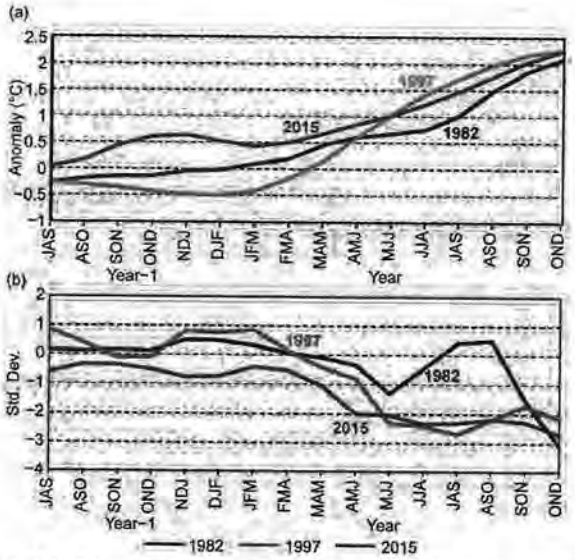

FIG. 4.1. The evolution of three strong El Niño events (1982, 1997, and 2015) is compared using time series of (a) the oceanic Niño index (ONI; °C), and (b) the standardized 3-month running equatorial Southern Oscillation index (EQ–SOI, std. dev.). Each time series starts with the JAS season in the year prior to the event (year–1) and ends with the OND season in the year that the event formed (year). For the 1982, 1997, and 2015 El Niños, "year–1" corresponds to 1981, 1996, and 2014, respectively. ONI values are derived from the ERSST.v4 dataset (Huang et al. 2014). EQ–SOI values are derived from the monthly EQ–SOI index based on the Climate Forecast System Reanalysis (CFSR) (Saha et al. 2010b). The EQ–SOI is calculated as the standardized anomaly of the difference between the area-average monthly sea level pressure over the eastern equatorial Pacific (5°N–5°S, 80°–130°W) and Indonesia (5°N–5°S, 90°–140°E). [Data available at: www.cpc.ncep.noaa.gov/data/indices/reqsoi.for and discussed by Barnston (2015).]

sess the strength of ENSO are the oceanic Niño index (ONI) and the equatorial Southern Oscillation index (EQ–SOI). The ONI (Fig. 4.1a) is the seasonal running average of sea surface temperature (SST) anomalies in the Niño-3.4 region (5°N–5°S, 170°–120°W) using ERSST.v4 data (Huang et al. 2015). NOAA's Climate Prediction Center classifies ENSO events historically using the ONI. At the end of 2015 ONI values were +2.25°C, comparable to the strongest El Niño (1997/98) in the 1950–2015 record.

The EQ–SOI measures the difference in surface air pressure anomalies between Indonesia and the eastern equatorial Pacific Ocean, two large areas along the equator (Barnston 2015). Therefore, the EQ–SOI is a more robust measure of ENSO than the traditional SOI, which is based on measurements at only two stations, both of which are off-equatorial (Tahiti at 18°S, Darwin at 12°S; Troup 1965; Trenberth 1984). Large negative values as seen during 2015 typify El Niño (Fig. 4.1b), and reflect the combination of decreased surface air pressure over the eastern equatorial Pacific and increased air pressure over Indonesia. Overall, the combined time series of the EQ–SOI and ONI suggest that the global climate during 2015 was affected by one of the three strongest El Niño episodes (1982/83, 1997/98, and 2015/16) dating back to 1950.

1) Oceanic conditions

The SST evolution across the Pacific basin during 2015 (Figs. 4.2, 4.3) is shown based on OISST data (Smith and Reynolds 1998). In 2015, the year began with above-average SSTs across the central and east-central equatorial Pacific, with the largest anomalies (>1°C) confined to the region around the date line (Fig. 4.2b). The corresponding weekly SST indices for the Niño-4 (Fig. 4.3a) and Niño-3.4 (Fig. 4.3b) regions were above 0.8°C and 0.5°C, respectively (regions shown in Fig. 4.3e). The ONI for December–February 2014/15 (DJF) was +0.52°C, which is near the NOAA threshold for El Niño conditions (ONI ≥ 0.5°C). However, this warmth was accompanied by little-to-no atmospheric response (Figs. 4.4a, 4.5a), indicating that El Niño had not fully developed.

SST anomalies then increased across the central and eastern equatorial Pacific during March–May (MAM; Figs. 4.2d, 4.3). This evolution, combined with a coupling of the SST anomalies to the atmospheric wind and convection patterns (Figs. 4.4b,

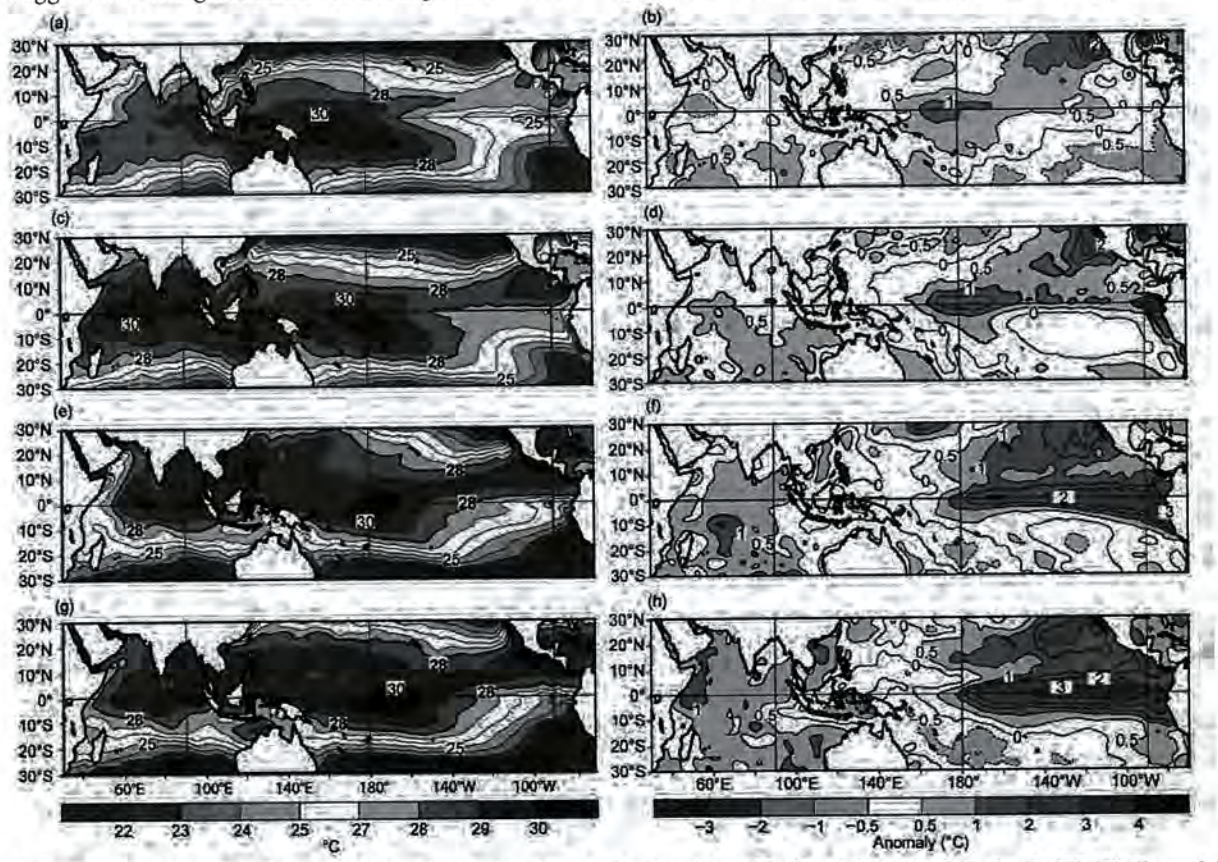

Fig. 4.2. Seasonal SST (left) and anomaly (right) for (a, b) DJF 2014/15, (c, d) MAM 2015, (e, f) JJA 2015, and (g, h) SON 2015. Contour interval for total SST is 1°C. For anomalous SST, contour interval is 0.5°C for anomalies between ±1°C, and interval is 1°C for anomalies > 1°C or < −1°C. Anomalies are departures from the 1981–2010 seasonal adjusted OI climatology (Smith and Reynolds 1998).

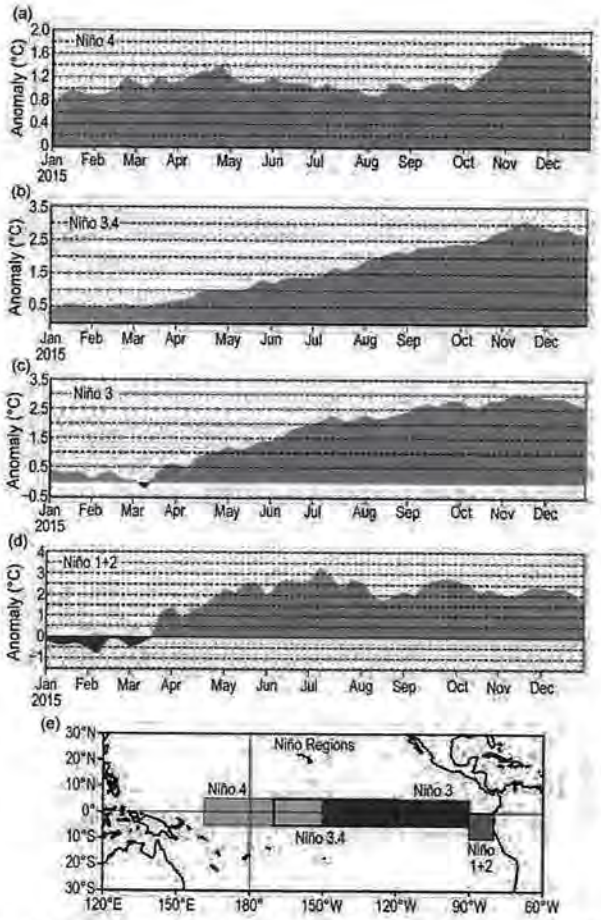

Fig. 4.3. Time series during 2015 of weekly area-averaged SST anomalies (°C) in the four Niño regions: (a) Niño-4 region [(5°N–5°S, 160°E–160°W, yellow box in (e)], (b) Niño-3.4 region [(5°N–5°S, 170°–120°W, thick black box in (e)], (c) Niño-3 region [5°N–5°S, 150°–90°W, red box in (e)], and (d) Niño-1+2 region [0°–10°S, 90°–80°W, blue box in (e)]. Values are departures from the 1981–2010 weekly adjusted OI climatology (Smith et al. 1998).

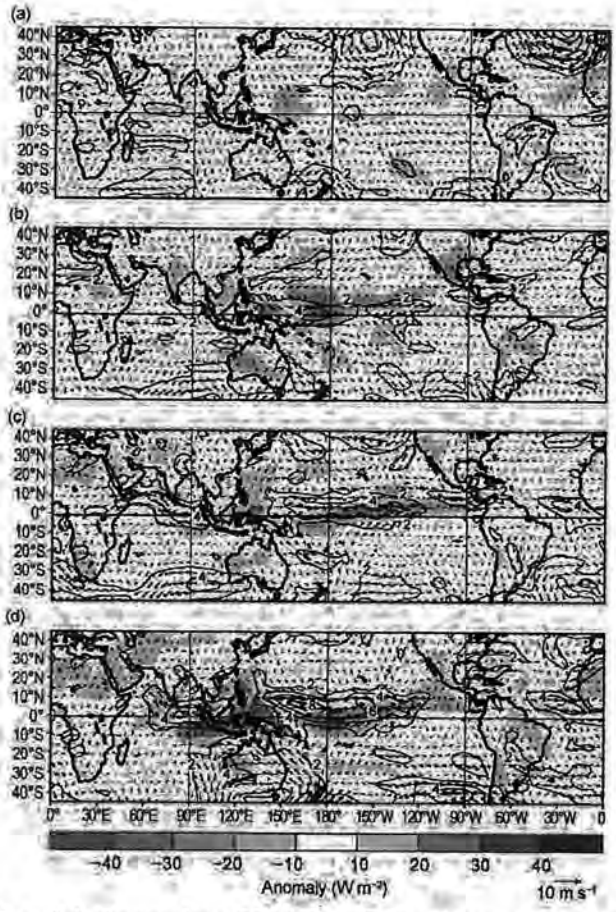

Fig. 4.4. Anomalous 850-hPa wind vectors and speed (contour interval is 2 m s^{-1}) and anomalous OLR (shaded, W m^{-2}) during (a) DJF 2014/15, (b) MAM 2015, (c) JJA 2015, and (d) SON 2015. Anomalies are departures from the 1981–2010 period monthly means.

4.5b), resulted in the development of fully-coupled El Niño conditions during March 2015. The presence of El Niño during MAM was also indicated by an eastward shift of the 30°C isotherm to the date line, along with a weaker and reduced westward extent of the equatorial cold tongue (Fig. 4.2c). In fact, the SSTs were nearly uniformly warm (above 27°C) throughout the eastern half of the cold tongue, indicating that the normal east–west SST gradient in that region had nearly disappeared.

El Niño's strengthening accelerated during June–August (JJA; Figs. 4.2e,f) and September–November (SON; Figs. 4.2g,h), as SST anomalies increased sharply across the eastern half of the equatorial Pacific. The ONI for JJA was 1.23°C, increased to 2.04°C during SON, and reached 2.25°C for the last three months of the year (October–December; Fig. 4.1a). These values are comparable to the strongest El Niño episodes in the 1950–2015 record.

This evolution is reflected by large SST index values for all four Niño regions, with the weekly Niño-4 index reaching +1.8°C in November and +1.7°C in December (Fig. 4.3a). The average Niño-4 index values for November and December 2015 were 1.75°C and 1.64°C, surpassing the previous record highs of 1.28°C and 1.2°C set in November and December 2009, respectively. Also, the weekly Niño-3.4 (Fig. 4.3b) and Niño-3 (Fig. 4.3c) indices reached +3.0°C by the end of 2015, while the weekly Niño-1+2 index remained near +2.5°C (Fig. 4.3d).

During the last half of the year, the anomalous warming largely reflected a weakening of the annual cycle in SSTs across the Pacific basin, with actual temperatures remaining nearly constant instead of cooling off as they would in a typical year, in association with a strengthening and expanding equatorial cold tongue. This cold tongue, which normally intensifies during JJA and SON, was nearly absent in 2015

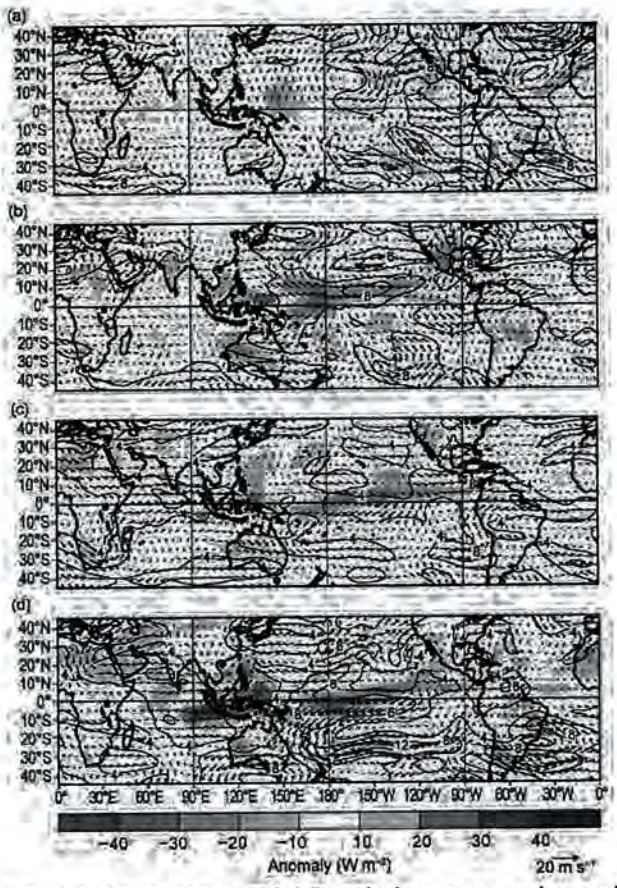

FIG. 4.5. Anomalous 200-hPa wind vectors and speed (contour interval is 4 m s^{-1}) and anomalous OLR (shaded, W m^{-2}) during (a) DJF 2014/15, (b) MAM 2015, (c) JJA 2015, and (d) SON 2015. Anomalies are departures from the 1981–2010 period monthly means.

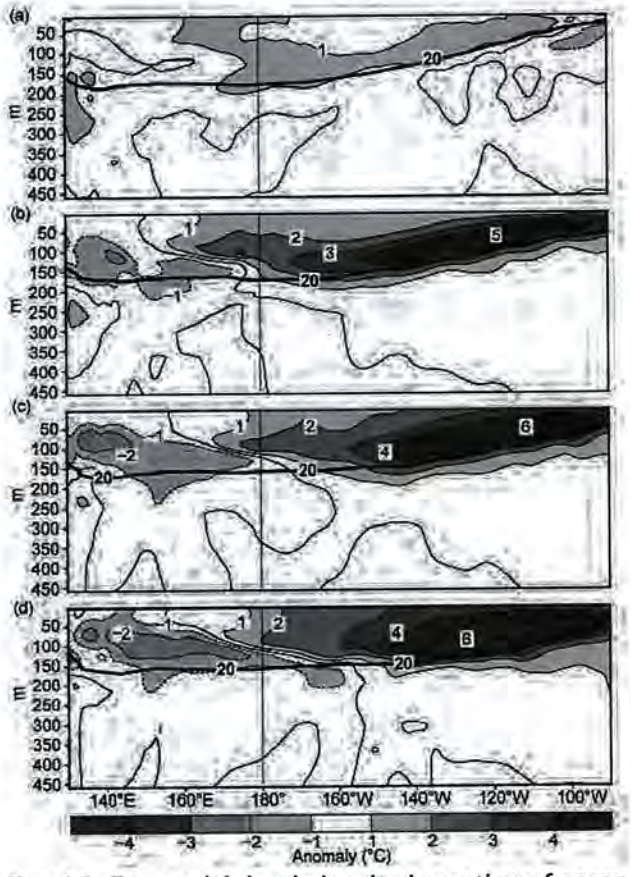

FIG. 4.6. Equatorial depth–longitude section of ocean temperature anomalies (°C) averaged between 5°N and 5°S during (a) DJF 2014/15, (b) MAM 2015, (c) JJA 2015, and (d) SON 2015. The 20°C isotherm (thick solid line) approximates the center of the oceanic thermocline. The data are derived from an analysis system that assimilates oceanic observations into an oceanic general circulation model (Behringer et al. 1998). Anomalies are departures from the 1981–2010 period monthly means.

(Figs. 4.2e,g), as was the typical westward advection of cooler waters toward the date line. Consistent with these conditions, the normal westward migration of the +30°C isotherm to New Guinea did not occur during JJA and SON. Instead, these exceptionally warm temperatures actually migrated eastward, further strengthening El Niño and its associated atmospheric response.

Consistent with the evolution of the equatorial SSTs, positive subsurface temperature anomalies increased east of the date line throughout the year (Fig. 4.6). A significant temperature increase occurred during MAM (Fig. 4.6b) in response to the combination of the evolving El Niño and the downwelling phase of a strong equatorial oceanic Kelvin wave (section 4c) that was initiated by a westerly wind burst.

Subsequent westerly wind bursts in late June/early July, early August, and early October also initiated downwelling equatorial oceanic Kelvin waves, which helped to maintain well-above-normal subsurface ocean temperatures through the end of the year (Figs. 4.6c,d). In contrast, in the western Pacific, subsurface temperature anomalies decreased during the year. These conditions reflected a progressive flattening of the oceanic thermocline (indicated by the 20°C isotherm, thick solid line), which is typical of a strong El Niño pattern of anomalous downwelling (upwelling) in the eastern (western) equatorial Pacific (Wang et al. 1999; Wang and Weisberg 2000).

2) Atmospheric circulation: tropics and subtropics

During DJF 2014/15, the atmospheric circulation across the tropical Pacific reflected ENSO-neutral conditions, with near-average low-level (850-hPa) winds (Fig. 4.4a) and no consistent El Niño signal in the upper-level winds (Fig. 4.5a). Also, convection was slightly suppressed over the east-central equatorial Pacific in the area of anomalously warm SSTs, indicating a lack of oceanic–atmospheric coupling.

In March, the atmospheric pressure, wind, and convection patterns became coupled to the increasingly warm SST anomalies, signifying the development of El Niño. The atmospheric response to El Niño was evident through the remainder of the year, intensifying as El Niño strengthened.

The tropical atmospheric response to El Niño during MAM through SON featured an east–west dipole pattern of anomalous convection, with convection expanding and strengthening over the central and east-central equatorial Pacific while becoming more suppressed over Indonesia and the eastern Indian Ocean (Figs. 4.4b–d, 4.5b–d). This pattern reflected 1) a pronounced eastward extension of the primary area of tropical convection to well east of the date line and, at times, an actual shift of the main region of tropical convection to the eastern half of the tropical Pacific (not shown), and 2) a strengthening and equatorward shift of the intertropical convergence zone (ITCZ) in the Northern Hemisphere.

A key El Niño–related feature of the low-level (850-hPa) winds during JJA through SON was an extensive area of anomalous westerlies that strengthened and expanded along the equator as the year progressed (Figs. 4.4b–d). This anomaly pattern reflected a marked weakening (3–6 m s^{-1} below normal) of the easterly trade winds, with departures exceeding 6 m s^{-1} near the date line in SON (Fig. 4.4d).

An El Niño–related upper-level wind pattern also became established during MAM and strengthened as the year progressed. This pattern featured an extensive area of easterly wind anomalies across the central and east-central tropical Pacific (Figs. 4.5b–d), along with near-average winds over both the eastern equatorial Pacific and Indonesia.

The overall circulation also featured a combination of anomalous upper-level convergence and low-level divergence over Indonesia and the western tropical Pacific, and a combination of anomalous upper-level divergence and low-level convergence over the central and east-central equatorial Pacific. The resulting vertical motion pattern was consistent with the observed east–west dipole pattern of tropical convection, as was also noted by Bell and Halpert (1998) for the 1997/98 El Niño. Collectively, these wind, convection, and vertical motion patterns reflect a markedly reduced strength of the equatorial Walker circulation typical of El Niño (Bjerknes 1969).

In the subtropics, the upper-level winds during JJA–SON 2015 featured anticyclonic anomalies in both hemispheres straddling the area of enhanced equatorial convection. This anticyclonic couplet is a typical feature of El Niño (Arkin 1982). In the winter hemisphere, anomalous westerly winds along the poleward flank of the anomalous anticyclonic circulation reflect major dynamical and kinematic changes in the jet stream over the Pacific basin. As seen during JJA and SON in the Southern Hemisphere (Figs. 4.5c,d), the westerly wind anomalies between 20° and 30°S reflected a strengthening and eastward extension of the wintertime jet steam to well east of the date line, along with an eastward shift of that jet's exit region to the eastern South Pacific. This wintertime jet stream pattern represents a fundamental manner in which El Niño's circulation impacts are communicated downstream and poleward into the extratropics.

3) Rainfall impacts

Because of the rapid strengthening and expansion of the El Niño–related convection and circulation anomalies during MAM and JJA, many typical El Niño rainfall impacts (Ropelewski and Halpert 1987) were evident during the year. The accumulated precipitation deficits and surpluses during June–December, along with time series of area-averaged monthly precipitation totals and percentiles during the year, highlight these impacts (Fig. 4.7).

Two main regions with above-average precipitation during June–December 2015 were the central equatorial Pacific and within the Pacific ITCZ. The enhanced rainfall for both regions began in March and subsequently intensified with area-averaged monthly totals during May–December (red line, Fig. 4.7b) all being in the upper 10th percentile of occurrences (black bars). For the June–December period, rainfall surpluses in both areas exceeded 800 mm, with the largest surpluses exceeding 1200 mm. During June–October, these conditions were associated with strong hurricane seasons for both the central and eastern Pacific hurricane basins (see section 4e3).

Two other regions that typically record above-average precipitation during El Niño include southeastern South America and the Gulf Coast region of the United States. The extended South Pacific jet stream contributed to precipitation surpluses of 100–200 mm in southeastern South America during June–December, with above-average precipitation recorded in nearly every month from July to December (Fig. 4.7c; section 7d). Along the U.S. Gulf Coast, above-average precipitation was recorded from October to December, with area-averaged totals above the 90th percentile of occurrences during November–December (Fig. 4.7d).

Many other areas typically record below-average precipitation during El Niño. One such region is Indonesia, where cumulative deficits during June–

December 2015 exceeded 1000 mm. The most significant deficits occurred during July–October, when monthly totals of less than 100 mm were generally half of normal and in the lowest 10th percentile of occurrences (Fig. 4.7e). Other regions with below-average precipitation during the period from June to December included:

- The South African monsoon season (October–April) is typically suppressed during El Niño, and from October–December precipitation totals were well below average, with monthly totals in the lowest 10th percentile of occurrences in all three months (Fig. 4.7f).
- The Amazon basin recorded significantly below-average rainfall throughout the year, with monthly totals generally in the lowest 10th percentile of occurrences (Fig. 4.7g). During June–December 2015, much of the region recorded deficits of 400–600 mm.
- The Central America/Caribbean Sea region (Fig. 4.7h) and the tropical Atlantic (Fig. 4.7i) had rainfall that was below average during almost every month from April to December, with monthly totals in the lowest 20th percentile of occurrences in most months. Below-average totals across the tropical Atlantic were also consistent with the overall below-average strength of the 2015 Atlantic hurricane season (see section 4e2).

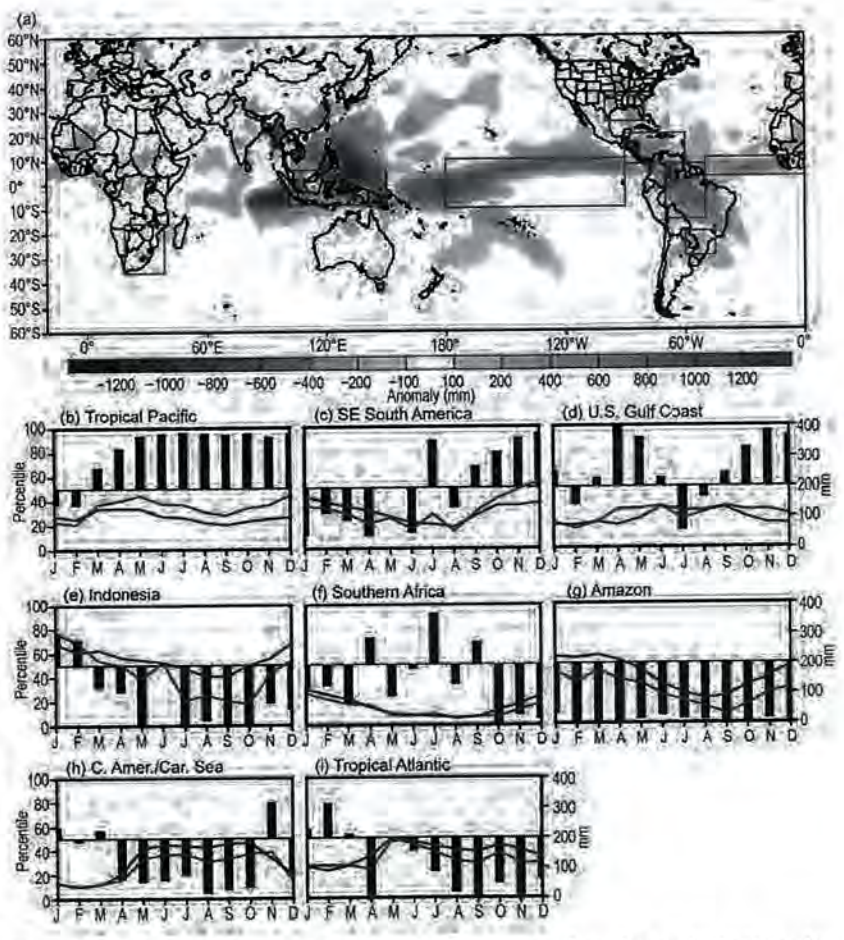

FIG. 4.7. Precipitation during 2015: (a) Accumulated precipitation departures during (b–i) Jun–Dec (mm), Time series of area-averaged monthly precipitation for regions indicated with red boxes in (a). Bars show monthly percentile percentiles (left y-axis), and red and blue lines show monthly observed and climatological mean precipitation (right y-axis), respectively. Rainfall amounts are obtained by merging rain gauge observations and satellite-derived precipitation estimates (Janowiak and Xie 1999). Precipitation percentiles are based on a gamma distribution fit to the 1981–2010 base period. Anomalies are departures from the 1981–2010 means.

c. Tropical intraseasonal activity—S. Baxter, C. J. Schreck, and G. D. Bell

Tropical intraseasonal variability was prominent during 2015 in both the atmosphere and ocean, even in the presence of strong lower-frequency variability associated with El Niño. In the atmosphere, two aspects of this intraseasonal variability were the Madden–Julian oscillation (MJO; Madden and Julian 1971, 1972, 1994; Zhang 2005) and convectively coupled equatorial waves, which include equatorial Rossby waves and atmospheric Kelvin waves (Wheeler and Kiladis 1999; Kiladis et al. 2009; Roundy 2012a,b). There were three distinct periods of MJO activity during 2015 affecting a total of six months (Figs. 4.8–4.10), which were interspersed with the convectively coupled waves. Between these three periods, the intraseasonal variability was dominated by atmospheric Kelvin waves and tropical cyclone activity. Within the Pacific Ocean, strong intraseasonal variability throughout the year was reflected in a series of upwelling and downwelling equatorial oceanic Kelvin waves (Fig. 4.11).

The MJO is a leading intraseasonal climate mode of tropical convective variability. Its convective anomalies often have the same spatial scale as ENSO, but differ in that they exhibit a distinct eastward propagation and generally traverse the globe in 30–60 days. The MJO impacts weather patterns around the globe

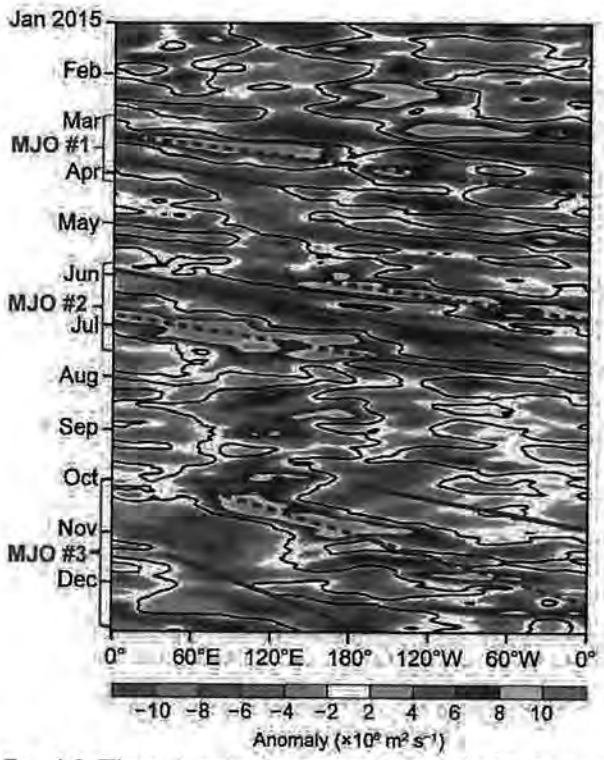

FIG. 4.8. Time–longitude section for 2015 of 5-day running anomalous 200-hPa velocity potential (× 10^6 m^2 s^{-1}) averaged for 5°N–5°S. For each day, the period mean is removed prior to plotting. Green (brown) shading highlights likely areas of anomalous divergence and rising motion (convergence and sinking motion). Red lines and labels highlight the main MJO episodes. Anomalies are departures from the 1981–2010 base period daily means.

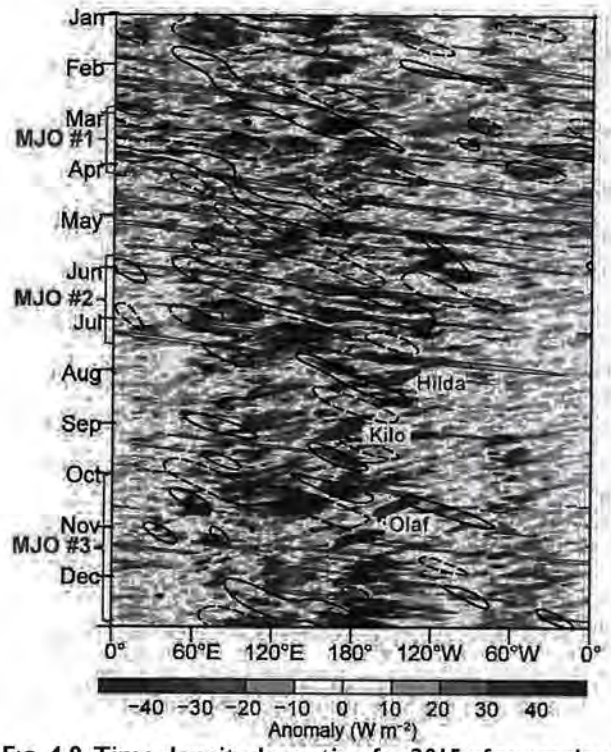

FIG. 4.9. Time–longitude section for 2015 of anomalous outgoing longwave radiation (OLR; W m^{-2}) averaged for 10°N–10°S. Negative anomalies indicate enhanced convection and positive anomalies indicate suppressed convection. Contours identify anomalies filtered for the MJO (black) and atmospheric Kelvin waves (red) as in Kiladis et al. (2006) and Straub and Kiladis (2002), respectively. Purple shaded ovals indicate hurricanes named on figure. Red labels highlight the main MJO episodes. Contours are drawn at ±10 W m^{-2}, with the enhanced (suppressed) convective phase of these phenomena indicated by solid (dashed) contours. Anomalies are departures from the 1981–2010 base period daily means.

(Zhang 2013), including monsoons (Krishnamurti and Subrahmanyam 1982; Lau and Waliser 2012), tropical cyclones (Mo 2000; Frank and Roundy 2006; Camargo et al. 2009; Schreck et al. 2012), and extratropical circulations (Knutson and Weickmann 1987; Kiladis and Weickmann 1992; Mo and Kousky 1993; Kousky and Kayano 1994; Kayano and Kousky 1999; Cassou 2008; Lin et al. 2009; Riddle et al. 2012; Schreck et al. 2013; Baxter et al. 2014). The MJO is often quite variable in a given year, with periods of moderate-to-strong activity sometimes followed by little or no activity. The MJO tends to be most active during ENSO neutral and weak El Niño periods, and is often absent during strong El Niño events (Hendon et al. 1999; Zhang and Gottschalck 2002; Zhang 2005). Given a background El Niño rivaling one of the strongest on record during 2015, the MJO events observed during the year are remarkable.

Common metrics for identifying the MJO include time–longitude plots of anomalous 200-hPa velocity potential (Fig. 4.8) and outgoing longwave radiation (OLR, Fig. 4.9), as well as the Wheeler–Hendon (2004) Real-time Multivariate MJO (RMM) index (Fig. 4.10). In the time–longitude plots, the MJO exhibits eastward propagation. In the RMM, the MJO propagation and intensity are seen as large, counterclockwise circles around the origin. These diagnostics point to three main MJO episodes during 2015. MJO #1 was a strong episode from March into early April. MJO #2 was a strong event that began in late May and lasted through mid-July. MJO #3 was a moderately strong event that lasted from October through the end of the year.

MJO #1 featured a zonal wave-1 pattern of strong convective anomalies, with a periodicity of approximately 40 days (Figs. 4.8, 4.9, 4.10a,b). The plot of anomalous velocity potential shows that this event circumnavigated the globe once (Fig. 4.8). The RMM index achieved record amplitude of 4.03 standard deviations on 16 March (Fig. 4.10a). Historically, the

only prior MJO event to eclipse 4.0 occurred 30 years ago in February 1985 (4.02). The 2015 event ended in April when the convective anomalies became dominated by a series of fast-propagating atmospheric Kelvin waves (Fig. 4.9).

One of the largest impacts from MJO #1 was the interaction with a high-amplitude downwelling equatorial oceanic Kelvin wave (Fig. 4.11b). This oceanic Kelvin wave was triggered during March by a westerly wind burst associated with enhanced convection over the western Pacific (Fig. 4.11a). This wave reached the eastern Pacific in May and produced a significant increase in the upper ocean heat content while El Niño was developing. MJO #1 also impacted the extratropical circulation, mainly during mid- to late March, when suppressed convection and anomalous upper-level convergence were present over the eastern Indian Ocean, and enhanced convection and anomalous upper-level divergence were present over the western and central Pacific Ocean (Fig. 4.8). These conditions contributed to an eastward extension of the East Asian jet stream and a subsequent cold air outbreak over the continental United States.

MJO #2 began in late May and lasted through mid-July, with its wave-1 signal also making a full trip around the globe. Its convective anomalies masked the strengthening El Niño in early and mid-June, then accentuated the El Niño signal during late June and early July (Fig. 4.9). The RMM index showed remarkable amplitude in early July, again approaching four standard deviations (Fig. 4.10c). As is common with many MJO episodes (Straub et al. 2006; Sobel and Kim 2012), the convective signal of MJO #2 was partially masked by atmospheric Kelvin wave activity (Fig. 4.9). This MJO provided especially conducive conditions for producing tropical cyclones. Twelve storms, spanning from the Arabian Sea to the North Atlantic, developed in association with this event. These storms included "twin" tropical cyclones Raquel and Chan-hom that straddled the equator in the western Pacific and contributed to a particularly strong westerly wind burst (Fig. 4.11a).

Following MJO #2, enhanced tropical cyclone activity across the central and eastern North Pacific from August through October contributed to the atmospheric intraseasonal variability. Some of these storms (named and purple shaded ovals, Fig. 4.9) can be identified as westward-moving patterns of anomalous upper-level divergence and enhanced OLR (storm names).

MJO #3 lasted from mid-October through the end of the year. The periodicity of this event is difficult to assess, though it likely exceeded 60 days and is at the slower end of the MJO spectrum (Fig. 4.10d). After being initiated over the western Pacific, the area of enhanced convection associated with MJO #3 propagated over the Indian Ocean, where it then became quasi-stationary for most of November. It could be argued that this event did not begin in earnest until its eastward propagation resumed in early December. Similar to MJO #2, this event at times masked the El Niño convection pattern and at other times accentuated it. Across the Pacific Ocean, intraseasonal variability associated with equatorial oceanic Kelvin wave activity was seen throughout the year (Fig. 4.11b). All three MJO events featured westerly wind bursts (Fig. 4.11a) that triggered downwelling Kelvin waves. Overall, downwelling Kelvin waves tended to be strong, helping to strengthen and maintain the anomalous warmth associated with El Niño.

In contrast, the upwelling Kelvin waves tended to be weak throughout the year and had little net impact on the surface and subsurface warmth associated with El Niño. This suppression of the upwelling waves is linked to sustained anomalous westerly winds over the central and western equatorial Pacific in association with El Niño (see Figs. 4.4b–d).

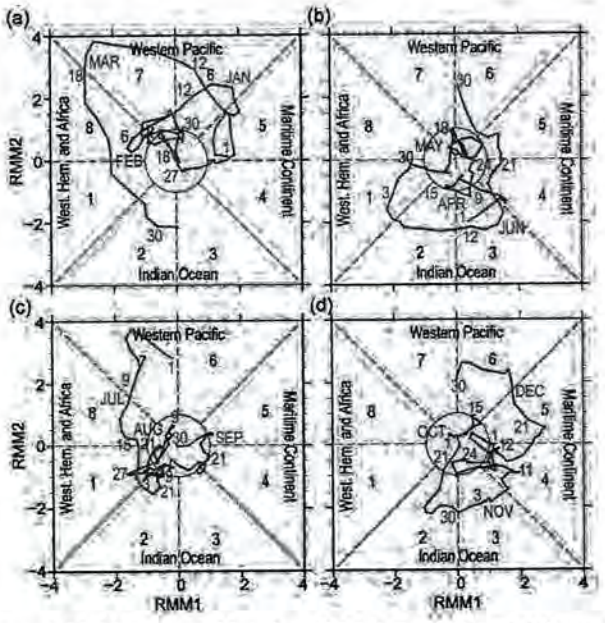

Fig. 4.10. Wheeler–Hendon (2004) Real-time Multivariate MJO (RMM) index for (a) Jan–Mar, (b) Apr–Jun, (c) Jul–Sep, and (d) Oct–Dec 2015. Each point represents the MJO amplitude and location on a given day, and the connecting lines illustrate its propagation. Amplitude is indicated by distance from the origin, with points inside the circle representing weak or no MJO. The 8 phases around the origin identify the region experiencing enhanced convection, and counterclockwise movement is consistent with eastward propagation.

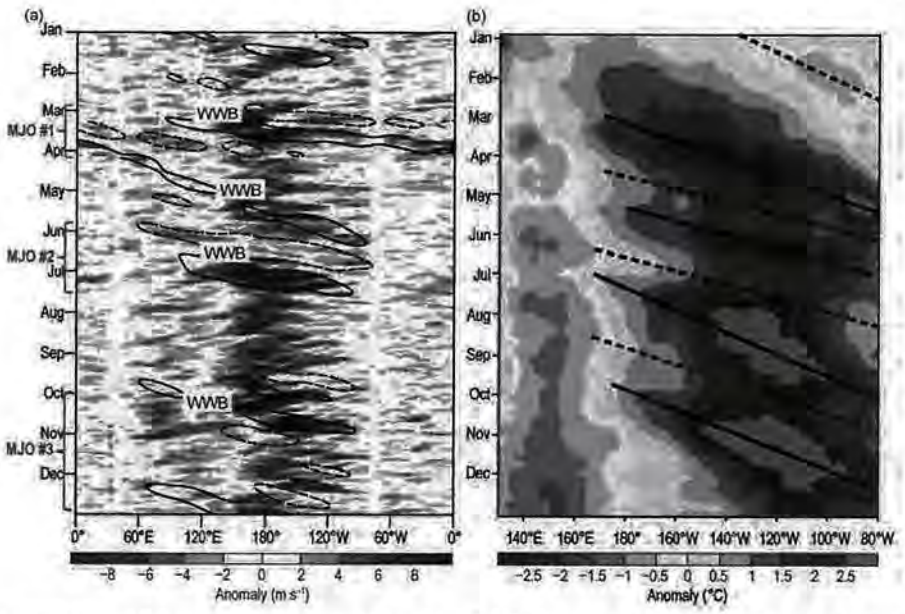

FIG. 4.11. (a) Time–longitude section for 2015 of anomalous 850-hPa zonal wind (m s^{-1}) averaged for 10°N–10°S. Black contours identify anomalies filtered for MJO. Red labels highlight the main MJO episodes. Significant westerly wind bursts (WWB) are labeled. (b) Time–longitude section for 2015 of the anomalous equatorial Pacific Ocean heat content, calculated as the mean temperature anomaly between 0 and 300 m depth. Yellow/red (blue) shading indicates above- (below-) average heat content. The relative warming (solid lines) and cooling (dashed lines) due to downwelling and upwelling equatorial oceanic Kelvin waves are indicated. Anomalies are departures from the 1981–2010 base period pentad means.

d. Intertropical convergence zones

1) PACIFIC—A. B. Mullan

The broad-scale patterns of tropical Pacific rainfall are dominated by two convergence zones, the intertropical convergence zone (ITCZ) and the South Pacific convergence zone (SPCZ). The ITCZ lies between 5° and 10°N and is most active during the August to December period, when it lies at its northernmost position. The SPCZ extends diagonally from around the Solomon Islands (10°S, 160°E) to near 30°S, 140°W, and is most active in the November–April half-year. Both convergence zones are strongly influenced by the state of ENSO.

During 2015, an El Niño event that had established itself in March continued to intensify through the end of the year. The monsoon of the western North Pacific extended far to the east to bring unusually strong and persistent westerly winds to the date line and beyond. Sea surface and subsurface temperatures were much warmer than normal, and the convergence zones were more active. For most months from May to December, the NASA ENSO Precipitation index (ESPI; Curtis and Adler 2000) was close to +2 or more, well above the +1 threshold associated with El Niño conditions.

Figure 4.12 summarizes the convergence zone behavior for 2015 and allows comparison of the 2015 seasonal variation against the longer term (1998–2014) climatology. Rainfall transects over 20°N to 30°S are presented for each quarter of the year, averaged across successive 30-degree longitude bands, starting in the western Pacific at 150°E–180°.

With the demise of the TRMM satellite in mid-2015, the rainfall data for this year's chapter are taken from NOAA's "CMORPH" global precipitation analysis (Joyce et al. 2004). This dataset, derived from low orbiter satellite microwave observations (as is TRMM 3B43), is available at the same 0.25° resolution as the TRMM 3B43 used previously (e.g., Mullan 2014). Although not identical, CMORPH and TRMM 3B43 rainfall are similar in pattern and magnitude at the broad scale discussed here.

In the western North Pacific, rainfall generally exceeded climatology from early in the year. The second quarter bulletin of the Pacific ENSO Applications Climate Center (www.weather.gov/media/peac/PEU/PEU_v21_n2.pdf) commented that: "In eastern Micronesia [5°–10°N, 140°–160°E,] ... extraordinary amounts of rainfall occur[ed] in March and April." As a result of the El Niño event, from March to December convection was greatly enhanced over climatology from the date line eastward, especially in the Northern Hemisphere for the ITCZ (Figs. 4.12b–d). Not only was the ITCZ closer to the equator, but the region of convection also had a broader latitude extent with a larger rainfall maximum. Convection at the equator itself was typically about double the climatological value for sectors 150°E–180° and 180°–150°W. Figure 4.13 gives the 2015 annual average precipitation in the Pacific and clearly shows the broader ITCZ: rainfall is twice the climatology along a line a few degrees north of the equator and again near 15°N, while rainfall is close to climatology along 10°N.

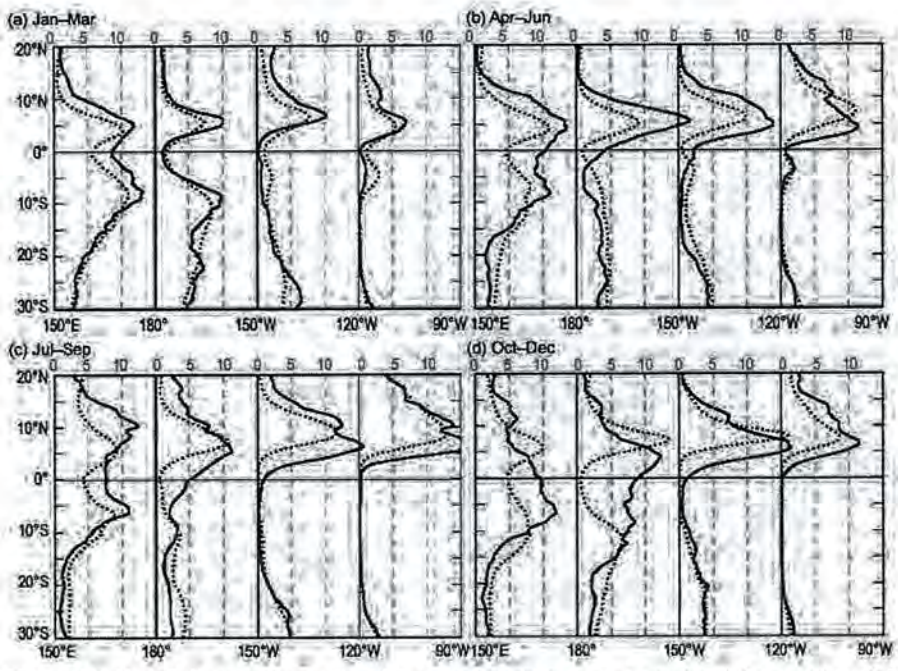

Fig. 4.12. Rainfall rate (mm day^{-1}) from CMORPH analysis for (a) Jan–Mar, (b) Apr–Jun, (c) Jul–Sep, and (d) Oct–Dec 2015. Each panel shows the 2015 rainfall cross section between 20°N and 30°S (solid line) and the 1998–2014 climatology (dotted line), separately for four 30° sectors from 150°E–180° to 120°–90°W.

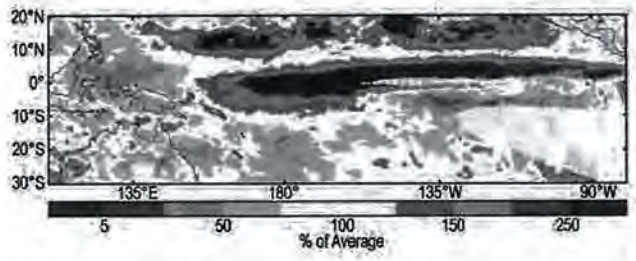

Fig. 4.13. Annual-average CMORPH precipitation for 2015, as a percentage of the 1998–2014 average. The white areas have precipitation anomalies within 25% of normal.

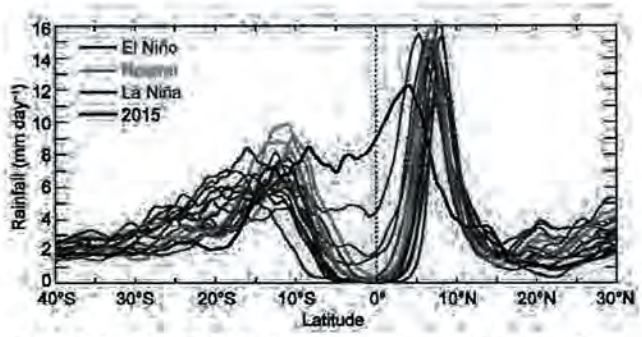

Fig. 4.14. CMORPH rainfall rate (mm day^{-1}) for Oct–Dec period for each year 1998 to 2015, averaged over the longitude sector 180°–150°W. The cross sections are color-coded according to NOAA's ONI, except for 2015 (an El Niño year) shown in black.

Enhanced convection near the equator, around and east of the date line, is typical of El Niño conditions. However, the degree of enhancement was quite extreme in 2015, as was the extent of warming in equatorial sea surface temperatures. Figure 4.14 shows precipitation transects for the last quarter of each year 1998–2015, averaged over the 180°–150°W sector. Rainfall within 5 degrees of the equator during 2015 was well above that for any other year in the relatively short CMORPH record (starting January 1998). It is likely, however, that October–December 1997 was similar, given the high rainfall along the equator in January–March 1998 under the very intense 1997/98 El Niño.

The CMORPH analysis matches reasonably well with observed rainfall in the Pacific Islands, although there is much more variability at the island scale. For Hawaii, at the northern edge of the 180°–150°W sector, the third quarter rainfall varied from about twice the average at Hilo, to ten times the average in Honolulu (www.weather.gov/media/peac/PEU/PEU_v21_n4.pdf).

Christmas Island (or Kiritimati) in eastern Kiribati lies on the equator in the same sector as Hawaii; rainfall was above normal for each of the last nine months of 2015 (www.niwa.co.nz/climate/icu), and Kiritimati received about ten times its normal December rainfall (667 mm). In contrast, islands along the southern edge of the SPCZ experienced well-below-normal rainfall from about April 2015 onward (www.niwa.co.nz/climate/icu). For example, the islands of New Caledonia, Fiji, Niue, and Tahiti were generally drier than normal for 8 or 9 of the last nine months of 2015.

2) Atlantic—A. B. Pezza and C. A. S. Coelho

The Atlantic ITCZ is a well-organized convective band that oscillates approximately between 5° and 12°N during July–November and 5°N and 5°S during January–May (Waliser and Gautier 1993; Nobre and Shukla 1996). Equatorial Kelvin waves can modulate the ITCZ intraseasonal variability (Guo et al. 2014). ENSO is also known to influence the ITCZ on the

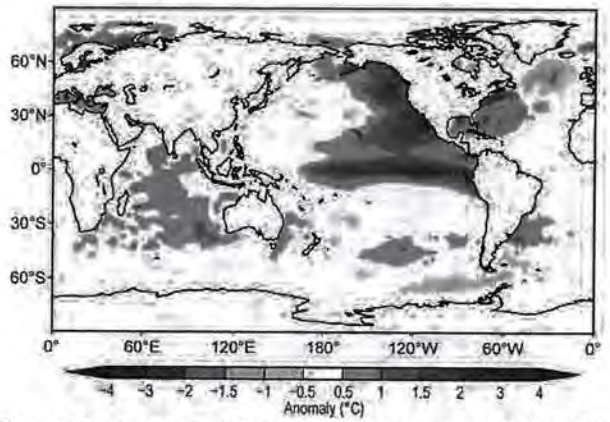

FIG. 4.15. Spatial distribution of average global SST anomalies (°C, Reynolds et al. 2002) during 2015.

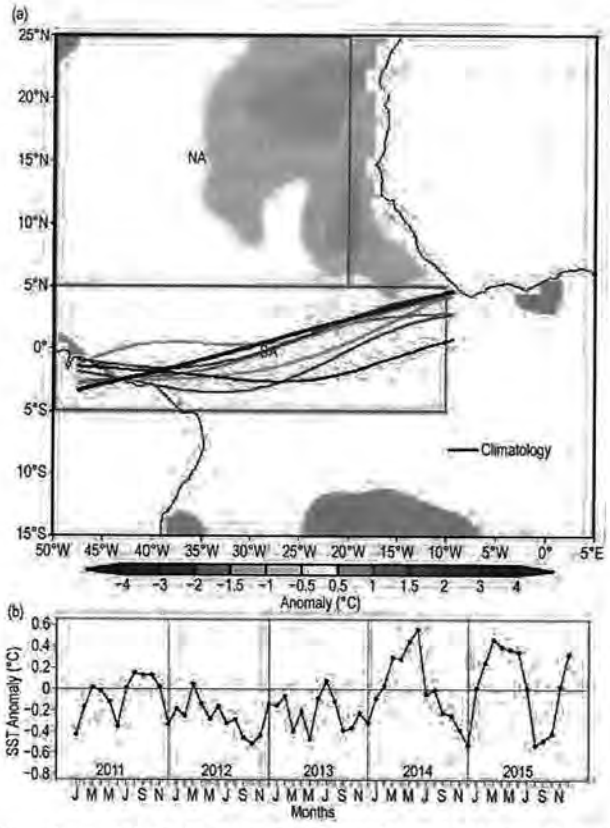

FIG. 4.16. (a) Atlantic ITCZ position inferred from outgoing longwave radiation during May 2014. The colored thin lines indicate the approximate position for the six pentads of the month. The black thick line indicates the Atlantic ITCZ climatological position. The SST anomalies for May 2014 based on the 1982–2013 climatology are shaded (°C). The two boxes indicate the areas used for the calculation of the Atlantic index in (b). (b) Monthly SST anomaly time series averaged over the South American sector (SA region, 10°–50°W, 5°S–5°N) minus the SST anomaly time series averaged over the North Atlantic sector (NA region, 20°–50°W, 5°–25°N) for the period 2010–14, forming the Atlantic index. The positive phase of the index indicates favorable conditions for enhanced Atlantic ITCZ activity.

interannual time scale (Münnich and Neelin 2005). In 2015, weak positive SST anomalies prevailed in the equatorial Pacific until March, followed by the development of a strong El Niño event from March onward, with a marked signature in the annual average (Fig. 4.15).

Consistent with Münnich and Neelin (2005), these conditions were associated with relatively warmer waters in the North Atlantic sector after the establishment of the El Niño, leading to a sharp negative peak in the Atlantic index (Fig 4.16a) in the second half of 2015, as measured by the north–south SST gradient (Fig. 4.16a). As a consequence, the ITCZ oscillated well north of its climatological position for most of the year, with an overall suppression of any significant activity in the Southern Hemisphere. An exception occurred in March and April (Fig. 4.16b), when the

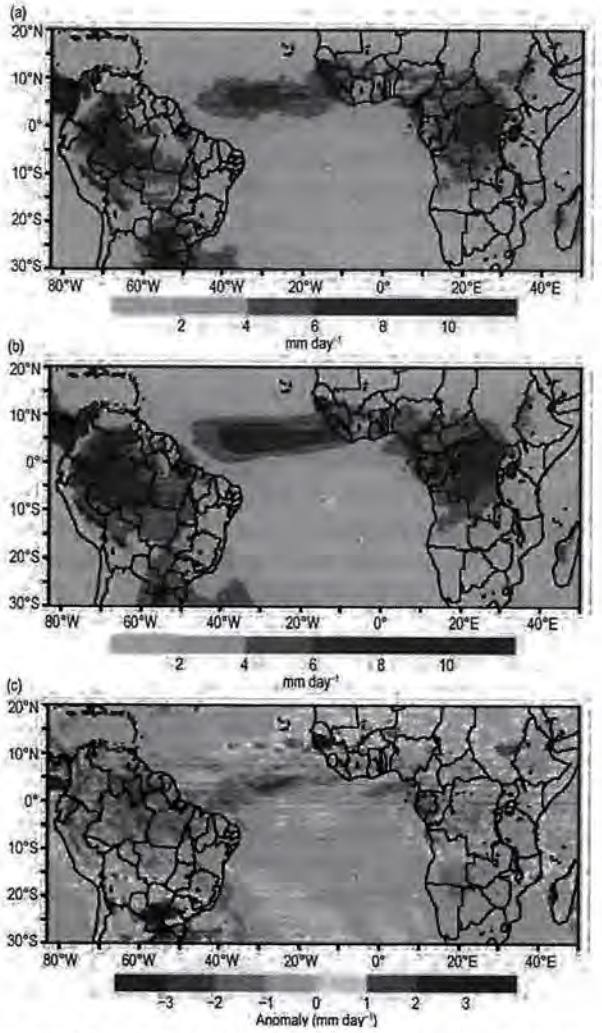

FIG. 4.17. (a) Observed precipitation (mm day^{-1}) during 2015, (b) 1998–2014 precipitation climatology (mm day^{-1}), and (c) observed anomaly (mm day^{-1}) in 2015 derived from CPC Morphing technique (CMORPH; Joyce et al. 2004).

ITCZ moved south of the equator during a short gap before the air–sea teleconnection effects of the strong ENSO event became fully established. This southern burst was accompanied by a brief but sharp increase of the Atlantic index.

Despite that, the effects of the southern passage of the ITCZ on potentially enhancing the convective activity over the drought-prone areas of northeastern Brazil were only minor, with an overall annual balance of well-below-average precipitation in most of the region (Fig. 4.17a-c). This "lack of convective coupling" was associated with a widespread drought within most of the Amazon as well as in central Brazil. Persistent low vegetation health indices and reduced soil moisture likely contributed to lowering the rate of evapotranspiration and relative humidity, facilitating higher temperatures as observed during heat waves in Europe (Whan et al. 2015). This large-scale drought pattern has also extended into southeastern Brazil in recent years (Coelho et al. 2015a,b) and was already established before the onset of the latest El Niño. Otto et al. (2015) explore whether droughts in different parts of Brazil could either be part of a longer-term natural oscillation or attributable to anthropogenic forcing.

e. *Tropical cyclones*

1) Overview—H. J. Diamond and C. J. Schreck

The IBTrACS dataset comprises historical tropical cyclone (TC) best-track data from numerous sources around the globe, including all of the WMO Regional Specialized Meteorological Centers (RSMC; Knapp et al. 2010). To date, IBTrACS represents the most complete compilation of global TC data and offers a unique opportunity to revisit the global climatology of TCs. Using IBTrACS data (Schreck et al. 2014) a 30-year average value for storms (from WMO-based RSMC numbers) is noted for each basin.

The global tallying of total TC numbers is challenging and involves more than simply adding up basin totals because some storms cross basin boundaries, some basins overlap, and multiple agencies are involved in the tracking and categorization of TCs. Compiling the activity using the IBTrACS dataset over all seven TC basins (Fig. 4.18), the 2015 season (2014/15 in the Southern Hemisphere) had 101 named storms [wind speeds ≥ 34 knots (kt; 1 kt = 0.51 m s^{-1}) or 18 m s^{-1}], which is well above the 1981–2010 average of 82 (Schreck et al. 2014) and 10 more than the 2014 total of 91 (Diamond 2015). The 2015 season also featured 62 Hurricanes/Typhoons/Cyclones (HTC; wind speeds ≥ 64 kts or 33 m s^{-1}), which is also well above the 1981–2010 average of 46 HTCs (Schreck et al. 2014). Of these, 36 storms reached major HTC status (wind speeds ≥ 96 kts or 49 m s^{-1}; WMO 2015), which is well above the average of 21. To assist in tallying the basin totals, this year we normalized the counts by basing them on WMO-defined basin boundaries and by using the Saffir–Simpson scale to represent intensities for all basins, realizing that the Saffir–Simpson scale is not operationally used in all basins. Therefore, Fig. 4.18 depicts as close to an overall picture of global TCs as possible, and each of the basin sections (4e2–4e8) has a graphic reflecting those normalized basin totals.

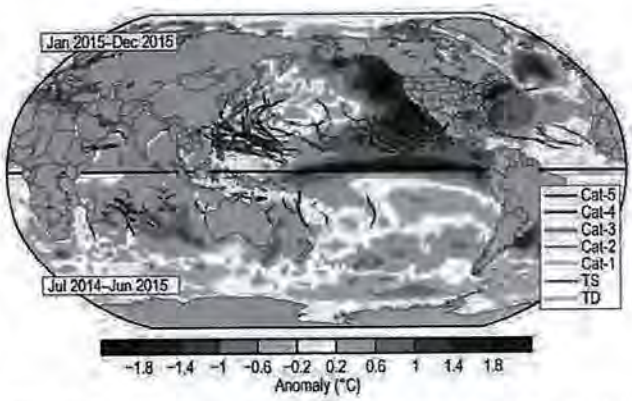

Fig. 4.18. Global summary of TC tracks with respect to SST anomalies for the 2015 TC season.

There were eight Saffir–Simpson level Category 5 systems during the year (one more than in 2014, and three more than in 2013): Patricia in the eastern North Pacific; Super Typhoons Maysak, Noul, Dolphin, Soudelor, and Atsani in the western North Pacific; Cyclone Eunice in the south Indian Ocean; and Tropical Cyclone Pam in the southwest Pacific. Patricia, with maximum sustained surface winds of 174 kt (88 m s^{-1}) and a minimum central pressure of 879 hPa, set records for these parameters for any tropical cyclone anywhere in the Western Hemisphere. Patricia was also characterized by an extraordinarily fast intensification, with a 100-hPa drop in its minimum central pressure within a 24-hour period.

There were also several Saffir–Simpson Category 3 and 4 intensity-level systems during 2015 that had major impacts: 1) Joaquin in the North Atlantic; 2) Hilda, Ignacio, and Kilo in the eastern North Pacific; 3) Koppu, Chan-hom, and Melor in the western North Pacific; 4) Chapala and Megh in the north Indian Ocean; 5) Chedza, Fundi, and Haliba in the south Indian Ocean; and 6) Marcia in the southwest Pacific. It should be noted that although TCs in the south Indian Ocean impacted life and property, the greatest impacts were caused by those storms that did not even become cyclones. This observation speaks to the damage that tropical cyclones can sometimes inflict

while not at the named storm level of intensity. The North Atlantic hurricane season was below normal (section 4e2), and both the central and eastern Pacific hurricane seasons were well above normal (section 4e3), consistent with the El Niño conditions in place (section 4b). Sidebar 4.1 also provides analysis and a summary of the overall Northern Hemisphere TC seasons and highlights the special role that El Niño plays with respect to TCs. Sidebar 4.2 describes a rare and interesting subtropical cyclone that developed over the southeast Pacific, a region usually not conducive to such development.

2) ATLANTIC BASIN—G. D. Bell, C. W. Landsea, E. S. Blake, J. Schemm, S. B. Goldenberg, T. B. Kimberlain, and R. J. Pasch

(i) 2015 seasonal activity

The 2015 Atlantic hurricane season produced 11 named storms, of which four became hurricanes and two became major hurricanes. These values are not far below the HURDAT2 30-year (1981–2010) seasonal averages of 11.8 tropical storms, 6.4 hurricanes, and 2.7 major hurricanes (Landsea and Franklin 2013). Many of the storms during 2015 were weak and short-lived, and the seasonal accumulated cyclone energy (ACE) value (Bell et al. 2000) was 67.8% of the 1981–2010 median (92.4×10^4 kt^2; Fig. 4.19). This value is below NOAA's upper threshold (71.4% of the median) for a below-normal season (see www.cpc.ncep.noaa.gov/products/outlooks/background_information.shtml), and consequently the season is classified as below-normal.

A single storm, Major Hurricane Joaquin, produced nearly one-half of the season's total ACE value; the remaining ten storms produced an ACE value of only 36.1% of the median. This result highlights the large number of weak and short-lived storms during the season. Combined with a near-normal hurricane season in 2014 and a below-normal season in 2013 (Bell et al. 2015), 2013–15 marks the first time since 1992–94 in which three consecutive seasons were not above normal.

Since the current high-activity era for Atlantic hurricanes began in 1995, 13 of 21 seasons (62%) have been above normal, and four seasons (19%) have been near normal. The 2015 season marks only the fourth below-normal season since 1995. The 2015 activity was well below the averages during the recent active period (1995–2014) of 15 named storms, 7.6 hurricanes, 3.5 major hurricanes, and 141.6% of the 1981–2010 median ACE. A yearly archive of conditions during these seasons can be found in previous *State of the Climate* reports.

A main delineator between more- and less-active Atlantic hurricane seasons is the number of hurricanes and major hurricanes that originate as named storms within the Main Development Region (MDR; green boxed region in Fig. 4.20a) which spans the tropical Atlantic Ocean and Caribbean Sea between 9.5° and 21.5°N (Goldenberg and Shapiro 1996; Goldenberg et al. 2001; Bell and Chelliah 2006). Only five named storms formed in the MDR during 2015, with two becoming hurricanes and one of those being a short-lived major hurricane. The resulting ACE value from these five storms was only about 27% of the median, which is comparable to the 1981–2010 below-normal season average for the MDR of 18.1%. These values are well below the above-normal and near-normal season ACE averages for the MDR of 151.1% and 57.9% of the median, respectively.

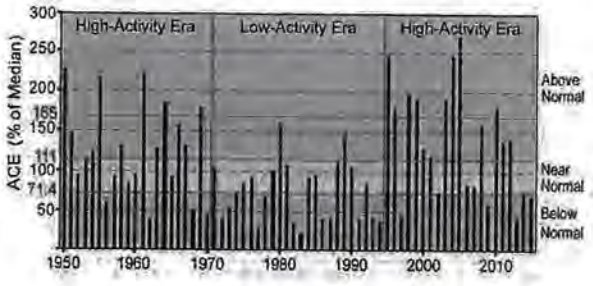

FIG. 4.19. NOAA's Accumulated Cyclone Energy (ACE) index expressed as percent of the 1981–2010 median value. ACE is calculated by summing the squares of the 6-hourly maximum sustained surface wind speed (knots) for all periods while the storm is at least tropical storm strength. Red, yellow, and blue shadings correspond to NOAA's classifications for above-, near- and below-normal seasons, respectively. The 165% threshold for a hyperactive season is indicated. Vertical brown lines separate high- and low-activity eras.

(ii) Storm tracks

Two tropical storms made landfall in the United States during 2015: Tropical Storm Ana which made landfall in South Carolina in May, and Tropical Storm Bill which made landfall in Texas in June. No hurricanes made landfall in the United States this season.

No hurricanes tracked through the Caribbean Sea during 2015. This region has seen only one hurricane in the last three seasons: Gonzalo in 2014. As discussed below, and also by Bell et al. (2014, 2015), this dearth of hurricane activity over the Caribbean Sea has reflected a lack of storms forming in the region due to strong vertical wind shear and anomalous sinking motion, and also a lack of storms propagating westward into the region.

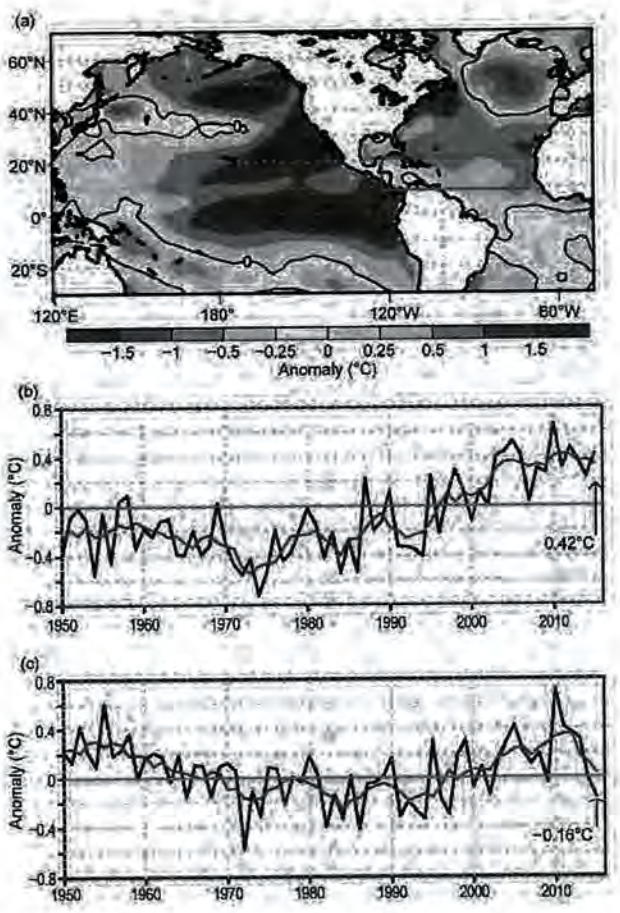

FIG. 4.20. (a) ASO 2015 SST anomalies (°C), with the MDR indicated by the green box. (b) Time series for 1950–2015 of ASO area-averaged SST anomalies in the MDR. (c) Time series showing the difference between ASO area-averaged SST anomalies in the MDR and those for the entire global tropics (20°N–20°S). Red lines show a 5-pt. running mean of each time series. Anomalies are departures from the ERSST.v3b (Smith et al. 2008) 1981–2010 period monthly means.

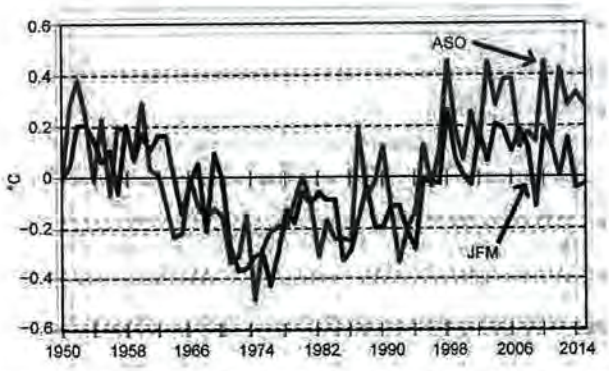

FIG. 4.21. Unfiltered index of the Atlantic multidecadal oscillation (AMO) during 1950–2015 averaged over ASO (red line) and JFM (blue line). Based on the Kaplan SST dataset (Enfield et al. 2001; www.esrl.noaa.gov /psd/data/timeseries/AMO).

(iii) Atlantic sea surface temperatures

SST anomalies warmed across the MDR as the summer progressed, with below-average SSTs during June–July and above-average SSTs during August–November. For the MDR as a whole, the area-averaged SST anomaly for October (+0.64°C) was the warmest in the 1950–2015 record, and the area-averaged anomaly for November (+0.48°C) tied for the warmest on record.

For the peak months (August–October, ASO) of the Atlantic hurricane season the mean SST departure in the MDR was +0.43°C (Fig. 4.20b), which ties for fifth warmest in the record (Fig. 4.20b). Consistent with the ongoing warmth in the MDR since 1995, objective measures of the Atlantic multidecadal oscillation (AMO; Enfield and Mestas-Nuñez 1999), such as NOAA's operational Kaplan AMO index, indicate a continuance of the AMO warm phase during ASO 2015 (Fig. 4.21). In contrast, the AMO index for January–March has been near zero for the past two years.

The warm AMO phase and the associated positive phase of the Atlantic Meridional Mode (Vimont and Kossin 2007; Kossin and Vimont 2007) are the primary climate factors associated with high-activity eras for Atlantic hurricanes (Goldenberg et al. 2001; Bell and Chelliah 2006; Bell et al. 2011, 2012). This warm phase features anomalously warm SSTs in the MDR compared to the remainder of the global tropics (Fig. 4.20c). However, the mean SST anomaly within the MDR during ASO 2015 was less than the mean anomaly for the entire global tropics, due partly to the intensifying El Niño (see section 4b).

(iv) Atmospheric conditions

a. Atlantic basin

The below-normal 2015 Atlantic hurricane season resulted mainly from a set of atmospheric conditions during ASO that made the central and western MDR extremely unfavorable for TC activity. These conditions included: 1) anomalously strong vertical wind shear extending from the Caribbean Sea northeastward to the central Atlantic (Fig. 4.22), 2) anomalous upper-level (200-hPa) convergence and lower-level (850-hPa) divergence (Fig. 4.23a), 3) anomalous sinking motion throughout the troposphere (Fig. 4.23b) and, 4) midlevel drier air (Fig. 4.23c).

The vertical wind shear averaged across the Caribbean Sea during ASO was the third strongest (12.4 m s^{-1}) in the ASO 1970–2015 record (Fig. 4.22b). The two ASO seasons with larger shear values in this region were the El Niño years of 1972 and 1986. For the June–November hurricane season as a whole, the vertical wind shear over the Caribbean Sea was

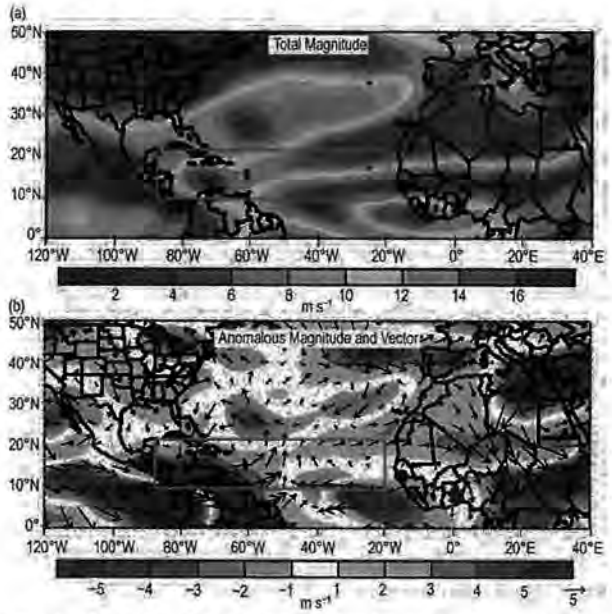

FIG. 4.22. 200–850 hPa vertical wind shear during ASO 2015: (a) magnitude (m s^{-1}) and (b) anomalous magnitude and vector. In (a), orange-red shading indicates areas where the vertical wind shear magnitude is ≤10 m s^{-1}. In (b), vector scale is below right of plot. Green box denotes the MDR. Anomalies are departures from the 1981–2010 means.

the strongest in the record (17.3 m s^{-1}), exceeding the previous largest value of 15.4 m s^{-1} recorded in 1972. On monthly time scales, shear values greater than 8–10 m s^{-1} are generally considered nonconducive to hurricane formation.

The main activity during the 2015 hurricane season reflected more conducive conditions over the eastern MDR and also over the western subtropical North Atlantic north of the MDR. In portions of the eastern MDR the combination of weak vertical wind shear (Fig. 4.22a), anomalous rising motion (Fig. 4.23b), and increased midlevel moisture (Fig. 4.23c) contributed to the development of five named storms, including two hurricanes. Over the western subtropical North Atlantic, a similar combination of conditions contributed to the development of five named storms north of the MDR. Two of these storms became hurricanes, with one becoming the only long-lived major hurricane of the season (Joaquin). Together, these five storms produced about 60% of the total seasonal ACE value.

b. El Niño impacts

The 200-hPa circulation patterns during ASO 2015 (Fig. 4.24) show that El Niño impacted atmospheric conditions across the tropical Pacific and Atlantic Oceans in both hemispheres, so as to weaken the Atlantic hurricane season and simultaneously strengthen both the central and eastern Pacific hurricane seasons (see section 4e3).

The velocity potential, which is related to the divergent component of the wind, showed an anomaly pattern during ASO that is typical of El Niño (Fig. 4.24a). This pattern featured a core of negative anomalies across the eastern half of the Pacific basin, along with cores of positive anomalies over the western Pacific/Australasia and also over the Amazon basin and MDR. The associated pattern of divergent wind vectors shows a suppressive pattern for Atlantic hurricanes of anomalous upper-level convergence over the Caribbean Sea and central MDR.

The 200-hPa streamfunction pattern also showed a typical El Niño signal, with anticyclonic anomalies across the subtropical Pacific Ocean in both hemispheres flanking the region of enhanced El Niño–related convection (see Fig. 4.5c), along with cyclonic anomalies extending downstream from the Americas (Fig. 4.24b).

Regionally, the streamfunction pattern included an anomalous upper-level subtropical trough that extended across the entire MDR. This feature reflected an amplification of the mean tropical upper tropospheric trough (TUTT; white dashed line) in

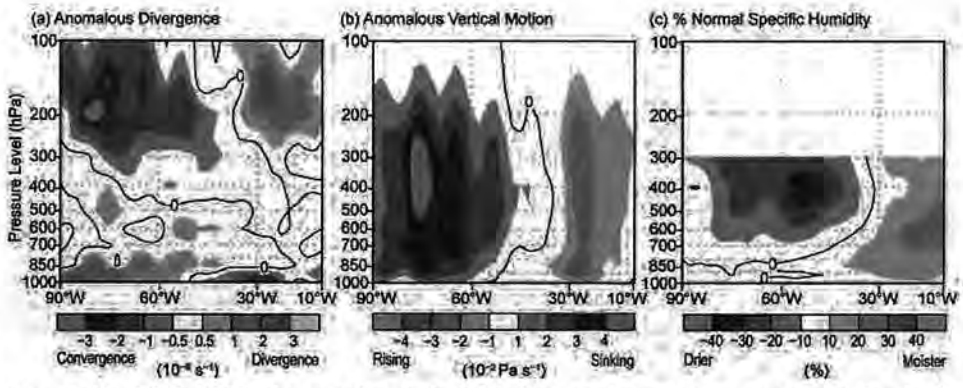

FIG. 4.23. ASO 2015: Atmospheric height–longitude sections averaged for 9.5°–21.5°N, of (a) anomalous divergence (× 10^{-6} s^{-1}), (b) anomalous vertical velocity (× 10^{-2} Pa s^{-1}), and (c) percent of normal specific humidity. Green shading indicates anomalous divergence, anomalous rising motion, and increased moisture, respectively. Brown shading indicates anomalous convergence, anomalous sinking motion, and decreased moisture. Zero lines are drawn on each panel. Anomalies are departures from the 1981–2010 means.

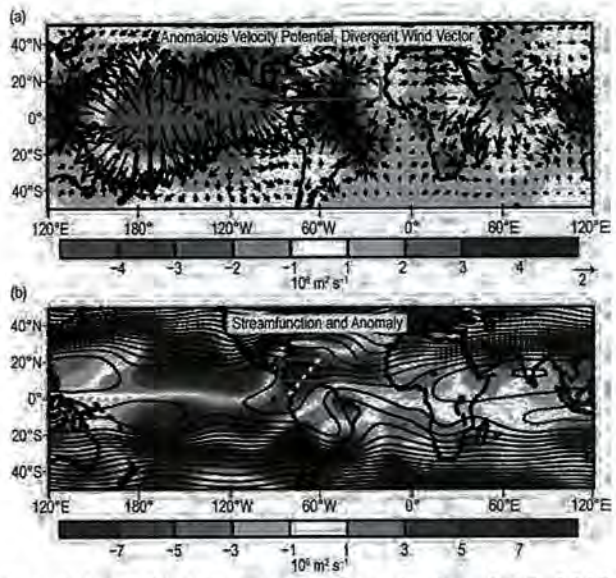

Fig. 4.24. 200-hPa circulation during ASO 2015: (a) anomalous velocity potential (× 10^6 m^2 s^{-1}) and anomalous divergent wind vector (m s^{-1}), and (b) total (contours) and anomalous (shaded) streamfunction (× 10^6 m^2 s^{-1}). Divergent wind vector scale in (a) is below right of plot. In (b), white dashed line indicates amplified tropical upper tropospheric trough (TUTT). Anticyclonic anomalies are indicated by positive values (orange/red) in the NH and negative values (blue) in the SH. Cyclonic anomalies are indicated by negative values in the NH and positive values in the SH. Green boxes indicate the Atlantic hurricane MDR. Anomalies are based on the 1981–2010 climatology.

the western MDR and a disappearance of the mean upper-level subtropical ridge normally located over the central and eastern MDR. These conditions contributed anomalous upper-level westerly winds, increased vertical wind shear, and anomalous sinking motion across the MDR (Figs. 4.22, 4.23), the combination of which suppressed the 2015 Atlantic hurricane season.

3) Eastern North Pacific and central North Pacific basins—M. C. Kruk, C. J. Schreck, and T. Evans

(i) Seasonal activity

The eastern North Pacific (ENP) basin is officially split into two separate regions for the issuance of warnings and advisories by NOAA's National Weather Service. NOAA's National Hurricane Center in Miami, Florida, is responsible for issuing warnings in the eastern part of the basin (ENP) that extends from the Pacific Coast of North America to 140°W, while NOAA's Central Pacific Hurricane Center in Honolulu, Hawaii, is responsible for issuing warnings in the central North Pacific (CNP) region between 140°W and the date line. This section summarizes the TC activity in both warning areas using combined statistics, along with information specifically addressing the observed activity and impacts in the CNP region.

The ENP/CNP hurricane season officially spans from 15 May to 30 November. Hurricane and tropical storm activity in the eastern area of the basin typically peaks in September, while in the central Pacific, TC activity normally reaches its seasonal peak in August (Blake et al. 2009). During the 2015 season, a total of 26 named storms formed in the combined ENP/CNP basin. This total included 16 hurricanes, 11 of which were major hurricanes. The 1981–2010 IBTrACS seasonal averages for the basin are 16.5 named storms, 8.5 hurricanes, and 4.0 major hurricanes (Schreck et al. 2014). The 2015 season's 26 named storms is the highest storm count since the 1992 season. In late August, Hurricanes Kilo, Ignacio, and Jimena reached Category 4 status at the same time (Fig. SB4.1a). This was the first time on record that three Category 4 or stronger TCs were present at the same time in any global TC basin.

Given that 68% of the ENP/CP hurricanes in 2015 reached major hurricane status, it is no surprise that

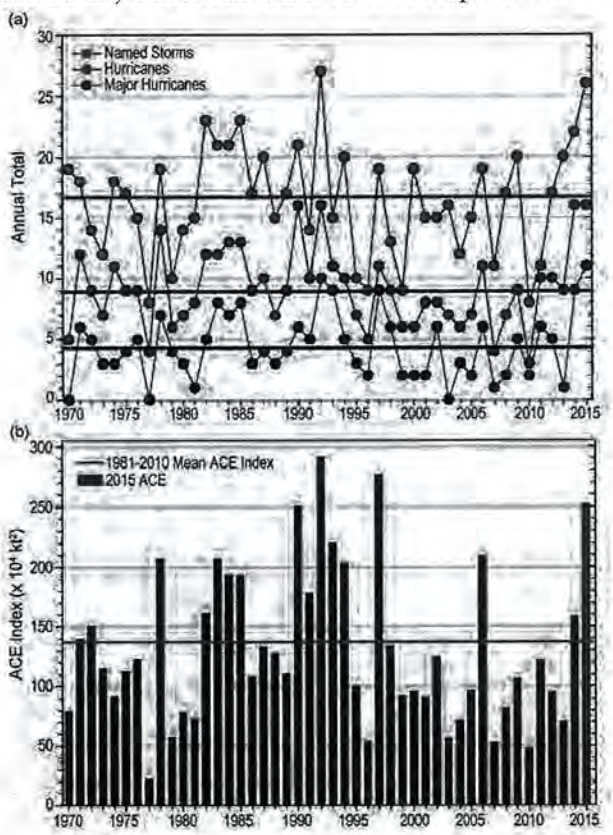

Fig. 4.25. Seasonal TC statistics for the full ENP/CNP basin over the period 1970–2015: (a) number of named storms, hurricanes, and major hurricanes, and (b) the ACE index (× 10^4 kt^2) with the 2015 seasonal total highlighted in red. The time series shown includes the corresponding 1981–2010 base period means for each parameter.

the ACE index for 2015 was high as well, with a seasonal value of 251.6×10^4 kt^2 (Fig. 4.25), which is nearly double the 1981–2010 mean of 132.0×10^4 kt^2 (Bell et al. 2000; Bell and Chelliah 2006; Schreck et al. 2014). A record-shattering 16 tropical cyclones developed in, or entered into, the CNP basin during 2015, with a distribution of eight hurricanes (five major), six tropical storms, and two depressions (Fig. 4.25); the previous record season was 1992 with a total of 12 TCs. The long-term 1981–2010 IBTrACS mean is 4.7 storms passing through the CNP per season.

(ii) Environmental influences on the 2015 season

Figure 4.26 illustrates the background conditions for TC activity in the ENP and CNP during 2015. Consistent with the strong El Niño conditions, the equatorial Pacific was dominated by anomalously warm SST anomalies (Fig. 4.26a). As in 2014, these warm SSTs extended throughout most of the subtropical ENP, which would be exceptionally favorable for TC activity. The ITCZ was also strongly enhanced in association with the warm SSTs, but the strongest enhancement of convection was southward of where TCs form (Fig. 4.26b). Vertical wind shear magnitudes were slightly below their climatological values (Fig. 4.26c). The vertical wind shear anomalies were generally easterly from 120°E to the date line, which likely contributed to the record season in the CNP. The broad area of warm SSTs, enhanced convection, and moderate shear in 2015 all contributed to favorable conditions that resulted in above-normal hurricane activity.

Figure 4.26d shows a broad area of 850-hPa westerly anomalies near the equator. Similar patterns were seen in 2012–14 (Diamond 2013, 2014, 2015), although these years also featured stronger easterly anomalies to the north. Even on their own, the westerly anomalies produced the region of enhanced cyclonic vorticity within which most of the ENP storms developed. Many of these storms developed where the enhanced vorticity intersected the westerly anomalies. The westerlies could have strengthened easterly wave activity in this region through barotropic energy conversion and wave accumulation (Maloney and Hartmann 2001; Aiyyer and Molinari 2008; Rydbeck and Maloney 2014).

ENP TC activity is strongly influenced by the MJO (Maloney and Hartmann 2001; Aiyyer and Molinari 2008; Slade and Maloney 2013), and recent studies have found a greater role for convectively coupled

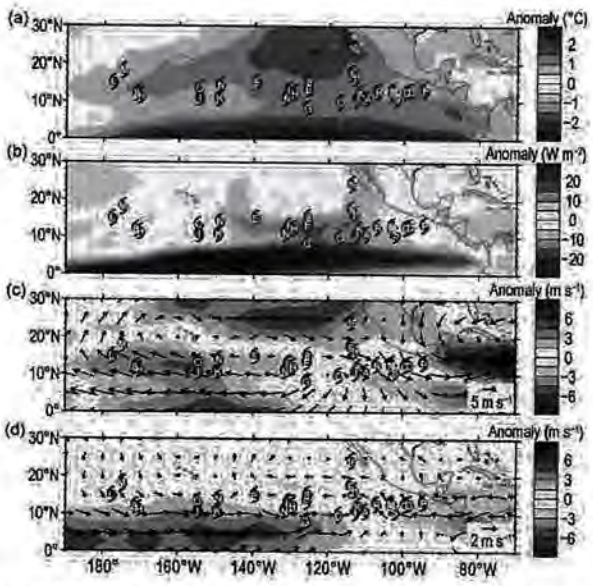

Fig. 4.26. May–Nov 2015 anomaly maps of (a) SST (°C, Banzon and Reynolds 2013), (b) OLR (W m^{-2}, Lee 2014), (c) 200–850-hPa vertical wind shear (m s^{-1}) vector (arrows) and scalar (shading) anomalies, and (d) 850-hPa winds (m s^{-1}, arrows) and zonal wind (shading) anomalies. Anomalies are relative to the annual cycle from 1981–2010, except for SST which is relative to 1982–2010 due to data availability. Hurricane symbols with letters denote where each ENP TC attained tropical storm intensity. Wind data obtained from NCEP–NCAR reanalysis I (Kalnay et al. 1996).

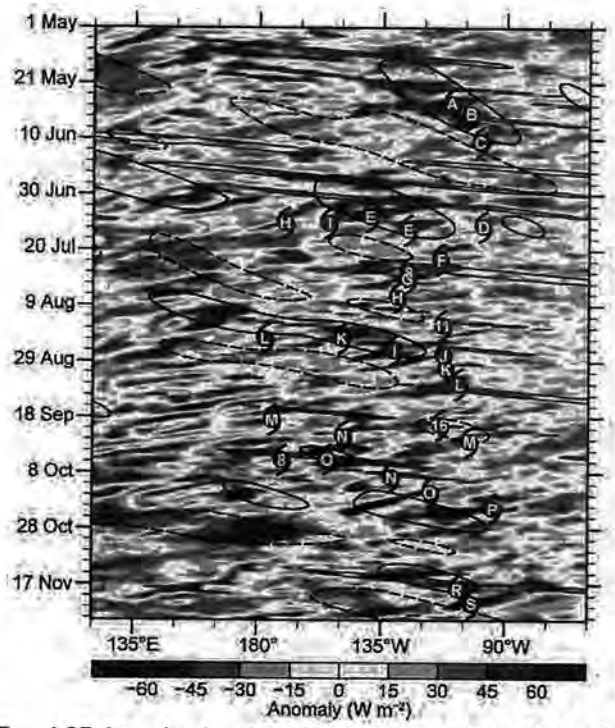

Fig. 4.27. Longitude–time Hovmoller of OLR (W m^{-2}, Lee 2014) averaged 5°–15°N. Unfiltered anomalies from a daily climatology are shaded. Negative anomalies (green) indicate enhanced convection. Anomalies filtered for Kelvin waves are contoured in blue at −10 W m^{-2}. Hurricane symbols and letters indicate genesis of ENP TCs.

Kelvin waves in modulating tropical cyclogenesis (Schreck and Molinari 2011; Ventrice et al. 2012a,b; Schreck 2015). Figure 4.27 uses OLR to examine the evolution of convection during the 2015 ENP hurricane season. Following Kiladis et al. (2009), the blue contours identify the Kelvin-filtered anomalies. Easterly waves are also apparent in the unfiltered anomalies (shading) as westward moving features, such as the ones leading up to Hurricanes Norbert and Simon.

During the 2015 ENP hurricane season, intraseasonal variability was dominated by eastward moving signals that straddled the boundaries between Kelvin waves and the MJO (Roundy 2012a,b). Three events are particularly noteworthy: early July, late August, and October. These events were all prolific TC producers, spawning strings of TC genesis from the north Indian Ocean to the North Atlantic. In the ENP/CNP alone, 5–7 TCs developed in association with each of these events, accounting for 18 of the 26 ENP/CNP TCs in 2015.

(iii) TC impacts

During the 2015 season, only 2 of the season's 26 combined ENP/CNP tropical storms made landfall along the western coast of Mexico or Baja California, while remarkably no storms in the CNP region made landfall in Hawaii. The long-term annual average number of landfalling storms on the western coast of Mexico is 1.8 (Raga et al. 2013).

The first storm to make landfall along the Mexican coastline was Hurricane Blanca (31 May to 9 June), which had maximum sustained winds of 120 kt (61 m s^{-1}) and a minimum central pressure of 936 hPa. Blanca weakened to a tropical storm before making landfall in Baja California and made the earliest landfall in that region on record. Even as the storm was weakening, strong rip currents associated with the storm claimed four lives off the coast of Mexico.

The second landfalling storm of 2015 was Major Hurricane Patricia from 20–24 October, with maximum sustained winds of 174 kt (88 m s^{-1}) and a minimum central pressure of 879 hPa. The barometric pressure and maximum sustained winds, both as measured by hurricane reconnaissance aircraft, are now the lowest on record for pressure and highest on record for winds anywhere in the Western Hemisphere. The hurricane also intensified extraordinarily quickly, dropping 100 hPa in just 24 hours. Fortunately for the major cities and towns in coastal Mexico, Patricia made landfall as a Category 5 storm near Jalisco, Mexico, a relatively rural area, though it still caused a range of impacts. Many trees were completely defoliated, power outages were common, and torrential rains flooded roads and resulted in landslides. In the town of Tamaulipas, 193 mm of rain was recorded from the storm. Roughly 9000 homes were damaged or destroyed and many agricultural croplands, in particular banana crops, were wiped out by the wind and rain from Patricia.

Despite no direct landfalls, high surf, coastal flooding, flooding rains, and oppressive heat impacted the Hawaiian Islands throughout the 2015 season. The largest surf came from Hurricane Ignacio as it passed to the east and northeast of the main Hawaiian Islands. Ignacio produced large waves and a small storm surge resulting in water and debris on roadways along the Big Island's (also known as Hawaii Island) and Oahu's eastern coastline, causing road and beach park closures. Heavy rain associated with Ignacio fell across the main Hawaiian Islands causing widespread flooding, including in portions of Honolulu. Hurricanes Hilda and Kilo forced deep tropical moisture over the main Hawaiian Islands, which led to significant flooding rains. Impacts of this flooding included a massive sewage spill when the Honolulu drainage system was overwhelmed, flooded homes and businesses, and one flash flood fatality. Hurricane Guillermo had the closest approach to the main Hawaiian Islands and produced coastal flooding as large waves closed roads and beach parks. Portions of the northwest Hawaiian Islands, which are not populated but host research teams, were evacuated due to large waves associated with Hurricane Kilo and Tropical Storm Malia.

4) Western North Pacific basin—S. J. Camargo

(i) Introduction

The WNP is unique in that TCs are tracked simultaneously by several agencies in that region. Among these are the United States military's Joint Typhoon Warning Center (JTWC) and the WMO-sanctioned RSMC-Tokyo, Japan Meteorological Agency (JMA). Data from JTWC are used here; best-track dataset for the period 1945–2014 and from the JTWC's preliminary operational data for 2015. The best-track data from the RSMC-Tokyo, Japan Meteorological Agency (JMA), was used in Fig. 4.28b. All other figures were produced using JTWC TC data. Climatology is defined using the period 1981–2010, with the exception of landfall statistics, where 1951–2010 is used.

(ii) Seasonal activity

The TC season in the western North Pacific (WNP) in 2015 was above normal by most measures of TC activity considered. According to the JTWC, the 2015

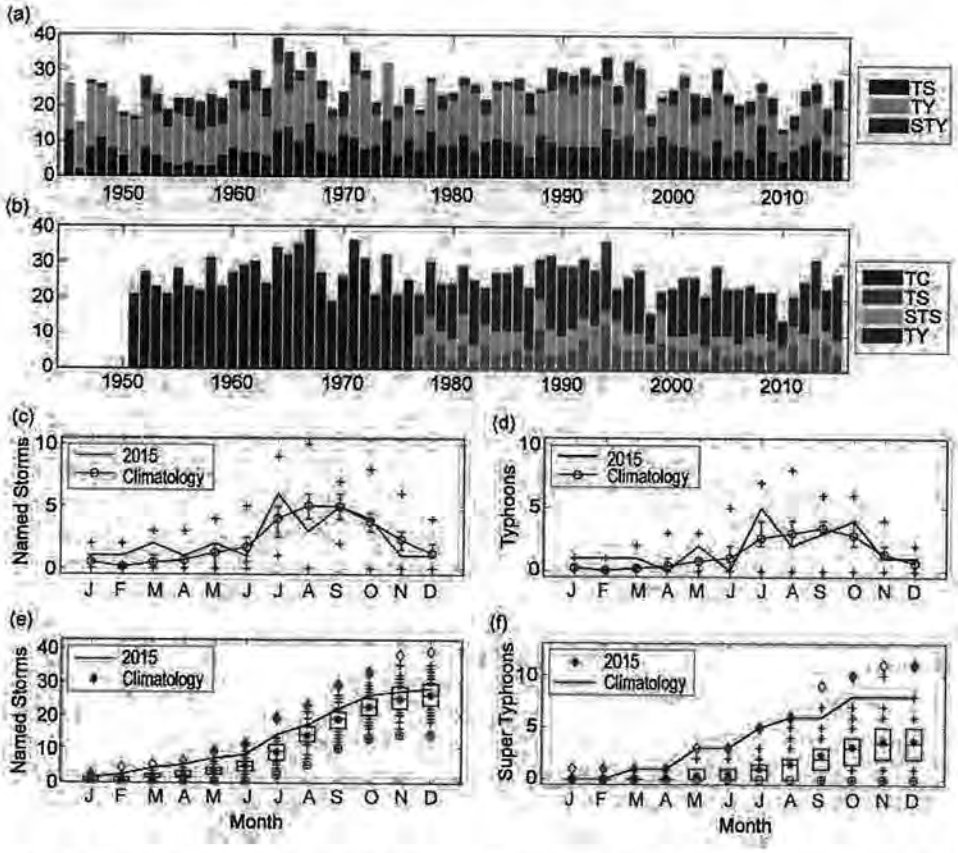

FIG. 4.28. (a) Number of tropical storms, typhoons, and super typhoons per year in the western North Pacific for the period 1945–2015 based on the JWTC best-track dataset. (b) Number of TCs (all storms which reach tropical storm intensity or higher) for 1951–76; number of tropical storms, severe tropical storms, and typhoons for 1977–2015 based on the JMA best-track dataset. (c), (d) The number of TCs with tropical storm intensity or higher [named storms (c) and typhoons (d)] per month in 2015 (black line) and the climatological means (blue line). The blue plus signs denote the maximum and minimum monthly historical records, and the red error bars show the climatological interquartile range for each month (in the case of no error bars, the upper and/or lower percentiles coincide with the median). (e), (f) The cumulative number of named storms (e) and super typhoons (f) per month in the WNP in 2015 (black line) and climatology (1971–2010) as box plots [interquartile range: box; median: red line; mean: blue asterisk; values in the top or bottom quartile: blue crosses; high (low) records in the 1945–2015 period: red diamonds (circles)]. [Sources: 1945–2014 JTWC best-track dataset, 2015 JTWC preliminary operational track data for (a), (c), (d), (e), and (f); 1951–2015 RSMC-Tokyo, JMA best-track dataset for panel (b).]

season had 29 TCs form in the basin, with two additional TCs (Halola and Kilo) that formed in the central North Pacific (CNP) then crossed into the WNP. This total of 31 storms active in the basin is above the median of the climatological distribution (the climatological median is 28.5, the 75th percentile is 33). Of these, 28 TCs reached tropical storm intensity or higher (the climatological median is 26, the 75th percentile is 29.5) and 27 of them were named (only one, 12W, was not formally named). There were 3 tropical depressions (TDs; slightly below the climatological median of 3.5), 7 tropical storms (below the 25th percentile of 8), 21 typhoons (above the 75th percentile of 20), 8 of which became super typhoons (winds ≥ 137 kt; 71 m s^{-1}; in the top 5th percentile, the 75th percentile is 5). In Fig. 4.28a, the number of tropical storms, typhoons, and super typhoons per year is shown for the period 1945–2015. The number of super typhoons is one of the measures for the intensity of the 2015 season that was well above normal. A high number of super typhoons is a typical feature of El Niño events (Camargo and Sobel 2005). The percentage of typhoons that reached super typhoon status in 2015 (38%) was in the top 10%. Climatologically, only 23% of typhoons reach super typhoon intensity each season.

The JMA total for 2015 was 27 TCs (above JMA's climatological median of 26), including Hurricanes/Typhoons Halola and Kilo. Tropical Storms 12W and Vamco were only considered to be tropical depressions by JMA, and TDs are not included in the JMA database. Of those 27, nine were greater than tropical storm strength (equal to the 25th percentile for JMA), and 18 were typhoons (top quartile for JMA). The number of TCs (1951–76), or tropical storms, severe tropical storms, and typhoons (1977–2015) according to the JMA are shown in Fig. 4.28b.[1]

[1] It is well known that there are systematic differences between the JMA and the JTWC and the datasets, which have been extensively documented in the literature (e.g., Wu et al. 2006; Nakazawa and Hoshino 2009; Song et al. 2010; Ying et al. 2011; Yu et al. 2012; Knapp et al. 2013; Schreck et al. 2014).

The number of named storms and typhoons per month in 2015, compared with the climatological distribution, is shown in Figs. 4.28c,d. Super Typhoon Maysak was one of the strongest March storms in the historical record, reaching the same record intensity of Super Typhoon Mitag (February–March 2002) for that month. In May, two super typhoons formed in the WNP, Noul and Dolphin, while only Tropical Storm Kujira was active in June.[2] July was an active month with six storms present in the WNP, including Super Typhoons Nangka and Soudelor. On 9 July, three storms (Chan-hom, Nangka, and Linfa) were active simultaneously on the WNP, a rare event for July. September and October had five active storms each, including Super Typhoons Champi and Lando in October.

Considering the number of TCs and named storms, the 2015 typhoon season had an active, early season (January–June), with 8 TCs (top quartile), an average peak season (July–October) with 20 TCs (median is 19), and a quiet late season with 3 TCs (bottom quartile), as can be seen in the cumulative number of named of storms per month in 2015 and the climatological distribution (Fig. 4.28e). The occurrence of a high number of super typhoons, a typical feature of El Niño years, was clear in 2015, with 8 super typhoons, 3 of which formed in the early season and 5 during the peak season. The occurrence of three super typhoons in the early season is quite unusual, having only occurred twice previously in the historical record, 2002 and 2004; these were also El Niño years. The cumulative number of super typhoons in 2015 compared with the climatological baseline is shown in Fig. 4.28f. Previously, only one super typhoon had formed in March, in 1961 (while STY Mitag reached is lifetime maximum intensity in March, it formed in February). The 2015 season is the first time in the historical record that two super typhoons formed in May; the previous historical maximum for that month was one. An active July, with two tropical storms, two typhoons, and two super typhoons was followed by a relatively quiet August. The two typhoons (one of them a super typhoon) in August is in the bottom quartile for that month. Two more super typhoons occurred in October, in the top 10% for that month.

Typical of El Niño years, the total ACE in 2015 was high (Camargo and Sobel 2005), reaching the third highest value in the historical record, just below the values in 2004 and 1997, both El Niño years (Fig. 4.29a). The bulk of the seasonal ACE occurred during July and August (Fig. 4.29b), contributing to 21% and 24% of the total ACE, respectively. The ACE for May was the largest in the historical record for that month. Other high monthly values of ACE reached the third (February and August), fourth (July), and fifth (March) highest values in the historical record for those months. In contrast, the June ACE was in the bottom quartile. Eight TCs in 2015 were in the top 10% of the ACE per storm, together contributing a total of 58.5% of the total ACE for the season. With the exception of Typhoon Goni, the other seven TCs with highest ACE in 2015 reached super typhoon status. The top ACE values in 2015 are from TCs Noul, Champ, Dolphin, Maysak, Soudelor, Atsani, Goni, and Nangka, in that order. Additionally, JTWC tracked the peak wind speed for Goni at 115 kt (59 m s^{-1}), but it is noteworthy that 5.5 of its 11 days had winds ≥ 100 kts. The ACEs of each of the top three named storms (Noul, Champ, Dolphin) reached the top 5% and contributed 25.7% of the total ACE in the season. Other storms in the top quartile of ACE per storm in 2015 were Koppu, Dujuan, Halola, In-fa, Kilo, and Chan-hom.

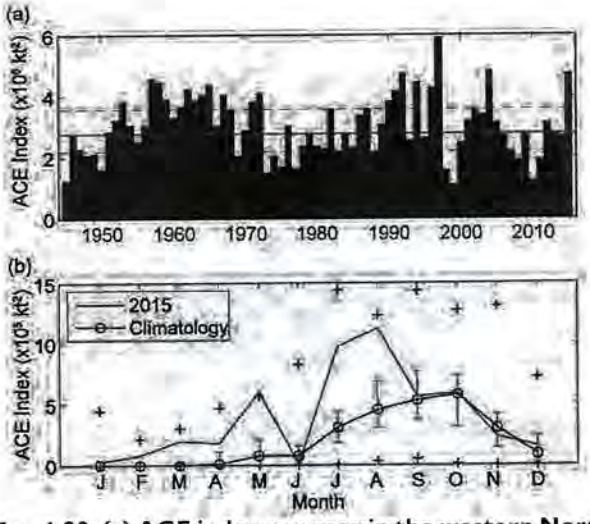

Fig. 4.29. (a) ACE index per year in the western North Pacific for 1945–2015. The solid green line indicates the median for the climatology years 1971–2010, and the dashed lines show the climatological 25th and 75th percentiles. (b) ACE index per month in 2015 (red line) and the median during 1971–2010 (blue line), where the green error bars indicate the 25th and 75th percentiles. In case of no error bars, the upper and/or lower percentiles coincide with the median. The blue "+" signs denote the maximum and minimum values during the period 1945–2014. (Source: 1945–2014 JTWC best-track dataset, 2015 JTWC preliminary operational track data.)

[2] Here, if a storm forms in the two last days of a month, it is counted for the following month if it lasts more than two days in the next month. This was the case in 2015 of typhoons Chan-hom (formed 29 June) and Mujigae (formed 30 September).

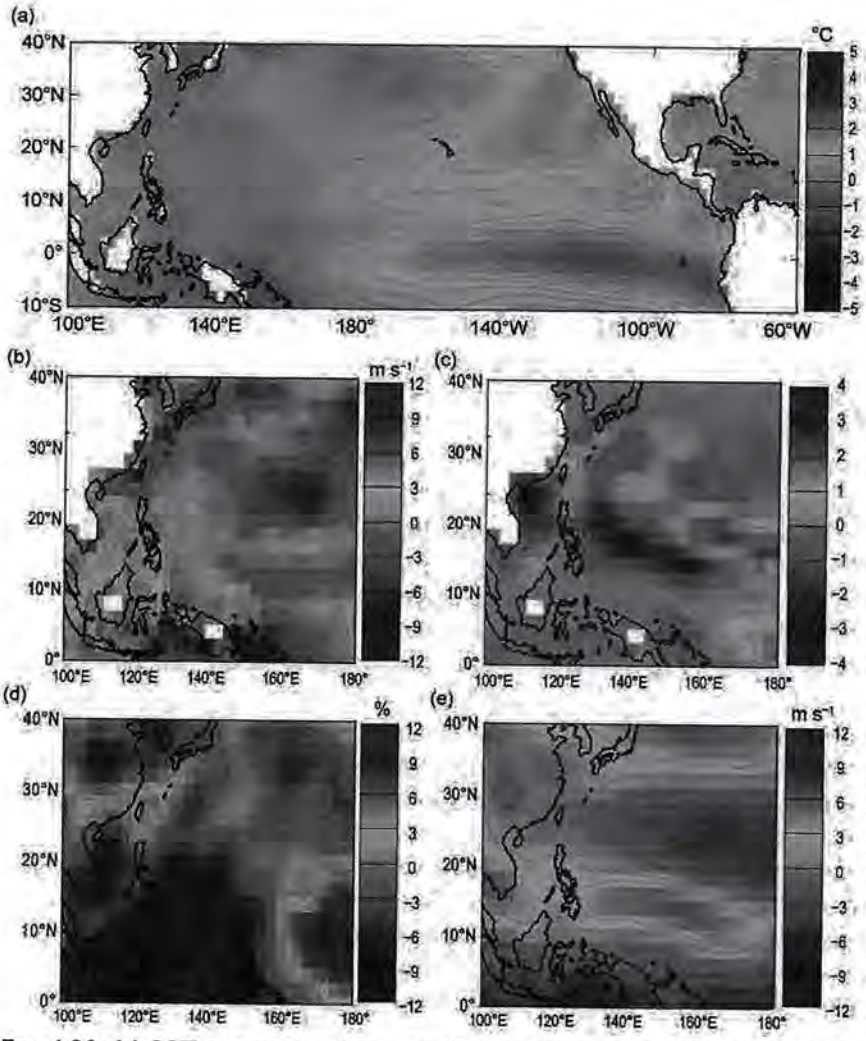

FIG. 4.30. (a) SST anomalies, (b) potential intensity anomalies, (c) relative humidity 600-hPa anomalies, (d) genesis potential index anomalies in JASO 2015, and (e) zonal winds in Jul–Oct 2015 (positive contours are shown in solid lines, negative contours in dash dotted lines and the zero contour in a dotted line). [Source: atmospheric variables: NCEP–NCAR reanalysis data (Kalnay et al. 1996); sea surface temperature (Smith et al. 2008).]

There were 174.75 days with TCs in 2015, near the 75th percentile (176.75 days), and 148.75 days with storms that reached tropical storm or higher, in the top 5% (median 111.75 days). From those active days, 90.75 days had typhoons, the third highest value in the historical record, less than only 1997 and 2004. There were 36.75 days with intense typhoons (Categories 3–5), in the top 10% (median 20 days). In 2015, the percentage of days with typhoons and intense typhoons were 51.9% and 21.0%, in the top 1% and 10%, respectively (median 37.9% and 12.2%, respectively). The median lifetime of named storms in 2015 was 8.75 days, slightly above the median of 8 days. The two longest-living storms were Kilo and Halola, which lasted 22 days (20 August to 11 September) and 17.75 days (10–26 July), while crossing both the central and western North Pacific basins. The longest-living storm that formed in the WNP was Super Typhoon Nangka, which lasted a total of 15.75 days from 3–19 July.

The mean genesis location for storms with genesis in the WNP in 2015 (13.4°N, 147.3°E) was slightly eastward from the climatological mean of WNP storms (13.2°N, 141.6°E, with standard deviations of 1.9° and 5.6°). The mean track position (16.7°N, 144.5°E) was also southeastward relative to the WNP climatological mean (17.3°N, 136.6°E, with standard deviations of 1.4° and 4.7°). Although a southeastward shift is typical of El Niño years (e.g., Chia and Ropelewski 2002; Camargo et al. 2007), this 2015 shift was mostly eastward, with almost no change (mean first position) or a small southward shift (mean track) in the meridional direction.

Figure 4.30 shows the environmental conditions associated with the typhoon activity in 2015. The warm SST anomalies during July–October (JASO; Fig. 4.30a) were large in the eastern and central Pacific, but small in the WNP. These large SST anomalies led to high values of potential intensity (Emanuel 1988 and 1995; Fig. 4.30b) and 600-hPa relative humidity (Fig. 4.30c) anomalies on the eastern and central Pacific in two bands, the first in the equatorial region, the second near Hawaii. The genesis potential index (GPI; Emanuel and Nolan 2004; Camargo et al. 2007) had positive anomalies on the eastern part of the basin and negative on the western side (Fig. 4.30d), typical of El Niño years. The maximum extent of the monsoon reached the date line, as documented via the zonal winds depicted in Fig. 4.30e; this monsoonal extent helps explain the eastward shift of the location of cyclogenesis in the basin for the season.

(iii) TC impacts

There were 18 storms that made landfall in 2015,[3] slightly above the 1951–2010 climatological median (17). Of these, three systems made landfall as a TD (median is three), seven storms made landfall as tropical storms (median is six), two struck as Category 1–2 typhoons (median is five). Five storms made landfall as intense typhoons, among the top 10% of the 1951–2010 climatological distribution (the median is two): Dujuan, Goni, Koppu, Melor, and Mujigae.

Many storms led to social and economic impacts in 2015. Typhoon Maysak made landfall in both Chuuk and Yap States of the Federated States of Micronesia in March and was responsible for four deaths and led to significant damage to homes and crops in both states. Typhoon Koppu (known as Lando in the Philippines) caused at least 58 deaths and flooding in the northern Philippines, as well as heavy agricultural and economical damage across the country. The double hit of Typhoon Melor and a tropical depression in December in the Philippines led to floods and at least 45 deaths. The storms with the largest economic impacts in 2015 were Typhoons Soudelor (3.2 billion U.S. dollars) and Chan-hom (1.5 billion U.S. dollars). Soudelor caused severe impacts in the Commonwealth of the Northern Mariana Islands, Taiwan, and eastern China (at least 38 deaths), as well as some lesser impacts in Japan, the Republic of Korea, and the Philippines. Chan-hom also affected many countries in the WNP basin, particularly Japan (Okinawa), Taiwan, China, the Republic of Korea (Jeju Island), and North Korea.

5) North Indian Ocean—M. C. Kruk

The north Indian Ocean (NIO) TC season typically extends from April to December, with two peaks in activity: during May–June and again in November, when the monsoon trough is positioned over tropical waters in the basin. TCs in the NIO basin normally develop over the Arabian Sea and Bay of Bengal between 8° and 15°N. These systems are usually short-lived and relatively weak and often quickly move into the Indian subcontinent.

According to the JTWC, the 2015 TC season produced five tropical storms, two of which were major cyclones (Fig. 4.31a). The 1981–2010 IBTrACS seasonal averages for the basin are 3.9 tropical storms, 1.4 cyclones, and 0.6 major cyclones. The season produced its highest ACE index since 1972 with a value of 30.4×10^4 kt^2, well above the 1981–2010 mean of 12.5×10^4 kt^2 (Fig. 4.31b). Typically, there is enhanced TC activity, especially in the Bay of Bengal, during the cool phase of ENSO (Singh et al. 2000); however, most of this season was characterized by a strong developing El Niño. Four of the five storms developed in the Arabian Sea, and only tropical storm Two (29–30 July) developed in the Bay of Bengal.

There were two noteworthy storms during the season: Cyclones Chapala and Megh. Chapala (28 October–4 November) formed in the Arabian Sea and became a "severe cyclonic storm" (wind ≥ 96 kts) on 29 October with maximum sustained winds near 114 kt (58 m s^{-1}) and a minimum central pressure of 940 hPa. What made these storms unique was how they tracked westward over the island of Socotra and into the Gulf of Aden—a very unusual track compared to historical records. This resulted in extreme damage across Socotra and the country of Yemen, which rarely experiences tropical cyclone landfalls, much less the tremendous rains associated with them. In fact, these were not only the first tropical cyclones to strike Socotra since 1922, but most interesting was that they did so during the same week. Rainfall data are spotty for the region, but satellite estimates suggest 610 mm of rainfall along the Yemeni coastline, which is 700% of the annual average for the region. Eight people died in Yemen, most by drowning, and several hundred homes and businesses were damaged by flooding. A storm surge of nearly 10 m was observed in the coastal town of Al Mukalla, destroying the city's seafront and inundating many coastal structures with saltwater.

The second major storm of the season was Very Severe Tropical Cyclone Megh, which occurred from 5 to 10 November in the Arabian Sea, about a week after Cyclone Chapala. The track of Megh was similar to that of Chapala, moving over the island of Socotra and into the Gulf of Aden. Maximum sustained wind speeds reached 95 kt (48 m s^{-1}) with a minimum central pressure of 964 hPa. Megh made landfall in Socotra as a Category 3 equivalent storm, causing extensive devastation, resulting in nearly 20 deaths. Additionally, upwards of 3000 homes were either completely destroyed or damaged by the cyclone, which also caused havoc with local fishing operations.

[3] Landfall is defined when the storm track is over land and the previous location was over ocean. In order not to miss landfall over small islands, first the tracks were interpolated from 6-hourly to 15-minute intervals, before determining if the storm track was over land or ocean using a high-resolution land mask.

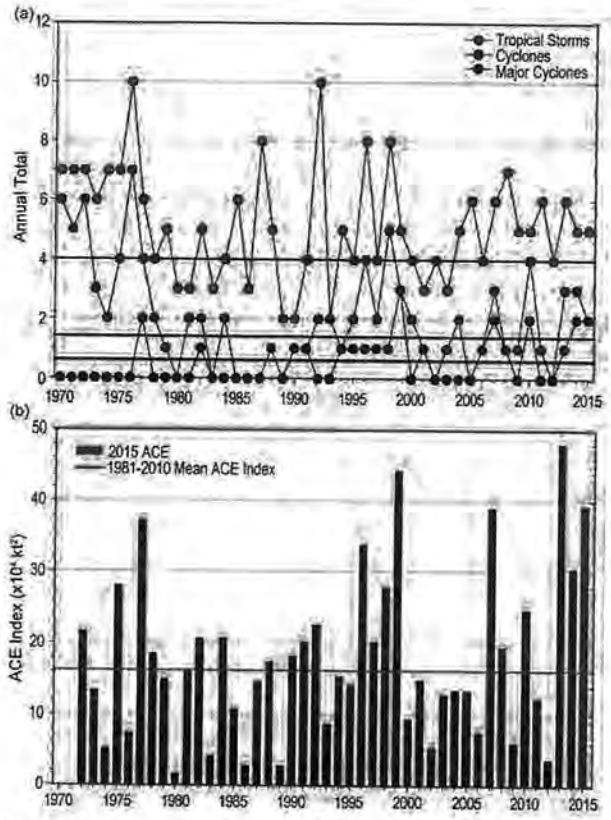

Fig. 4.31. Annual TC statistics for the NIO for 1970–2015: (a) number of tropical storms, cyclones, and major cyclones and (b) the estimated annual ACE index (in kt² × 10⁴) for all TCs during which they were at least tropical storm strength or greater intensity (Bell et al. 2000). The 1981–2000 means (green lines) are included in both (a) and (b).

6) South Indian Ocean—M. C. Kruk and C. Schreck

The south Indian Ocean (SIO) basin extends south of the equator from the African coastline to 90°E, with most cyclones developing south of 10°S. The SIO TC season extends from July to June encompassing equal portions of two calendar years (the 2015 season is comprised of storms from July to December 2014 and from January to June 2015). Peak activity typically occurs during December–April when the ITCZ is located in the Southern Hemisphere and migrating toward the equator. Historically, the vast majority of landfalling cyclones in the SIO affect Madagascar, Mozambique, and the Mascarene Islands, including Mauritius and Réunion Island. The RSMC on La Réunion serves as the official monitoring agency for TC activity within the basin.

The 2014/15 SIO storm season was much above average, with 14 tropical storms, of which 6 were cyclones and 4 were major cyclones (Fig. 4.32a). The 1981–2010 IBTrACS seasonal median averages are eight tropical storms, four cyclones, and one major cyclone. The active season is also reflected in the 2014/15 ACE index of 114.7 × 10^4 kt², which was above the 1981–2010 average of 91.5 × 10^4 kt² (Fig. 4.32b). This is the second consecutive year with above-average ACE values for the SIO. As a result of warmer-than-normal SSTs, coupled with generally below-average wind shear (Fig. 4.32), the overall season was above average. Figure 4.33a indicates that the seasonally averaged SST anomalies were above normal, stretching between 10° and 30°S across the width of the southern Indian Ocean. Moreover, Fig. 4.33c demonstrates that deep-layer vertical wind shear was also anomalously low across the same latitude belt, on the order of 1–3 m s^{-1}, below normal for the season. It appears likely that the combination of warm waters and a favorable low-shear environment helped to sustain not only the number of storms this season but also their above-average intensities, as reflected by the ACE index.

During the 2014/15 season, the strongest storm was Cyclone Eunice (27 January–2 February), which reached Category 5 equivalency with peak maximum

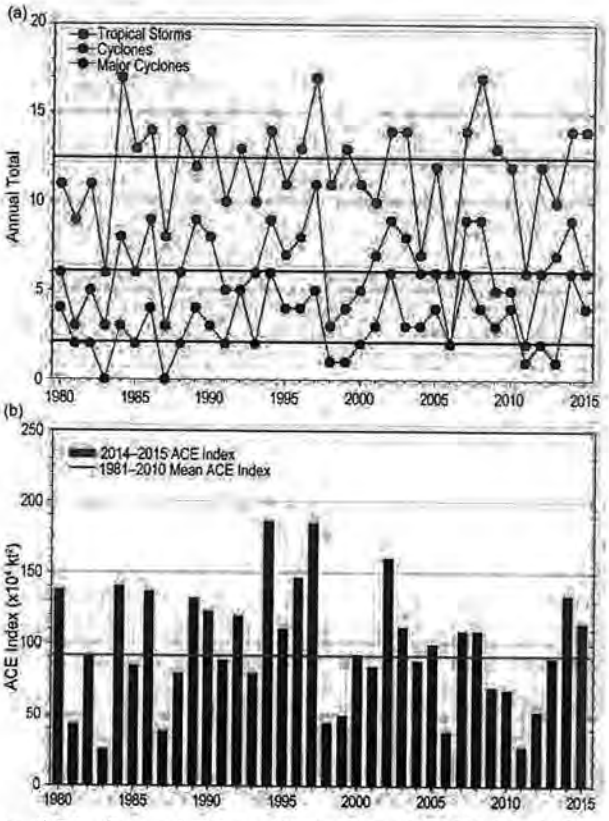

Fig. 4.32. Annual TC statistics for the SIO for 1980–2015: (a) number of tropical storms, cyclones, and major cyclones and (b) the estimated annual ACE index (in kt² × 10⁴) for all TCs during which they were at least tropical storm strength or greater intensity (Bell et al. 2000). The 1981–2000 means (green lines) are included in both (a) and (b). Note that ACE index is estimated due to lack of consistent 6-h sustained winds for each storm.

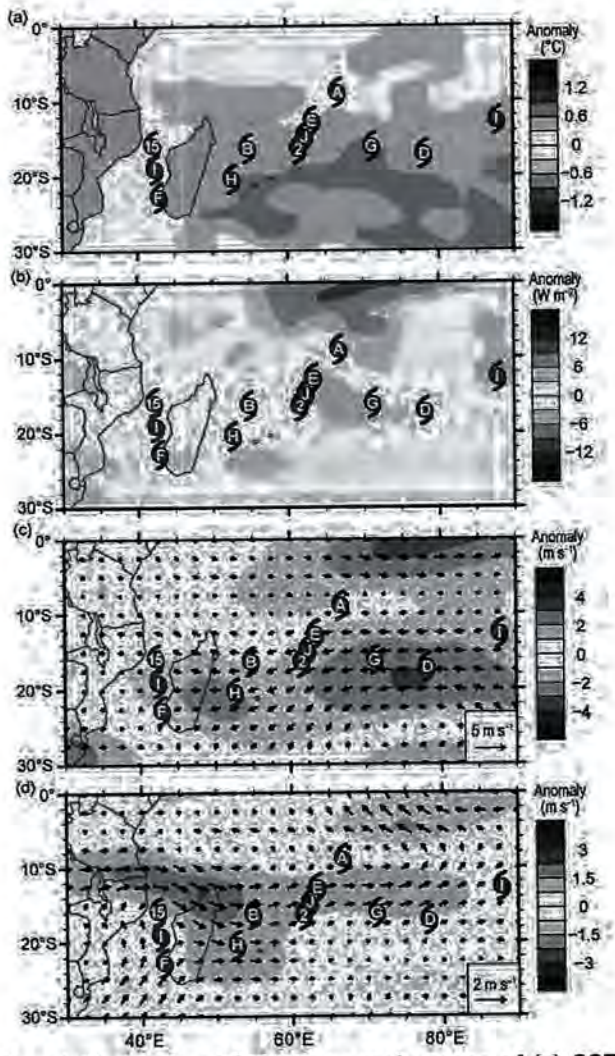

FIG. 4.33. Jul–Jun 2014/15 anomaly maps of (a) SST (°C, Banzon and Reynolds 2013), (b) OLR (W m^{-2}, Lee 2014), (c) 200–850-hPa vertical wind shear (m s^{-1}) vector (arrows) and scalar (shading) anomalies, and (d) 850-hPa winds (m s^{-1} arrows) and zonal wind (shading) anomalies. Anomalies are relative to the annual cycle from 1981–2010, except for SST which is relative to 1982–2010 due to data availability. Letter symbols denote where each SIO TC attained tropical storm intensity. Wind data obtained from NCEP–DOE Reanalysis 2 (Kanamitsu et al. 2002).

sustained winds of 139 kt (70 m s^{-1}) and an estimated minimum central pressure of 900 hPa. The storm formed in the middle of the south Indian Ocean and remained there throughout its lifecycle, generally moving southeast before weakening over cooler waters.

Severe Tropical Storm Chedza (14–22 January 2015) was the deadliest storm of the season. Chedza formed off the southeast coast of Africa and intensified over the Mozambique Channel where it attained maximum sustained winds of 57 kt (29 m s^{-1}) and a minimum central pressure of 975 hPa. On 16 January, Chedza made landfall in western Madagascar, resulting in extensive flooding following weeks of extreme wet weather across the island. This resulted in widespread mudslides across the region, damaging roads and homes. Nearly 4400 homes were destroyed by the floods and unfortunately the storm resulted in 80 fatalities, most of which were from landslides. The flooding rains inundated over 9000 ha (24 000 acres) of rice fields and displaced 1200 cattle.

In early February, Severe Tropical Storm Fundi developed over the southwestern shores of Madagascar, and by 6 February, the storm had reached maximum sustained winds of 55 kt (28 m s^{-1}) and a minimum central pressure of 985 hPa. Fundi brought 109 mm of rainfall to the southwestern Madagascar town of Tulear and as far inland as Toliara where five people died due to floods. While the storm never made landfall, the damage to water and sewer infrastructure caused by weeks of antecedent heavy rains, including those from Chedza, hindered ongoing relief efforts and increased the number of personal health and hygiene risks.

The final notable storm of the season was Moderate Tropical Storm Haliba (7–10 March), which was a tropical disturbance that formed east of Madagascar and tracked southeast near Réunion Island. During its development stages, Haliba produced heavy rains across eastern Madagascar, affecting over 95 000 people and killing 26. The storm intensified on 8 March with maximum sustained winds of 43 kt (22 m s^{-1}) and a minimum central pressure of 993 hPa. As it moved southeast, exceptional rain was recorded at Ganga Talao, with 135.6 mm falling in just 24 hours. The storm went on to produce 796 mm of rainfall over northern Réunion Island, and while that is a large amount of precipitation, it is not a particularly unusual amount for a tropical system at this latitude.

7) Australian basin—B. C. Trewin

(i) Seasonal activity

The 2014/15 TC season was near normal in the broader Australian basin (areas south of the equator and between 90° and 160°E,[4] which includes Australian, Papua New Guinea, and Indonesian areas of responsibility), with a slightly below-normal number of cyclones but an above-normal number of severe cyclones. The season produced 9 TCs, near the 1983/84–2010/11 average[5] of 10.8 and consistent with neutral to warm ENSO conditions. The 1981–2010

[4] The Australian Bureau of Meteorology's warning area overlaps both the southern Indian Ocean and southwest Pacific.

[5] Averages are taken from 1983/84 onwards as that is the start of consistent satellite coverage of the region.

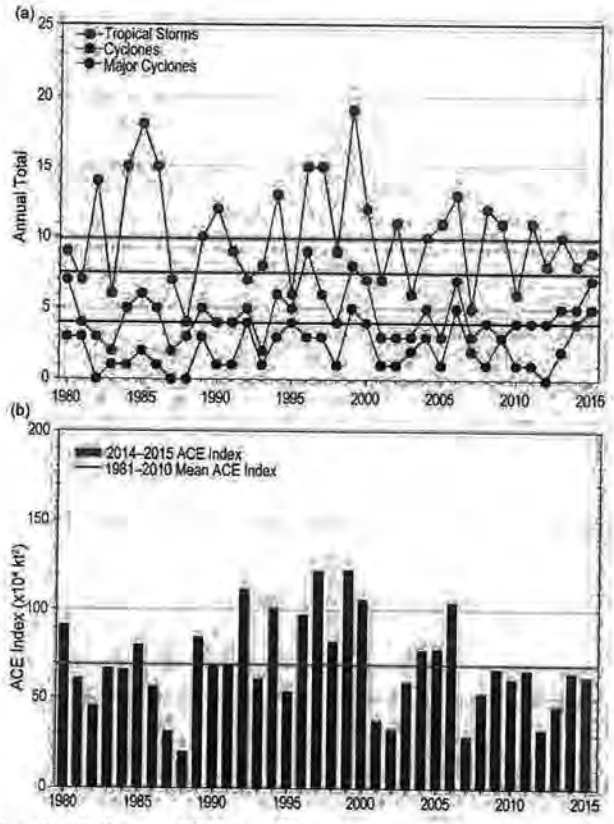

FIG. 4.34. Annual TC statistics for the Australian basin for 1980–2015: (a) number of tropical storms, cyclones, and major cyclones and (b) the estimated annual ACE index (in $kt^2 \times 10^4$) for all TCs during which they were at least tropical storm strength or greater intensity (Bell et al. 2000). The 1981–2000 means (green lines) are included in both (a) and (b). Note that ACE index is estimated due to lack of consistent 6-h sustained winds for each storm.

IBTrACS seasonal averages for the basin are 9.9 NSs, 7.5 TCs, and 4.0 major TCs, which compares with the 2014/15 counts of 9, 7, and 5 respectively.

There were four TCs in the eastern sector[6] of the Australian region during 2014/15, two in the northern sector, and five in the western sector.[7] Four systems made landfall in Australia as tropical cyclones, one in Western Australia, two in the Northern Territory (one after an initial landfall in Queensland), and a fourth in Queensland (Fig. 4.34). Fig. 4.34 (as noted in section 4e1) is standardized on the Saffir–Simpson scale.

[6] The western sector covers areas between 90° and 125°E. The eastern sector covers areas east of the eastern Australian coast to 160°E, as well as the eastern half of the Gulf of Carpentaria. The northern sector covers areas from 125°E east to the western half of the Gulf of Carpentaria.

[7] Lam and Nathan each passed through both the eastern and northern sectors.

(ii) Landfalling and other significant TCs

The most intense cyclone of the season was Marcia. TC Marcia formed in the monsoon trough to the northeast of Cairns on 15 February and moved slowly east, reaching tropical cyclone intensity on 18 February. It then intensified rapidly on 19 February, intensifying from Category 1 to Category 5 on the Australian scale (see www.bom.gov.au/cyclone/about/intensity.shtml for details) in the space of 15 hours on 19 February, with maximum 10-minute sustained winds of 110 kt (57 m s^{-1}), as it moved southwest towards the central Queensland coast. Marcia made landfall at near peak intensity in Shoalwater Bay at 2200 hours UTC on 19 February (0800 20 February local time), weakening rapidly as it tracked southward over land and falling below tropical cyclone intensity by 1500 hours UTC on 20 February near Monto. The remnant tropical low moved back out over water off southeast Queensland on 21 February and drifted in the Coral Sea for several days, but did not regain cyclone intensity.

Marcia caused significant wind damage near the landfall point, especially in and around the towns of Yeppoon and Byfield, and less intense but more widespread damage in the major regional centre of Rockhampton, where it was the most significant cyclone impact since at least 1949. Some flooding also occurred in regions south of Rockhampton. Marcia is the southernmost known Category 5 landfall on the east coast of Australia.

Cyclone Lam formed in the monsoon trough south of Papua New Guinea on 12 February. It moved westward as a tropical low, crossing Cape York Peninsula, and then intensified over the northern Gulf of Carpentaria, where it reached cyclone intensity on 16 February. The system intensified steadily as it passed near the Wessel Islands, then turned southwest and reached Category 4 intensity west of Elcho Island early on 19 February, with maximum 10-minute sustained winds of 100 kt (51 m s^{-1}). Lam crossed the coast between Milingimbi and Elcho Island at peak intensity later that day (early on 20 February local time). Lam caused significant wind damage to a number of Aboriginal communities along eastern parts of the northern Arnhem Land coast and nearby islands, with Ramingining on the mainland coast and Galiwin'ku on Elcho Island the most severely impacted. This was the first known instance of two tropical cyclones of Category 4 or greater intensity making landfall in Australia on the same day.

Cyclone Olwyn formed as a tropical low approximately 900 km north of Exmouth on 8 March, moving southward and slowly strengthening. It reached

tropical cyclone intensity at 0600 hours UTC on 11 March, and continued to intensify as it approached the coast at North West Cape. It reached its peak intensity of Category 3, with 10-minute sustained winds of 75 kt (39 m s^{-1}), while it was located near North West Cape, just west of Exmouth, at 1800 hours UTC on 12 March. Olwyn then moved southward along the west coast with only minimal weakening, passing just to the west of Carnarvon at 0600 hours UTC on 13 March and crossing the coast in the Shark Bay area a few hours later. Reported wind gusts included 97 kt (50 m s^{-1}) at Learmonth and 79 kt (41 m s^{-1}) at Carnarvon. It was the most significant cyclone impact in the Carnarvon area for many years, with major crop losses (including the near-total loss of the banana crop), substantial wind damage to buildings in the town, and power and water outages that lasted for several days. Damage in Exmouth, where cyclones are a more common occurrence, was much less severe.

The fourth landfalling cyclone of the season was Nathan. Nathan formed on 10 March in the Coral Sea, south of the eastern tip of Papua New Guinea. It made an initial approach towards the east coast of Cape York Peninsula as a Category 1 system on 13 March before turning east again but then turned toward the coast again on 18 March and intensified, reaching its peak intensity of Category 4 on 19 March with maximum 10-minute sustained winds of 90 kt (46 m s^{-1}). Nathan made landfall at near peak intensity near Cape Melville around 1800 hours UTC on 19 March and weakened to a tropical low as it crossed Cape York Peninsula. It reintensified as it reached the Gulf of Carpentaria, making a second landfall as a Category 2 system near Nhulunbuy on 22 March. Nathan continued to track along the north coast before turning southwest and weakening. Minor to moderate damage was reported, principally to communities in northeast Arnhem Land and Elcho Island, and on Lizard Island off the Cape York Peninsula coast.

Three other cyclones reached Category 4 intensity during the season, all in the Indian Ocean: Kate in December, Ikola in April, and Quang in late April and early May. Neither Kate nor Ikola approached the mainland coast, although Kate passed near the Cocos (Keeling) Islands on 25 December with some minor flooding reported. Quang weakened as it neared the coast, causing a brief period of storm-force winds and associated minor damage in the Exmouth area before weakening to a tropical low at landfall on 1 May.

A noteworthy out-of-season cyclone was Raquel (a twin of Typhoon Chan-hom in the western North Pacific), which reached Category 1 intensity briefly from 1800 hours UTC on 30 June[8] in the western South Pacific northeast of the Solomon Islands. It is the first instance in the satellite era of a July tropical cyclone in the Australian sector of the South Pacific, and the first instance since 1972 in the Southern Hemisphere winter months (June, July, or August).

8) Southwest Pacific basin—P. R. Pearce, A. M. Lorrey, and H. J. Diamond

(i) Seasonal activity

The 2014/15 TC season in the southwest Pacific began in late November. The first storm developed as a tropical depression near Wallis and Futuna, and the season concluded very late with TC Raquel affecting the Solomon Islands in late June-early July. Storm-track data for November 2014–July 2015 was gathered by the Fiji Meteorological Service, Australian Bureau of Meteorology, and New Zealand MetService, Ltd. The southwest Pacific basin as defined by Diamond et al. (2012) (135°E–120°W) had nine tropical cyclones, including five severe tropical cyclones (based on the Australian TC intensity scale). As noted in section 4e1, Fig. 4.35 shows the standardized TC distribution based on the basin spanning the area from 160°E–120°W to avoid overlaps with the Australian basin that could result in double counting of storms. However, it is important to use the above definition of the southwest Pacific basin as that is how annual TC outlooks are produced and disseminated.

The 1981–2010 South Pacific Enhanced Archive of Tropical Cyclones (SPEArTC) indicates a seasonal average of 10.4 named tropical cyclones and 4.3 major tropical cyclones. The ratio of severe TCs relative to the total number of named TCs in 2014/15 was 56%, up from 36% during the previous season. Severe Tropical Cyclones Pam, Lam, and Marcia caused considerable damage and loss of life across the basin. Severe TC Pam, which devastated Vanuatu in March, was the most intense TC in the basin since Zoe in 2002.

(ii) Landfalling and other significant TCs

The first named TC of the 2014/15 season was reported as a tropical disturbance on January 19 to the northeast of the island of Tahiti in French Polynesia. On 20 January, the disturbance was upgraded to a Category 1 storm and named TC Niko. Over the next two days the system gradually intensified further and

[8] By definition, the formal TC year in the Southern Hemisphere goes from July to June, and any storm forming in June would be considered to be in the previous TC season (in this case the 2014/15 season).

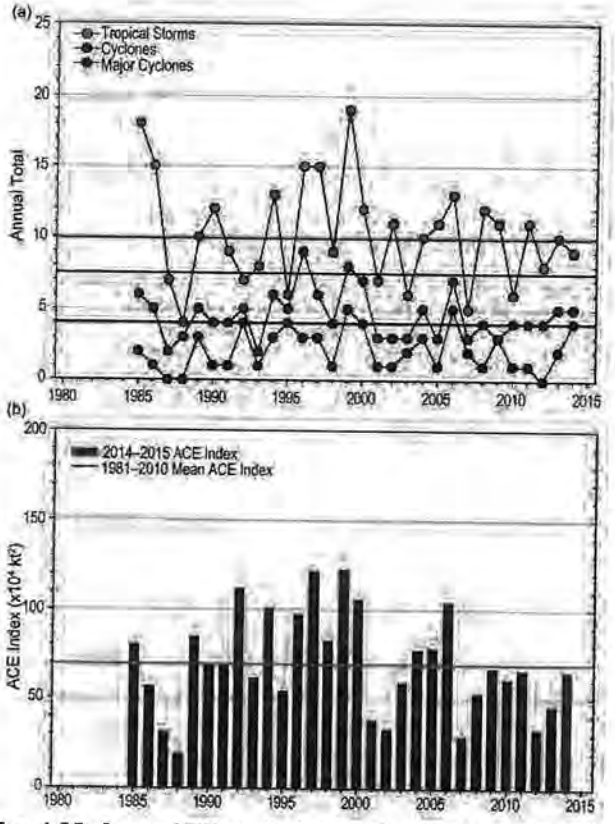

FIG. 4.35. Annual TC statistics for the southwest Pacific for 1980–2015: (a) number of tropical storms, cyclones, and major cyclones and (b) the estimated annual ACE index (in $kt^2 \times 10^4$) for all TCs during which they were at least tropical storm strength or greater intensity (Bell et al. 2000). The 1981–2000 means (green lines) are included in both (a) and (b). Note that ACE index is estimated due to lack of consistent 6-h sustained winds for each storm.

became a Category 2 TC early on 22 January. On 25 January, Niko completed its extratropical transition. Severe Tropical Cyclone Ola was named on 30 January as a Category 1 storm. Over the next two days, the system intensified and became a Category 3 TC early on 1 February. Ola's peak 10-minute sustained wind speed was 81 kt (42 m s^{-1}) and central pressure was 955 hPa at its lowest.

The third TC of the season was Severe Tropical Cyclone Lam, which began as a tropical disturbance over the Gulf of Carpentaria on 13 February. See section 4e7 for a detailed timeline of Lam's development, landfall, decay, and impacts. Lam was the strongest storm to strike Australia's Northern Territory since TC Monica in 2006. In its formative stages, Lam produced heavy rainfall and flooding in Far North Queensland, and later set daily precipitation records in the Northern Territory. Total damage in the Northern Territory reached at least 64 million U.S. dollars.

The first Category 5 TC of the season was Severe Tropical Cyclone Marcia, which developed in the Coral Sea on 16 February. See section 4e7 for a detailed timeline of Marcia's development, landfall, decay, and impacts. Due to explosive intensification, Marcia became a Category 5 TC early on 20 February, with a peak 10-minute sustained wind speed of 110 kt (57 m s^{-1}) and a minimum central pressure of 930 hPa. The storm wrought extensive damage in Queensland, with losses amounting to 590 million U.S. dollars.

The most significant TC of the 2014/15 season was Severe Tropical Cyclone Pam, which developed on 6 March east of the Solomon Islands. On 9 March, Pam was named as a Category 1 storm. Located in an area of favorable conditions, Pam gradually intensified into a powerful Category 5 severe TC by 12 March. Pam's 10-minute maximum sustained wind speed peaked at 135 kt (69 m s^{-1}), along with a minimum central pressure of 896 hPa, making Pam the most intense TC of the southwest Pacific basin since Zoe in 2002, and the third-most intense storm in the Southern Hemisphere, after Zoe in 2002 and Gafilo in 2004. In addition, Pam had the highest 10-minute sustained wind speed (135 kt; 69 m s^{-1}) recorded of any South Pacific TC, and it is tied with Orson in 1989 and Monica in 2006 for having the strongest winds of any cyclone in the Southern Hemisphere.

Early in Pam's history, a damaging storm surge was felt in Tuvalu, forcing a state of emergency declaration after 45% of the nation's residents were displaced. Torrential rainfall occurred in the southeast Solomon Islands, with trees and crops flattened. In the Santa Cruz Islands, a 24-hour rainfall total of 495 mm was recorded. The storm also struck the remote islands of Anuta and Tikopia on 12 March, causing extensive damage. Approximately 1500 homes were damaged or destroyed, and Tikopia lost 90% of its food crop and fruit trees. Several hours after being named a Category 5 TC on 12 March, the TC began to curve towards the south-southeast, passing by some islands in Vanuatu but making a direct hit on others. Pam caused catastrophic damage to Efate, the main island of Vanuatu where the capital, Port Vila, is located. The islands of Erromango and Tanna were also devastated.

Pam became the single worst natural disaster in the history of Vanuatu, crippling its infrastructure. An estimated 90% of the nation's buildings were impacted by the storm's effects, telecommunications were paralyzed, and water shortages occurred. Communications with many islands were completely

severed during the storm, and four days after the storm nearly 60% of the nation's inhabited islands remained cut off from the outside world. According to UNESCO, 268 million U.S. dollars was required for total recovery and rehabilitation of Vanuatu.

The storm's winds gradually slowed afterwards as Pam tracked west of the Tafea Islands. However, the Fiji Meteorological Service indicated that the TC's pressure dropped farther to 896 hPa on 14 March. As Pam travelled farther south, the storm's eye faded away and Pam's low-level circulation became displaced from its associated thunderstorms, indicating a rapid weakening phase. Later on 15 March, Pam entered a phase of extratropical transition and affected northeast New Zealand and the Chatham Islands with high winds, heavy rain, and rough seas. A state of emergency was declared in the Chatham Islands. At least 15 people lost their lives either directly or indirectly as a result of Pam, with many others injured.

Shortly after Pam was classified, its outer rainbands led to the formation of a tropical low east of Cape York Peninsula, Australia, on 9 March. The Category 1 TC Nathan was named later that day. It slowly executed a cyclonic loop over the next few days, moving across Arnhem Land, Northern Territory, and into Western Australia. See section 4e7 for a detailed timeline of Nathan's development, landfall, decay, and impacts. On 19 March, a tropical disturbance developed about 375 km to the southwest of Apia, Samoa. From 20 to 22 March, the resulting tropical depression produced heavy rain and strong winds over Fiji's Lau Islands. The system moved southward as it was classified as a tropical depression. Early on 22 March, Tropical Cyclone Reuben was named as a Category 1 storm, located about 220 km to the south of Nuku'alofa, Tonga. On 23 March, TC Reuben began extratropical transition.

Tropical Cyclone Solo developed within the monsoon trough on 9 April, about 465 km to the south of Honiara, Solomon Islands. Due to ideal conditions, the system rapidly developed as it moved southward and was named a Category 1 storm. Solo peaked with winds of 54 kt (28 m s^{-1}), making it a Category 2 storm. As Solo turned to the south-southeast from 11 to 12 April, it moved between mainland New Caledonia and the Loyalty Islands. Rainfall totals up to 222 mm were recorded in New Caledonia. Significant damage was reported there, with roads impassable in places and contaminated drinking water in the municipality of Pouébo. Finally, and as noted in section 4e7, Tropical Cyclone Raquel, the last storm of the 2014/15 season, developed as a tropical disturbance about 718 km to the northeast of Honiara, Solomon Islands, on 28 June. Over the next couple of days, the system moved westward into the Australian region, where it was named a TC. Raquel then moved eastward into the South Pacific basin, where it weakened into a tropical depression. On 4 July, the system moved south-westward and impacted the Solomon Islands with high wind gusts and heavy rain.

f. Tropical cyclone heat potential—G. J. Goni, J. A. Knaff, and I.-I. Lin

This section summarizes the previously described tropical cyclone (TC) basins from the standpoint of tropical cyclone heat potential (TCHP) by focusing on vertically integrated upper ocean temperature conditions during the season for each basin with respect to their average values. The TCHP (Goni and Trinanes 2003), defined as the excess heat content contained in the water column between the sea surface and the depth of the 26°C isotherm, has been linked to TC intensity changes (Shay et al. 2000; Goni and Trinanes 2003; Lin et al. 2014). The magnitude of the in situ TCHP was also identified as impacting the maximum potential intensity (MPI) through modulating near-eyewall SSTs (and heat fluxes) occurring when TC winds mechanically mix the underlying ocean (Mainelli et al. 2008; Lin et al. 2013). In general, fields of TCHP show high spatial and temporal variability associated mainly with oceanic mesoscale features, interannual variability (e.g., ENSO), or long-term decadal variability. This variability can be assessed using satellite altimetry observations (Goni et al. 1996; Lin et al. 2008; Goni and Knaff 2009; Pun et al. 2013) or using a combination of altimetry and hydrographic data (Domingues et al. 2015), and has been used to assess meridional heat transport and the overturning circulation in the Atlantic Ocean (Dong et al. 2015).

Globally, the number of tropical cyclones was 10% higher than the previous season; however, in the eastern North Pacific (ENP), the number increased significantly from an already high number in 2014. The 2014 and 2015 ENP hurricane seasons were the most active in recorded history. In the western North Pacific (WNP) basin, the 2015 number was similar to the long-term climatological average. Nevertheless, it is a ~40% increase as compared to the very low occurrence in 2014.

The two following factors best illustrate the overall global TCHP interannual variability within and among the basins: 1) the TCHP anomalies (departures from the 1993–2014 mean values) during the TC seasons in each hemisphere; and 2) differences in TCHP between the 2015 and 2014 seasons.

Most basins exhibited positive TCHP anomalies (Fig. 4.36), except for the WNP and the western portion of the South Pacific basin. The WNP basin experienced a significant reduction in TCHP of ~20%, which is typical of El Niño years (Zheng et al. 2015). The TCHP in the Gulf of Mexico exhibited large positive anomalies due to the intrusion of the Loop Current and a long residence time of Loop Current rings. Despite these positive anomalies, there were no hurricanes in the Gulf of Mexico (just one tropical storm—Bill).

In the ENP basin, the positive TCHP anomalies were consistent with strong El Niño conditions and a continued positive phase of the Pacific decadal oscillation. The combination of these two phenomena is manifest in positive SST anomalies in that region and extending to the date line. Consequently, the TCHP values in this region during the season were even higher than in previous years (Fig. 4.37). As in 2014, positive TCHP and SST anomalies contributed to elevated tropical cyclone activity, with 16 hurricanes in the ENP during 2015 (Fig. 4.36).

The WNP basin also usually exhibits anomalies related to ENSO variability (Lin et al. 2014; Zheng et al. 2015). From the 1990s to 2013, it experienced a long-term decadal surface and subsurface warming associated with prevalent La Niña–like conditions

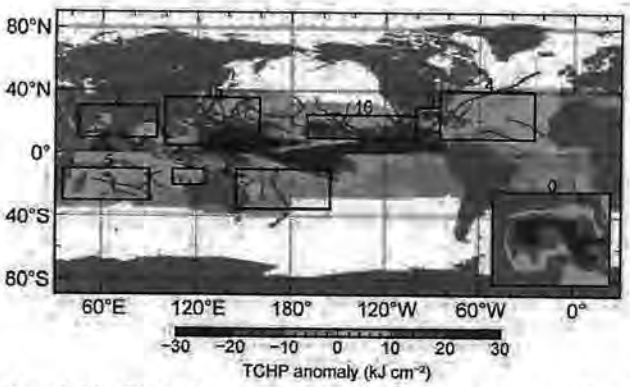

Fig. 4.36. Global anomalies of TCHP corresponding to 2015 computed as described in the text. The boxes indicate the seven regions where TCs occur, from left to right: Southwest Indian, North Indian, West Pacific, Southeast Indian, South Pacific, East Pacific, and North Atlantic (shown as Gulf of Mexico and tropical Atlantic separately). The green lines indicate the trajectories of all tropical cyclones reaching at least Category 1 status (1-min average wind ≥64 kts, 33 m s^{-1}) and above during Nov–Apr 2014/15 in the Southern Hemisphere and Jun–Nov 2015 in the Northern Hemisphere. The numbers above each box correspond to the number of Category 1 and above cyclones that travel within each box. The Gulf of Mexico conditions during Jun–Nov 2015 are shown in the inset in the lower right corner.

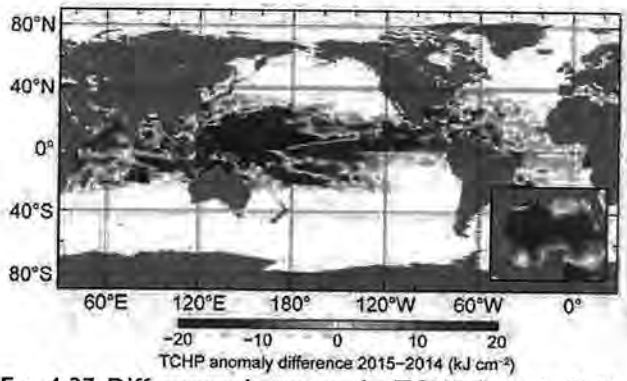

Fig. 4.37. Differences between the TCHP fields in 2015 and 2014 (kJ cm^{-2}).

(Pun et al. 2013; England et al. 2014). However, with the developing El Niño, the warming had stopped. With 2015 being the strongest El Niño event since 1997, the TCHP over the WNP MDR (4°–19°N, 122°E–180°) fell considerably, as characterized by evident negative anomalies (Figs. 4.36, 4.37; Zheng et al. 2015). With the relaxation of the trade winds during El Niño, warm water returning from the western to the eastern Pacific produced a positive anomaly in the ENP while the WNP exhibited a negative anomaly (Figs. 4.36, 4.37; Zheng et al. 2015).

For each basin, the differences in the TCHP values between the most recent cyclone season and the previous season (Fig. 4.37) indicate that the southwest Indian Ocean, the northwest Indian Ocean, and the western portion of the ENP continued to exhibit an increase in TCHP values. TC activity in terms of Category 4 and 5 storms was correspondingly elevated in these basins. The largest changes with respect to the previous seasons occurred in the ENP and WNP basins, with differences greater in magnitude than 20 kJ cm^{-2}. Compared to 2014, the percentage of Category 5 TCs in the WNP was quite low, with only two of 15 TCs (13%) attaining Category 5. In contrast, in 2014, though there were only eight TCs during the TC season, there were three Category 5 TCs or 38%. The evident reduction in TCHP over the WNP may have acted as a damper by increasing the ocean cooling effect on restraining TC intensification (Zheng et al. 2015).

The 2015 season was noteworthy for several reasons with respect to intensification of TCs, including Hurricane Patricia, the strongest Western Hemisphere hurricane ever recorded and Hurricane Joaquin, the most intense TC on record to strike the Bahamas. A summary of the ocean conditions for these and some other selected TCs are as follows.

- Typhoon Koppu (Lando; Fig. 4.38a) was a Category 4 TC that formed east of the Commonwealth

of the Northern Mariana Islands (CNMI) on 10 October. This storm reached its peak intensity on 17 October, with sustained winds of over 100 kt (51 m s^{-1}), and 1-minute sustained winds of approximately 130 kt (67 m s^{-1}). Though it eventually reached Category 4, Koppu did not intensify as rapidly as most intense TCs over the WNP (e.g., Haiyan in 2013; Lin et al. 2014). The negative TCHP may have slowed down its intensification rate (Zheng et al. 2015). However, since the TCHP over the WNP is among the highest globally in a climatological sense, even with reduced TCHP, it is possible for intense TCs to develop (Zheng et al. 2015). During El Niño years, TCs tend to form towards the southeast and closer to the date line. As a result, a TC can travel a longer distance across the ocean during intensification, through over reduced TCHP conditions (Zheng et al. 2015). Koppu made landfall in the north of the Philippines and quickly weakened due to its interaction with land. The cooling of SSTs caused by this typhoon was more evident west of 130°E, in both the surface and upper layer.

- Typhoon Chan-hom (Falcon; Fig. 4.38b) was characterized by its large size and long duration over the ocean. Chan-hom developed on 29 June from an atmospheric system that also developed TC Raquel in the southwest Pacific Ocean. Chan-hom's sustained winds reached values up to 89 kt. (46 m s^{-1}). This typhoon continuously intensified while traveling over warm waters with moderate (> 80 kJ cm^{-2}) TCHP values. A cooling of the surface (–2°C) and the upper layer (40 kJ cm^{-2}) under the track of this typhoon occurred when its intensity reached Category 1.
- Category 5 typhoon Soudelor (Hanna; Fig. 4.38c) was the second-strongest tropical cyclone to develop in the Northern Hemisphere in 2015. Though not as intense as Haiyan in 2013 (Lin et al. 2014), it was as intense as Vongfong in 2014 (Goni et al. 2015). This is in spite of the reduced TCHP in the WNP, associated with the 2015 El Niño year. This drop from the preexisting extremely high TCHP condition (Pun et al. 2013; Lin et al. 2014) was still able to provide favorable conditions for intensification. Soudelor intensified over a very favorable TCHP field of over 120 kJ cm^{-2}, which may have contributed to its ability to attain wind

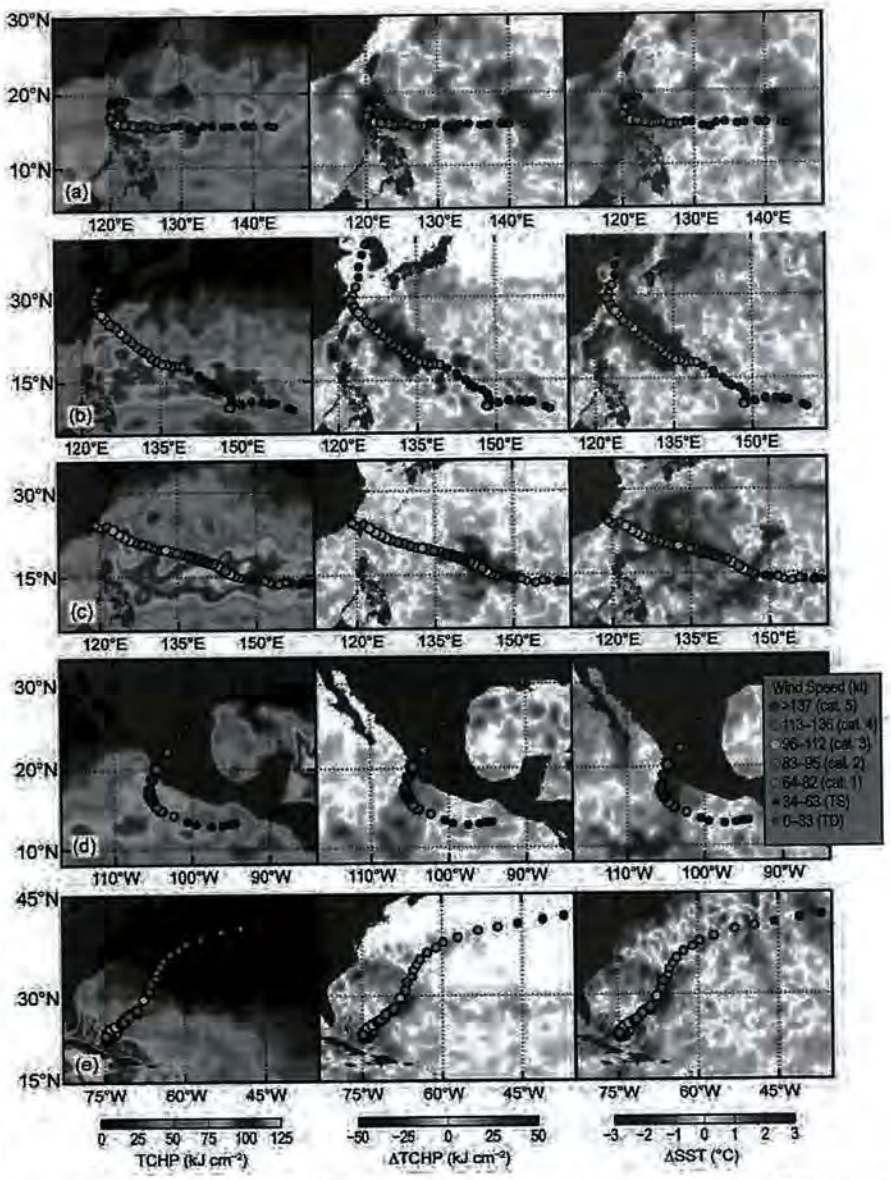

Fig. 4.38. (left) Oceanic TCHP and surface cooling given by the difference between post- and pre-storm values of (center) tropical cyclone heat potential and (right) sea surface temperature, for 2015 Tropical Cyclones (a) Koppu (b) Chan-hom, (c) Soudelor, (d) Patricia, and (e) Joaquin. The TCHP values correspond to two days before each storm reached its maximum intensity value.

speeds of 116 kt (60 m s^{-1}) on 3 August. Its high translation speed (~5–8 m s^{-1}) during intensification helped to reduce the ocean cooling during the TC life cycle, thus supplying more air–sea flux for intensification (Lin et al. 2009). This was the most intense storm to strike Saipan, CNMI, in the last 25 years. Cooling of the surface waters of over 5°C was observed under the full track of this typhoon, while cooling of the upper ocean layers (TCHP) was restricted to between 135° and 150°E.

- Hurricane Patricia (Fig. 4.38d) was the most intense tropical cyclone ever recorded in the Western Hemisphere in terms of barometric pressure, and the strongest ever recorded globally in terms of maximum sustained winds of 185 kt (95 m s^{-1}; Kimberlain et al. 2016). Patricia started as a tropical depression off the coast of Mexico on 20 October, and developed into a Category 5 storm within 66 hours. During its rapid intensification the TCHP values were higher than 80 kJ cm^{-2}.
- Hurricane Joaquin (Fig. 4.38e) was an intense TC that evolved near the Bahamas on 26 September and was one of the strongest storms to affect these islands. Joaquin underwent rapid intensification and became a Category 3 hurricane on 1 October, exhibiting maximum sustained winds of approximately 135 kt (69 m s^{-1}) on 3 October (Berg 2016). The upper ocean conditions were supportive of Atlantic tropical cyclone intensification (Maineli et al. 2008). This rapid intensification occurred during a short travel time over very high TCHP values (> 100 kJ cm^{-2}). The cooling of the ocean waters was evident both in the upper layer and at the surface.

g. *Atlantic warm pool*—C. Wang

The description and characteristics of the Atlantic warm pool (AWP), including its multidecadal variability, have been previously described (e.g., Wang 2015). Figure 4.39 shows the extension of the AWP time series through 2015 varying on different time scales.

While the AWP in 2015 showed similarities to 2014, there were some key differences. As in 2014, the AWP in 2015 was larger than its climatological mean each month, with the largest AWP occurring in September (Fig. 4.40a). However, the AWP in 2015 started in February and lasted through December, longer than its normal period of May to October, and had an anomalously larger value in November. After starting in February, the AWP appeared in the Gulf of Mexico in June (Fig. 4.40b). By July and August, the AWP was well developed in the Gulf of Mexico and Caribbean Sea and reached eastward into the western

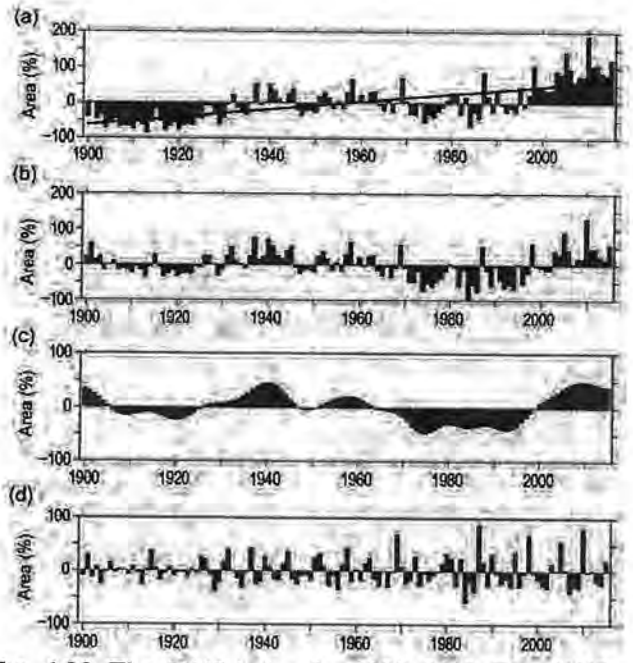

FIG. 4.39. The AWP index for 1900–2015. The AWP area index (%) is calculated as the anomalies of the area of SST warmer than 28.5°C divided by the climatological Jun–Nov AWP area. Shown are the (a) total, (b) detrended (removing the linear trend), (c) multidecadal, and (d) interannual area anomalies. The multidecadal variability is obtained by performing a 7-year running mean to the detrended AWP index. The interannual variability is calculated by subtracting the multidecadal variability from the detrended AWP index. The black straight line in (a) is the linear trend that is fitted to the total area anomaly. The extended reconstructed SST dataset is used.

tropical North Atlantic (Figs. 4.40c,d). By September, the AWP had further expanded southeastward and the 28.5°C isotherm covered nearly the entire tropical North Atlantic (Fig. 4.40e). The AWP started to decay after October when the waters in the Gulf of Mexico began cooling (Fig. 4.40f). In November, the 28.5°C isotherm still covered the Caribbean Sea and part of the western North Atlantic Ocean (Fig. 4.40g).

The effect of the AWP on TC steering flows and tracks has been previously documented (Wang 2015). The TC steering flow anomalies were consistent with those of other observed large AWP years (Wang et al. 2011). The TC steering flow anomalies during the North Atlantic TC season are depicted in Fig. 4.41. With the exception of June and November, the TC steering flow anomalies were unfavorable for TCs making landfall in the United States. From July to October, the TC steering flow anomalies were mostly southward or eastward in the western tropical North Atlantic, and northward and northeastward in the open ocean of the North Atlantic. This distribution

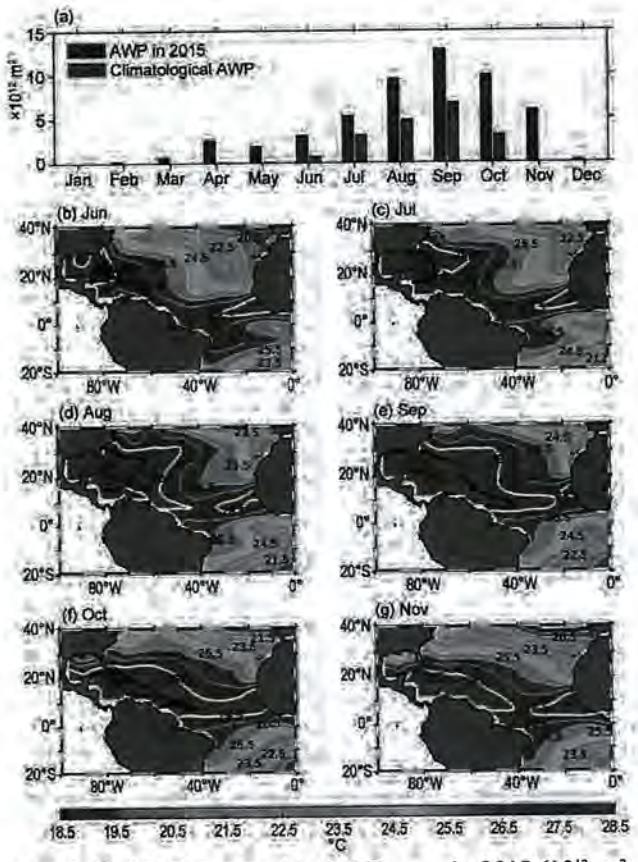

FIG. 4.40. (a) The monthly AWP area in 2015 (10^{12} m^2; blue) and the climatological AWP area (red) and the spatial distributions of the 2015 AWP in (b) Jun, (c) Jul, (d) Aug, (e) Sep, (f) Oct, and (g) Nov. The AWP is defined by SST larger than 28.5°C. The black thick contours in (b)–(g) are the climatological AWP based on the data from 1971 to 2000 and the white thick contours are the 2015 28.5°C SST values. The extended reconstructed SST dataset is used.

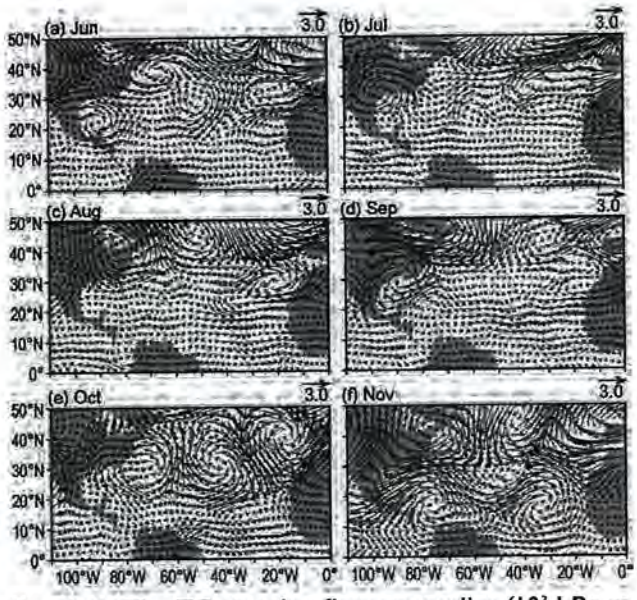

FIG. 4.41. The TC steering flow anomalies (10^3 hPa m s^{-1}) in the 2015 Atlantic TC season of (a) Jun, (b) Jul, (c) Aug, (d) Sep, (e) Oct, and (f) Nov. The TC steering flow anomalies are calculated by the vertically averaged wind anomalies from 850 hPa to 200 hPa relative to the 1971–2000 climatology. The NCEP–NCAR reanalysis field (Kalnay et al. 1996) is used.

of these anomalies was consistent with the fact that for all TCs that formed in the Atlantic MDR, none made landfall in the United States. For the two landfalling North Atlantic TCs (Ana and Bill), neither one formed in the Atlantic MDR (see section 4e2).

h. Indian Ocean dipole—J.-J. Luo

Year-to-year climate variability in the tropical Indian Ocean (IO) is largely driven by local ocean–atmosphere interactions and ENSO (e.g., Luo et al. 2010). Among the former, the Indian Ocean dipole (IOD) represents one major internal climate mode in the IO, which may exert significant climate impacts on countries surrounding the IO. The IOD often starts to grow in boreal summer, peaks in September–November, and deteriorates rapidly in December in association with the reversal of monsoonal winds along the west coast of Sumatra. During late boreal summer to fall 2015, a positive IOD occurred for the first time since the last positive IOD event in 2012 (Luo 2013). The positive IOD in 2015 is the 10th such event since 1981.

SSTs and upper ocean (0–300 m) mean temperature in most of the tropical IO were warmer than normal throughout the year (Figs. 4.42, 4.43), in association with the influence of a strong El Niño in the Pacific and a pronounced long-term warming trend of the IO SST in recent decades (e.g., Luo et al. 2012). During December–February 2014/15, surface westerly anomalies occurred across the equatorial IO, corresponding to the dry–wet contrast between the IO and the Maritime Continent–western Pacific (Figs. 4.42a, 4.43a). This is consistent with a central Pacific–El Niño condition. The westerly anomalies across the equatorial IO shallow (deepen) the oceanic thermocline in the western (eastern) IO, which helps induce cold (warm) SST anomalies in the equatorial western (eastern) IO (Figs. 4.42a, 4.43a). From March to November, in accordance with a rapid development of a strong El Niño in the Pacific (see Fig. 4.3), rainfall over the Indonesia–western Pacific decreased due to a weakened Walker Cell. Meanwhile, SSTs in the western IO increased quickly and reached ~0.8°C greater than the climatology (1982–2014) during September–November (Figs. 4.42, 4.44). Correspondingly, easterly anomalies developed in the IO beginning in boreal spring (Figs. 4.43, 4.44). Weak anomalous southeasterlies initially appeared along the west coast

of Sumatra in May and then grew gradually with a westward expansion. This might have been largely driven by the surface divergence over the Indonesia–western Pacific due to the weakened Walker Cell. During June–August, considerable dry anomalies appeared west of Sumatra, consistent with a positive IOD index and easterly anomalies in the eastern IO (Figs. 4.42c, 4.43c, 4.44c). The positive IOD kept growing and reached a peak in September–November (Figs. 4.42d, 4.43d). In December, the eastern IO SST anomaly increased sharply, which reduced the IOD (Figs. 4.44a–d).

There is no clear evidence that supports local processes generating the positive IOD in 2015. Rather, it appears that the development of a strong El Niño in the Pacific played an important, if remote, role. The 2015 IOD shows distinct features compared to previous events (Fig. 4.44). Compared to the 1997 IOD that occurred with a similarly strong El Niño, the 2015 IOD was much weaker. Although the western IO SST in 2015 is warmer than that in 1997, the eastern IO SST anomalies in 2015 are positive, in stark contrast to the strong cold anomalies in 1997. Indeed, both the western and eastern IO SSTs in 2015 are warmer than those in previous nine positive IOD events, in association with warmer general conditions across the tropical IO basin (Fig. 4.44f). While the 10 positive IOD occurred with either El Niño or La Niña, the probability of the occurrence of positive IOD during El Niño is about twice that during La Niña (Figs. 4.44c, e).

In summary, the positive IOD event in 2015 was likely driven by the development of a strong El Niño in the Pacific. However, the intensity of this IOD is much weaker than that in 1997, mainly because of the absence of cold SST anomalies in the eastern IO

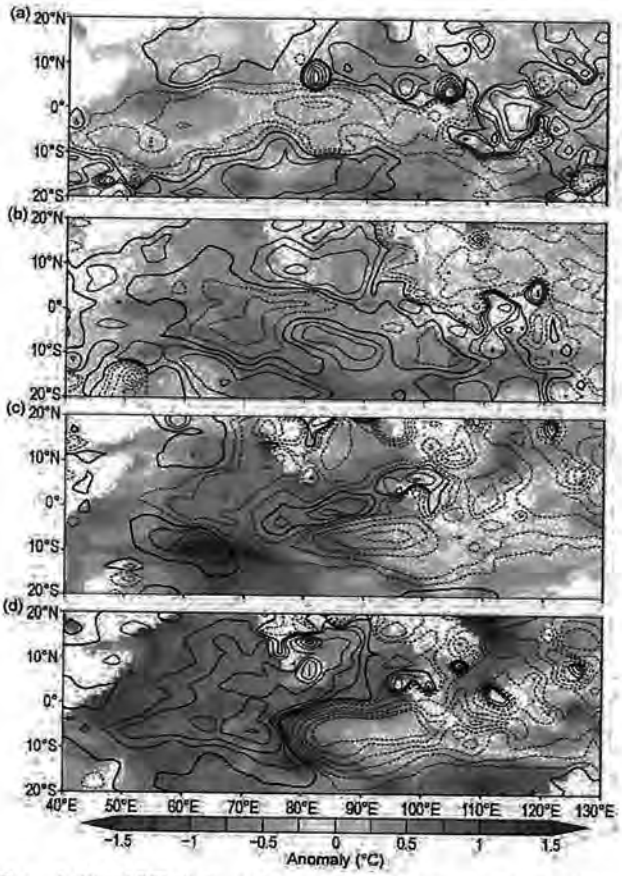

Fig. 4.42. SST (°C, colored scale) and precipitation (contour interval: 0, ±0.5, ±1, ±2, ±3, ±4, and ±5 mm day^{-1}; solid/dashed lines denote positive/negative values, and thick solid lines indicate zero contour anomalies during (a) Dec–Feb 2014/15, (b) Mar–May 2015, (c) Jun–Aug 2015, and (d) Sep–Nov 2015. The anomalies were calculated relative to the climatology over the period 1982–2014. These are based on the NCEP optimum interpolation SST (Reynolds et al. 2002) and monthly GPCP precipitation analysis (available at http://precip.gsfc.nasa.gov/).

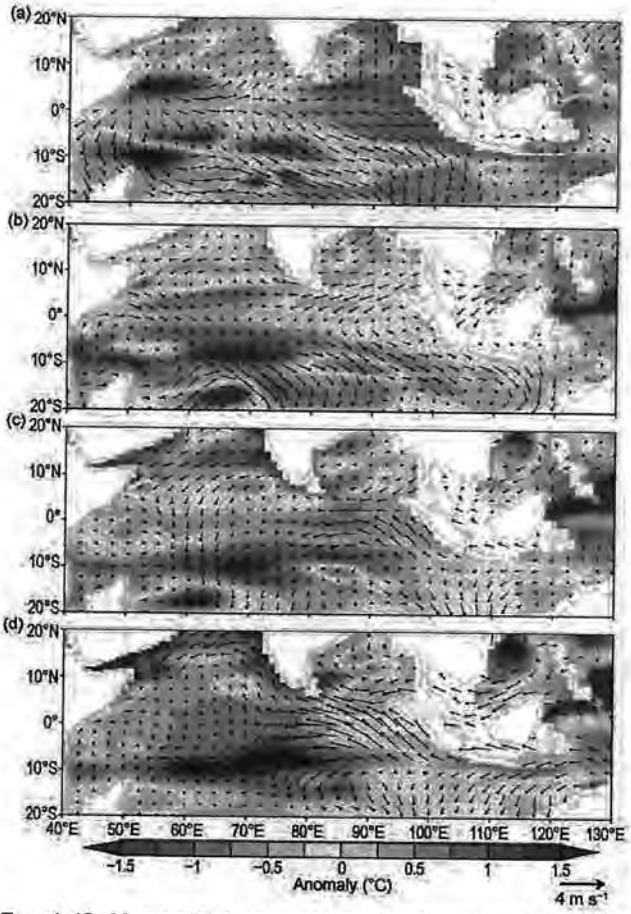

Fig. 4.43. Upper 300-m mean ocean temperature (°C, colored scale) and surface wind (m s^{-1}) anomalies during (a) Dec–Feb 2014/15, (b) Mar–May 2015, (c) Jun–Aug 2015, and (d) Sep–Nov 2015. These are based on the NCEP ocean reanalysis (available at www.cpc.ncep.noaa.gov/products/GODAS/) and JRA-55 atmospheric reanalysis (Ebita et al. 2011).

in 2015. It appears that the multidecadal basinwide warming trend of the tropical IO SST (partly due to increasing radiative forcing) might have affected and will continue to affect the evolution of IOD.

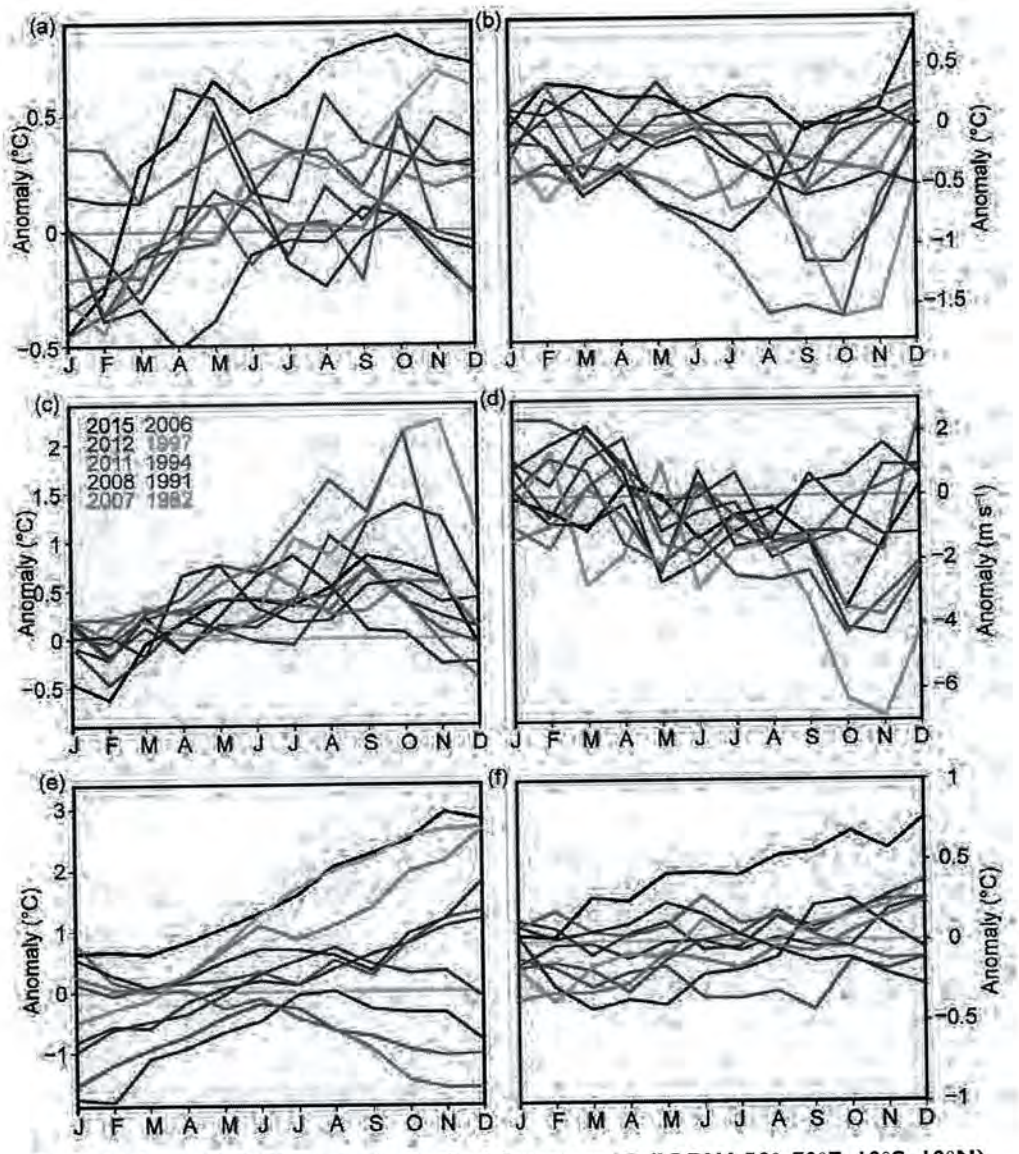

FIG. 4.44. Monthly SST anomalies in the (a) western IO (IODW, 50°–70°E, 10°S–10°N) and (b) eastern IO (IODE, 90°–110°E, 10°S–0°) and (c) the IOD index (measured by the SST anomaly difference between the IODW and the IODE) during 10 positive IOD events since 1981. (d) As in (c) but for the surface zonal wind anomaly in the central equatorial IO (70°–90°E, 5°S–5°N). (e)–(f) As in (a)–(b), but for the monthly SST anomalies in the Niño-3.4 region (190°–240°E, 5°S–5°N) and the tropical IO basin (40°–120°E, 20°S–20°N).

SIDEBAR 4.1: THE RECORD-SHATTERING 2015 NORTHERN HEMISPHERE TROPICAL CYCLONE SEASON—P. J. KLOTZBACH AND C. T. FOGARTY

The 2015 Northern Hemisphere tropical cyclone (TC) season was one for the record books. The Atlantic basin hurricane season recorded below-average activity with an ACE of 60 × 10^4 kt^2. The 1981–2010 median ACE for the Atlantic is 92, and NOAA defines any season with less than 66 ACE units as a below-average season. The remainder of the Northern Hemisphere basins (the eastern North Pacific, the western North Pacific, and the north Indian) were conversely quite active. Some of the most notable records set during this record-breaking year for these three basins individually, then collectively, for the Northern Hemisphere are documented. Table SB4.1 summarizes the statistics by basin and denotes records achieved in 2015. All statistics described are based on operational advisories from the National Hurricane Center, Central Pacific Hurricane Center, and Joint Typhoon Warning Center, and are then compared with archived best-track data compiled by those agencies. The data in these basins date back to 1851 in the North Atlantic, 1949 in the northeast Pacific, 1945 in the northwest Pacific, and 1972 in the north Indian; however, it should be noted that the data quality among these datasets is not uniform prior to about 1985 (Chu et al. 2002).

Eastern North Pacific

The eastern North Pacific (to 180°) season in 2015 tied its record for number of hurricanes and set a record for major hurricanes. ACE for the eastern North Pacific in 2015 was also quite high, trailing only 1992. Two of the most notable storm events of 2015 occurred in this basin. In late August, Hurricanes Kilo, Ignacio, and Jimena

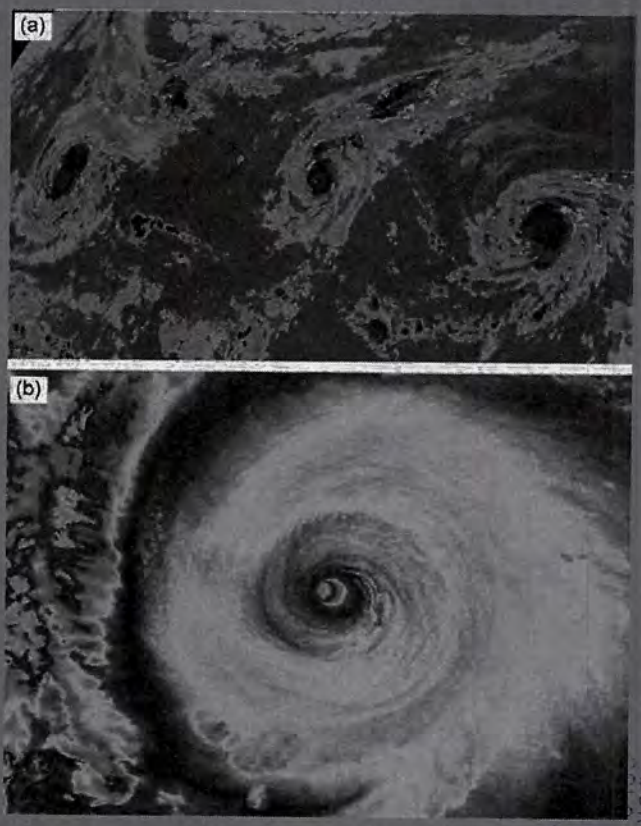

FIG. SB4.1. Satellite imagery showing (a) from left to right: Kilo, Ignacio, and Jimena at Category 4 intensity on 30 Aug 2015 and (b) Hurricane Patricia near time of peak intensity on 23 Oct 2015.

TABLE SB4.1. Northern Hemisphere TC summary statistics by basin.

Basin	Named Storms	Hurricanes	Major Hurricanes	Cat. 4–5 Hurricanes	ACE
North Atlantic	11 (12)	4 (6.5)	2 (2)	1 (1)	60 (92)
Eastern North Pacific	*26* (17)	**16*** (9)	**11** (4)	**10** (2)	*288* (119)
Western North Pacific	26 (26.5)	20 (17)	**16** (9)	**14** (7)	479 (305)
North Indian	5 (5)	2 (1)	*2** (1)	*1** (0)	36 (16)
Northern Hemisphere	68 (59)	42 (33.5)	**31** (16.5)	**26** (11)	*865* (545)

The 1981–2010 median values are in parentheses. Record high values are highlighted in bold-faced font, while second highest values are italicized. An asterisk by a record means that several years tied for that record. A TC is counted based in the basin where the storm first achieved a specific intensity. Northern Hemisphere ACE does not exactly add as sum of four individual basins due to rounding. In the case of Halola, it was counted as a named storm in the northeast Pacific and a hurricane in the northwest Pacific. Hurricanes are used colloquially to refer to all hurricane-strength TCs in the Northern Hemisphere.

CONT. SIDEBAR 4.1: THE RECORD-SHATTERING 2015 NORTHERN HEMISPHERE TROPICAL CYCLONE SEASON—P. J. KLOTZBACH AND C. T. FOGARTY

reached Category 4 status at the same time (FIG. SB4.1a). This was the first time on record that three Category 4 or stronger TCs were present at the same time in any global TC basin. On October 23, Hurricane Patricia became the strongest hurricane on record in the Western Hemisphere when an aircraft reconnaissance plane estimated 1-minute maximum sustained winds of 175 knots (Fig. SB4.1b). The central North Pacific (180°–140°W) portion of the eastern North Pacific was extraordinarily active (Collins et al. 2016, manuscript submitted to *Geophys. Res. Lett.*). Eight named storms formed in this portion of the basin, shattering the old record of four named storms set in 1982, and an additional eight storms spent some portion of their life in the basin. The central Pacific alone also accounted for an ACE level of 127×10^4 kt^2, breaking the record of 107×10^4 kt^2 set in 1994. The 127×10^4 kt^2 ACE level is especially impressive given that the 1981–2010 median for the full northeast Pacific basin was 119×10^4 kt^2.

Western North Pacific

The western North Pacific was quite active from an ACE perspective, generating the third highest ACE value of all time for the basin. In addition, 16 major (Category 3–5) typhoons occurred, breaking the record of 15×10^4 kt^2 set in 1958 and tied in 1965, both well before the era of reliable best track data (Chu 2002). As is typically the case in strong El Niño seasons, while ACE increases significantly, the number of storm formations changes little (Camargo and Sobel 2005). The western North Pacific was extraordinarily active during the month of May. Two typhoons, Noul and Dolphin, reached Category 5 status (> 137 knots) in May. This was the first time on record that two typhoons reached Category 5 status in May.

North Indian

The north Indian Ocean also experienced well above-average ACE in 2015, with 30×10^4 kt^2 generated, which is over twice the median value for the basin. Cyclones Chapala and Megh were significant storms that resulted in serious impacts on the island of Socotra. This was the first time in recorded history that two cyclone-strength TCs made landfall on Socotra in the same year (see section 4e5). Chapala also became the first cyclone-strength storm to make landfall in Yemen in recorded history, and just a week later Cyclone Megh also made landfall in Yemen.

Northern Hemisphere

The Northern Hemisphere shattered several records for intense TCs. A total of 31 major (Category 3–5) TCs occurred in 2015, breaking the old record of 23 major hurricanes set in 2004. The previous record of 18 Category 4–5 TCs, set in 1997 and tied in 2004, was also eclipsed in 2015, with 26 Category 4–5 TCs occurring. In addition, 62% of all hurricane-strength TCs that formed in 2015 reached Category 4–5 intensity, breaking the old record of 50% that happened four different times (1994, 1997, 2002, and 2011). As noted in Klotzbach and Landsea (2015), significant underestimates in Category 4–5 TCs are likely prior to ~1990. In terms of integrated metrics, Northern Hemisphere ACE was at its second highest level on record. The 2015 season generated 821×10^4 kt^2, trailing only the 876×10^4 kt^2 value generated in 1992. In summary, the Northern Hemisphere TC season was extraordinarily active, due in large part to the strong El Niño conditions that prevailed throughout the year.

SIDEBAR 4.2: A SOUTHEAST PACIFIC BASIN SUBTROPICAL CYCLONE OFF THE CHILEAN COAST—S. H. YOUNG

TCs are formally defined by NOAA's National Hurricane Center as "a warm-core nonfrontal synoptic-scale cyclone, originating over tropical or subtropical waters, with organized deep convection and a closed surface wind circulation about a well-defined center." However, closely related to TCs are subtropical cyclones, which derive a significant proportion of their energy from baroclinic sources and are generally cold core in the upper troposphere and are often associated with an upper-level low or trough. Additionally, maximum winds and convection are often at a distance generally more than 110 km from the center (see www.nhc.noaa.gov/aboutgloss.shtml#s).

Until recently, TCs were believed not to form in the Mediterranean Sea, the Atlantic basin south of the equator, and the far eastern Pacific basin south of the equator (Gray 1968). Here we describe a subtropical storm identified in the southeastern Pacific basin off the Chilean coast farther east than any in the historic record as documented in either the IBTrACS (Knapp et al. 2010) or SPEArTC (Diamond et al. 2012) datasets and outside of the responsibility of any global RSMC.

The formation of Hurricane Catarina off the coast of Brazil in 2004 (McTaggart et al. 2006; Gozzo et al. 2014) demonstrated that TCs can occasionally form in previously unsuspected areas such as the South Atlantic. The existence of possible TCs in the Mediterranean Sea, which are overwhelmingly subtropical in nature, has also generated interest in recent years (Moscatello et al. 2008; Pantillon et al. 2013; and Cavicchia et al. 2014).

In late April, Earth Observing (EOSDIS) satellite imagery showed a cyclonic circulation in the southeastern Pacific basin that appeared to meet the definition of a subtropical cyclone. Originating from a stalled frontal zone near 25°S, 102°W the storm developed into a clearly nonfrontal system with the majority of convection initially to the southeast of low-level circulation. This cyclonic storm was approximately 30° east of any previously recorded TC. ASCAT satellite derived winds were as much as 50 kt. The system was visible on imagery during the period from 30 April to 5 May (Fig. SB4.2).

The NCEP–NCAR reanalysis data (Kalnay et al. 1996) for 29 April at 1200 hours UTC showed a broad low pressure area located near 25°S, 102°W. As the system developed, it drifted toward the southeast before stalling near 28°S, 100°W for approximately 36 hours. From 2 to 3 May, the system moved west then northwest, dissipating on 6 May near 18°S, 110°W.

FIG. SB4.2. *Aqua* satellite image of sub-TC Katie on 1 May 2015 at 2055 UTC.

The location of the system was in a "no man's land" of sorts as it is not within the forecast or warning area of responsibility of any RSMC. It was too far to the east of the Nadi RSMC's area of responsibility, and while there is no formal RSMC covering the area east of 120°W, the system will be incorporated into the SPEArTC dataset under the informal name of Katie. Therefore, while the system will not necessarily be formally picked up by the IBTrACS dataset, which reflects RSMC tracks on behalf of the World Meteorological Organization's TC Programme, the more research-oriented SPEArTC dataset, which focuses on the southwest Pacific, will include this storm in its listing of 2014/15 storms with appropriate notation of its unique subtropical nature. An upper air analysis using NCAR data shows a trough over the system at the 300-hPa surface and a possible warm core at the 850-hPa surface. This is consistent with the NHC definition of a subtropical system.

From 29 April to 4 May, the Chilean Navy Weather Service included the system in their high seas warnings, reporting an

CONT. SIDEBAR 4.2: A SOUTHEAST PACIFIC BASIN SUBTROPICAL CYCLONE OFF THE CHILEAN COAST—S. H. YOUNG

estimated minimum central pressure of 993 hPa on 1 May at 0600 hours UTC. Using the method described by Knaff and Zehr (2007), this corresponds to a maximum sustained wind speed of approximately 40 kt (21 m s^{-1}). Several RapidScat passes (W. L. Poulsen 2015, personal communication) from 1 to 2 May showed winds in excess of 40 kt (21 m s^{-1}), with some returns of 50 kt (26 m s^{-1}). These peak winds were at some distance from the center of circulation, which is also consistent with a subtropical nature of the system (Fig. SB4.3). Phase diagrams (Hart 2003) using relative 900–600-hPa thickness symmetry and thermal winds for the system indicated that this system was warm core and symmetrical in early May (Fig. SB4.4), and the conditions described also support the identification of the system as either a tropical or subtropical cyclone.

Satellite imagery, phase diagrams, and surface analysis show that "Katie" was a tropical system located far from any previously identified TC listed in IBTrACS for the South Pacific basin. Although it may briefly have exhibited TC characteristics, and while the imagery is consistent with a subtropical cyclone, the system should be further examined for inclusion as a Southern Hemisphere tropical cyclone in the formal global archives.

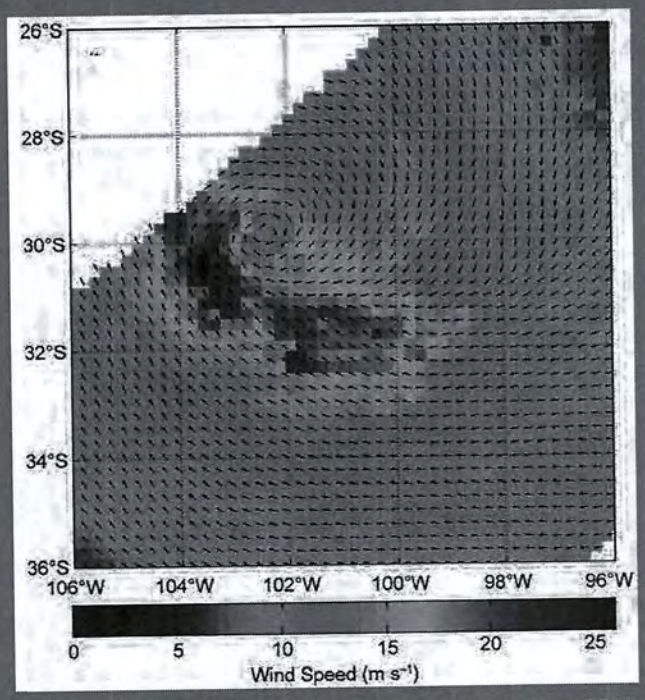

FIG. SB4.3. RapidScat Wind retrieval for 2 May 2015 starting at 1038 UTC (m s^{-1}).

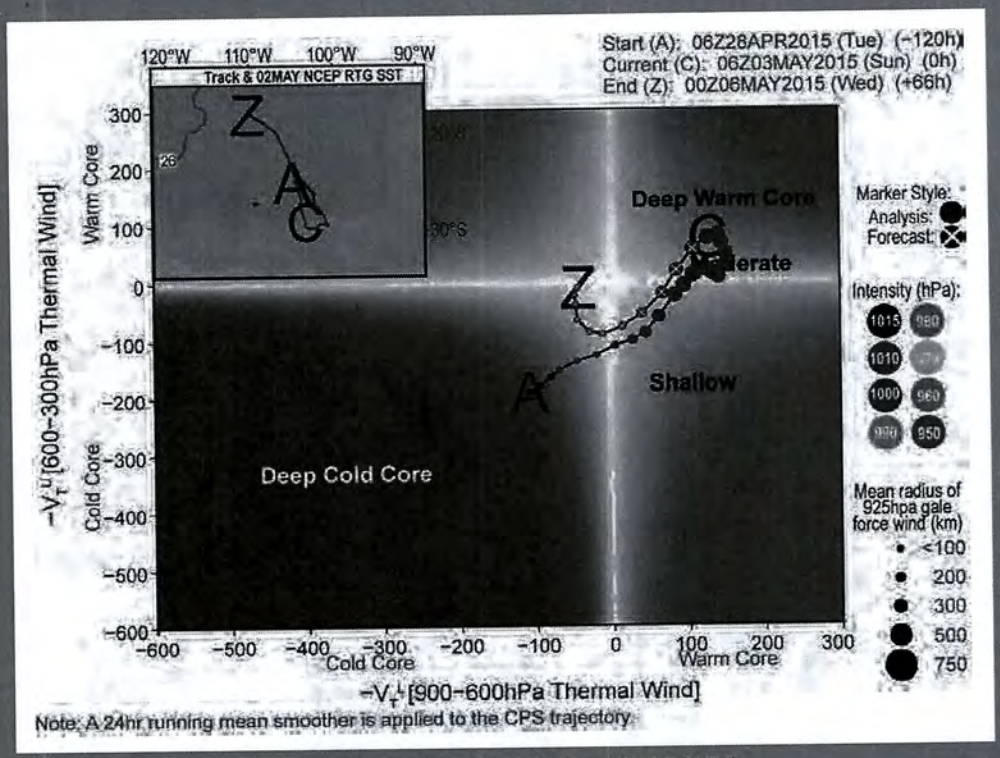

FIG. SB4.4. System phase diagram for 3 May 2015 at 0600 UTC.

5. THE ARCTIC—J. Richter-Menge and J. Mathis, Eds.

a. *Introduction*—J. Richter-Menge and J. Mathis

The Arctic chapter describes a range of observations of essential climate variables (ECV; Bojinski et al. 2014) and other physical environmental parameters, encompassing the atmosphere, ocean, and land in the Arctic and subarctic. As in previous years, the 2015 report illustrates that although there are regional and seasonal variations in the state of the Arctic environmental system, it continues to respond to long-term upward trends in air temperature. Over Arctic landmasses, the rate of warming is more than twice that of low and midlatitude regions.

In 2015, the average annual surface air temperature anomaly over land north of 60°N was +1.2°C, relative to the 1981–2010 base period. This ties the recent years of 2007 and 2011 for the highest value in the temperature record starting in 1900 and represents a 2.8°C increase since the beginning of the 20th century. Evidence of strong connections between the Arctic and midlatitude regions occurred from 1) November 2014 through June 2015, when anomalously warm conditions in the Pacific Arctic region were associated with southerly air flow into and across Alaska, and 2) February through April 2015, when anomalously cold conditions from northeastern North America to southwest Greenland were associated with northerly air flow.

There is clear evidence of linkages among the various components of the Arctic system. Under the influence of persistent warming temperatures, the Arctic sea ice cover is diminishing in extent and thickness. The lowest maximum sea ice extent in the 37-year satellite record occurred on 25 February 2015, at 7% below the average for 1981–2010. This date of occurrence was the second earliest in the record and 15 days earlier than the average date of 12 March. Minimum sea ice extent in September 2015 was 29% less than the 1981–2010 average and the fourth lowest value in the satellite record. In February and March, the oldest ice (>4 years) and first-year ice made up 3% and 70%, respectively, of the pack ice compared to values of 20% and 35%, respectively, in 1985.

As the extent of sea ice retreat in the summer continues to increase, allowing previously ice-covered water to be exposed to more solar radiation, sea surface temperature (SST) and upper ocean temperatures are increasing throughout much of the Arctic Ocean and adjacent seas. The Chukchi Sea northwest of Alaska and eastern Baffin Bay off west Greenland have the largest warming trends: ~0.5°C per decade since 1982. In 2015, SST was up to 4°C higher than the 1982–2010 average in eastern Baffin Bay and the Kara Sea north of central Eurasia.

The impact of sea ice retreat and warming ocean temperatures on the ecosystem is well demonstrated by changes in the behavior of walrus and fish communities. In the Pacific Arctic, vast walrus herds are now hauling out on land rather than on sea ice as the ice retreats far to the north over the deep Arctic Ocean, raising concern about the energetics of females and young animals. Warming trends in water temperatures in the Barents Sea, which started in the late 1990s, are linked to a community-wide shift in fish populations: boreal communities are now found farther north and the local Arctic (cold-water affinity) community has been almost pushed out of the area.

Ice on land, including glaciers and ice caps outside Greenland (Arctic Canada, Alaska, Northern Scandinavia, Svalbard, and Iceland) and the Greenland Ice Sheet itself, continues to lose mass. In 2015, the Greenland Ice Sheet, with the capacity to contribute ~7 m to sea level rise, experienced melting over more than 50% of the ice sheet for the first time since the exceptional melting of 2012 and exceeded the 1981–2010 average on 50 of 92 days (54%). Reflecting the pattern of ice melt, which is driven by the pattern of surface air temperature anomalies, the average albedo in 2015 was below the 2000–09 average in northwest Greenland and above average in southwest Greenland.

Despite above-average snow cover extent (SCE) in April, Arctic SCE anomalies in May and June 2015 were below the 1981–2010 average, a continuation of consistent early spring snowmelt during the past decade. June SCE in both the North American and Eurasian sectors of the Arctic was the second lowest in the satellite record (1967–present). The rate of June SCE reductions since 1979 (the start of the passive microwave satellite era) is 18% per decade.

In 2014, the most recent year with complete data, the combined discharge of the eight largest Arctic rivers [2487 km^3 from Eurasia (Pechora, S. Dvina, Ob', Yenisey, Lena, and Kolyma) and North America (Yukon and Mackenzie)] was 10% greater than the average discharge during 1980–89. Since 1976, discharge of the Eurasian and North American rivers has increased 3.1% and 2.6% per decade, respectively.

Regional variability in permafrost temperature records indicates more substantial permafrost warming since 2000 in higher latitudes than in the subarctic, in agreement with the pattern of average air temperature anomalies. In 2015, record high temperatures at 20-m depth were measured at all permafrost observatories on the North Slope of Alaska, increasing between

0.21°C and 0.66°C decade^{-1} since 2000. Permafrost warming in northernmost Alaska exemplifies what is happening to permafrost on a pan-Arctic scale.

Arctic cloud cover variability significantly influences ultraviolet index (UVI) anomaly patterns. Reflecting this influence, monthly average noontime UVIs for March 2015 were below the 2005–14 means in a belt stretching from the Greenland Sea and Iceland in the east to Hudson Bay and the Canadian Arctic Archipelago in the west. This region roughly agrees with the regions where the atmospheric total ozone columns (TOC) were abnormally high in March 2015. At the pan-Arctic scale, the minimum TOC in March was 389 Dobson Units (DU), 17 DU (5%) above the average of 372 DU for the period 1979–2014 and 23 DU (6%) above the average for the past decade (2000–14).

This overview alone refers to a number of different periods of observation for which average values and departures from average (anomalies) have been calculated. For the World Meteorological Organization, and national agencies such as NOAA, 1981–2010 is the current standard reference period for calculating climate normals (averages) and anomalies. In this report, the current standard reference period is used when possible, but it cannot be used for all the variables described; some organizations choose not to use 1981–2010 and many observational records postdate 1981. The use of different periods to describe the state of different elements of the Arctic environmental system is unavoidable, but it does not change the fact that change is occurring throughout the Arctic environmental system.

b. Air temperature—J. Overland, E. Hanna, I. Hanssen-Bauer, S.-J. Kim, J. Walsh, M. Wang, U. S. Bhatt, and R. L. Thoman

Arctic air temperatures are both an indicator and a driver of regional and global changes. Although there are year-to-year and regional differences in air temperatures due to natural variability, the magnitude and Arctic-wide character of the long-term temperature increase are major indicators of global warming (Overland 2009).

The mean annual surface air temperature anomaly for 2015 for land stations north of 60°N was +1.2°C, relative to the 1981–2010 mean value (Fig. 5.1). This ties the recent years of 2007 and 2011 for the highest value in the record starting in 1900. Currently, the Arctic is warming at more than twice the rate of lower latitudes (Fig. 5.1).

The greater rate of Arctic temperature increase compared to the global increase is referred to as Arctic amplification. Mechanisms for Arctic amplification include reduced summer albedo due to sea ice and snow cover loss, the decrease of total cloudiness in summer and an increase in winter, and the additional heat generated by increased sea ice free ocean areas that are maintained later into the autumn (Serreze and Barry 2011; Makshtas et al. 2011). Arctic amplification is also enhanced because radiational loss of heat from the top of the atmosphere is less in the Arctic than in the subtropics (Pithan and Mauritsen 2014).

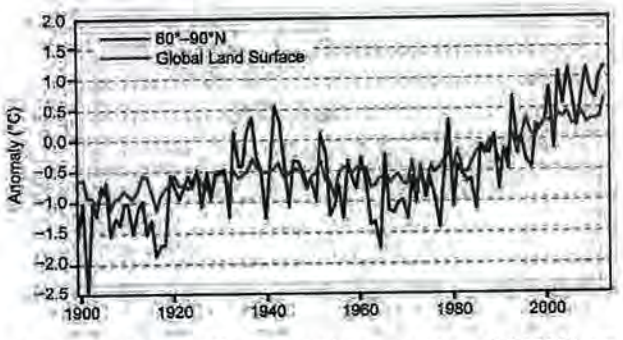

FIG. 5.1. Arctic (land stations north of 60°N) and global mean annual land surface air temperature (SAT) anomalies (in °C) for the period 1900–2015 relative to the 1981–2010 mean value. Note that there were few stations in the Arctic, particularly in northern Canada, before 1940. (Source: CRUTEM4.)

Although there is an Arctic-wide long-term pattern of temperature increases, regional differences can be manifest in any given season based on natural variability of the atmospheric circulation (Overland et al. 2011; Kug et al. 2015).

Seasonal air temperature anomalies are described in Fig. 5.2 for winter [January–March (JFM)], spring [April–June (AMJ)], summer [July–September (JAS)], and autumn [October–December (OND)] of 2015. All seasons show extensive positive temperature anomalies across the central Arctic with many regional seasonal temperature anomalies greater than +3°C, relative to a 1981–2010 base period.

Warm temperature anomalies in winter 2015 extended across the Arctic, from the Pacific sector to the Atlantic sector (Fig. 5.2a). The warmest temperature anomalies were centered on Alaska and far eastern Siberia, including the Chukchi and East Siberian Seas. In Svalbard, in the Atlantic sector northeast of Greenland, winter temperatures were typically 2°C above the 1981–2010 average. In contrast, cold (negative) temperature anomalies of −2° to −3°C extended from southwest Greenland to central Canada and into the eastern United States.

A broad swath of warm temperature anomalies continued to stretch across the Arctic in spring

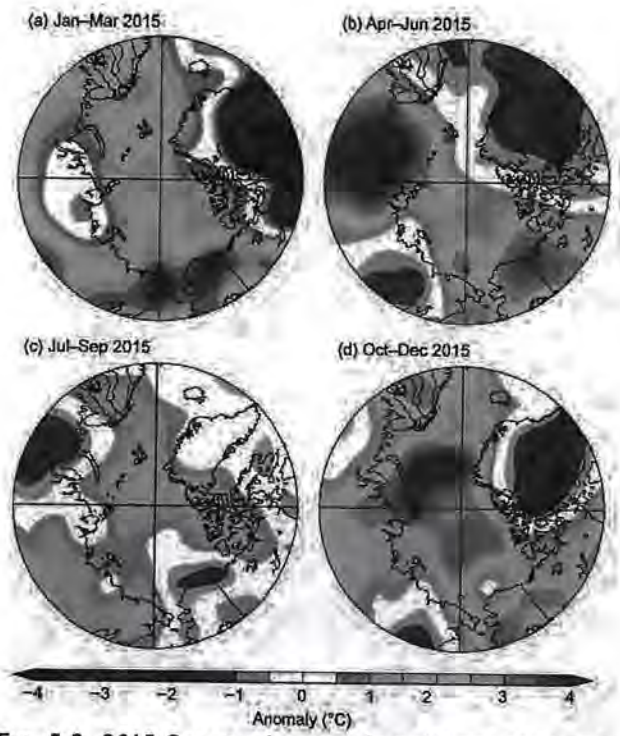

FIG. 5.2. 2015 Seasonal anomaly patterns for near-surface air temperatures (°C) relative to the baseline period 1981–2010 in (a) winter, (b) spring, (c) summer, and (d) autumn. Temperatures are from somewhat above the surface layer (at 925 mb level) to emphasize large spatial patterns rather than local features. (Source: NOAA/ESRL.)

2015, with a continuing warm anomaly over Alaska (Fig. 5.2b). However, unlike the winter pattern (Fig. 5.2a), spring saw a shift to a very warm anomaly (+4°C) over central Eurasia. A significant cold anomaly (−3°C) was centered over Greenland. In contrast to Greenland, spring temperatures at the weather station in Svalbard were typically 2°C above the 1981–2010 average, as Svalbard was located on the margin of the broad swath of positive temperature anomalies that extended from Alaska to Eurasia.

A warm temperature anomaly over much of the Arctic Ocean, with the exception of a moderately cold anomaly over the Beaufort Sea north of Alaska, characterized summer 2015 (Fig. 5.2c). Particularly cold anomalies occurred over western Eurasia. As noted in section 5f, a new record August low temperature of −39.6°C occurred on 28 August at Summit (elevation 3216 m in the center of the ice sheet), while summer temperatures measured at most coastal weather stations were above average (Tedesco et al. 2015). Similar to coastal Greenland locations, at the Svalbard weather station the average temperature was 1°–2°C above the 1981–2010 average, the highest JAS average ever recorded in the composite Longyearbyen–Svalbard Airport record that dates to 1898 (Nordli et al. 2014).

In autumn, particularly warm air temperature anomalies were seen in the subarctic regions of the Barents and Bering Seas (Fig. 5.2d). While the central Arctic remained relatively warm, cold anomalies were seen in northeastern North America similar to winter 2015. A difference, however, is that central Asia was also relatively cold in autumn compared to the warmer previous winter.

Both winter and autumn 2015 illustrate extensive interaction of large-scale weather systems between the Arctic and midlatitudes. The anomalously warm temperatures across Alaska in winter and spring 2015 (Fig. 5.2a,b) extend a pattern that began during autumn 2014. The persistent positive (warm) near-surface air temperature anomalies in Alaska and extending into the Chukchi and Beaufort Seas were associated with warm sea surface temperatures in the Gulf of Alaska and a pattern of geopotential height anomalies characterized by higher values along the Pacific Northwest coast of North America and lower values farther offshore (Fig. 5.3a). Consequently, warm air over the northeast Pacific Ocean was advected by southerly winds into and across Alaska, contributing to high mass loss on glaciers (see section 5f). Associated with the southerly winds, a downslope component of the wind on the north side of the Alaska Range and into Interior Alaska caused dry conditions and reinforced high temperatures. The warm and dry conditions in Interior Alaska during May and June contributed to the second worst fire season on record for those months, eclipsed only by 2004.

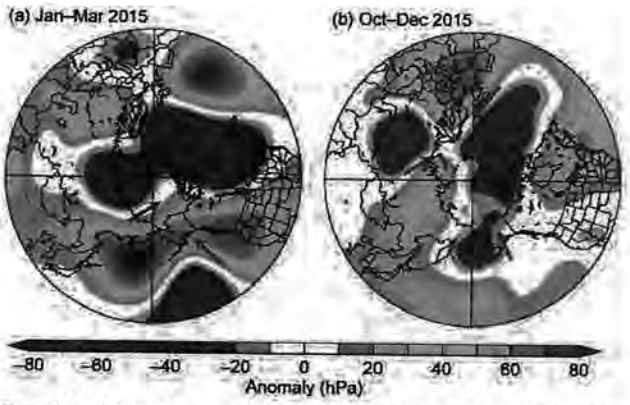

FIG. 5.3. (a) Large geopotential height anomalies over western and eastern North America and continuing into the North Atlantic sector in winter 2015. (b) Negative geopotential height anomalies over the North Atlantic and Bering Sea sectors in autumn 2015. The arrows indicate anomalous warm (red) and cold (blue) air flow generated as a result of these anomaly patterns.

In contrast to the warm temperature anomalies in winter in Alaska (Fig. 5.2a) due to warm, southerly air flow (Fig. 5.3a), the cold anomalies extending from eastern Canada to southwest Greenland (Fig. 5.2a) were associated with strong northwesterly air flow. These cold anomalies extended into early spring. The potential source of these relatively cold temperatures is illustrated by the extensive winter (JFM) negative geopotential height anomaly pattern (Fig. 5.3a) that shows high values over northwestern North America and low values over eastern North America, Greenland, and across the central Arctic Ocean to central Eurasia. Northwesterly winds on the west side of the trough between the two height centers channeled cold air southward from the source region in the central Arctic into northeastern North America. This geopotential height anomaly pattern may also explain the above-average winter air temperatures in Svalbard, which were associated with warm air advection across western Eurasia and into the central Arctic Ocean (Figs. 5.2a,b).

Autumn 2015 was noted for large active low pressure systems in the North Atlantic and Bering Sea (Fig 5.3b). These low height anomaly patterns with southerly wind components to their east kept the Chukchi and Barents Seas relatively warm and sea ice free well into the autumn season.

c. Sea ice cover—D. Perovich, W. Meier, M. Tschudi, S. Farrell, S. Gerland, and S. Hendricks

Three key variables are used to describe the state of the ice cover: the ice extent, the age of the ice, and the ice thickness. Sea ice extent is used as the basic description of the state of Arctic sea ice cover. Satellite-based passive microwave instruments have been used to determine sea ice extent since 1979. There are two months each year that are of particular interest: September, at the end of summer, when the ice reaches its annual minimum extent, and March, at the end of winter, when the ice typically reaches its maximum extent. Maps of monthly average ice extents in March 2015 and September 2015 are shown in Fig. 5.4.

Based on estimates produced by the National Snow and Ice Data Center (NSIDC), the 2015 sea ice cover reached its maximum extent on 25 February, at a value of 14.54 million km^2. This was 7% below the 1981–2010 average and the lowest maximum value in the satellite record. Also notable, the maximum extent occurred 15 days earlier than the 1981–2010 average (12 March) and was the second earliest of the satellite record. The annual minimum extent of 4.41 million km^2 was reached on 11 September. This was substantially higher (30%) than the record minimum of 3.39 million km^2 set in 2012. However, the 2015 summer minimum extent was still 1.81 million km^2 (29%) less than the 1981–2010 average minimum ice extent and 0.62 million km^2 (12%) less than the 2014 minimum.

Sea ice extent has decreasing trends in all months and nearly all regions (the exception being the Bering Sea during winter). In 2015, the largest losses were in the eastern Arctic in regions of warm air temperature anomalies in spring and summer (section 5b, Fig. 5.2). The September monthly average decline for the entire Arctic Ocean is now −13.4% decade^{-1} relative to the 1981–2010 average (Fig. 5.5). The trend is smaller dur-

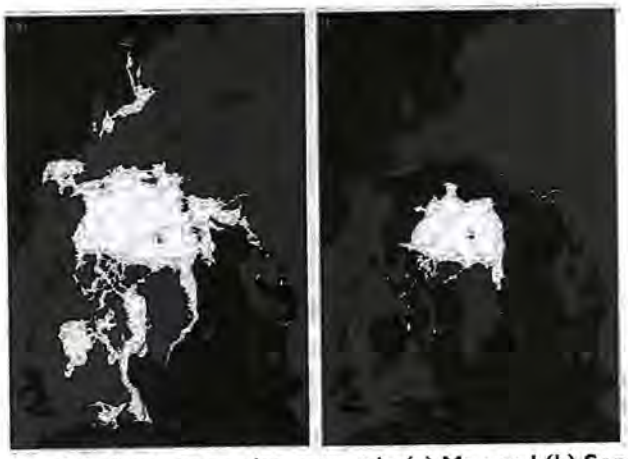

Fig. 5.4. Average sea ice extent in (a) Mar and (b) Sep 2015 illustrate the respective winter maximum and summer minimum extents. The magenta line indicates the median ice extents in Mar and Sep, respectively, during the period 1981–2010. (Source: NSIDC.)

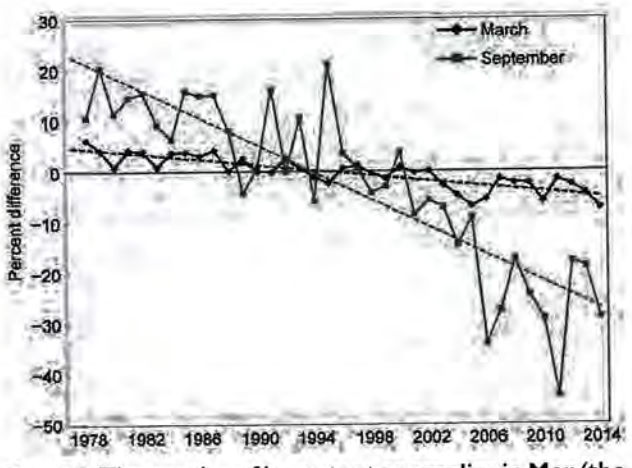

Fig. 5.5. Time series of ice extent anomalies in Mar (the month of maximum ice extent) and Sep (the month of minimum ice extent). The anomaly value for each year is the difference (in %) in ice extent relative to the mean values for the period 1981–2010. The black and red lines are least squares linear regression lines. Both trends are significant at the 99% confidence level.

ing March (–2.6% decade^{-1}) but is still a statistically significant rate of decrease in sea ice extent.

Prior to 2007, there had not been a March to September loss of more than 10 million km^2 of ice in the record, but now such large losses are not unusual. More typical of recent years, 10.13 million km^2 of ice was lost between the March maximum and September minimum extent in 2015.

The age of sea ice serves as an indicator for ice physical properties, including surface roughness, melt pond coverage, and thickness. Older ice tends to be thicker and thus more resilient to changes in atmospheric and oceanic forcing than younger ice. The age of the ice is estimated using satellite observations and drifting buoy records to track ice parcels over several years (Tschudi et al. 2010; Maslanik et al. 2011). This method has been used to provide a record of the age of the ice since the early 1980s (Tschudi et al. 2015).

The oldest ice (>4 years old) continues to make up a small fraction of the Arctic ice pack in March, when the sea ice extent has been at its maximum in most years of the satellite record (Figs. 5.6a,b). In 1985, 20% of the ice pack was >4 years old, but in March 2015, this ice category only constituted 3% of the ice pack. Furthermore, we note that first-year ice now dominates the ice cover, comprising ~70% of the March 2015 ice pack, compared to about 50% in the 1980s. Given that older ice tends to be thicker, the sea ice cover has transformed from a strong, thick pack in the 1980s to a more fragile, thin, and younger pack in recent years. The thinner, younger ice is more vulnerable to melting out in the summer, resulting in lower minimum ice extents. The distribution of ice age in March 2015 was similar to that in March 2014 (Fig. 5.6a).

Most of the oldest ice accumulates along the coast of North Greenland and the Queen Elizabeth Islands of the Canadian Arctic Archipelago, and much of this ice has resided in this area for several years (Fig. 5.6b). In 2015, as in most years, ice transport patterns resulted in the movement of old ice from this area into the Beaufort Sea. The lack of ice older than one year in the eastern Arctic (on the Eurasian side of the Arctic basin) foreshadows its susceptibility to melt out in summer. The ice in the southern Beaufort and Chukchi Seas has also melted completely in the past few summers, with even the oldest ice not surviving the season.

Observations of sea ice thickness and volume from multiple sources have revealed the continued decline of the Arctic sea ice pack over the last decade (Kwok and Rothrock 2009; Laxon et al. 2013; Kwok and Cunningham 2015). Figure 5.6c shows ice thicknesses derived from CryoSat-2 satellite results and IceBridge aircraft observations in March–April 2015. The oldest ice north of Greenland and the Canadian Arctic Archipelago remains thicker than 3 m. There is a strong gradient to thinner, seasonal ice in the Canada basin and the eastern Arctic Ocean, where ice is 1–2 m thick.

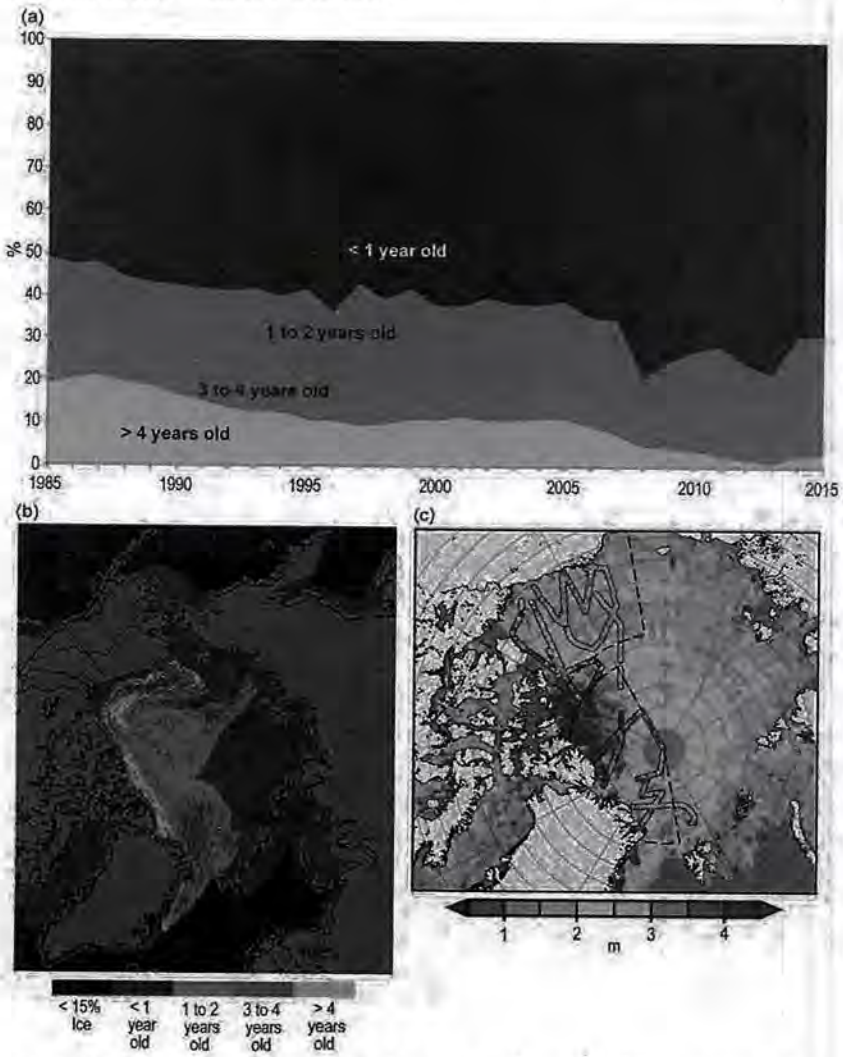

FIG. 5.6. (a) Time series of sea ice age in Mar for 1985–present, (b) sea ice age in Mar 2015, and (c) sea ice thickness derived from ESA CryoSat-2 (background map) and NASA Operation IceBridge measurements (color coded lines) for Mar/Apr 2015.

SIDEBAR 5.1: WALRUSES IN A TIME OF CLIMATE CHANGE—
K. M. KOVACS, P. LEMONS, AND C. LYDERSEN

Climate change-induced alterations in Arctic ecosystems are having impacts at all trophic levels, which are already being described as "transformative" (Johannessen and Miles 2011). However, it remains a challenge to predict impacts in terms of population trends of even highly visible, top trophic animals on multidecadal scales, based on changes occurring in primary physical features that determine habitat suitability. For example, sea ice declines are clearly a major threat to ice-associated marine mammals (e.g., Kovacs et al. 2012; Laidre et al. 2015), but documented regional patterns in sea ice losses are not necessarily reflected in the trajectories of ice-dependent marine mammal populations on a regional basis. In this regard, walruses (*Odobenus rosmarus*) make an interesting case study.

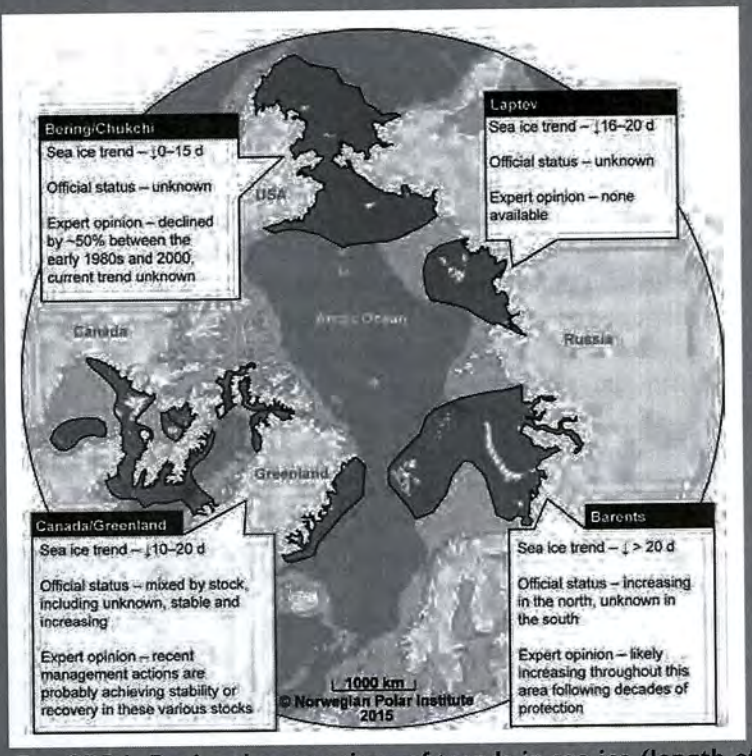

FIG. SB5.1. Regional comparison of trends in sea ice (length of the summer season – number of days less coverage decade^{-1}) and walrus stocks according to Laidre et al. (2015) and expert opinion for Pacific (purple) and Atlantic walrus (red) by region. Stocks are identified by black boundary lines.

Walruses of both subspecies, *O. r. divergens* in the North Pacific Arctic and *O. r. rosmarus* in the North Atlantic Arctic, mate along ice edges in the drifting pack ice during winter and give birth on sea ice in the late spring. Both subspecies use sea ice extensively as a haul-out platform throughout much of the year if it is available close enough to foraging areas. This habitat also provides shelter from storms and protection from some predators. Despite these shared critical links to sea ice, the population trajectories for the two subspecies do not consistently reflect the relative patterns of sea ice losses in the two broad regions occupied by the two subspecies.

The latest research indicates that the Pacific walrus population in the Bering and Chukchi Seas likely declined from about 1980 to 2000 (Taylor and Udevitz 2015). Prior to this time, subsistence harvest restrictions had allowed this population to recover from earlier overexploitation (Fay et al. 1989) to a level that likely approached the carrying capacity of the environment (e.g., Hills and Gilbert 1994). But, population models suggest that a subsequent decline of approximately 50% took place in the Pacific population (Taylor and Udevitz 2015), which was likely initially stimulated by changes in vital rates (e.g., birth rates, calf survivorship) within the population. This decline has almost certainly been exacerbated by declines in sea ice in the region (Fig. SB5.1), associated with global climate change (Taylor and Udevitz 2015). Hypothesized mechanisms include: (1) the retreat of sea ice to a position over the deep Arctic Ocean basin, forcing walruses to use land-based haulouts where trampling increases mortality of young animals (Fischbach et al. 2009; Udevitz et al. 2012) and (2) the decline in sea ice reducing walruses' access to prey, which could impact the adult female body condition, ultimately reducing calf survival and recruitment (Jay et al. 2011; Taylor and Udevitz 2015). The use of land-based haulout areas is not novel for Pacific walruses, but females with dependent young typically utilize sea ice for hauling out (Fay 1982), which allows them to avoid particularly large land-based groups where crowding and trampling events can result in high calf mortality. A lack of sea ice over the shelf in summer in the Bering and Chukchi Seas is already resulting in increased use of coastlines and islands by females with calves, which has in turn resulted in significant calf mortalities in recent years (Fishbach et al. 2009). Additionally, there is ongoing concern about the impacts of declining sea ice on the future energetics of females and young animals. These conditions require the animals to take significantly longer feeding trips between the coastal haul outs and offshore areas with high prey abundance (180 km one-way), rather than utilizing nearby ice edges for resting as they did in the past.

Sea ice losses in the North Atlantic Arctic, in particular the Barents Sea region, have been much more extreme than in the North Pacific (Fig. SB5.1). But, Atlantic walrus abundance is increasing or stable for all stocks for which the trend is known (see Laidre et al. 2015) despite reductions in carrying capacity that are almost certainly taking place due to the sea ice declines. Concern does remain regarding possible overharvesting of several stocks with currently unknown trends in Canada/Greenland. However, the positive turnarounds that have occurred are responses to protective management regimes that have been instituted in the early- and mid-1900s (1928 in Canada, 1952 in Norway, and 1956 in Russia), and, in the case of Greenland, much more recently, with quotas being established there in 2006 (see Wiig et al. 2014 for more details). Perhaps the most extreme example of walrus abundance increasing where environmental conditions are deteriorating due to climate change occurs in the Svalbard Archipelago. Svalbard is an Arctic hot spot that is experiencing dramatic sea ice declines and warming ocean and air temperatures, and yet walrus numbers in the archipelago are increasing exponentially (Kovacs et al. 2014). Walruses in this area were hunted without restriction over several hundred years, up until the 1950s. When they finally became protected in 1952, there were at best a few hundred animals left. Now, after 60 years of complete protection from hunting, with some special no-go reserve areas, recovery is taking place, despite major reductions in sea ice. More females with calves are documented during surveys and historically used sites are being reoccupied as walruses continue to expand through the archipelago. These changes are occurring despite the fact that overall carrying capacity of the region for walruses is likely declining.

The population trajectories of many walrus stocks are currently a result of distant past, or more recent, hunting regimes. However, there is little question that sea ice declines are going to be a challenge for walruses in the future along with other climate change related factors such as increased shipping and development in the north, increased disease and contaminant risks, and ocean acidification impacts on the prey of walruses.

d. Sea surface temperature—M.-L. Timmermans and A. Proshutinsky

Summer sea surface temperatures in the Arctic Ocean are set by absorption of solar radiation into the surface layer. In the Barents and Chukchi Seas, there is an additional contribution from advection of warm water from the North Atlantic and Pacific Oceans, respectively. Solar warming of the ocean surface layer is influenced by the distribution of sea ice (with more solar warming in ice-free regions), cloud cover, water color, and upper-ocean stratification. In turn, warmer SSTs can drive intensified cyclonic activity; cyclones propagating in marginal ice zones are associated with large ocean-to-atmosphere heat fluxes in ice-free regions (e.g., Inoue and Hori 2011). Here, August SSTs are reported, which are an appropriate representation of Arctic Ocean summer SSTs and are not affected by the cooling and subsequent sea ice growth that takes place in the latter half of September. SST data are from the NOAA Optimum Interpolation (OI) SST Version 2 product, which is a blend of in situ and satellite measurements (Reynolds et al. 2002, 2007; www.esrl.noaa.gov/psd/data/gridded/data.noaa.oisst.v2.html).

Mean SSTs in August 2015 in ice-free regions ranged from ~0°C in some places to around +7°C to +8°C in the Chukchi, Barents, and Kara Seas and eastern Baffin Bay off the west coast of Greenland (Fig. 5.7a). August 2015 SSTs show the same general spatial distribution as the August mean for the period 1982–2010 (Timmermans and Proshutinsky 2015; Fig. 5.24b). The August 2015 SST pattern is also similar to that of recent years, for example 2012 (Fig. 5.7b), which was the summer of lowest minimum sea ice extent in the satellite record (1979–present).

Most boundary regions and marginal seas of the Arctic had anomalously warm SSTs in August 2015 compared to the 1982–2010 August mean (Fig. 5.7c). SSTs in these seas, which are mostly ice free in August, are linked to the timing of local sea ice retreat; anomalously warm SSTs (up to +3°C relative to 1982–2010) in August 2015 in the Beaufort and Chukchi Seas were associated with low sea ice extents and exposure of surface waters to direct solar heating (Fig. 5.7c; see also section 5c). The relationship between warm SSTs and reduced sea ice is further apparent in a comparison between August 2015 and August 2014 SSTs: anomalously warm regions (including to the east of Svalbard, where SSTs were up to +3°C warmer in 2015) are associated with relatively lower sea ice extents in 2015 compared to 2014 (Fig. 5.7d). Although SSTs were warmer in general, August 2015 SSTs were cooler relative to average in some regions, for example, along the southern boundaries of the Beaufort and East Siberian Seas (Fig. 5.7c), where summer air temperatures were also below average (see section 5b).

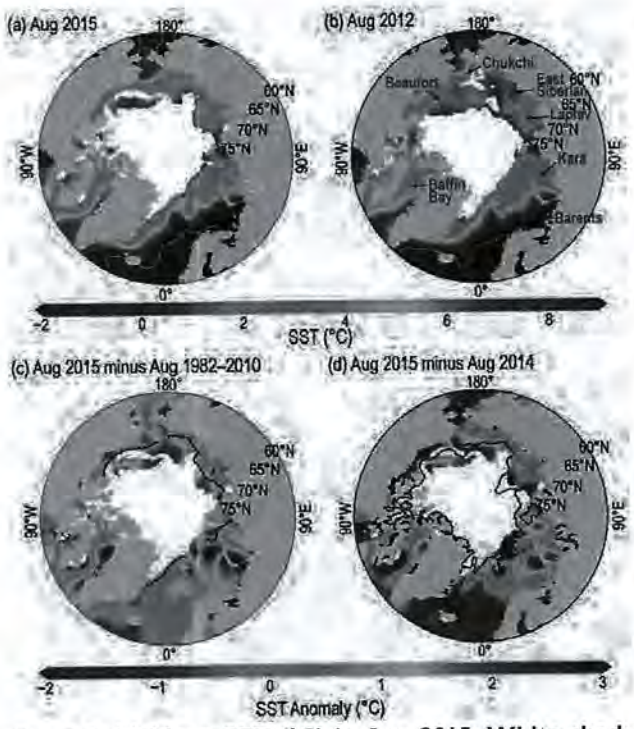

Fig. 5.7. (a) Mean SST (°C) in Aug 2015. White shading is the Aug 2015 mean sea ice extent. (b) Mean SST in Aug 2012. White shading is the Aug 2012 sea ice extent. Gray contours in (a) and (b) indicate the 10°C SST isotherm. (c) SST anomalies (°C) in Aug 2015 relative to the Aug mean for the period 1982–2010. White shading is the Aug 2015 mean ice extent and the black line indicates the median ice edge in Aug for the period 1982–2010. (d) SST anomalies (°C) in Aug 2015 relative to Aug 2014; white shading is the Aug 2015 mean ice extent and the black line indicates the median ice edge for Aug 2014. Sea ice extent and ice edge data are from NSIDC.

Anomalously warm August 2015 SSTs in eastern Baffin Bay were notable, with values as much as 4°C higher than the 1982–2010 August mean; SSTs over the region indicate a general warming trend of about 0.5°C decade^{-1} since 1982 (Fig. 5.8a). Over the past two decades, the linear warming trend in the surface waters of eastern Baffin Bay has accelerated to about 1°C decade^{-1} (+0.10°C yr^{-1}). Along the boundaries of the Arctic basin, the only marginal seas to exhibit statistically significant warming trends are the Chukchi and the Kara Seas. Chukchi Sea August SSTs are warming at a rate of about +0.5°C decade^{-1}, commensurate with declining trends in summer sea ice extent in the region. In the Kara Sea, August 2015 SSTs were also up to 4°C higher than the 1982–2010 August mean; SSTs in this sea have warmed by about +0.3°C decade^{-1} since 1982. In other marginal seas, warm August SST anomalies observed in 2015 are of similar magnitude to warm anomalies observed in past decades (Timmermans and Proshutinsky 2015, their Fig. 5.26a).

The seasonal evolution of SST in the marginal seas exhibited the same general trends and regional differences in 2015 (Fig. 5.8b) as for the preceding decade. Seasonal warming in the marginal seas begins as early as May, and the seasonal cooling period begins as early as mid-August, with cooling observed through December. The asymmetry in rates of seasonal warming and cooling, most notable in the Chukchi Sea and East Baffin Bay, suggests a source of heat in addition to solar radiation. Advection of warm water from the Bering Sea and North Atlantic likely inhibits SST cooling (e.g., Carton et al. 2011; Chepurin and Carton 2012).

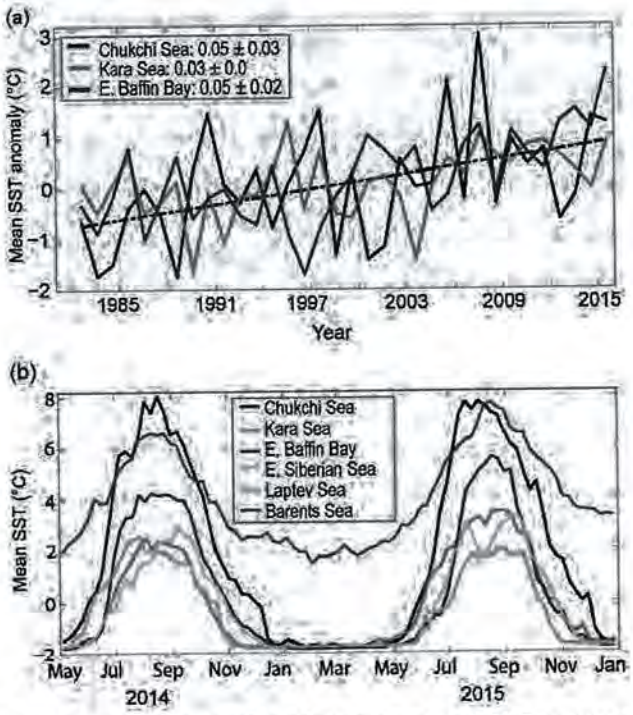

Fig. 5.8. (a) Time series of area-averaged SST anomalies (°C) for Aug of each year relative to the Aug mean for the period 1982–2010 for the Chukchi and Kara Seas and eastern Baffin Bay (see Fig. 5.7b). The dash-dotted black line shows the linear SST trend for the Chukchi Sea (the same warming trend as eastern Baffin Bay). Numbers in the legend correspond to linear trends (with 95% confidence intervals) in °C yr^{-1}. (b) SST (°C) in 2014–15 for each of the marginal seas, where the OISST V2 weekly product has been used in the calculation. For sea ice concentrations greater than 50%, the SST product uses a linear relationship with sea ice concentration to infer SST; variations in freezing temperature as a consequence of salinity variations imply that SSTs inferred from sea ice can be erroneously cool by as much as 0.2°C, with the highest errors in the Canadian sector (see Timmermans and Proshutinsky 2015).

SIDEBAR 5.2: CLIMATE CHANGE IS PUSHING BOREAL FISH NORTHWARD TO THE ARCTIC: THE CASE OF THE BARENTS SEA—M. FOSSHEIM, R. PRIMICERIO, E. JOHANNESEN, R. B. INGVALDSEN, M. M. ASCHAN, AND A. V. DOLGOV

Under climate warming, species tend to shift their distributions poleward (IPCC 2014). Some of the most rapid shifts are taking place in the Arctic, where warming is currently twice the global average (see section 5.b, Fig. 5.1; Hoegh-Guldberg and Bruno 2010; Doney et al. 2012). Poleward shifting marine species have been entering the Arctic Ocean from both the Atlantic and the Pacific (Grebmeier et al. 2010; Wassmann et al. 2011). Boreal (warm-water affinity) species of fish have shifted extensively northward into the Arctic (Mueter and Litzow 2008; Grebmeier et al. 2006; Rand and Logerwell 2011; Christiansen et al. 2013; Fossheim et al. 2015).

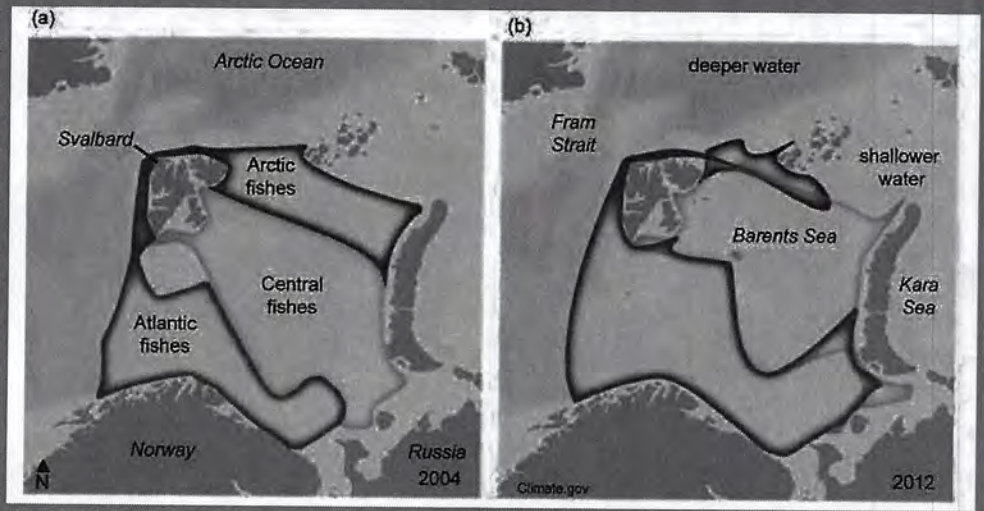

FIG. SB5.2. Comparison of the fish communities between the beginning of the Ecosystem Survey taken in the Barents Sea in (a) 2004 and (b) 2012, indicates a significant change in distribution. The Atlantic (red) and central (yellow) communities (boreal fish species) have shifted north and east, taking over areas previously occupied by the Arctic (blue) community (arctic fish species). Data are available only for the shaded areas. (After Fig. 1 in Fossheim et al. 2015.)

As an example, we present the recent climate-induced changes in the fish communities of the Barents Sea, the entrance point to the Arctic Ocean from the Atlantic. The results are based on a large-scale annual Ecosystem Survey that monitors the whole ice-free shelf of the Barents Sea in August–September, the season with the least sea ice. This cooperative survey between Russia (Knipovich Polar Research Institute of Marine Fisheries and Oceanography) and Norway (Institute of Marine Research) was initiated in 2004. Our focus is on observations for the period 2004–12, as they have been most thoroughly assessed.

In the Barents Sea, the present warming trend in water temperatures started in the late 1990s (Boitsov et al. 2012). The late summer temperature at the seafloor has increased by almost 1°C during the last decade alone. In this region, sub-zero water masses in late summer have almost disappeared and the sea ice is retreating. In association with this warming, boreal fish species have entered the northern parts of the Barents Sea in large numbers. The expansions of these fish species have led to a community-wide shift: boreal communities are now found farther north and the local Arctic (cold-water affinity) community has been almost pushed out of the area (Fig. SB5.2).

The fish species increasing in the north are large boreal fish predators, such as cod (*Gadus morhua*), beaked redfish (*Sebastes mentella*), and long rough dab (*Hippoglossoides platessoides*). These fish species are considered "generalists" in that they can use a wide range of habitats and feed on a diverse set of prey. As such, they are better able to thrive in a changing environment. Their northward expansion is likely related to warmer water temperatures and greater food availability for these fish species (Fossheim et al. 2015). For instance, increased primary productivity in the previously ice-covered area (Dalpadado et al. 2014) and increasing abundance and biomass of Atlantic zooplankton in the northern Barents Sea (Dalpadado et al. 2012) likely favor boreal over Arctic fish species.

Cod, the most important commercial species, has reached a record high population size due to a favorable climate and lower fishing pressure (Kjesbu et al. 2014). The cod stock in the Barents Sea has not been this high since the 1950s. High abundances have also been recorded for haddock (*Melanogrammus aeglefinus*), the other main commercial species, and for long rough dab, a common and widespread species in the Barents Sea. A poleward expansion of cod and haddock and a northeastward displacement of beaked redfish (*Sebastes mentella*) have been documented (Renaud et al. 2012; Hollowed et al. 2013; Fossheim et al. 2015).

The Arctic fish community, including various snail-

CONT. SIDEBAR 5.2: CLIMATE CHANGE IS PUSHING BOREAL FISH NORTHWARD TO THE ARCTIC: THE CASE OF THE BARENTS SEA—M. FOSSHEIM, R. PRIMICERIO, E. JOHANNESEN, R. B. INGVALDSEN, M. M. ASCHAN, AND A. V. DOLGOV

fishes, sculpins, and eel pouts, does not seem to cope well with warming water temperatures (Fossheim et al. 2015). Most of these Arctic fish species are relatively small, stationary, and feed on organisms living on the sea bottom. These species have a more specialized diet than the boreal fish species and are thus more vulnerable to climate change (Kortsch et al. 2015). In addition, they are adapted to life on the shallow shelf of the Barents Sea. Because the central Arctic Ocean is much deeper, it is unlikely that these species will move farther north. However, they can be found farther to the east on the neighboring shelf (e.g., Kara Sea; Fig. SB5.2).

Large fish and marine mammals can move quickly over large distances, while other species, such as small Arctic fish species and organisms that live on or near the seafloor, are more stationary. As a result, two previously separate communities are now mixing together (Fossheim et al. 2015). The larger fish species from the south will compete with the smaller Arctic species for food, and even prey on them directly. Thus, the Arctic community is being pressured from two sides: the marine environment is changing due to rising water temperatures, and new competitors and predators are arriving. It is anticipated that this could result in the local extinction of some Arctic fish species, such as the gelatinous snailfish (*Liparis fabricii*) and even the most abundant Arctic species, the Polar cod (*Boreogadus saida*).

One consequence of the general nature of large boreal fish moving into the Arctic is the development of novel feeding links between incoming and resident species, ultimately changing the configuration of the Arctic marine food web (Kortsch et al. 2015). Arctic food webs contain fewer feeding links than boreal food webs. As cod and other large fish species feeding on many prey move into arctic waters, they establish many new links in the Arctic food web, which becomes more tightly connected. The ecological effects of perturbations will spread faster and more widely in a more interconnected arctic food web, making it more susceptible to environmental stress (Kortsch et al. 2015).

e. *Greenland Ice Sheet*—M. Tedesco, J. E. Box, J. Cappelen, X. Fettweis, K. Hansen, T. Mote, C. J. P. P. Smeets, D. van As, R. S. W. van de Wal, I. Velicogna, and J. Wahr

The Greenland Ice Sheet covers an area of 1.71 million km^2. With a volume of 2.85 million km^3, it is the second largest glacial ice mass on Earth, smaller only than the Antarctic ice sheet. The amount of freshwater stored in the Greenland Ice Sheet has a sea level equivalent of ~7 m. The discharge of the ice to the ocean through runoff and iceberg calving not only increases sea level, but can also alter the ocean thermohaline circulation and global climate (Rahmstorf et al. 2015). Moreover, the high albedo (reflectivity) of the ice sheet surface (together with that of sea ice and snow on land) plays a crucial role in the regional surface energy balance (Tedesco et al. 2011) and the regulation of global air temperatures.

Estimates of the spatial extent of Greenland Ice Sheet surface melting (e.g., Mote 2007; Tedesco 2007; Tedesco et al. 2013) show that in 2015 (Fig. 5.9a) melting occurred over more than half of the ice sheet for the first time since the exceptional melt events of July 2012 (Nghiem et al. 2012). The 2015 melt extent exceeded two standard deviations above the 1981–2010 average, reaching a maximum of 52% of the ice sheet area on 4 July (Fig. 5.9d). By comparison, melt extent in 2014 reached a maximum of 39% of the ice sheet area and ~90% in 2012. A second period of melting, which began in late August, covered between 15% and 20% of the ice sheet (a mean of ~5% over the same period) and lasted until early September. In the summer of 2015 (June–August), the number of melting days along the southwestern and southeastern margins of the ice sheet was close to or below the long-term average, with maximum negative anomalies (i.e., below the 1981–2010 average) of 5–10 days (Fig 5.9a). In contrast, the number of melt days in the northeastern, western, and northwestern regions was up to 30–40 days above the 1981–2010 average, setting new records in terms of meltwater production and runoff over the northwestern regions.

The surface mass balance measured along the southwestern portion of the ice sheet at the K-transect for September 2014 through September 2015 (van de Wal et al. 2005, 2012) was the third least negative since the beginning of the record in 1990 (Tedesco et al. 2015). This is consistent with the negative melting anomalies along the southwestern portion of the ice sheet (Fig. 5.9a). At all PROMICE network stations (www.promice.dk; Ahlstrøm et al. 2008; van As et al. 2011) summer 2015 ablation was low with respect to the 2011–15 period of record (Fig. 5.9b), except at

the most northerly latitudes (Kronprins Christian Land, KPC, 80°N, 25°W; Thule, THU, 76°N, 68°W), where melt totals were slightly above average. The highest recorded melt in 2015, 5.1 m on the Qassimiut lobe (QAS_L station, 61°N, 47°W), was just over half the record-setting 9.3 m at that site in 2010 (Fausto et al. 2012).

Consistent with the distribution of melt anomalies, measurements at weather stations of the Danish Meteorological Institute (DMI; Cappelen 2015) during spring 2015 indicate that summer average temperature anomalies (relative to the 1981–2010 average) were positive at several northerly stations around the Greenland coastline, with values exceeding one standard deviation at Pituffik (+1.2 °C), Upernavik (+1.2°C) and Danmarkshavn (+0.9°C). In contrast, temperatures in south and southwest Greenland (e.g.,Paamiut, Narsarsuaq, Qaqortoq, and Prins Christian Sund) were 1.5 standard deviations below the 1981–2010 average, with temperature anomalies as much as –2.6°C at Narsarsuaq (Tedesco et al. 2015). These widespread low temperatures are consistent with a strong negative spring temperature anomaly centered over Greenland (see section 5b, Fig. 5.2b). Danmarkshavn also experienced its warmest January on record, with a +7.7°C anomaly. A new record August low temperature of –39.6°C occurred on 28 August at Summit (3216 m a.s.l.).

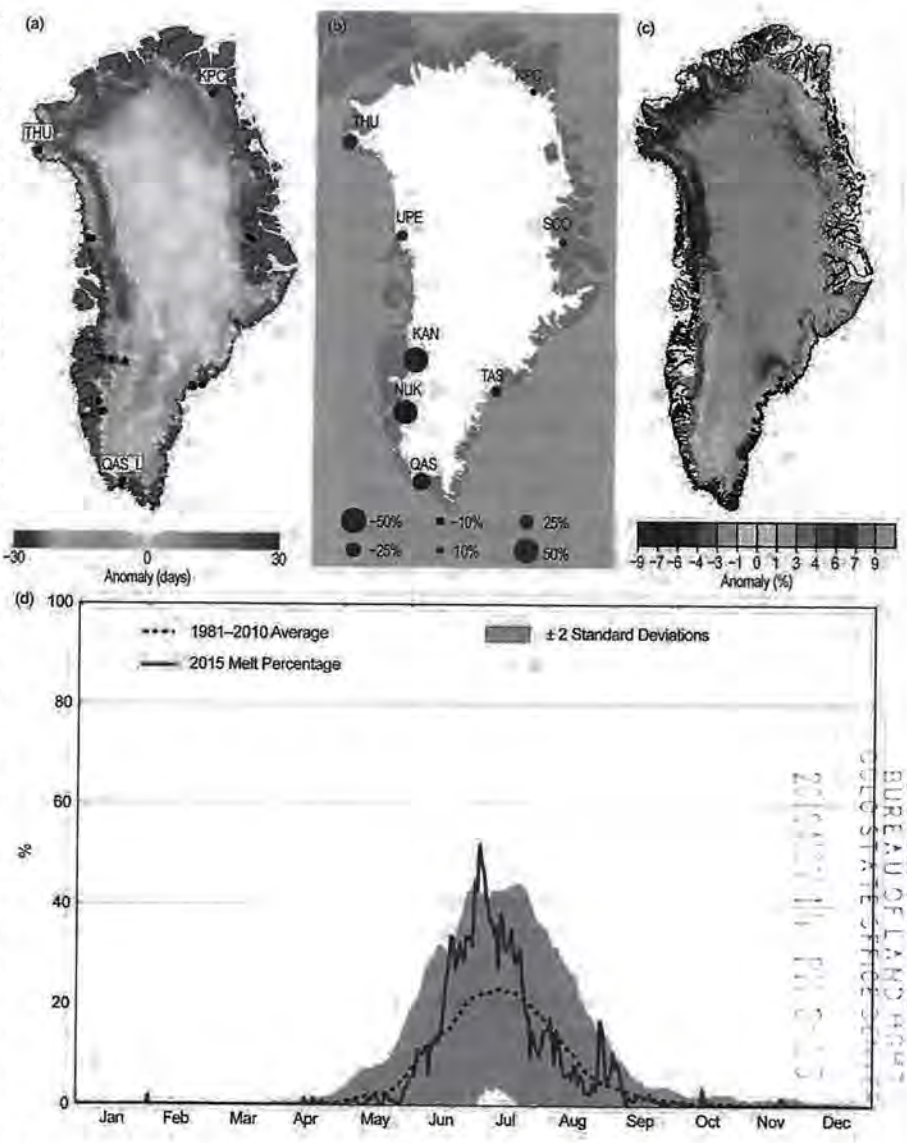

Fig. 5.9. (a) Map of the anomaly (with respect to the 1981–2010 average) of the number of days when melting was detected in summer 2015 using spaceborne passive microwave data. The locations of the stations used for the in situ analysis of surface mass balance and temperature are reported on the map as black disks (PROMICE) and cyan triangles (K-transect). (b) Summer 2015 ablation at PROMICE stations with respect to the 2011–15 period of record. (c) Greenland Ice Sheet surface albedo anomaly for JJA 2015 relative to the average for those months between 2000 and 2009 derived from MODIS data. (d) Daily spatial extent of melting from Special Sensor Microwave Imager/ Sounder (SSMIS) as a percentage of the total ice sheet area for all of 2015. The 1981–2010 average spatial extent of melting (dashed line) and ±2 std. dev. of the mean (shaded) are also plotted for reference.

The average albedo for the Greenland Ice Sheet in summer 2015, derived from data collected by the Moderate-resolution Imaging Spectroradiometer (MODIS, after Box et al. 2012), was below the 2000–09 average over the northwestern region and above the average in the southwest (Fig. 5.9c), consistent with the negative surface mass balance and melting day anomalies measured over the same region (Fig. 5.9a). The trend of mean summer albedo over the entire ice sheet for the period 2000–15 remained negative and was estimated to be –5.5% ± 0.4%. In July 2015, when extensive melting occurred (Fig. 5.9d), albedo

averaged over the entire ice sheet was 68%. Albedo in July 2015 was as much as 15%–20% below average along the northwestern ice sheet and along the west coast, where a large increase in melting days was observed in 2015. Over the entire summer, however, the albedo anomaly along the southwestern ice sheet margin coast was positive, consistent with a relatively shorter melt season and with the presence of summer snow accumulation.

GRACE satellite data (Velicogna et al. 2014) are used to estimate monthly changes in the total mass of the Greenland Ice Sheet, including mass gain due to accumulation and summer losses due to runoff and calving (Fig. 5.10). Between the beginning of September 2014 and the beginning of September 2015 GRACE recorded a 174 ± 45 Gt (Gt ≡ 10^9 tons) mass loss, versus an average September-to-September loss of 278 ± 35 Gt for the 2002–15 period. As a comparison, the 2013–14 September-to-September loss was 236 ± 45 Gt (7% of the total loss of ~ 3500 Gt since the beginning of the GRACE record in 2002) and that for 2011–12 was 638 ± 45 Gt (18% of the total loss). The relatively modest loss for the 2014–15 period is consistent with reduced melting over the southwest portion of the ice sheet and increased summer snowfall.

Glacier front classification in LANDSAT and ASTER imagery (after Jensen et al. 2016) reveals that 45 of the widest and fastest flowing marine-terminating glaciers retreated at a slower rate in 2013–15 than in the 1999–2012 period (Fig. 5.11). Between the end of the 2014 melt season and the end of the 2015 melt season, 22 of the 45 glaciers retreated, but the advance of 9 relatively wide glaciers resulted in the lowest annual net area loss in the 16-year period of observations (1999–2015), being –16.5 km^2 or 7.7 times lower than the annual average area change trend of –127 $km^2\ yr^{-1}$ (Fig. 5.11). Specifically, Petermann Glacier advanced by 0.68 km across a width of 17.35 km, and Kangerdlugssuaq Glacier advanced by 1.68 km across a width of 6.01 km.

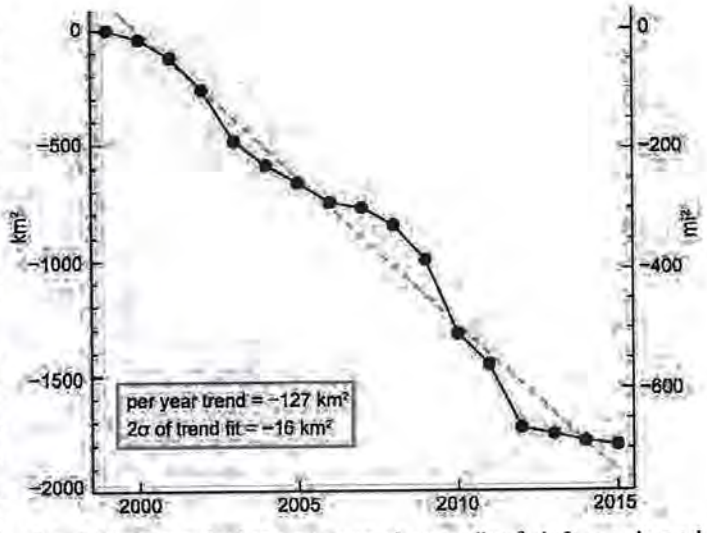

Fig. 5.11. Cumulative net area change (km^2, left y-axis and square miles, right y-axis) of 45 of the widest and fastest-flowing marine-terminating glaciers of the Greenland Ice Sheet (Box and Hansen 2015; Jensen et al. 2016). The linear regression is dashed.

f. Glaciers and ice caps outside Greenland—G. Wolken, M. Sharp, L. M Andreassen, A. Arendt, D. Burgess, J. G. Cogley, L. Copland, J. Kohler, S. O'Neel, M. Pelto, L. Thomson, and B. Wouters

Mountain glaciers and ice caps cover an area of over 400 000 km^2 in the Arctic and are a leading contributor to global sea level change (Gardner et al. 2011, 2013; Jacob et al. 2012). They gain mass by snow accumulation and lose mass by surface melt runoff, and by iceberg calving where they terminate in water (ocean or lake). The total mass balance (ΔM) is defined as the difference between annual snow accumulation and annual mass losses (by iceberg calving plus surface melt runoff). Of the 27 glaciers currently monitored, however, only three (Kongsvegen, Hansbreen, and Devon Ice Cap NW) lose any mass by iceberg calving into the ocean. For all glaciers discussed here, the climatic mass balance is reported (B_{clim}, the difference between annual snow accumulation and annual runoff). B_{clim} is a widely used index of how glaciers respond to climate variability and change.

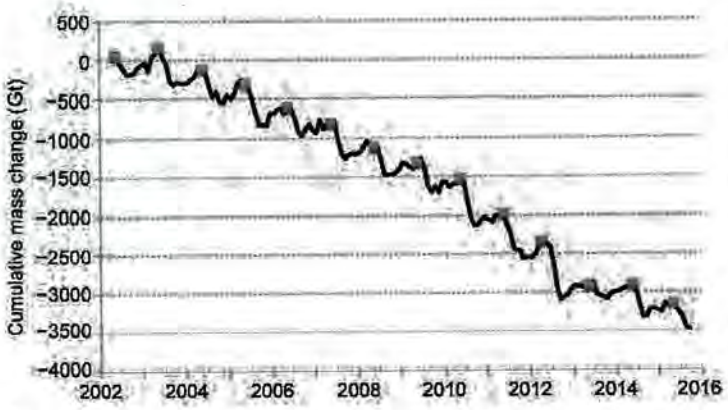

Fig. 5.10. Cumulative change in the total mass (Gt) of the Greenland Ice Sheet between Apr 2002 and Sep 2015 estimated from GRACE measurements. The square symbols denote Apr values for reference.

B_{clim} measurements for mass balance year 2014/15 are available for only 9 of the 26 glaciers that are monitored across the Arctic (three each in Alaska and Svalbard, and one in Norway), and some of these are still provisional. Therefore, we focus on the 2013/14 B_{clim} measurements, which are available for 21 glaciers (WGMS 2015b). These glaciers are located in Alaska (three), Arctic Canada (four), Iceland (seven), Svalbard (three), Norway (three), and Sweden (one; Fig. 5.12; Table 5.1). For these glaciers as a group, the mean B_{clim} in 2013/14 was negative. However, five glaciers [one each in Arctic Canada (Meighen Ice Cap) and Iceland (Dyngjujökull) and three in Svalbard (Midre Lovenbreen, Austre Broggerbreen, and Kongsvegen)] had positive balances.

For the Arctic as a whole, 2013/14 was the 17th most negative mass balance year on record (the first record dates from 1946) and the 12th most negative year since 1989 (i.e., the median for the 25-year period), when annual measurements of at least 20 glaciers began. This balance year continues the increasingly negative trend of cumulative regional climatic mass balances, calculated by summing the annual mean mass balances for all glaciers in each reporting region of the Arctic (Fig. 5.13). For Svalbard, 2013/14 was among the least negative mass balance years on record, and the climatic balances of each of its three glaciers were among the 3–9 most positive since 1987. Local meteorological observations suggest that the positive balances in Svalbard were attributable to high winter (October–May) precipitation, especially at low elevations, that was followed by a relatively cool summer (June–August). Melt suppression over Svalbard, as well as the Russian Arctic Archipelagos and the northernmost islands of Arctic Canada, was likely linked to negative 850-hPa air temperature anomalies in June–September. In contrast, in 2013/14 the mean measured climatic balance of glaciers in Alaska was the fifth most negative since 1966, with Lemon Creek and Wolverine glaciers registering their third and fourth most negative years on record, respectively. The negative balances of Alaska, Iceland, and northern Scandinavia glaciers in 2013/14 were most likely linked to melt increases caused by positive air temperature anomalies at the 850-hPa level in July–September that exceeded +2.5°C in northern Norway and Sweden (data from NCEP–NCAR reanalysis). Indeed, in 2014, many locations in northern Scandinavia reported their highest summer air temperatures since records began (Overland et al. 2015).

Among the nine glaciers for which 2014/15 B_{clim} measurements have been reported, the balances of glaciers in Alaska, Svalbard, and northern Norway

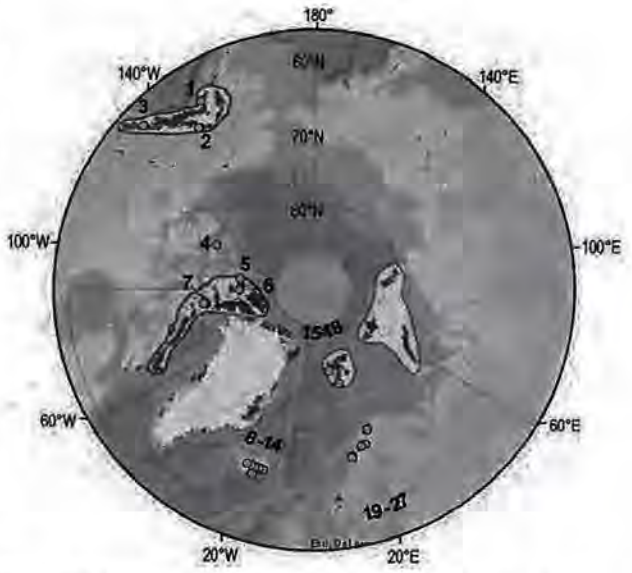

FIG. 5.12. Locations (green circles) of 27 Arctic glaciers with long-term records of annual climatic mass balance (B_{clim}). See Table 5.1 for glacier names. Regions outlined in yellow are the Randolph Glacier Inventory (RGI) regions of the Arctic (Pfeffer et al. 2014). In regions where individual glaciers are located too close together to be identifiable on the map, their numbers are shown at the edge of the RGI region in which they occur. Red shading indicates glaciers and ice caps, including ice caps in Greenland outside the ice sheet. Yellow shading shows the solution domains for regional mass balance estimates for Alaska, Arctic Canada, Russian Arctic, and Svalbard derived using gravity data from the GRACE satellites (see Fig. 5.3).

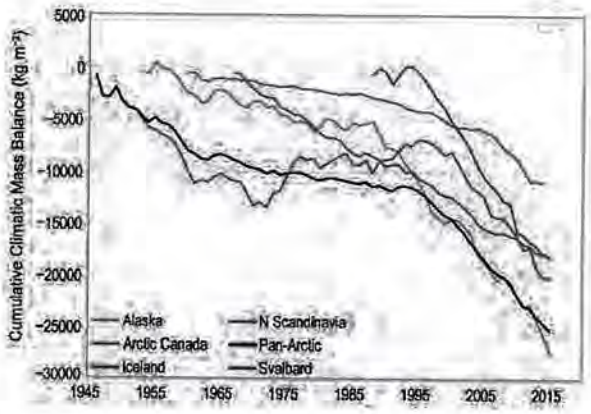

FIG. 5.13. Cumulative climatic mass balances (B_{clim} in kg m^{-2}) for glaciers in five regions of the Arctic and for the Arctic as a whole (Pan-Arctic). Mean balances are calculated for glaciers monitored in each region in each year and these means are summed over the period of record. Note that the period of monitoring varies between regions and that the number and identity of glaciers monitored in a given region may vary between years.

Table 5.1. Measured annual climatic mass balance (B_{clim}) of glaciers in Alaska, the Canadian Arctic, Iceland, Svalbard, and northern Scandinavia for 2013/14 and 2014/15, along with the 1980–2010 mean and standard deviation for each glacier (column 3). Mass balance data are from the World Glacier Monitoring Service (2015; 2016), with corrections to Svalbard data provided by J. Kohler and to Alaska data provided by S. O'Neel, and with updates from the Norwegian Water Resources and Energy Directorate (NVE) database. Numbers in column 1 identify glacier locations in Fig. 5.1. Note that 2014/15 results may be based upon data collected before the end of the 2015 melt season and may be subject to revision.

Region	Glacier (Record length, years)	Mean Climatic Balance 1980–2010 (kg m^{-2} yr^{-1})	Standard Deviation of Climatic Mass Balance 1980–2010 (kg m^{-2} yr^{-1})	Climatic Balance 2013/14 (kg m^{-2} yr^{-1})	Climatic Balance 2014/15 (kg m^{-2} yr^{-1})
Alaska					
1	Wolverine (50)	−285	1205	−1950	−1130
3	Lemon Creek (63)	−584	709	−1825	−2270
2	Gulkana (50)	−505	738	−220	−1440
Arctic Canada					
7	Devon Ice Cap (54)	−153	176	−246	
5	Meighen Ice Cap (53)	−173	284	+57	
4	Melville South Ice Cap (52)	−295	369	−159	
6	White (52)	−239	260	−417	
Iceland					
8	Langjökull S. Dome (18)	−1448	817	−1950	
9	Hofsjökull E (24)	−602	1009	−990	
9	Hofsjökull N (25)	−606	787	−950	
9	Hofsjökull SW (24)	−978	947	−990	
14	Köldukvislarjökull (22)	−529	738	−887	
10	Tungnaarjökull (23)	−1170	873	−1535	
13	Dyngjujökull (17)	−133	912	+170	
12	Brúarjökull (22)	−367	660	−34	
11	Eyjabakkajökull (23)	−867	813	−353	
Svalbard					
17	Midre Lovenbreen (48)	−356	305	+30	−450
16	Austre Broggerbreen (49)	−469	342	+10	−610
15	Kongsvegen (29)	−70	378	+140	−160
18	Hansbreen (26)	−431	512	−227	
Nortern Scandinavia					
20	Engabreen (45)	+463	1091	−892	+668
21	Langfjordjøkelen (25)	−927	781	−780	−800
22	Marmaglaciaren (23)	−430	525		
23	Rabots Glaciar (29)	−394	560		
24	Riukojietna (26)	−592	805		
25	Storglaciaren (68)	−113	698	−890	
26	Tarfalaglaciaren (18)	−212	1101		
27	Rundvassbreen (8)	−777		−790	−20

(Langfjordjøkelen) were negative, while those of glaciers in central Norway were near balance (Rundvassbreen) or positive (Engabreen). The pattern of negative balances in Alaska and Svalbard is also captured in time series of regional total stored water estimates (Fig. 5.14), derived using GRACE satellite gravimetry available since 2003. Annual storage changes are proxy for changes in the regional annual glacier mass balance (ΔM) for the heavily glacierized regions of the Arctic (Luthcke et al. 2013). Measurements of ΔM in 2014/15 for all the glaciers and ice caps in Arctic Canada and the Russian Arctic also

show a negative mass balance year. The GRACE-derived time series clearly show a continuation of negative trends in ΔM for all measured regions in the Arctic. These measurements of B_{clim} and ΔM are consistent with anomalously warm (up to +1.5°C) June–August air temperatures over Alaska, Arctic Canada, the Russian Arctic, and Svalbard in 2015 (section 5b), and anomalously cool temperatures in northern Scandinavia, particularly in June and July (up to −2°C).

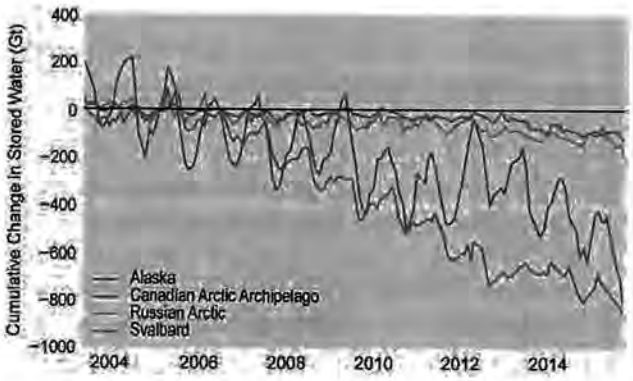

Fig. 5.14. Cumulative changes in regional total stored water for 2003–15 (Gt), derived using GRACE satellite gravimetry. Annual storage changes are proxy for changes in the regional annual glacier mass balance (ΔM). The estimated uncertainty in regional mass changes is 10 Gt yr^{-1} for the Gulf of Alaska, 8 Gt yr^{-1} for the Canadian Arctic, 8 Gt yr^{-1} for the Russian Arctic, and 4 Gt yr^{-1} for Svalbard. These errors include the formal error of the least squares fit and the uncertainties in the corrections for glacial isostatic adjustment, Little Ice Age, and terrestrial hydrology.

g. Terrestrial snow cover—C. Derksen, R. Brown, L. Mudryk, and K. Luojus

The Arctic (land areas north of 60°N) is always completely snow-covered in winter and almost snow free in summer, so the transition seasons of autumn and spring are significant when characterizing variability and change. The timing of spring snowmelt is particularly significant because the transition from highly reflective snow cover to the low albedo of snow-free ground is coupled with increasing solar radiation during the lengthening days of the high-latitude spring. The 2015 spring melt season provided continued evidence of earlier snowmelt across the terrestrial Arctic. There is increased awareness of the impact of these changes on the Arctic climate system, the freshwater budget, other components of the cryosphere (such as permafrost and associated geochemical cycles), and Arctic ecosystems (Callaghan et al. 2011).

Snow cover extent (SCE) anomalies (relative to the 1981–2010 reference period) for the 2015 Arctic spring (April, May, June) were computed separately for the North American and Eurasian sectors of the Arctic from the NOAA snow chart Climate Data Record, maintained at Rutgers University (Estilow et al. 2015; http://climate.rutgers.edu/snowcover/). Consistent with nearly all spring seasons of the past decade, both May and June SCE anomalies were strongly negative in 2015 (Fig. 5.15); June SCE in both the North American and Eurasian sectors of the Arctic was the second lowest in the snow chart record, which extends back to 1967.

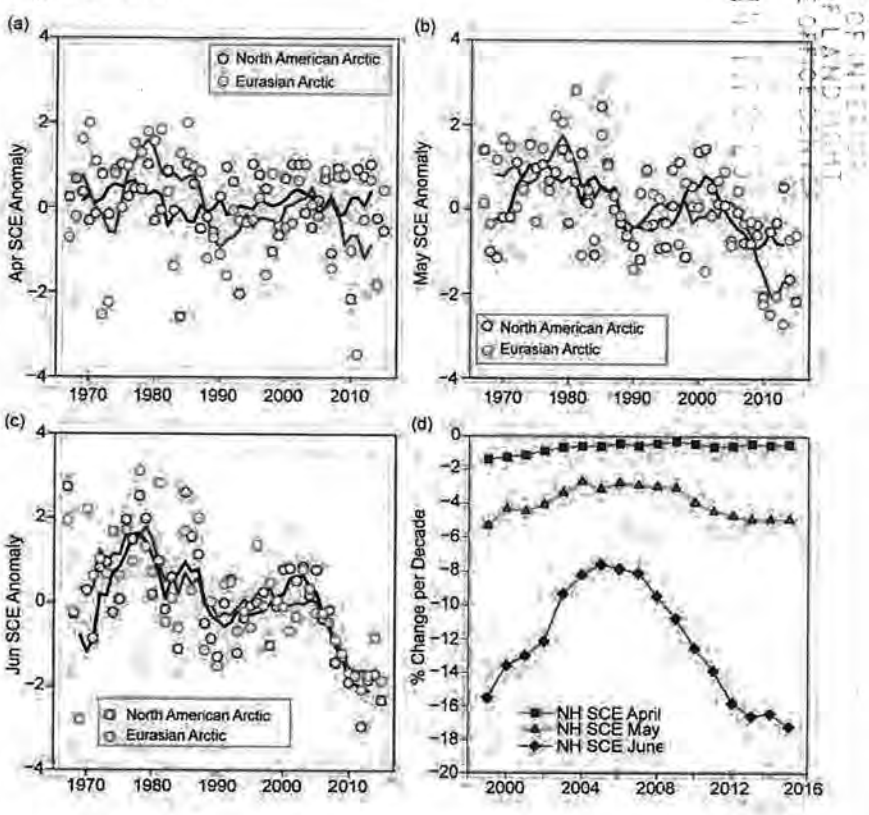

Fig. 5.15. Monthly Arctic snow cover extent standardized (and thus unitless) anomaly time series (with respect to 1981–2010) from the NOAA snow chart Climate Data Record for (a) Apr, (b) May, and (c) Jun 1967–2015 (solid lines denote 5-yr moving average); (d) % change decade^{-1} in spring snow cover extent for running time series starting in 1979 (1979–98, 1979–99, 1979–2000, etc.).

For the fifth time in the past six years (2010–15), Arctic SCE in June was below 3 million km^2 despite never falling below this threshold in the previous 43 years of the snow chart data record (1967–2008). Figure 5.15d shows the changing rate of SCE loss across the Arctic since 1998 via calculations over running time periods since 1979, the first year of the satellite passive microwave record used to track sea ice extent. The April and May SCE reductions have remained relatively consistent year over year, ranging between –1% and –2% decade^{-1} (April; insignificant at 95%) and –3% and –5% per decade^{-1} (May; significant at 99%). A significant rate of June SCE loss was identified over the first 20 years (nearly –16% for 1979–98) due to rapid reductions in the 1980s, which then plateaued due to a period of stable spring snow cover during the 1990s. Since 2005, the rate of June SCE loss has increased again, reaching almost 18% decade^{-1} for the period 1979–2015 (compared to the 1981–2010 mean June SCE). Since 2011, the rate of June snow cover loss has exceeded the much publicized rate of September sea ice loss (section 5c).

There are complex interactions between regional variability in the onset of snow cover in the autumn, subsequent winter season snow accumulation patterns (which themselves are driven by the complex interplay of temperature and precipitation anomalies), and continental-scale spring SCE anomalies (shown in Fig. 5.15). Snow cover duration (SCD) departures (relative to the 1998–2010 period) derived from the NOAA daily Interactive Multi-sensor Snow and Ice Mapping System (IMS) snow cover product (Helfrich et al. 2007) suggest earlier snow cover onset in the autumn over much of the Arctic for the 2014/15 snow year (Fig. 5.16a). This is consistent with premelt April snow depth anomalies (relative to the 1999–2010 average), derived from the Canadian Meteorological Centre (CMC) daily gridded global snow depth analysis (Brasnett 1999), which were largely positive over much of the Arctic land surface (25.1% and 33.7%, respectively, for the North American and Eurasian sectors of the Arctic). There was a notable east–west snow depth gradient across Eurasia in April 2015 with above-average snow depth in eastern Siberia and below-average snow depth across western Siberia and northern Europe. The North American Arctic was characterized by a more latitudinal gradient of deeper-than-normal snow depth north of the boreal tree line and shallower-than-normal snow depth across the boreal forest. Note that the CMC results shown in Figs. 5.17a–c mask out anomalies over high elevation areas (in the Canadian Arctic Archipelago, Baffin Island, coastal Alaska) known to be affected by a bias toward higher winter snow depths since 2006 due to changes in the resolution of the precipitation forcing used as part of the CMC analysis. Strong positive surface temperature anomalies over central Siberia, Alaska, and the western Canadian Arctic in May (which persisted into June; section 5b) were associated with rapid reductions in regional snow depth reflected in the May and June depth anomalies (Figs. 5.17b,c) and earlier than normal snowmelt in these regions (Fig. 5.16b), which drove the negative continental-scale SCE anomalies in May and June (Figs. 5.16b,c).

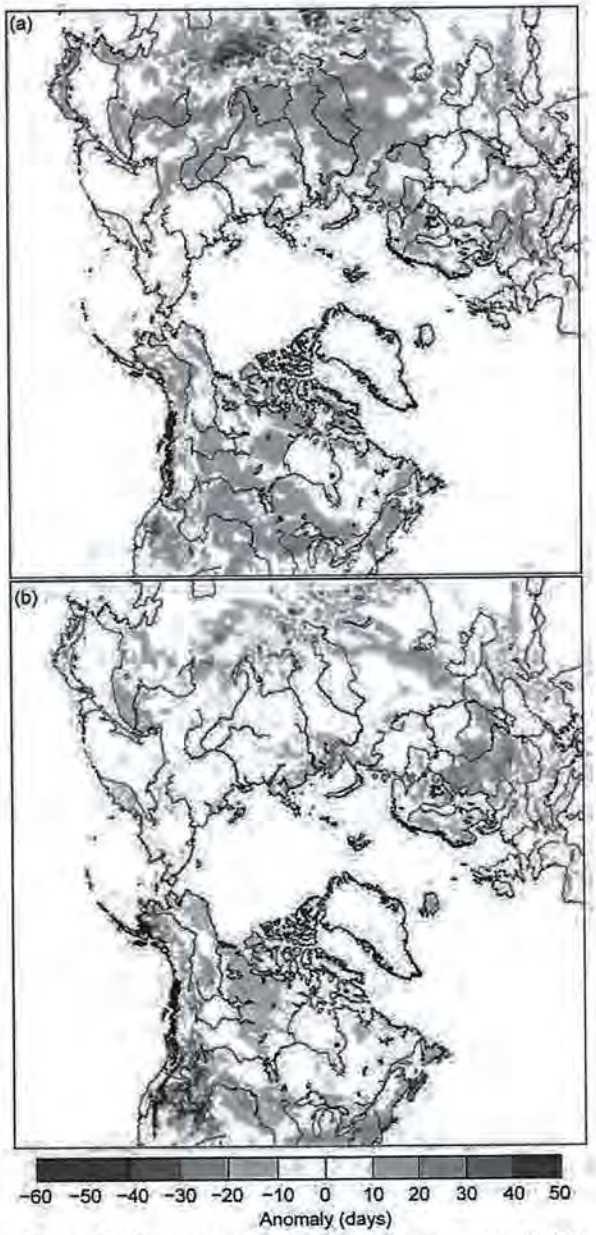

Fig. 5.16. Snow cover duration departures (with respect to 1998–2010) from the NOAA IMS data record for the (a) 2014 autumn season and (b) 2015 spring season.

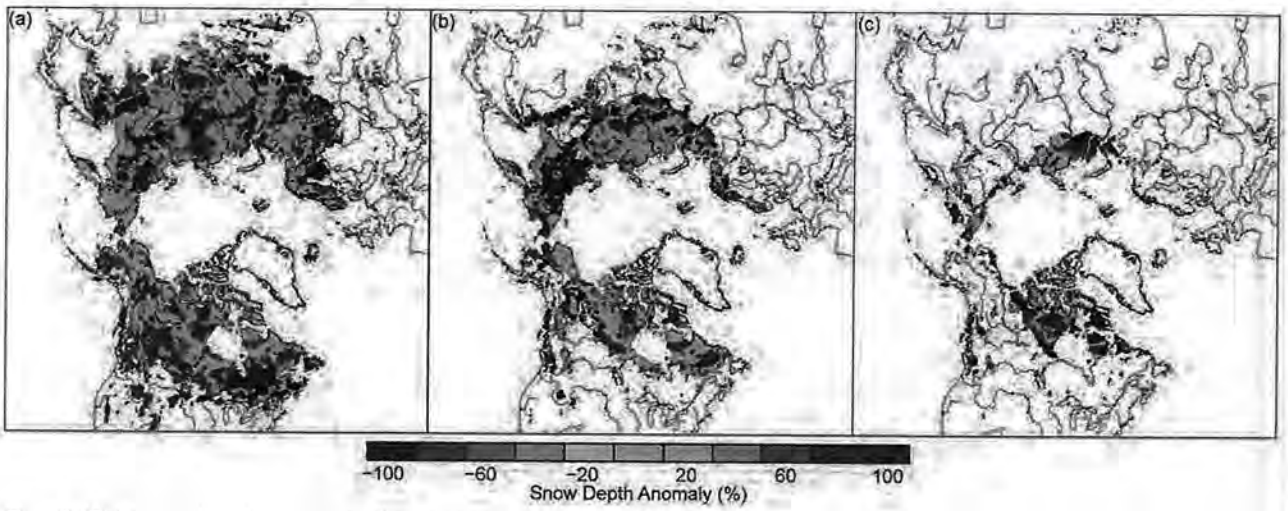

FIG. 5.17. Snow depth anomaly (% of 1999–2010 average) from the CMC snow depth analysis for (a) Apr, (b) May, and (c) Jun 2015.

h. River discharge—R. M. Holmes, A. I. Shiklomanov, S. E. Tank, J. W. McClelland, and M. Tretiakov

River discharge integrates hydrologic processes occurring throughout the surrounding landscape. Consequently, changes in the discharge of large rivers can be a sensitive indicator of widespread changes in watersheds (Rawlins et al. 2010; Holmes et al. 2013). Changes in river discharge also impact coastal and ocean chemistry, biology, and circulation. This interaction is particularly strong in the Arctic, given the relative volume of river discharge to ocean volume. Rivers in this region transport >10% of the global river discharge into the Arctic Ocean, which represents only ~1% of the global ocean volume (Aagaard and Carmack 1989; McClelland et al. 2012).

In this section, annual river discharge values since 2011 are presented for the eight largest Arctic rivers, and recent observations are compared to a 1980–89 reference period (the first decade with data from all eight rivers). Six of the rivers lie in Eurasia and two are in North America. Together, the watersheds of these rivers cover 70% of the 16.8×10^6 km^2 pan-Arctic drainage area and, as such, account for the majority of riverine freshwater inputs to the Arctic Ocean (Fig. 5.18). Discharge data for the six Eurasian rivers are analyzed through 2015, whereas data from the Yukon and Mackenzie Rivers in North America are only available through 2014. Most of these data are now available through the Arctic Great Rivers Observatory (www.arcticgreatrivers.org).

A long-term increase in Arctic river discharge has been well documented and may be linked to increasing precipitation associated with global warming (Peterson et al. 2002; McClelland et al. 2006; Shiklomanov and Lammers 2009; Overeem and Syvitski 2010; Rawlins et al. 2010). The long-term discharge trend is greatest for rivers of the Eurasian Arctic and constitutes the strongest evidence of intensification of the Arctic freshwater cycle (Rawlins et al. 2010).

In 2015, the combined discharge of 2051 km^3 for the six largest Eurasian Arctic rivers was 15% greater than the 1980–89 average (Fig. 5.19; Table 5.2), and the peak discharge occurred earlier than the average over the same period (Fig. 5.20). This is the fourth highest combined discharge value since measurements began in 1936. The four highest values have

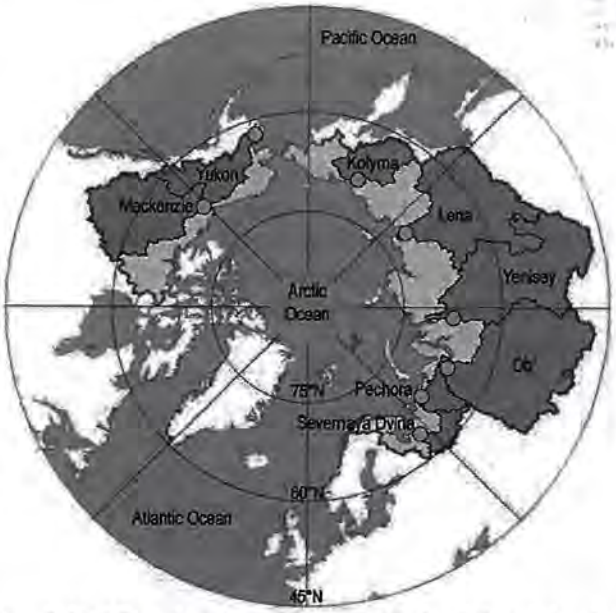

FIG. 5.18. Map showing the watersheds of the eight rivers featured in this section. The blue dots show the location of the discharge monitoring stations and the red line shows the boundary of the pan-Arctic watershed.

TABLE 5.2. Annual discharge for 2012, 2013, and 2014 for the eight largest Arctic rivers, compared to long-term and decadal averages back to the start of observations. Values for 2015 are provided for the six Eurasian rivers. Red values indicate provisional data, which are subject to modification before official data are released.

Discharge ($km^3\ yr^{-1}$)									
	Yukon	Mackenzie	Pechora	S. Dvina	Ob'	Yenisey	Lena	Kolyma	Sum
2015			123	80	527	654	585	82	
2014	227	272	116	91	448	640	607	86	2487
2013	213	311	82	97	372	527	600	80	2282
2012	232	306	103	117	300	458	665	59	2240
Average 2010–15	212	293	108	93	409	594	583	75	2366
Average 2000–09	207	305	124	103	415	640	603	78	2475
Average 1990–99	217	275	117	111	405	613	532	68	2338
Average 1980–89	206	273	108	100	376	582	549	68	2262
Average 1970–79	184	292	108	94	441	591	529	65	2304
Average 1960–69		273	112	98	376	546	535	73	
Average 1950–59			110	108	380	566	511	74	
Average 1940–49			102	100	424	578	498	72	
Average for Period of Record	206	286	111	100	401	589	540	71	2305

all occurred in the past 14 years. Overall, the most recent data indicate a continuing long-term increase in Eurasian Arctic river discharge, at a rate of 3.5% ± 2.1% $decade^{-1}$ since 1976. Looking more closely at recent years, Eurasian Arctic river discharge generally declined between 2007 and 2012 and then began to increase again in 2013. Values for 2012 (1702 km^3), 2013 (1759 km^3), and 2014 (1989 km^3) were 5% less, 1% less, and 2% greater than the 1980–89 period, respectively. The short-term variability in Eurasian Arctic river discharge is consistent with previous increases and decreases over 4–6 year intervals in the past (Fig. 5.19).

For the North American Arctic rivers considered here (Yukon and Mackenzie), the combined discharge declined each year from 2012 (538 km^3) to 2014 (499 km^3), yet in each of those years the combined discharge was greater than the long-term average (493 $km^3\ year^{-1}$; Fig. 5.19; Table 5.2). Thus, as discussed for Eurasian rivers, these most recent data indicate a longer-term pattern of increasing river discharge (Fig. 5.19). At a rate of 2.6% ± 1.7% $decade^{-1}$ since 1976, the overall trends of increasing discharge are remarkably similar for the North American and Eurasian rivers. (Increases per decade follow a Mann–Kendall trend analysis; error bounds are 95% confidence intervals for the trend.)

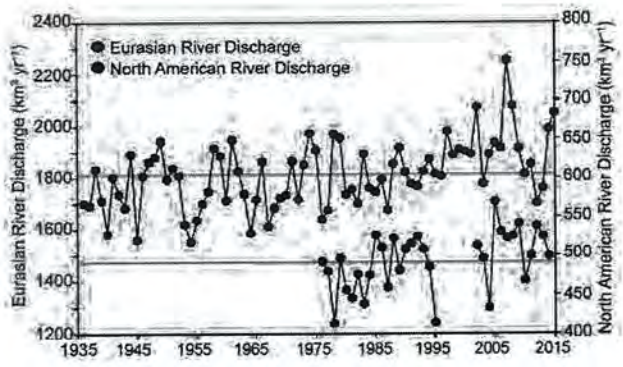

FIG. 5.19. Long-term trends in annual discharge for Eurasian and North American Arctic rivers. The Eurasian rivers are Severnaya Dvina, Pechora, Ob', Yenisey, Lena, and Kolyma. The North American rivers are Yukon and Mackenzie. Note the different scales for the Eurasian and North American river discharge; discharge from the former is 3–4 times greater than the latter. Reference lines show long-term means for the Eurasian (1812 $km^3\ yr^{-1}$, 1936–2015) and North American (493 $km^3\ yr^{-1}$, 1976–2014) rivers.

FIG. 5.20. Combined daily discharge for the six Eurasian Arctic rivers in 2015 compared to the 1980–89 average.

Considering the eight Eurasian and North American Arctic rivers together, their combined discharge in 2014 (2487 km^3) was 10% greater than the average discharge for 1980–89. Comparing 2014 to 2012, the combined discharge of these eight rivers was almost 250 km^3 greater in 2014. For perspective, 250 km^3 is approximately 14 times the annual discharge of the Hudson River, the largest river on the east coast of the United States.

i. Terrestrial permafrost—V. E. Romanovsky, S. L. Smith, K. Isaksen, N. I. Shiklomanov, D. A. Streletskiy, A. L. Kholodov, H. H. Christiansen, D. S. Drozdov, G. V. Malkova, and S. S. Marchenko

Permafrost is defined as soil, rock, and any other subsurface earth material that exists at or below 0°C continuously for two or more consecutive years. On top of permafrost is the active layer, which thaws during the summer and freezes again the following winter. The mean annual temperature of permafrost and the active layer thickness (ALT) are good indicators of changing climate and therefore designated as essential climate variables (Smith and Brown 2009; Biskaborn et al. 2015) by the Global Climate Observing System Program of the World Meteorological Organization. Changes in permafrost temperatures and ALT at undisturbed locations in Alaska, Canada, Russia, and the Nordic region (Fig. 5.21) are reported here. Regional variability in permafrost temperature records, described below, indicates more substantial permafrost warming since 2000 in higher latitudes than in the subarctic. This is in general agreement with the pattern of average air temperature anomalies.

In 2015, record high temperatures at 20-m depth were measured at all permafrost observatories on the North Slope of Alaska (Barrow, West Dock, Franklin Bluffs, Happy Valley, and Galbraith Lake in Fig. 5.22a; Romanovsky et al. 2015). The permafrost temperature increase in 2015 was substantial and comparable to the highest rate of warming observed in this region so far, which occurred during the period 1995–2000; 20-m depth temperatures in 2015 were from 0.10°C to 0.17°C higher than those in 2014 (Fig. 5.22a) on the North Slope. Since 2000, temperature at 20-m depth in this region has increased between 0.21°C and 0.66°C $decade^{-1}$ (Fig. 5.22a; Table 5.3). Permafrost temperatures in Interior Alaska were higher in 2015 than 2014 at all sites (Old Man, College Peat, Birch Lake, Gulkana, and Healy in Fig. 5.22b), except for Coldfoot. Notably, this warming followed slight cooling of 2007–13 (Fig. 5.22b). However, the recent warming in the interior (see section 5b; Fig. 5.2) was not strong enough to bring permafrost temperatures back to the record highs observed between the mid-1990s and the mid-2000s except at Gulkana (Fig. 5.22b; Table 5.3).

In northwestern Canada, temperatures in warm permafrost of the central Mackenzie Valley (Norman Wells and Wrigley in Fig. 5.22b) were similar in 2014/15 to those observed the previous year.

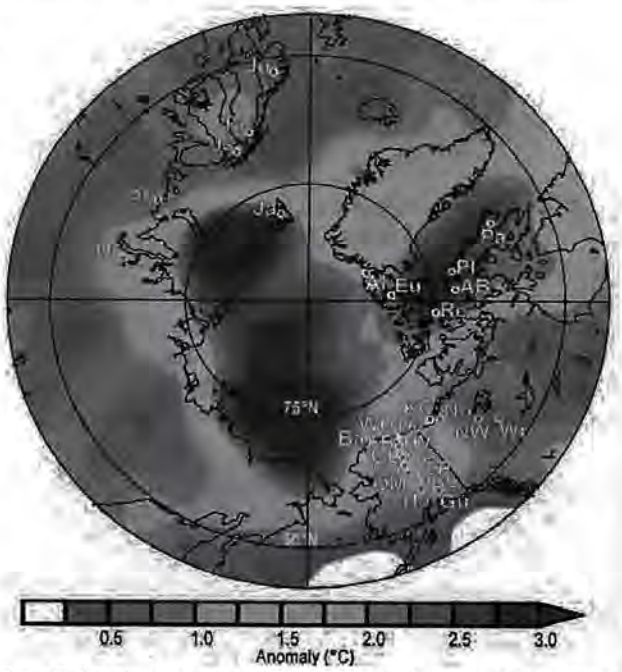

FIG. 5.21. Location of the permafrost monitoring sites shown in Fig. 5.22 superimposed on average air temperature anomalies during 2000–14 (with respect to the 1971–2000 mean) from the NCEP–NCAR reanalysis (Kalnay et al. 1996) (Source: NOAA/ESRL.) Sites shown in Fig. 5.22 are (a) Barrow (Ba), West Dock (WD), KC-07 (KC), Deadhorse (De), Franklin Bluffs (FB), Galbraith Lake (GL), Happy Valley (HV), Norris Ck (No); (b) College Peat (CP), Old Man (OM), Chandalar Shelf (CS), Birch Lake (BL), Coldfoot (Co), Norman Wells (NW), Wrigley 2 (Wr), Healy (He), Gulakana (Gu), Wrigley 1 (Wr); (c) Eureka EUK4 (Eu), Alert BH2 (Al), Alert BH5 (Al), Resolute (Re), Alert BH1 (Al), Arctic Bay (AB), Pond Inlet (PI), Pangnirtung (Pa); (d) Janssonhaugen (Ja), Urengoy #15-10 (Ur), Juvvasshøe (Ju), Tarfalaryggen (Ta), Bolvansky #59 (Bo), Bolvansky #65 (Bo), Urengoy #15-06 (Ur), Bolvansky #56 (Bo), Iskoras Is-B-2 (Is).

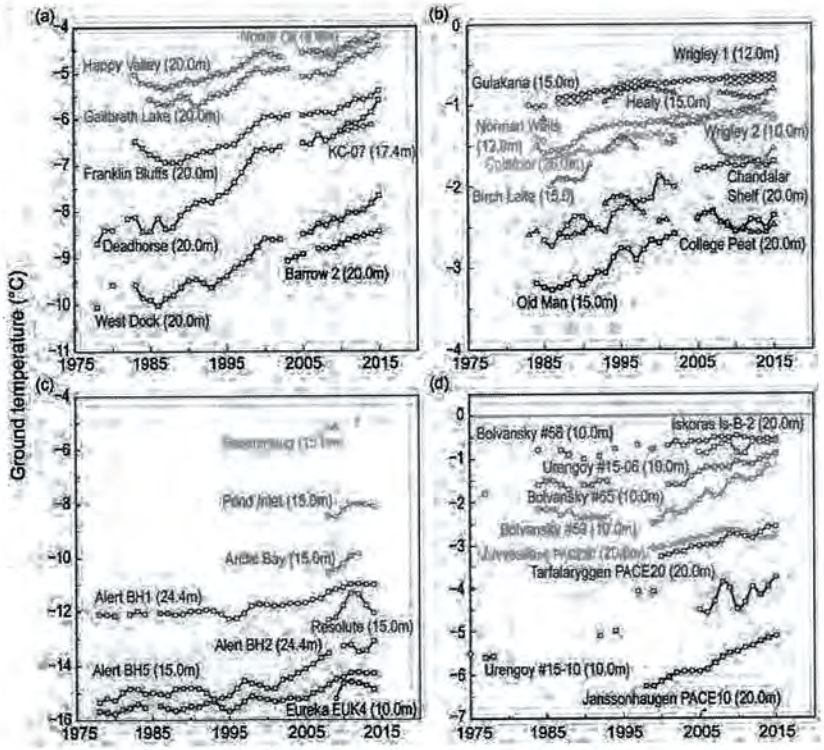

FIG. 5.22. Time series of mean annual ground temperature at depths of 9–26 m below the surface at selected measurement sites that fall roughly into the Adaptation Actions for a Changing Arctic Project (AMAP 2015) priority regions: (a) cold continuous permafrost of NW North America (Beaufort–Chukchi region); (b) discontinuous permafrost in Alaska and northwestern Canada; (c) cold continuous permafrost of eastern and high Arctic Canada (Baffin Davis Strait); (d) continuous to discontinuous permafrost in Scandinavia, Svalbard, and Russia/Siberia (Barents region). Temperatures are measured at or near the depth of penetration of the seasonal ground temperature variations. Data series are updated from Christiansen et al. 2010; Romanovksy et al. 2015; Smith et al. 2015; Ednie and Smith 2015.

TABLE 5.3. Change in mean annual ground temperature (MAGT; °C decade^{-1}) for sites shown in Fig. 5.22, for which data are available for 2015 († indicates discontinuous permafrost regions). For sites with records initiated prior to 2000, the rate for the entire available record is provided along with the rate for the period after 2000. (Note records for some sites only began after 2007 as shown in Fig. 5.22).

Region	Sites	Entire Record	Since 2000
Central Mackenzie Valley †	Norman Wells (NW), Wrigley (Wr)	+0.1 to +0.2	<+0.1 to +0.2
Northern Mackenzie Valley	Norris Ck (No), KC-07(KC)	NA	+0.4 to +0.7
Baffin Island	Pond Inlet (PI)	NA	+0.7
High Canadian Arctic	Resolute (Re), Eureka (Eu)	NA	+0.4 to +0.7
High Canadian Arctic	Alert (Al), BH5, BH1, BH2	+0.53, +0.3 to +0.4	+1.2, +0.7 to +0.9
Alaskan Arctic plain	West Dock (WD), Deadhorse (De), Franklin Bluffs (FB), Barrow (Ba)	+0.33 to +0.81	+0.36 to +0.66
Northern foothills of the Brooks Range, Alaska	Happy Valley (HV), Galbraith Lake (GL)	+0.25 to +0.37	+0.21 to +0.35
Southern foothills of the Brooks Range, Alaska †	Coldfoot (Co), Chandalar Shelf (CS), Old Man (OM)	+0.07 to +0.31	+0.13 to +0.18
Interior Alaska †	College Peat (CP), Birch Lake (BL), Gulkana (Gu), Healy (He)	+0.03 to +0.15	−0.05 to +0.02
North of West Siberia	Urengoy 15-06 and 15-10 (Ur)	+0.31 to +0.47	+0.1 to +0.19
Russian European North	Bolvansky 56, 59, and 65 (Bo)	+0.18 to +0.46	+0.1 to +0.83
Svalbard	Janssonhaugen (Ja)	+0.7	+0.7
Northern Scandinavia †	Tarfalarggen (Ta), Iskoras Is-B-2 (Is)	NA	+0.1 to +0.4
Southern Norway †	Juvvasshøe (Ju)	+0.2	+0.2

Permafrost in this region has generally warmed since the mid-1980s, with less warming observed since 2000 (Table 5.3), corresponding to a period of steady air temperatures. In contrast, greater recent warming has been observed in the colder permafrost of the northern Mackenzie (Norris Ck, KC-07 in Fig. 5.22a and Table 5.3) with 2014/15 temperatures higher than those recorded over the previous 5–7 years, reflecting an increase in air temperatures over the last decade (Fig. 5.21).

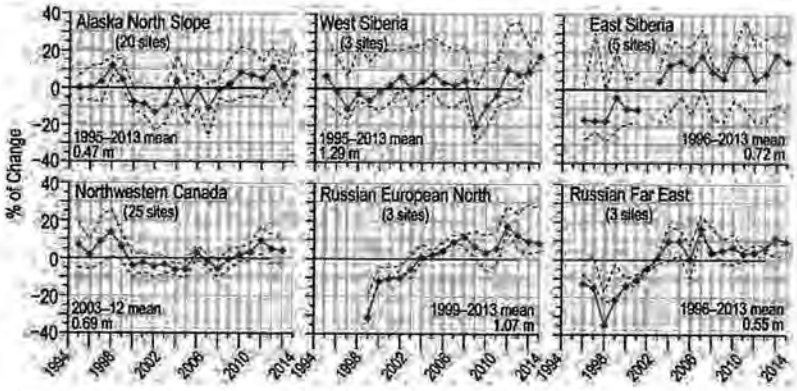

FIG. 5.23. Long-term active-layer change from selected sites in six different Arctic regions as observed by the Circumpolar Active Layer Monitoring project (Shiklomanov et al. 2012). The data are presented as annual percentage deviations from the mean value for the period of observations. Thaw depth observations from the end of the thawing season were used. Only sites with at least 10 years of continuous thaw depth observations are shown in the figure. Solid red lines show mean values. Dashed black lines represent maximum and minimum values. In the Nordic countries (not shown here) active layer records (1996–2015) indicate a general increase in ALT since 1999. Maximum ALT was observed in 2011 followed by a period of thinner active layers.

Mean temperatures for 2014/15 in the upper 25 m of the ground at Alert, northernmost Ellesmere Island in the high Canadian Arctic, were among the highest recorded since 1978 (Fig. 5.22c). Since 2010, temperatures have changed little or even declined, consistent with lower air temperatures since 2010 (Smith et al. 2015). However, higher permafrost temperature at 15-m depth in 2014/15 compared to 2013/14 appears to reflect an increase in air temperature since 2013. Since 2000, Alert permafrost temperatures have increased at a higher rate (Table 5.3) than that for the entire record (Smith et al. 2015), consistent with air temperature anomaly patterns (Fig. 5.21). Short records, from other high Arctic sites in the Queen Elizabeth Islands (Resolute and Eureka) and on Baffin Island (Pond Inlet) in the eastern Arctic, indicate some cooling of permafrost since 2012/13 at 10–15-m depth (Fig. 5.22c). However, a general warming trend is observed (Table 5.3) with higher temperatures in 2014/15 than in 2008/09 when measurements began.

Similar to northern Alaska and the Canadian high Arctic, permafrost temperature has increased by 1–2°C in northern Russia during the last 30 to 35 years. In the Russian European North and in the western Siberian Arctic, for example, temperatures at 10-m depth have increased by ~0.4°C to 0.6°C decade^{-1} since the late 1980s at colder permafrost sites (in Fig. 5.22d, Bolvansky #59, Urengoy #15-5, and #15-10). Less warming has been observed at warm permafrost sites (Table 5.3; in Fig. 5.22d, sites Bolvansky #56 and Urengoy #15-6; Drozdov et al. 2015).

In the Nordic countries (including Svalbard), regional warming and thawing of permafrost have been observed recently (Christiansen et al. 2010; Isaksen et al. 2011; Farbrot et al. 2013). Since 2000, temperature at 20-m depth has increased between 0.1°C and 0.7°C decade^{-1} (Fig. 5.22d; Table 5.3) with lower rates of increase occurring at sites in the discontinuous permafrost zone that are affected by latent heat exchange at temperatures close to 0°C. Higher temperature increases occurred at colder permafrost sites on Svalbard and in northern Scandinavia. In southern Norway permafrost was warmer in 2015 compared to 2014, a warming that followed a period of cooling between 2011 and 2014.

Active layer thickness [determined by probing according to Brown et al. (2000) and Shiklomanov et al. (2012)] at North Slope and Alaska Interior locations was on average greater in 2015 than in 2014 (Fig. 5.23). An increase in the thickness of the ALT indicates warming surface temperature. Of 26 North Slope sites observed in 2015, only nine had ALT values within 1 cm of those observed in 2014, while the majority of sites had greater ALT values than in 2014. The average ALT in 2015 for the 20 North Slope sites with records of at least 10 years was 0.51 m, which is 3 cm higher than the 1995–2013 average. In the interior of Alaska, three of the four active sites reported an ALT increase in 2015. The most pronounced change occurred at a site where surface cover was burned in 2010. Here ALT was 1.78 m in 2015, which is 0.10 m greater than the 2014 value and 1.23 m greater than the prefire 1990–2010 average.

Records from 25 sites with thaw tubes in the Mackenzie Valley, northwestern Canada, indicate that ALT in 2014 (the most recent year data are available) was

on average about 4% greater than the 2003–12 mean (Fig. 5.23). Although ALT in this region has generally increased since 2008 (Duchesne et al. 2015), there has been a decrease since 2012.

In Russia, active layer observations were conducted at 44 sites in 2015. Since 2009, a progressive increase in ALT is evident for western Siberian locations (Fig. 5.23), with a substantial increase in 2015 of 0.05–0.20 m. Locations in the Russian European North have been characterized by almost monotonic thickening of the active layer over the 1999–2012 period. However, after reaching its maximum in 2012, the ALT decreased for three consecutive years (Fig. 5.23). In central Siberia (Low Yenisey region) ALT increased by 0.07–0.10 m, while ALT in the East Siberian region (Yakutsk) was largely unchanged from 2014 values. In northeastern Siberia, ALT in 2015 was 4% lower than the 2014 peak values. Similarly, in Chukotka (Russian Far East) 2015 ALT values were on average 2% lower than in 2014 (Fig. 5.23).

However, ALT was still greater in 2012–15 than the long-term average value. The summer of 2014 was particularly warm in the Nordic countries and contributed to the thickest active layer measured to date at some places. On Svalbard (Janssonhaugen) ALT increased by 10% in 2015 compared to the 2000–14 mean and was the highest in the entire 1998–2015 observational record.

j. Ozone and UV radiation—G. Bernhard, I. Ialongo, J.-U. Grooß, J. Hakkarainen, B. Johnsen, G.L. Manney, V. Fioletov, A. Heikkilä, K. Lakkala

The minimum Arctic daily total ozone column (TOC) measured by satellites (Levelt et al. 2006) in March 2015 was 389 Dobson Units (DU). Measurements from March are used for assessing the temporal evolution of Arctic ozone because chemically induced loss of ozone typically peaks in the month of March (WMO 2014). The March 2015 value was 17 DU (5%) above the average of 372 DU for the period of available measurements (1979–2014) and 23 DU (6%) above the average for the past decade, 2005–14 (Fig. 5.24). The record low was 308 DU in 2011. Figure 5.24 also indicates that the Arctic ozone interannual variability is large: the standard deviation for the period 1979–2014 is 35 DU. This large variability is caused by dynamical effects that affect vortex size and longevity, transport of ozone into the lower stratosphere, and stratospheric chemistry via its sensitivity to temperature (e.g., Tegtmeier et al. 2008; WMO 2014).

Between December 2014 and April 2015, ozone concentrations measured at an altitude of 20 km by the Microwave Limb Sounder (MLS) aboard the *Aura* satellite were the highest in the MLS record, which started in August 2004 (Manney et al. 2015). The altitude of 20 km is representative of the lower stratosphere (altitude range of 15 km to 25 km) where chemical destruction of ozone is typically observed in spring when temperatures drop below –78°C (equal to about –108°F or 195 K). Chemically induced loss of ozone was minimal in the spring of 2015 because of a minor sudden stratospheric warming (SSW) event in early January. This event caused lower stratospheric temperatures to rise above the critical temperature for the formation of polar stratospheric clouds, which is a prerequisite for heterogeneous chemical reactions that destroy ozone. A second reason for the abnormally high ozone concentrations observed in 2015 was larger-than-usual transport of ozone-rich air into the lower stratosphere from higher altitudes, as observed by MLS (Manney et al. 2015). As a consequence, TOCs in the spring of 2015 were relatively high (Figs. 5.24, 5.25b).

Spatial deviations of monthly average TOCs from historical (2005–14) means were estimated with measurements by the Ozone Monitoring Instrument (OMI), which is collocated from MLS on the *Aura* satellite (Figs. 5.25a, 5.25b). Monthly average TOCs for March 2015 exceeded historical means by more than 10% over Iceland, southern Greenland, the Davis Strait between Greenland and Canada, and eastern Canada (Fig. 5.25a). In contrast, TOCs over most of Siberia were 2.5%–7.5% below the 2005–14 average

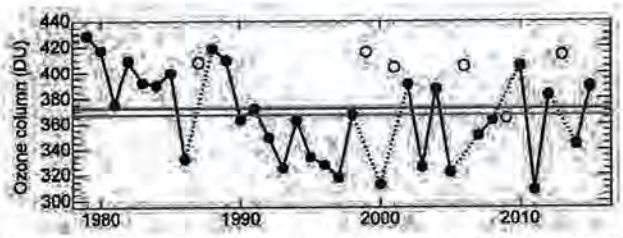

FIG. 5.24. Time series of area-averaged minimum total ozone (DU) for Mar in the Arctic, calculated as the minimum of daily average column ozone poleward of 63° equivalent latitude (Butchart and Remsberg 1986). Open circles represent years in which the polar vortex broke up before Mar. Ozone in those years was relatively high due to mixing with air from lower latitudes and higher altitudes and a lack of significant chemical ozone depletion. Red and green lines indicate the average TOC for 1979–2014 and 2005–14, respectively. [Sources: Data are adapted from Müller et al. (2008) and WMO (2014), updated using ERA-Interim reanalysis data (Dee et al. 2011). Ozone data from 1979 to 2012 are based on the combined total column ozone database version 2.8 produced by Bodeker Scientific (www.bodekerscientific.com/data/total-column-ozone). Data for 2013–15 are from OMI.]

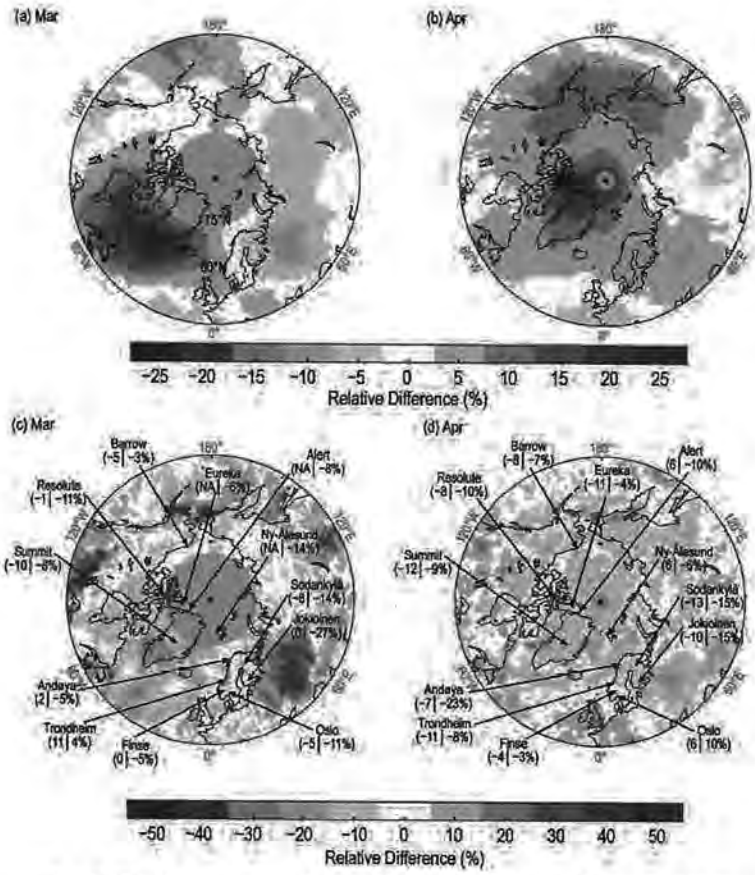

FIG. 5.25. Anomalies of total ozone column and the noontime UV index in 2015 relative to 2005–14 means. TOC anomaly for (a) Mar and (b) Apr. UVI anomaly for (c) Mar and (d) Apr (first value in parenthesis). Data are based on measurements from the OMI. Monthly means calculated from OMTO3 Level 3 total ozone products (Bhartia and Wellemeyer 2002) that are provided in 1° × 1° spatial gridding. (c) and (d) also indicate UVI anomalies measured by ground-based instruments at 12 locations (second value presented). Gray shading indicates areas where no OMI data are available.

with somewhat larger negative departures east of Moscow. Monthly average TOCs for April 2015 were above 2005–2014 means over almost the entire Arctic (Fig. 5.25b). Positive TOC anomalies between 10% and 20% were observed at the North Pole, northern Greenland, and the Canadian Arctic Archipelago.

UV radiation is quantified with the UV index (UVI), a measure of the ability of UV radiation to cause erythema (sunburn) in human skin (WHO 2002). In addition to its inverse dependence on TOC, the UVI depends greatly on the sun angle, cloud cover, and surface albedo (Weatherhead et al. 2005). In the Arctic, the UVI ranges from 0 to about 7, with sites closest to the North Pole having the smallest peak radiation and UVI values <4 all year. UVI values <5 indicate low to moderate risk of erythema (WHO 2002).

Maps shown in Figs. 5.25c,d quantify differences of monthly average noontime UVIs from historical (2005–14) means for March and April and are based on observations derived from OMI. The OMI UV algorithm uses a surface albedo climatology (Tanskanen et al. 2003) that does not change from year to year. At places where the actual surface albedo deviates greatly from the OMI albedo climatology (e.g., when snowmelt occurred earlier than usual), OMI UVI data may be biased by more than 50%, although differences in absolute values rarely exceed 2 UVI units (Bernhard et al. 2015). Figures 5.25c,d therefore also compare UVI anomalies measured by OMI and ground-based instruments deployed throughout the Arctic and Scandinavia. Anomalies derived from the two datasets agree to within ±12% at all locations, with the exception of Andøya for April (OMI overestimates the actual anomaly by 16%) and Jokioinen for March (overestimate by 27% or 0.3 UVI units). The large discrepancy for Jokioinen can be explained by early snowmelt on 9 March while the OMI climatology assumes snow cover through the month of March. Persistent cloud cover in the second half of March also contributed to this discrepancy.

Monthly average noontime UVIs for March 2015 were below the 2005–14 means in a belt stretching from the Greenland Sea and Iceland in the east to Hudson Bay and the Canadian Arctic Archipelago in the west (Fig. 5.25c). This region roughly agrees with the region where TOCs were abnormally high in March 2015 (Fig. 5.25a), but UVI anomalies show a larger spatial variability than TOCs because of their added dependence on cloud cover. Monthly average noontime UVIs for April 2015 were 5%–15% below the 2005–14 means over almost the entire Arctic (Fig. 5.25d), consistent with the positive ozone anomalies observed in this month (Fig. 5.25b).

6. ANTARCTICA—S. Stammerjohn, Ed.

a. *Overview*—S. Stammerjohn

In strong contrast to 2014, 2015 was marked by low regional variability in both atmospheric and oceanic anomalies, at least for the first half of the year. The Antarctic-wide distribution of anomalies coincided with a strong positive southern annular mode (SAM) index. However, by October; the high-latitude response to El Niño became evident, but the associated anomalies were rather atypical compared to the mean response from six previous El Niño events. Simultaneously, a somewhat tardy but unusually large and persistent Antarctic ozone hole developed. These springtime conditions imparted strong regional contrasts late in the year, particularly in the West Antarctic sector. Other noteworthy Antarctic climate events from 2015 are below:

- For most of the year surface pressure was lower and temperatures were cooler than the 1981–2010 climatology, along with stronger-than-normal circumpolar westerly winds, slightly higher-than-normal precipitation over the ocean areas, and mostly shorter-than-normal melt seasons on the continent. These anomalies were consistent with the positive SAM index registered in all months except October. February had a record high SAM index value of +4.92 (13% higher than the previous high value recorded over 1981–2010).
- There was an abrupt but short-lived switch in the mean surface temperature anomaly for the continent (from cold to warm) and a weakening of the negative surface pressure anomaly in October 2015. These atmospheric circulation changes coincided with the emerging high-latitude response to El Niño, the ozone hole, and a shift in the SAM index from positive to negative.
- The 2015 Antarctic ozone hole was amongst the largest in areal coverage and most persistent, based on the record of ground and satellite observations starting in the 1970s. This very large ozone hole was caused by unusually weak stratospheric wave dynamics, resulting in a colder- and stronger-than-normal stratospheric polar vortex. The persistently below-normal temperatures enabled larger ozone depletion by human-produced chlorine and bromine compounds, which are still at fairly high levels despite their continuing decline resulting from the Montreal Protocol and its Amendments.
- Although the 2015 El Niño produced strong atmospheric circulation anomalies in the South Pacific, thus affecting temperatures and sea ice in the West Antarctic sector, its impact across the rest of Antarctica was weaker due to an atypical teleconnection pattern.
- There was a continuation of near-record high Antarctic sea ice extent and area for the first half of 2015, with 65 sea ice extent and 46 sea ice area daily records attained by July. However, at mid-year, there was a reversal of the sea ice anomalies, shifting from record high levels in May to record low levels in August. This was then followed by a period of near-average circumpolar sea ice (relative to the 36-year satellite record).
- Together with unusually high sea ice extent, particularly in the West Antarctic sector, SSTs were also cooler than average, in contrast to warmer-than-normal SSTs equatorward of the polar front. South of the polar front, sea surface height anomalies were negative, consistent with the mostly positive SAM index. Compared to 2014, there was a small decrease in sea level detected around the continental margin as well, leading to a slight increase in the estimated volume transport of the Antarctic Circumpolar Current. These changes are, however, superimposed on longer-term increases in sea level and a potential small decrease in volume transport. The 2015 deep ocean observations at 140°E indicate a continued freshening of Antarctic Bottom Water, relative to observations in the late 1960s and more frequent observations since the 1980s.

Details on the state of Antarctica's climate in 2015 and other climate-related aspects of the Antarctic region are provided below, starting with the atmospheric circulation, surface observations on the continent (including precipitation and seasonal

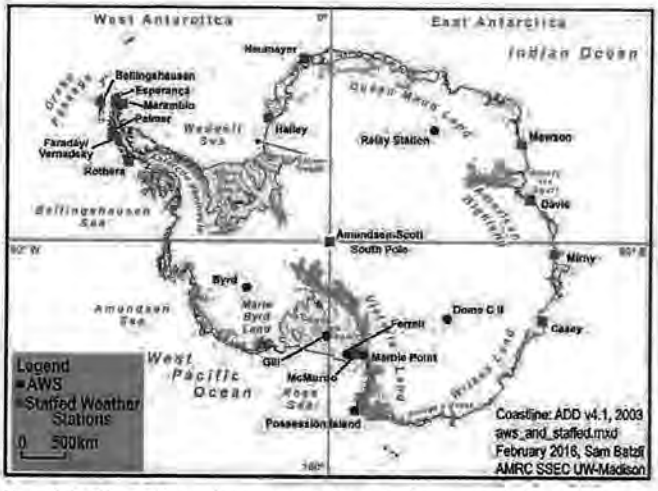

FIG. 6.1. Map of stations and other regions used throughout the chapter.

melt), ocean observations (including sea ice and ocean circulation), and finally the Antarctic ozone hole. Newly included this year is the southern high latitude response to El Niño (Sidebar 6.1) and the state of Antarctic ecosystems in the face of climate perturbations (Sidebar 6.2). Place names used in this chapter are provided in Fig. 6.1.

b. Atmospheric circulation—K. R. Clem, S. Barreira, and R. L. Fogt

The 2015 atmospheric anomalies across Antarctica were dominated by below-average surface temperatures over much of coastal and interior Antarctica from January to September, particularly across the Antarctic Peninsula and the surrounding Weddell and Bellingshausen Seas. Negative pressure anomalies in the Antarctic troposphere during the first half of the year weakened in August, while the stratosphere poleward of 60°S became very active beginning in June with strong negative pressure and temperature anomalies and an amplification of the stratospheric vortex. Using a station-based SAM index (normalized difference in zonal mean sea level pressure between 40°S and 65°S; Marshall 2003), the generally low pressure conditions gave rise to positive SAM index values, which were observed in every month except October during 2015. Figure 6.2 depicts a vertical cross section of the geopotential height anomalies (Fig. 6.2a) and temperature anomalies (Fig. 6.2b) averaged over the polar cap (60°–90°S), as well as the circumpolar zonal wind anomalies (Fig. 6.2c) averaged over 50°–70°S and the Marshall (2003) SAM index average for each month.

Climatologically, the year was split into four time periods (denoted by vertical red lines in Fig. 6.2) that were selected based on periods of similar temperature and pressure anomalies (Fig. 6.3). The composite anomalies (contours) and standard deviations (from the 1981–2010 climatological average; shading) for each of the time periods are shown in Fig. 6.3; surface pressure anomalies are displayed in the left column and 2-m temperature anomalies in the right column.

During January–March, the large-scale circulation was marked with negative geopotential height (Fig. 6.2a) and surface pressure (Fig. 6.3a) anomalies over Antarctica and positive surface pressure anomalies over much of the middle latitudes. The Marshall SAM index was strongly positive, and reached a record monthly mean high value during February [+4.92; Fig. 6.2; Marshall (2003); SAM index values start in 1957]. At this time, the circumpolar zonal winds exceeded 2 m s^{-1} (>1.5 standard deviations) above the climatological average throughout the

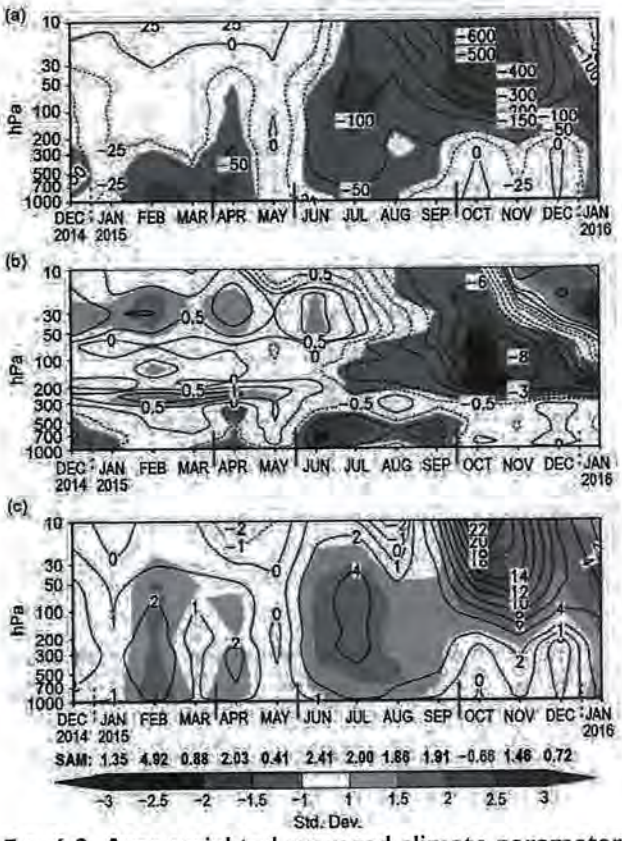

FIG. 6.2. Area-weighted averaged climate parameter anomalies for the southern polar region in 2015 relative to 1981–2010: (a) polar cap (60°–90°S) averaged geopotential height anomalies (contour interval is 50 m up to ±200 m with additional contour at ±25 m, and 100 m contour interval after ±200 m); (b) polar cap averaged temperature anomalies (contour interval is 1°C up to ±4°C with additional contour at ±0.5°C, and 2°C contour interval after ±4°C); (c) circumpolar (50°–70°S) averaged zonal wind anomalies (contour interval is 2 m s^{-1} with additional contour at ±1 m s^{-1}). Shading represents standard deviation of anomalies from the 1981–2010 climatological average. (Source: ERA-Interim reanalysis.) Red vertical bars indicate the four separate climate periods used for compositing in Fig. 6.2; the dashed lines near Dec 2014 and Dec 2015 indicate circulation anomalies wrapping around the calendar year. Values from the Marshall (2003) SAM index are shown below panel (c) in black (positive values) and red (negative values).

troposphere and lower stratosphere (Fig. 6.2c). Much of the coastal Antarctic 2-m temperatures were below average (Fig. 6.3b), with the exception of areas of the Ross Ice Shelf and Wilkes Land (~90°E–180°). Positive temperature anomalies were observed throughout much of the stratosphere over the polar cap (Fig. 6.2b).

Positive SAM index values continued during April but weakened in May. This was due to a strong positive surface pressure anomaly southwest of Australia, while the remainder of the middle latitudes experi-

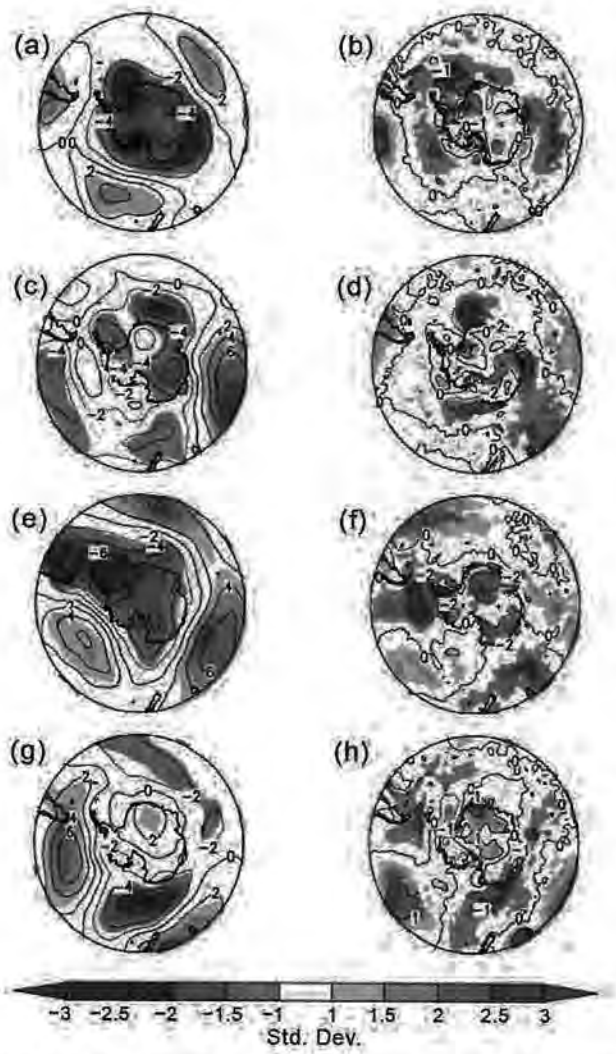

FIG. 6.3. (left) Surface pressure anomalies and (right) 2-m temperature anomalies relative to 1981–2010 for (a) and (b) Jan–Mar 2015; (c) and (d) Apr–May 2015; (e) and (f) Jun–Sep 2015; and (g) and (h) Oct–Dec 2015. Contour interval for (a), (c), (e), and (g) is 2 hPa; contour interval for (b) and (h) is 1°C and contour interval for (d) and (f) contour interval is 2°C. Shading represents standard deviations of anomalies relative to the selected season from the 1981–2010 average. (Source: ERA-Interim reanalysis.)

enced negative surface pressure anomalies with a weakening of the circumpolar zonal winds in May (Fig. 6.2c). Much of East Antarctica was colder than average, particularly offshore along coastal Queen Maud Land (30°W–0°) and portions of the Ross Sea westward towards Mirny station (~90°E), while the Amundsen Sea and the Ronne-Filchner Ice Shelf were slightly warmer than average (Fig. 6.3d).

During June–September, negative polar-cap averaged geopotential height anomalies and positive circumpolar zonal wind anomalies were observed throughout the troposphere and stratosphere. Strong positive surface pressure anomalies occurred over the South Pacific, southwest of Australia, and over the South Atlantic, while strong negative surface pressure anomalies occurred over the Weddell Sea (Fig. 6.3e); these conditions led to positive SAM index values through September. Antarctic 2-m temperatures were primarily below average (Fig. 6.3f), with anomalies over the Antarctic Peninsula, Bellingshausen Sea, and eastern Amundsen Sea more than 2.5 standard deviations below the climatological average.

By October–December, positive surface pressure and 2-m temperature anomalies developed over interior East Antarctica, with the strongest warming noted over Queen Maud Land, while the Drake Passage and coastal Wilkes Land remained colder than average (Figs. 6.3g,h). A strong negative surface pressure anomaly was observed south of New Zealand and a strong positive surface pressure anomaly was observed in the southeastern South Pacific, likely tied to the strengthening of the El Niño conditions in the tropical Pacific. These circulation anomalies over the South Pacific brought cold, southerly flow to the coastal and offshore regions of Wilkes Land and the offshore region of the northwestern Antarctic Peninsula, respectively. Meanwhile, the stratosphere over the polar cap became very active after September. Negative temperature and geopotential height anomalies of 1–2 standard deviations below the climatological average propagated down through the stratosphere from October to December. A marked strengthening of the stratospheric circumpolar vortex occurred in response to the stratospheric cooling, with positive zonal wind anomalies exceeding 1–2 standard deviations above the climatological average throughout the stratosphere to finish the year. Over this time period (October–December) the SAM index values also weakened, and a negative value was observed in October 2015, coincident with the weaker and more regional nature of the near-surface conditions (Fig. 6.3).

c. Surface manned and automatic weather station observations—S. Colwell, L. M. Keller, M. A. Lazzara, A. Setzer, R. L. Fogt, and T. Scambos

The circulation anomalies described in section 6b are discussed here in terms of observations at staffed and automatic weather stations (AWS). Climate data that depict regional conditions are displayed for four staffed stations (Bellingshausen on the Antarctic Peninsula, Halley in the Weddell Sea, Mawson in the Indian Ocean sector, and Amundsen-Scott at the South Pole; Figs. 6.4a–d) and two AWSs (Byrd in West

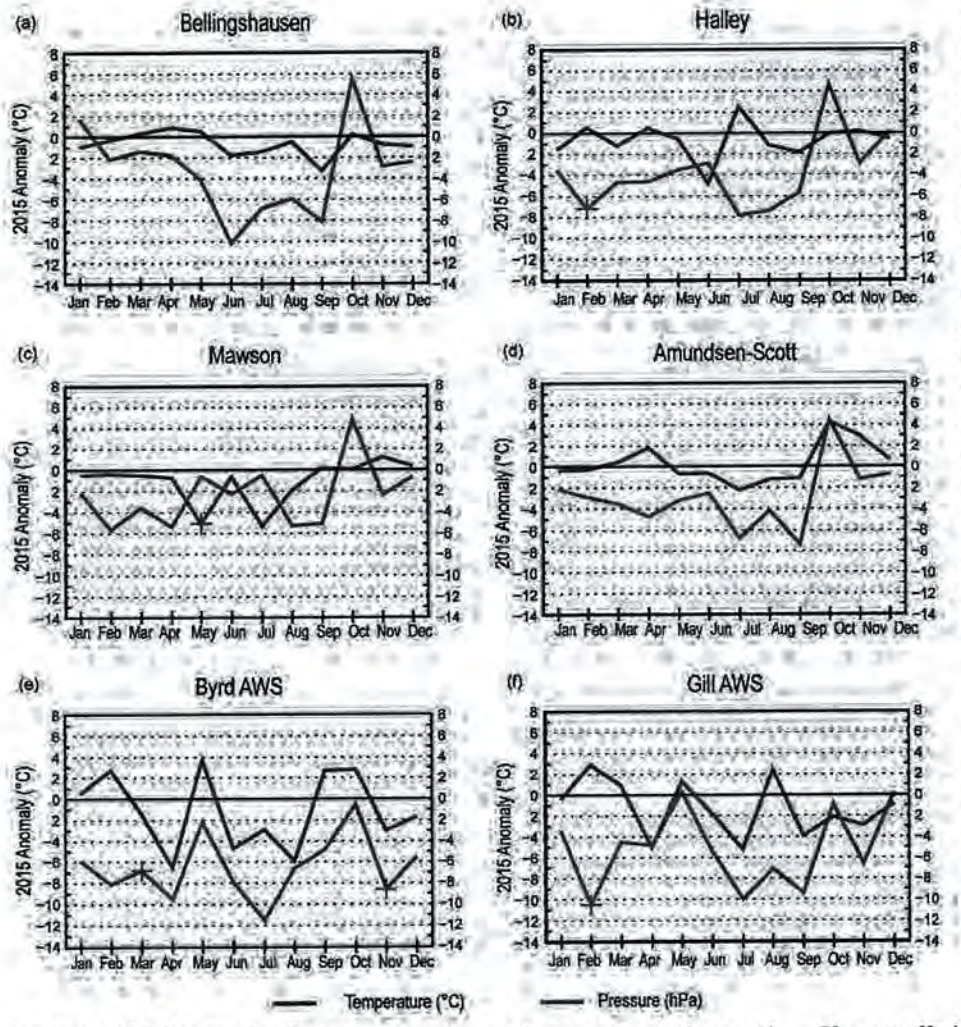

FIG. 6.4. 2015 Antarctic climate anomalies at six representative stations [four staffed (a)–(d) and two automatic (e)–(f)]. Monthly mean anomalies for temperature (°C) and surface pressure (hPa) are shown, with + denoting record anomalies for a given month at each station in 2015. All anomalies are based on differences from 1981–2010 averages, except for Gill, which is based on averages during 1985–2013. Observational data start in 1968 for Bellingshausen, 1957 for Halley and Amundsen-Scott, 1954 for Mawson, 1985 for Gill AWS, and 1981 for Byrd AWS.

Antarctica and Gill on the Ross Ice Shelf; Figs. 6.4e,f). To better understand the statistical significance of records and anomalies discussed in this section, references can be made to the spatial anomaly maps in Fig. 6.3 (the shading indicates the number of standard deviations the anomalies are from the mean).

Monthly mean temperatures at Bellingshausen station (Fig 6.4a) on the western side of the Antarctic Peninsula were similar to the 1981–2010 mean at the start and end of the year, but from May to September, the values were consistently lower than the mean. Midway down on the west side of the Antarctic Peninsula, the temperatures at Rothera (not shown) followed a similar pattern. In the Weddell Sea region, the monthly mean temperatures at Halley (Fig. 6.4b) and Neumayer (not shown) were within ±2°C of the 1981–2010 mean, with the exception of June and July at Halley. In June, the mean monthly value nearly matched the lowest recorded mean monthly value and included a new record for the extreme daily minimum value, which was −56.2°C. The anomalously cold conditions in June were followed by a respite to anomalously warm conditions in July that were then followed by below- to near-average temperatures for the rest of the year.

Around the coast of East Antarctica, all of the Australian stations had near-average temperatures at the start and end of the year and colder-than-average temperatures from April to August, except for Casey (not shown) in June when the temperature was slightly higher than average. Davis (not shown) and Mawson (Fig. 6.4c) both had very low monthly mean temperatures in May (a record low at Mawson). Temperatures at Mawson were also anomalously low again in July. At Amundsen-Scott station (Fig. 6.4d), the monthly mean temperatures were close to the long-term means with the exception of October and November when they were warmer than average.

In the Antarctic Peninsula, an all-time record warm air temperature for the continent may have been set at Esperança on 24 March, reaching +17.5°C during an intense foehn wind event that spanned much of the northeastern Peninsula. Temperatures rose as much as 30°C within 48 hours as an intense high pressure region over the Drake Passage and strong low pressure over the northwestern Weddell Sea drove strong downslope winds all along eastern Graham Land. An automated sensor at Foyn Point in